Laboratory Experiments of Multi-phase Plumes in Stratification and Crossflow

by

Scott A. Socolofsky

Submitted to the Department of Civil and Environmental Engineering
in partial fulfillment of the requirements for the degree of

Doctor of Philosophy in Civil and Environmental Engineering

at the

MASSACHUSETTS INSTITUTE OF TECHNOLOGY

February 2001

Author .....
Department of Civil and Environmental Engineering
November 9, 2000

Certified by .....
Dr. E. Eric Adams
Senior Research Engineer and Lecturer
Thesis Supervisor

Accepted by .....
Oral Buyukozturk
Chairman, Department Committee on Graduate Students

Laboratory Experiments of Multi-phase Plumes in Stratification and Crossflow

by

Scott A. Socolofsky

Submitted to the Department of Civil and Environmental Engineering
on November 9, 2000, in partial fulfillment of the
requirements for the degree of
Doctor of Philosophy in Civil and Environmental Engineering

Abstract

This thesis presents laboratory experiments of bubble, droplet, and sediment plumes in stratification and crossflow. The experiments were conducted to study the behavior of multi-phase plumes in the deep ocean, with applications ranging from carbon sequestration to the fate of oil and gas released from an oil well blowout.

Experimental techniques included LASER induced fluorescence, shadowgraph visualization, salinity and dye concentration profiling, stratification generated by the two-tank method (using a 1.2 m square by 2.4 m deep, glass-walled tank), and crossflow generated by a towed source (using a 28 m long flume with 0.8 m square cross-section).

Size spectra of droplets and bubbles were measured using a phase Doppler particle analyzer. To control particle size, sediment was also used; sediment size was measured using a micrometer. Slip velocities among all buoyancy sources ranged from 3 to 35 cm/s.

Stratified experiments investigated the dependence of plume properties on the non-dimensional slip velocity, $U_N = u_s/(BN)^{1/4}$, where u_s is the slip velocity, B is the total kinematic buoyancy flux, and N is the Brunt-Vaisälä buoyancy frequency. First, U_N predicts the transitions among characteristic plume types, and a new plume type was identified where the bubbles are dispersed by the intruding fluid. Second, non-dimensional variables (including characteristic length scales, volume and buoyancy fluxes, and fraction peeled) correlate with U_N and were chosen to provide insight and calibration data to models.

Crossflow experiments demonstrated fractionation (sorting of bubbles based on slip velocity) and separation (entrained fluid completely separating from the dispersed phase). Plumes were observed to have a fully-developed plume stage followed by separation at a critical height, h_S, dependent on B, u_s, and the crossflow velocity, u_∞. A single-phase model was applied to these plumes by treating the separated fluid as a buoyant momentum jet. Stratified crossflow experiments showed that separation occurs at the lower of h_S or the peel height in stagnant stratification (which correlates with U_N).

Thesis Supervisor: Dr. E. Eric Adams
Title: Senior Research Engineer and Lecturer

Acknowledgments

This work was supported by the MIT Sea Grant College Program, the Federal Energy Technology Center of the U.S. Department of Energy, and the Deep Spills Task Force, comprised of the Minerals Management Service of the U.S. Department of Interior and a consortium of 13 member oil companies of the Offshore Operations Committee.

In additional to financial support, many people at MIT contributed to this research. My advisor, E. Eric Adams was invaluable in providing direction and insight. I am thankful for his willingness to spend time discussing my research questions and for his generosity in involving me in the Hawai'i project. His support for my stay at the University of Hawai'i (UH) to gather the PDPA measurements is greatly appreciated, and I thank Steve Masutani at UH for opening his facilities to us. I would also like to thank Ole S. Madsen for providing the flume for the crossflow experiments. A special thanks goes to my research committee— for their insight, understanding and support I am very grateful. A number of students also contributed to this research. Specifically, I thank Brian Crounse for his efforts in modeling, his contribution to Chapter 2, and his help with the PDPA measurements. Anna Leos-Urbel helped build and run the crossflow experiments; for her assistance I am very thankful. Finally, I wish to thank Gordon Ruggaber for helping to construct important peripheral equipment for the research tank and for his flexibility in sharing the facility.

Outside the research arena, the support of my friends was a great help. I thank all my friends who continually asked about my experiments, hoping I would say I've finally finished them, but offering words of encouragement when another part of the apparatus needed repair/modification. Their desire to see me succeed helped push me to the completion of this project. Thanks especially to Jeff Niemann for keeping me company over so many lunch hours and for sharing in the MIT Ph.D. experience.

I would also like to thank my family for their constant support; their belief in me gives me the strength to persevere. Lastly, I would like to recognize that the planet I am blessed to study is a gift from God; may we treat it with proper stewardship.

Contents

List of Figures

List of Tables

Chapter 1

Introduction

> "It is not our part to master all the tides of the world, but to do what is in us for the succor of those years wherein we are set, uprooting the evil in the fields that we know, so that those who live after may have clean earth to till. What weather they shall have is not ours to rule."
>
> —J.R.R. Tolkien, *The Return of the King*

Here, Tolkien writes what he thought was a generous view of environmental stewardship—that we should provide those after us with "clean earth to till." Passage of the Clean Water Act in 1972 was a major step by the U.S. Congress in that direction and has resulted in a doubling of the nation's swimmable and fishable waters since its enactment (U.S. EPA 1997). More recently, however, global climate change, due to emissions from the burning of fossil fuels, has been identified as an unfortunate by-product of industrialization. Although the weather is not "ours to rule," a consensus is now growing that providing a clean earth includes protecting the atmosphere from increased levels of CO_2.

This thesis addresses both types of environmental stewardship in the context of the deep ocean (below 800 m). First, CO_2 sequestration is analyzed as a means of pumping CO_2 directly into the ocean, thereby, reducing peak concentrations of CO_2 in the atmosphere and minimizing the overall environmental impact. Second, deep-ocean oil spills, resulting from oil well blowouts and pipeline leaks, are analyzed for clean-up and contingency planning.

Both of these applications can be viewed as particular types of multi-phase plumes. To study these plumes, laboratory experiments, using air, oil and sediment (forming an inverted

plume), were conducted in both stratification and crossflow. The experiments investigate the role of the slip velocity of the dispersed phase in affecting plume behavior, length scaling, pumping flux, and separation criteria.

1.1 Multi-phase plumes

A distinguishing feature of multi-phase plumes, as compared to single-phase plumes, is the possibility of separation between the dispersed phases (the bubbles, droplets, or particles) and the continuous phase (the entrained ambient fluid). Separation occurs when horizontal fluid motion strips entrained fluid away from the dispersed phase. Horizontal motion arises in stratification when the entrained water intrudes into the ambient at a level of neutral buoyancy. Horizontal motion arises in a crossflow due to the crossflow itself.

For clarity, I will use bubbles throughout this thesis to refer to the dispersed phase in a generic multi-phase plume, and I will use bubbles, droplets or particles, as appropriate, when discussing specific plumes.

1.1.1 Typical multi-phase plume applications

In addition to CO_2 sequestration and oil well blowout plumes, multi-phase plumes occur in many applications. These include air bubble plumes used for reservoir destratification (Asaeda & Imberger 1993, Schladow 1993, Lemckert & Imberger 1993), aeration (Wüest et al. 1992), ice prevention in harbors (McDougall 1978), and contaminant containment (Milgram 1983); continuous particle clouds resulting from the release of dredged sediments (HAVIS Environmental 1994, Koh & Chang 1973); and, a host of multi-phase bubble, droplet, and powder flows in industry (Taitel et al. 1995, Johnson & White 1993), one of which is to provide mixing where mechanical stirrers are prohibited due to a hostile environment as in corrosive chemicals or high temperatures (Park & Yang 1997).

Among the environmental applications, reservoir bubble plumes used for destratification and aeration have been discussed in detail in the literature (Asaeda & Imberger 1993, Lemckert & Imberger 1993, Schladow 1993, Hugi 1993, Wüest et al. 1992, Baines & Leitch 1992, Zic

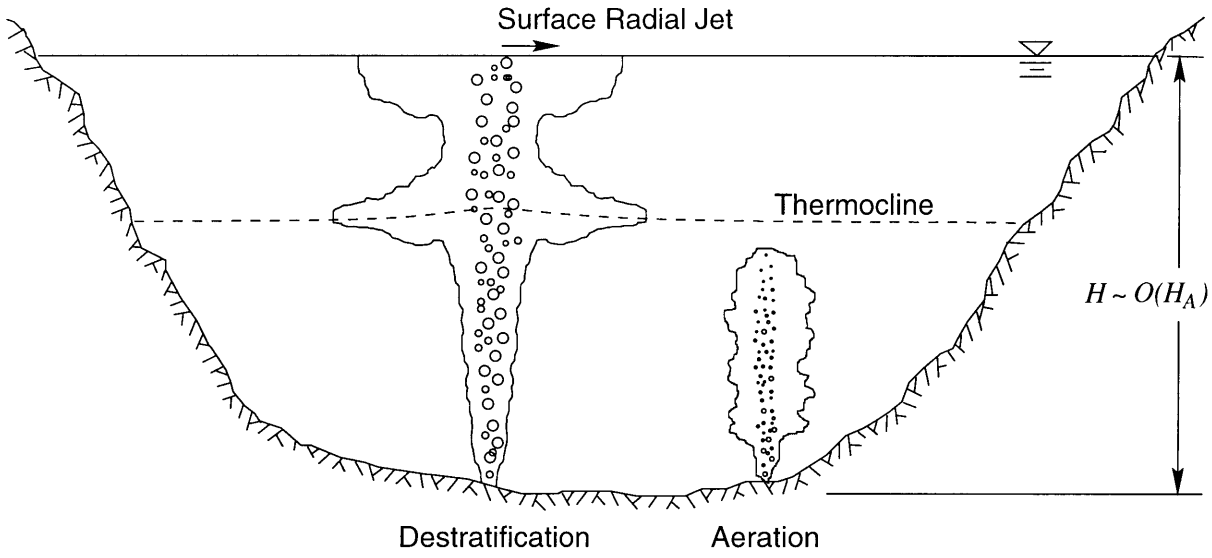

FIGURE 1-1: Schematic of reservoir bubble plumes for destratification and aeration.

et al. 1992, Leitch & Baines 1989, Patterson & Imberger 1989, Milgram 1983, Goossens 1979, McDougall 1978). Figure 1-1 shows a schematic of these plumes. For destratification purposes, the plumes are vigorous, carrying dense bottom water into the epilimnion and eroding the thermocline, the zone of the highest vertical density gradient. Asaeda & Imberger (1993) showed with a calibrated numerical model that the most efficient destratification plumes should have one intermediate intrusion and another intrusion formed by the reservoir surface. In the aeration case, the plumes are weaker, have small bubbles, and are designed to fully dissolve within the hypolimnion and to minimize vertical mixing. Wüest et al. (1992) developed a coupled plume reservoir model for reservoir aeration that included bubble dissolution and tracking of the increased oxygen content in the hypolimnion. As indicated in the figure, reservoirs are generally step stratified and have a depth on the order of the atmospheric pressure head, H_A. Because plume length scales are also of the order H_A, bubble expansion (adiabatic expansion predicted from the Idea Gas Law) has always been included as an important physical process affecting these plumes and is introduced through the reservoir depth, H. For similar sized plumes in the deep ocean, bubble expansion (and, therefore, the injection depth) are negligible, and the ambient stratification is much more

linear. Hence, additional analysis for CO_2 sequestration and oil well blowout plumes is necessary.

1.1.2 Deep-ocean CO_2 sequestration

The subject of man's impact on climate in the context of global warming was first analyzed by Arrhenius in 1896. Arrhenius (1896) predicted that a global mean temperature rise of 8-9 °C would result from increasing atmospheric CO_2 by 2.5-3 times. Estimates have not changed much in 100 yrs, as the latest estimates by the United Nations (UN) Intergovernmental Panel on Climate Change (IPCC), which rely on sophisticated global climate models, give a 2 °C rise for doubled CO_2, expected by the year 2100 (Bolin 1995). Although CO_2 is not the only greenhouse gas, it has the potential for the largest anthropogenic impact to the earth's radiative balance. The current mean CO_2 concentration of about 360 ppm, up 30% from the pre-industrial value, is attributed to a 0.6 °C rise in global mean temperature (Bolin 1995).

As a means of mitigating potential global warming, deep-ocean sequestration of CO_2 has been proposed. The oceans provide a good storage reservoir for CO_2 because they have a capacity about 100 times that of the atmosphere, because they are relatively accessible, and because their stratification inhibits leakage of CO_2 back into the atmosphere. Adams et al. (1994) and Adams & Herzog (1996) reviewed the range of CO_2 injection methods and found that bubble and droplet plumes were the most promising sequestration methods because they are the simplest and the least costly both in terms of energy and maintenance. Both papers addressed the operation of a 500 MWe, coal-fired power plant with 90% CO_2 capture. Coal power was chosen because it represents 85% of the CO_2 emissions in the United States from power production. For such a power plant, 130 kg/s of CO_2 are produced. Assuming a mix of conventional and advanced coal combusters, a 20% energy penalty (the excess energy required to cover the energy costs of sequestration) is believed achievable for the buoyant droplet plume case.

Dewey et al. (1996) analyzed droplet plume injection scenarios at several sites around the world using a meso-scale ocean dispersion model and a global carbon cycle model. Their

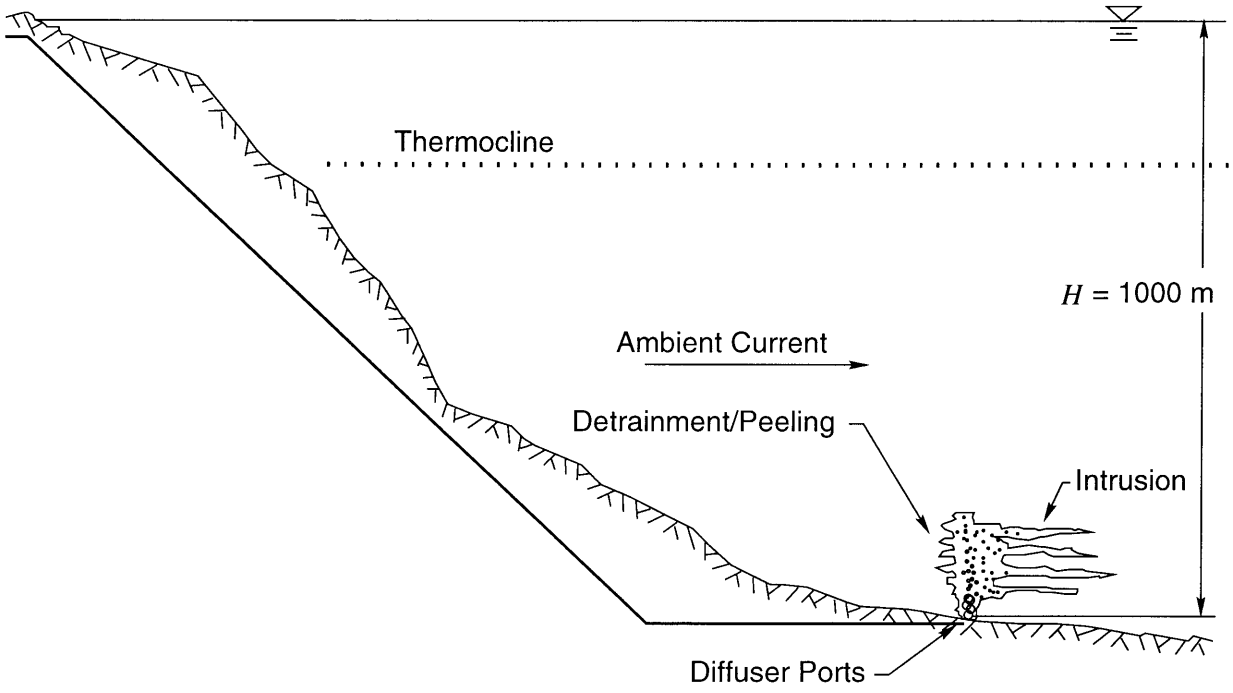

FIGURE 1-2: Schematic of a deep-ocean CO_2 plume with related nomenclature.

sequestration scenarios assumed a 90% capture efficiency and a conservative 25% energy penalty for a pool of one hundred 500 MWe power plants (totaling 0.1 GtC/yr). The analysis identified two features of ocean sequestration. First, compared to the no-sequestration base case, sequestration reduced the increased atmospheric CO_2 concentration from these one hundred plants by 50% over the next 200 yrs. Second, the long-term equilibrium between the oceans and atmosphere was the same for the base case and sequestration scenarios and was reached on a time scale of 1000 yrs. Hence, ocean sequestration reduces the rate of CO_2 increase in the atmosphere and the peak concentration; however, it does not change the long-term impact of fossil fuel burning. Due to the non-linear nature of the climate system, any reduction in atmospheric CO_2 concentration could be significant (Bolin 1995).

Figure 1-2 shows a typical CO_2 droplet plume and the influence of ambient stratification in a weak crossflow. CO_2 is collected land-side and transported to the injection point by a pipeline. The CO_2 is injected around 1000 m depth, where the liquid CO_2 forms immiscible, positively buoyant droplets, likely covered by a hydrate film. A stratified, two-phase plume

results—the droplets entrain ambient fluid and rise through the stratification. Eventually, the denser fluid that is dragged along by the droplets will no longer be supported by their buoyancy, and the plume is said to detrain, or peel, as some of the entrained fluid falls out of the plume. The ejected fluid forms an outer, downdraught plume of dense water. The outer plume comes to rest lower in the profile, intruding at a level of neutral buoyancy. The droplets, however, are not diluted by the entrained water, and they continue to rise through the detrainment zone, forming a secondary plume above the intrusion layer which rises until a second detrainment point is reached. This process continues until the droplets are dissolved into the surrounding fluid and is depicted in Figure 1-2 as a series of intrusion layers.

Currents in the ambient ocean can further affect the CO_2 plume. So long as the ambient current does not overpower the plume, the entrainment and peeling described in the previous paragraph continues; however, as shown in Figure 1-2, the intrusions form asymmetrically and flow downstream with the current, advecting some of the smaller droplets downstream as well. As the current becomes stronger, it begins to strip the entrained fluid away from the droplets, reducing the upward plume flux. When the crossflow becomes strong enough, all of the entrained fluid can be stripped away, leaving the bubbles to rise through water continually refreshed by the crossflow—peeling and intrusion levels would not form, and the CO_2 would be distributed continuously in the water column as the droplets dissolve.

In addition to the effects of stratification and crossflow, deep-ocean CO_2 plumes are complicated by chemistry effects of the dispersed CO_2. First, as the CO_2 dissolves, the CO_2-enriched seawater becomes more dense, just as if additional salt were dissolved into the water. The enriched water peels earlier than predicted for a simple, two-phase plume, and may intrude at a level below the injection point of the plume. Crounse (2000) has shown with a numerical model that a CO_2 plume may be completely shrouded by downdraught plumes due to the density effect of dissolution. Second, at the temperature and pressure in the oceans at 1000 m, clathrate hydrates are thermodynamically stable. Due to their chemistry, they are expected to form a shell around the droplets that would reduce the dissolution rate of the CO_2. Because these chemical processes feedback on the physics, they complicate the plume dynamics.

To address these complications, many researchers have investigated the CO_2 droplet

plume using numerical techniques. An integral model of a CO_2 plume for a 500 MWe power plant was developed by Liro et al. (1992); the model accounted for the dissolution (disappearance) of CO_2 droplets and the possibility of several peeling events, but it neglected the density feedback of the dissolution. Caulfield (1996) extended the Liro et al. (1992) model to include the density effect of CO_2-enriched seawater and predicted the resultant pH change in the far-field water column. Caulfield et al. (1997) also developed a stochastic random-walk model to quantify the time-history pH experience of a passive organism swept through the plume. Based on dose response data compiled by Auerbach et al. (1997), the model was used to estimate passive organism mortality for various plume designs. Among the important parameters determining the organism mortality flux were the intrusion layer thickness, the number of intrusions, and the intrusion layer flux (Caulfield 1996, Caulfield et al. 1997, Adams et al. 1997). The droplet size and the possible formation of clathrate hydrate scales were also important factors, and they are under investigation at a number of high-pressure laboratory facilities (Aya et al. 2000, Ogasawara & Yamasaki 2000, Hirai et al. 2000, Masutani et al. 2000). Although these models and a similar model by Thorkildsen et al. (1994) predict many peeling events, the models must arbitrarily set parameters controlling the separation process because of a lack of experimental observations; thus, organism mortality remains uncertain.

Other researchers have used more physically-based models of the peeling process (e.g. Sato & Hama 2000, Chen et al. 2000, Crounse 2000, Alendal et al. 1998, Asaeda & Imberger 1993, McDougall 1978); however, the amount of peeled water at each detrainment and the location of detrainment events remains arbitrary. The Alendal et al. (1998) and Sato & Hama (2000) models have the highest level of complexity, solving a three-dimensional, eddy-diffusivity model on a fine mesh in the near-field of the plume. Chen et al. (2000) solves a two-dimensional finite difference model to study the effects of currents, allowing for separation between the droplets and the entrained fluid. Unfortunately, detrainment is too fine-scale of an event to be modeled explicitly, even in such rigorous models. The sensitivity analysis by Caulfield (1996) and Adams et al. (1997) shows that potential organism impacts for CO_2 plume injections for a 500 MWe power plant could be avoided by a variety of designs if the peeling parameters could be quantified. The efficiency and performance of each design

would also depend on a detailed understanding of the plume peeling and intrusion dynamics. Therefore, experimental studies of the separation processes for two-phase plumes in stratified and flowing environments are needed.

1.1.3 Deep-ocean oil spills

The desire to tap deep oil reserves in the Gulf of Mexico (GOM) and the North Sea has renewed interest in predicting the fate of oil accidentally released in the deep ocean. Sources of spilled oil include broken pipelines, sunken tankers, and oil well blowouts (Yapa & Zheng 1997*a*, Yapa & Zheng 1999), but oil released from a blowout is potentially the more damaging and more complicated (McDougall 1978, Yapa & Zheng 1997*a*, Yapa & Zheng 1999, Rye et al. 1998, Rygg & Emilsen 1998). Pipeline and tanker leaks involve low flow rates of pure oil or pure gas at small exit velocities; whereas, in the blowout scenario oil is released together with natural gas in variable ratios, depending on geographic location and source formation, under high pressure and through small, broken orifices, giving high exit velocities and uncertain initial conditions. Blowouts may also take from days to months to repair and can have oil flow rates more than one hundred times that from a pipeline leak (Rygg & Emilsen 1998).

Figure 1-3 shows a schematic of an oil well blowout in a strong current. In a weak current the oil and gas would stay together, and several peeling events would occur as shown for a CO_2 plume in Figure 1-2. Here, on the other hand, the oil and gas eventually separate. Near the source, the oil and gas plume rises as a coherent mixture, entraining ambient fluid and advecting it vertically upward. At a critical height, the gas bubbles leave the oil plume, and the two phases separate. The separated gas plume rises with the vector sum of the bubble slip velocity and the current speed, and newly entrained fluid is stripped from the plume by the current and advected downstream. Initially, the separated oil plume behaves like a single-phase plume in a crossflow—it bends over and eventually traps due to the combined effects of the stratification and the crossflow. Then, the oil droplets slowly make their way out of the intrusion level and rise similarly to the gas bubbles and are dispersed over a wide area by the current. The high turbulence near the jet-like region of the blowout might cause

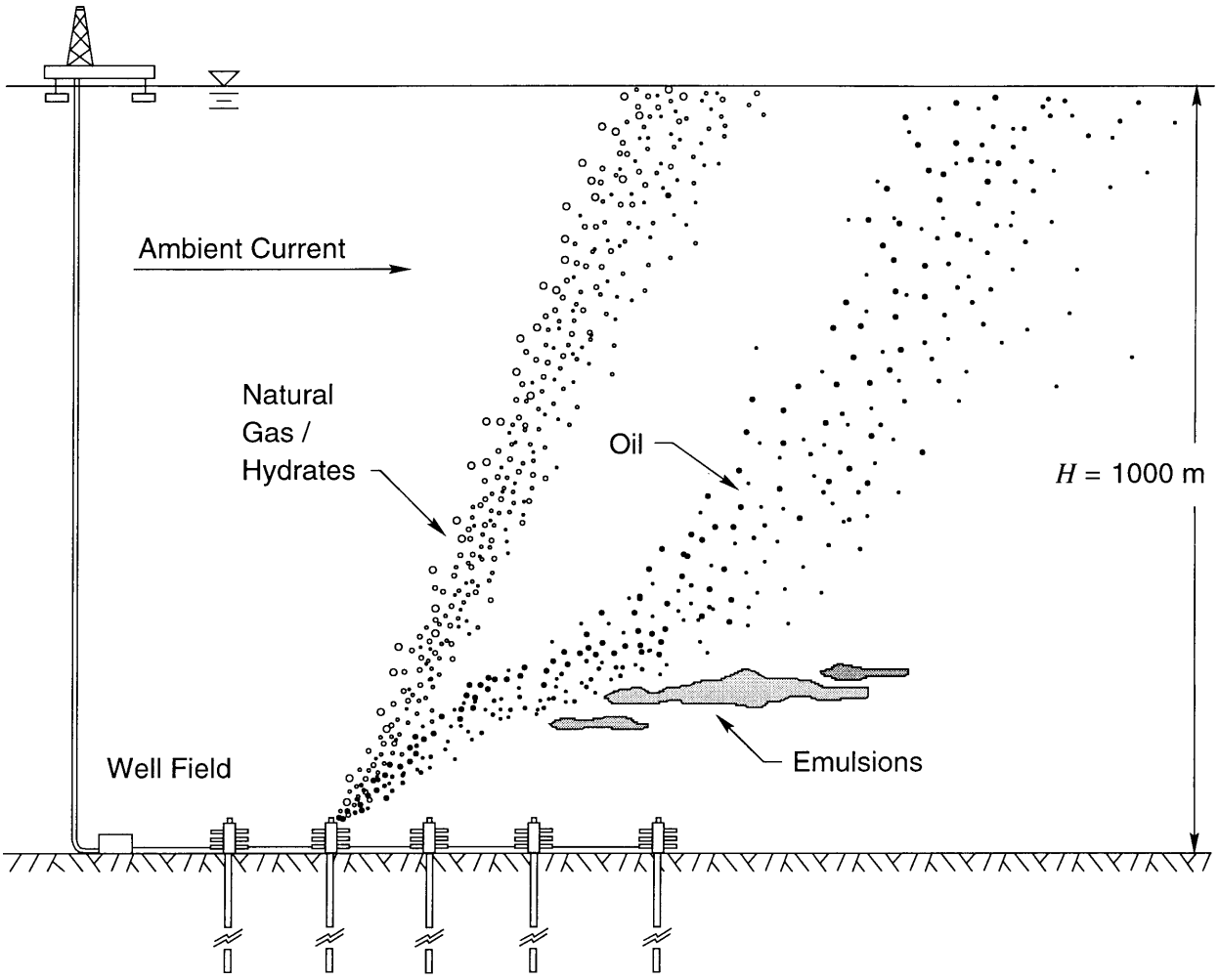

FIGURE 1-3: Schematic of an oil well blowout, showing the separation of the oil and natural gas, the formation of emulsions, and indicating the formation of gas hydrates.

the oil to form an emulsion; the emulsions would coagulate and rise at a very slow velocity. Hydrates may form on the gas bubbles as well. The gas hydrates remain positively buoyant, so they would continue to rise and dissolve in the gas plume.

Two of the early investigations of the behavior of deep-ocean oil well blowouts were by McDougall (1978) and Topham (1975). McDougall (1978) formulated an integral plume model based on laboratory experiments of stratified air-bubble plumes. Topham (1975) performed field experiments with air at 60 m depth in seawater. McDougall (1978) observed that the gas bubbles remain confined to an inner core, surrounded by an annular plume of pure water that rises in the entrainment region and falls in the detrainment zone. Based on his observations, he formulated a integral, double-plume model, where an outer, annular plume was always present surrounding an inner axial plume. McDougall (1978) applied the model to an oil well blowout and predicted that the oil would trap in several intrusion layers and not reach the surface.

Other researchers studying reservoir plumes have extended the double-plume model approach in stratification and investigated the effects of crossflow. Asaeda & Imberger (1993), modified the double-plume representation of McDougall (1978). In the Asaeda & Imberger (1993) model, all the upward moving fluid and bubbles are modeled in a single, integral plume; whereas, the downward, detraining plume, is modeled as an annular, double plume. Hugi (1993) conducted laboratory experiments of bubble plumes in a crossflow. Because of his combination of bubble sizes and crossflow velocities, he did not observe a mixed plume phase. Instead, he observed that the current strips the entrained fluid away and sorts the bubbles so that faster rising bubbles are found at the front of the plume with slower rising bubbles in the wake, as shown in the upper regions of Figure 1-3. Hence, these studies show that both stratification and crossflow can cause separation among the plume phases.

Yapa & Zheng (1997*a,b*) and Yapa & Zheng (1999) developed a rigorous single-plume model for an oil well blowout that includes several effects of stratification, crossflow, and chemistry. The model allows for a three-dimensional current field and computes the trajectory and forced entrainment for the plume assuming behavior similar to a single-phase plume. As a result of the single-phase simplification, separation due to stratification or to crossflow is neglected. Yapa & Zheng (1999) verified the model in 100 m depth using field-

experimental data from the North Sea. To match the data, they modified the model to allow the oil to separate from the single, stratification-induced intrusion layer by combining the original model with an intermediate-field dispersion model and an oil spill process model to simulate the transport of oil from the intrusion level to the surface and the resulting surface processes on the oil slick.

For a pipeline leak, the initial droplet formation is a controlling factor in the resulting plume structure and the environmental impact of the spill. Correlations exist for predicting the oil and gas droplet size given a set of exit conditions (Rygg & Emilsen 1998, Rye et al. 1998). Faster rising droplets are more likely to strip away from the entrained fluid and behave like the bubble plumes observed by Hugi (1993). As the bubbles and droplets become smaller, the stripping effect of the crossflow is reduced, and the plume behavior approaches that of the single-phase plume.

As indicated in these studies, stratification and crossflow separation are expected to be fundamental processes affecting both CO_2 sequestration and oil well blowout plumes. Although models have addressed stratification separation, their algorithms are empirical and do not have adequate supporting experimental data. Algorithms for separation due to crossflow have not been developed in the literature. Hence, the laboratory experiments presented in this thesis to investigate separation in stratification and crossflow fill a data gap in the literature.

1.2 Thesis organization

This thesis is presented as a series of papers, followed by a summary of the issues for further research and three appendices that give the details of the experimental methods, observations, and selected results.

Chapter 2 is a book chapter written by myself, Brian C. Crounse and E. Eric Adams to be published in *Environmental Fluid Mechanics–Theories and Applications* edited by Hayley Shen et al. (2000). It presents a detailed literature review and introduction to the physics and model equations of multi-phase plumes in uniform, stratified, and flowing ambients. Since it also contains our research group's contribution to the literature, it gives a brief

summary of the results contained in the remaining chapters of this thesis as well as results from Crounse (2000).

Chapter 3 is a paper submitted to the *Journal of Fluid Mechanics* that presents correlations of multi-phase plume properties in quiescent stratification with the non-dimensional slip velocity, defined as the ratio of the terminal rise velocity of a bubble to a characteristic plume fluid rise velocity. This contrasts with previous studies that made correlations that include the depth (to include bubble expansion effects). Plume properties presented in the paper and correlated with the non-dimensional slip velocity include characteristic plume type, trap and peel heights, mass fraction of passive tracer detrained at the first peel, and the bubble spreading ratio. All the experiments in Chapter 3 were conducted in the 1.2 m square by 2.4 m tall stagnant stratified tank at the MIT Parsons Laboratory. The apparatus and methods are described in detail in Appendix A; the experiments and observations are described in Appendix B.

Additional volume flux measurements for stagnant stratified two-phase plumes were also made and are presented in a companion paper submitted to the *Journal of Fluid Mechanics* which appears in Chapter 4. The results in this chapter extend those in Chapter 3 by providing more detailed quantitative measurements. The plume volume fluxes were used by Crounse (2000) to calibrate a two-phase plume model; the model showed good agreement with the obtained correlations to the non-dimensional slip velocity. Appendix C presents the data and calculated values for the flux measurements presented in the paper and Appendix D presents the fit statistics applied to correlations derived in the paper.

Chapter 5 is a final paper submitted to the *Journal of Hydraulic Research* that presents the results of the experiments in uniform and stratified crossflows. The critical separation height between the dominant dispersed phase and the entrained fluid (and weaker dispersed phases) was correlated with the bubble slip velocity, the crossflow velocity, and a characteristic plume fluid velocity. A single-phase model was then adapted *via* the separation height, to predict the fates of the separated phases. These experiments were conducted in a 0.8 m square cross-section by 28 m long flume in the MIT Parsons Laboratory. Like the stagnant stratified experiments, the apparatus and methods are described in detail in Appendix A; the experiments and observations are described in Appendix B.

As each of the individual papers have their own conclusions section, the final chapter, Chapter 6, provides a summary of the remaining issues for further research. Although each of the journal submissions contained their own list of references, these were omitted within the individual chapters in this thesis and are instead presented as a complete listing in the Bibliography section at the end of the thesis.

Chapter 2

Background and literature review[1]

Abstract: Multi- phase plumes in uniform, stratified, and flowing environments have been studied through both laboratory and limited field experiments and through numerical modeling. Of particular interest to the authors is the behavior of multi-phase plumes in the deep ocean, with applications ranging from carbon sequestration to the fate of oil released from an oil-well blowout. Here, we review the pertinent literature and present some initial experimental and analytical results of our own. We start with a description of a multi-phase plume in a uniform ambient, then build in complications of stratification and crossflow. Laboratory experiments are presented for a 2.4 m deep stagnant, stratified ambient and a 0.7 m deep uniform crossflow. The experiments supplement observations of plume type from the literature and quantify entrained fluid volume fluxes in stratification to help validate numerical models. Our theoretical analysis includes a re-examination of the governing dimensionless parameters, with specific focus on deep water applications, and presentation of a double plume model, which incorporates the effects of plume peeling and bubble dissolution.

2.1 Introduction

Multi-phase plumes are buoyancy driven flows where the buoyancy is provided by a continuous release of an immiscible dispersed phase, such as gas bubbles, liquid droplets or solid particles. Some environmental applications include air bubble plumes used for reservoir

[1]This chapter is accepted for publication as Socolofsky, Crounse & Adams (2000), "Multi-phase plumes in uniform, stratified and flowing environments," *in* H. Shen, A. Cheng, K.-H. Wang & M. H. Teng, eds, *Environmental Fluid Mechanics–Theories and Applications*, ASCE/Fluids Committee.

destratification (Schladow 1993, Lemckert & Imberger 1993), reaeration (Wüest et al. 1992), ice prevention in harbors (Baddour 1994, McDougall 1978), and contaminant containment (Milgram 1983); continuous particle clouds resulting from the release of dredged sediments (Koh & Chang 1973, HAVIS Environmental 1994); liquid CO_2 plumes for deep-ocean carbon sequestration (Liro et al. 1992, Adams et al. 1997, Alendal & Drange 2000); and deep sea blowouts of oil and gas (Yappa & Zheng 1997*a*, 1997*b*, Johansen 1999). Our recent research has focused on the latter two applications.

While these plumes result from a range of dispersed phases, we will adopt the general term bubble plume and focus mainly on bubble plumes in water. Physically, a bubble plume is described by the release conditions of the dispersed phase as well as the ambient environmental conditions. Important parameters describing the release include the composition and physical characteristics of the dispersed phase (e.g. density ρ_b, viscosity μ_b, and surface tension σ_b), its flow rate, and the geometry of the release. Pertinent environmental conditions include ambient density stratification and currents.

Bubble plumes are similar in many ways to single-phase plumes, such as sewage plumes in sea water or heated water plumes resulting from the use of once-through cooling in electric power production, but they also have some important differences. The main difference between single- and multi-phase plumes results from the discrete nature of the buoyant dispersed phase. In the case of a single-phase plume, the buoyancy is well mixed with the bulk fluid—the advection of buoyancy is controlled by the motion of the fluid. In contrast, the bubbles themselves comprise the buoyancy in a bubble plume; they exhibit a slip velocity, u_s, relative to the bulk plume fluid, and their distribution over the plume cross section is controlled both by bubble dynamics as well as motion of the bulk plume fluid. Section 2.2 discusses the complications of a dispersed phase in detail for a uniform ambient.

In the presence of ambient stratification, the dynamics of single- and multi-phase plumes are significantly altered. Figure 2-1 depicts classic single- and two-phase plumes in stratification. As the single-phase plume rises, it loses buoyancy relative to the environment. Because of its excess momentum, however, it initially overshoots a point of neutral buoyancy, becomes negatively buoyant, and eventually falls back, or traps, to form an intrusion.

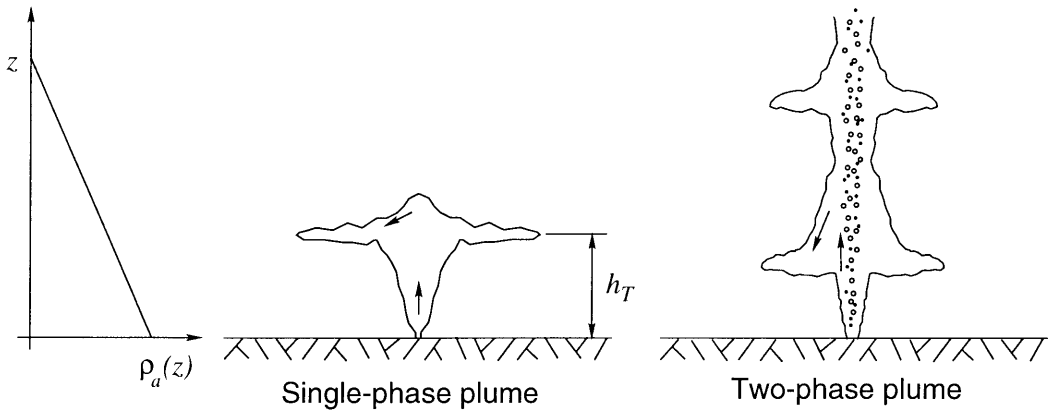

FIGURE 2-1: Schematic of single- and two-phase plumes in stratification.

From dimensional analysis a prediction for the plume trap height, h_T, should have the form

$$h_T = 2.8 \left(\frac{B}{N^3} \right)^{1/4} \tag{2.1}$$

where $B = gQ_b(\rho - \rho_b)/\rho$ is the total kinematic buoyancy flux, Q_b is the volume flux of effluent at the source, ρ is the ambient density, $N = [-(g/\rho)(\partial\rho/\partial z)]^{1/2}$ is the Brunt-Vaisälä buoyancy frequency, and 2.8 is an empirical constant (Fischer et al. 1979, Turner 1986, Crawford & Leonard 1962). This relationship has been verified from laboratory scales to the scales of forest fires and volcanic eruptions (Turner 1986).

Contrast this with a bubble plume. As fluid is entrained and lifted by the bubbles, it becomes negatively buoyant but will continue to rise as long as the bubble drag force exceeds the negative buoyancy of the fluid itself (McDougall 1978). Eventually, the plume will reach a point where the bubbles can no longer support the negative buoyancy of the water. At this height, some portion of the plume water will separate, or peel, from the plume and form a negatively buoyant outer plume (Asaeda & Imberger 1993). If there is no ambient current, this downward plume will surround the upward plume and interact with it. Eventually, the peeled fluid will fall to a point where it is neutrally buoyant, significantly below the height at which it left the upward plume, and intrude as a horizontal density current (Asaeda & Imberger 1993, Lemckert & Imberger 1993, McDougall 1978). Meanwhile, unless their slip velocity is very small, the buoyant bubbles will continue to rise past the peeling location, carrying some fraction of the plume water with them. These peeling events

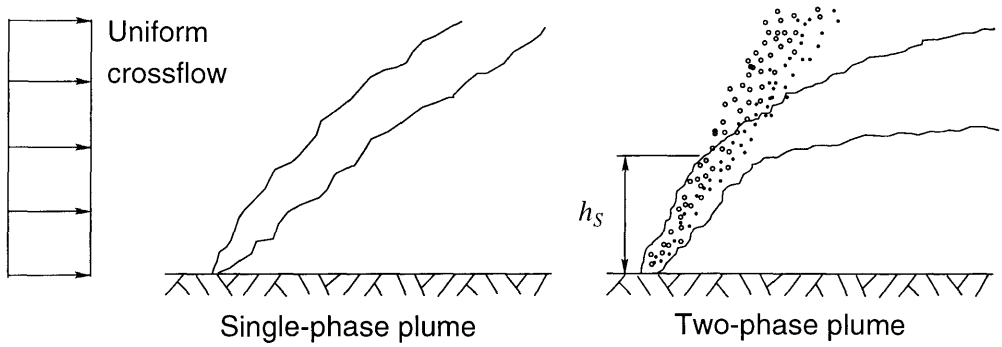

FIGURE 2-2: Schematic of single- and two-phase plumes in a uniform crossflow.

will continue at higher elevations, until either the surface is reached, the dispersed phase reaches neutral buoyancy, or the dispersed phase dissolves (Wüest et al. 1992, Socolofsky & Adams 2000*a*, Crounse 2000). Section 2.3 discusses stratification in detail and presents both laboratory experiments and numerical results demonstrating these effects.

In a crossflow, the velocity difference between the slipping bubbles and the rising entrained fluid can lead to another type of separation. Figure 2-2 shows single- and two-phase plumes in a uniform crossflow. If the crossflow is strong enough to push fluid out of the plume and advect it downstream, the bubbles will separate from the entrained fluid, at some height, h_S, forming a bubble column that rises as a result of the bubble slip velocity alone. Above h_S, fluid advected into the front of the bubble column by the current is lifted a short distance as it interacts with the buoyant bubbles before it is released in the lee of the plume (Socolofsky & Adams 2000*c*, Hugi 1993). Section 2.4 discusses the effects of crossflow in more detail and presents the results of some laboratory experiments and dimensional analysis.

2.2 Simple bubble plumes

This section describes the behavior of axisymmetric bubble plumes in a stagnant, unstratified environment, which we will call simple bubble plumes. By definition, the initial momentum for a bubble plume is negligible. We limit our discussion further to plumes where the volume fraction of the dispersed phase is low, or dilute, so that the plume behavior is controlled by fluid forces, rather than particle collisions (Crowe et al. 1998) and to fully

turbulent, steady, unbounded flows. We will describe bubble plume behavior in terms of a one-dimensional integral model. Although such models are approximate, they are useful both heuristically and as a quantitative tool.

2.2.1 Theory

Similarity

Looking first to simple single-phase plumes, one important characteristic is that they are self-similar. Physically, self-similar behavior indicates that the flow has established a sort of moving equilibrium, in which the evolution of the flow is self-governing (Townsend 1976, Turner 1986, Fischer et al. 1979). Quantitatively, this means that time-average cross-sectional profiles of plume quantities (taken normal to the mean flow) maintain a fixed, near-Gaussian shape and a constant spreading rate (Fischer et al. 1979). Thus, plume properties are fully described by a characteristic centerline value and a characteristic radius, both functions of height. The self-similar region of a simple plume is known as the zone of established flow (Morton et al. 1956, Fischer et al. 1979, Turner 1986).

The advantage of assuming self-similarity is that it reduces the complexity of the mathematical model. Since characteristic plume variables change only with height, a plume may be modeled by a one-dimensional, i.e. ordinary, set of differential equations. Assumption of similarity also allows us to ignore some details of the turbulent flow.

In contrast to single-phase plumes, bubble plumes are not strictly self-similar because the ratio of the decreasing continuous phase fluid velocity to the constant bubble slip velocity is variable. Nonetheless, invoking the self-similarity assumption for the analysis of simple bubble plumes yields useful results. The implications of this assumption will be revisited in Section 2.2.2.

Flux model

The descriptive variables of a simple bubble plume are its width, $b(z)$, the time-averaged velocity profile of the entrained fluid, $u(z,r)$, and the fraction of the plume cross-sectional area occupied by bubbles, or void fraction, $C(z,r)$. Figure 2-3 shows typical profiles of u

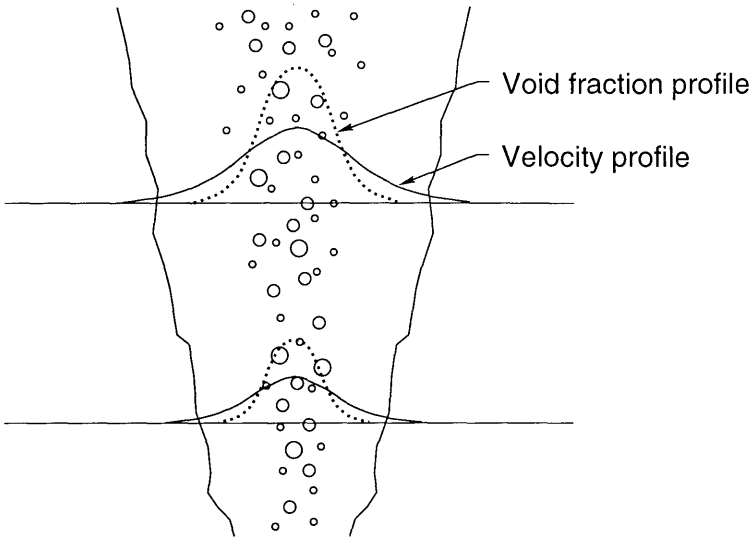

FIGURE 2-3: Schematic of a simple bubble plume with profiles of velocity and void fraction.

and C at two heights in a simple bubble plume. Other variables which are pertinent include the density of the bulk fluid, ρ_w, the density of the bubbles, $\rho_b(z)$, the characteristic bubble radius, $r_b(z)$, and the slip velocity of the bubbles, $u_s(z)$. We define z as the vertical distance above the plume origin.

These variables may be integrated through a plane normal to the mean flow to give fluxes of volume, mass, momentum and buoyancy. By employing the laws of mass and momentum conservation, along with a closure scheme, we arrive at a complete set of ordinary differential equations which describe the evolution of plume characteristics with height.

Two volume fluxes are defined: the flux of plume water, Q_p, and the flux of the dispersed phase, Q_b. The plume water flux is

$$Q_p(z) = \int_0^\infty 2\pi r(1 - C(z,r))u(z,r)dr. \tag{2.2}$$

The definition of Q_b is complicated by the bubble slip velocity. Typically, the transport velocity for the bubbles is assumed to be the sum of the plume fluid rise velocity and an additional bubble slip velocity, such that $u_b = u + u_s$ (Kobus 1968, McDougall 1978, Milgram

1983, Asaeda & Imberger 1993). Making this assumption,

$$Q_b(z) = \int_0^\infty 2\pi r C(z,r)(u(z,r) + u_s(z,r))dr. \tag{2.3}$$

The mass fluxes of plume water and the dispersed phase are $\rho_w Q_p$ and $\rho_b Q_b$, respectively.

The total kinematic momentum flux, M, is defined by

$$\begin{aligned} M(z) &= \gamma \int_0^\infty 2\pi r[u^2(z,r)(1 - C(z,r)) \\ &\quad + \frac{\rho_b(z)}{\rho_w}(u(z,r) + u_s(z,r))^2 C(z,r)]dr \end{aligned} \tag{2.4}$$

where γ, an amplification term defined in Milgram (1983), accounts for the fact that use of the mean velocity, u, in (2.4) implicitly ignores turbulent momentum transport. Momentum amplification is discussed in Section 2.2.2.

As the driving force for the plume, the density difference between the dispersed phase and the ambient is $\Delta\rho_b = \rho_w - \rho_b$, which is positive for rising bubbles. As the void fraction is small, the Boussinesq approximation is applicable, so that the reduced gravity is defined as $g' = g\Delta\rho_b/\rho_w$ (Liro et al. 1992). In an unstratified environment, ρ_w is constant.

With these definitions, the total kinematic buoyancy flux, B, of a simple bubble plume is defined as

$$B(z) = \int_0^\infty 2\pi r C(z,r) g \frac{\Delta\rho_b(z)}{\rho_w}[u(z,r) + u_s(z,r)]dr = g' Q_b(z). \tag{2.5}$$

Another useful quantity involving buoyancy is the integrated buoyant force, $\hat{B}_b$, acting on a unit height of the plume,

$$\hat{B}_b(z) = \int_0^\infty 2\pi r C(z,r) g \Delta\rho_b(z) dr. \tag{2.6}$$

Note that this is a force per unit height, unlike the preceding flux quantities.

Evaluation of these integrals requires selection of a shape for the profiles depicted in Figure 2-3. As noted, simple single-phase plumes exhibit near-Gaussian property profiles.

Here, we assume that simple bubble plumes do as well. This assumption is supported by experimental results and is discussed further is Section 2.2.2. Thus,

$$u(z,r) = U_m(z)e^{-r^2/b^2} \tag{2.7}$$

$$C(z,r) = C_m(z)e^{-r^2/(\lambda_1 b)^2} \tag{2.8}$$

where U_m and C_m are centerline values. Because the bubble column does not occupy the full plume width, λ_1 is introduced, defined as the spreading ratio of the bubbly region relative to the plume width ($0 < \lambda_1 \leq 1$). $1/\lambda_1^2$ is a turbulent bubble Schmidt number that would be constant for a strictly similar flow (Ditmars & Cederwall 1974).

With the profiles (2.7) and (2.8), the volume flux of plume water becomes

$$Q_p(z) = \pi U_m b^2 \left(1 - C_m \frac{\lambda_1^2}{\lambda_1^2 + 1}\right).$$

Because the bubbles are dilute, such that $C_m \ll 1$, the volume flux reduces to

$$Q_p(z) \approx \pi U_m b^2. \tag{2.9}$$

To evaluate Q_b, we make the assumption that u_s is independent of the radial location. If the distribution of u_s for a given application were available, its variation across the cross-section could be included. For now, the volume flux of the dispersed phase becomes

$$Q_b(z) = \frac{\pi \lambda_1^2 b^2 C_m}{\lambda_1^2 + 1}(U_m + U_b). \tag{2.10}$$

where we define $U_b = (1 + \lambda_1^2)u_s$ for convenience (McDougall 1978).

The momentum flux equation is simplified by considering the magnitude of each term in (2.4). The first term describes the momentum flux associated with the mean bulk fluid flow, while the second term describes that of the mean bubble flow. Taking the ratio of these two terms indicates that the momentum flux of the fluid is $\rho_w(1 - C)/\rho_b C$ times the momentum flux of the bubbles. Limiting to dilute plumes where $C \ll 1$, we may neglect the bubble momentum term. For air bubbles in water, ρ_w/ρ_b is also large, further supporting this

approximation. Thus, dropping the bubble momentum flux term, and letting $1-C(z,r) \approx 1$, the momentum flux equation becomes

$$M(z) \approx \frac{\gamma}{2}\pi b^2 U_m^2. \tag{2.11}$$

The buoyancy flux can be written immediately as $g'Q_b(z)$; thus, the remaining integral is the buoyant force, $\hat{B}_b$, which becomes

$$\hat{B}_b(z) = \pi g \lambda_1^2 b^2 C_m g \Delta\rho_b = \frac{1+\lambda_1^2}{U_m + U_b} Q_b g \Delta\rho_b. \tag{2.12}$$

We see here that the slip velocity, which appears in the denominator, acts to reduce the buoyant force at a given elevation.

Governing differential equations

The evolution of the plume in space is controlled by two physical processes: the turbulent entrainment of ambient water and the buoyant forcing of the bubbles. In this section the governing dynamic equations are derived by invoking volume and momentum conservation. Because bubble evolution can be de-coupled from the dynamic equations, the bubbles themselves are treated in a separate bubble sub-model.

Volume conservation is governed by turbulent entrainment: the buoyant bubbles induce a turbulent flow, which in turn causes eddies from the plume to engulf ambient liquid and mix it into the plume (Turner 1986). The most successful method to date for quantifying the rate of entrainment is the entrainment hypothesis, formally introduced by Morton et al. (1956). This hypothesis states that the mean entrainment velocity across a shear flow boundary, perpendicular to the direction of flow, is proportional to a characteristic velocity of the flow (Turner 1986). Thus, the entrainment volume flux is the entrainment velocity multiplied by the surface area of the flow. Adoption of this hypothesis leads to

$$\frac{dQ_p}{dz} = 2\pi b \alpha u \tag{2.13}$$

where α is a turbulent entrainment coefficient. It is constant for single-phase jets and plumes, but varies with local plume conditions for simple bubble plumes (see Section 2.2.2).

Momentum conservation represents a force balance: buoyant forces cause the bubbles to rise relative to the bulk fluid; the subsequent drag on the bubbles effectively transfers the buoyant forcing to the bulk fluid. Thus, momentum conservation can be expressed using the integrated buoyant force:

$$\frac{dM}{dz} = \frac{\hat{B}_b(z)}{\rho_w} = \pi\lambda_1^2 b^2 g' C_m. \tag{2.14}$$

Together, (2.13) and (2.14) describe the dynamics of a simple bubble plume. Due to dissolution and changes in hydrostatic pressure, the bubbles undergo additional transformation.

Bubble plume applications in which bubble dissolution is significant include lake aeration (Wüest et al. 1992) and deep-ocean CO_2 sequestration (Liro et al. 1992). Bubble dissolution is dependent on factors such as bubble size. If the flux of the number of bubbles, N_b, is assumed to be constant in the zone of established flow, then the average bubble mass may be defined as $m_b = \rho_b Q_b(z)/N_b$; a characteristic bubble radius is then $r_b = [3m_b/(4\pi\rho_b)]^{1/3}$. The time rate of change of the mass of a single bubble is commonly modeled as

$$\frac{dm_b}{dt} = -4\pi r_b K \rho_b (C_s - C_\infty) \tag{2.15}$$

where C_s is the solubility and, thus, surface concentration of the dispersed phase, C_∞, for the substance in question, and K is a mass transfer coefficient. K is a function of bubble characteristics; its determination is examined in detail in Clift et al. (1978).

As the effective velocity of the dispersed phase is $(U_m + U_b)/(1+\lambda_1^2)$, (2.15) can be written with respect to distance by invoking the chain rule:

$$\frac{d(\rho_b Q_b)}{dz} = -4\pi N_b K r_b \rho_b \frac{1+\lambda_1^2}{U_m + U_b}(C_s - C_\infty). \tag{2.16}$$

Often, the flux of the dissolved phase of the solute is also of interest and must be tracked separately (see Section 2.3).

While dissolution decreases the bubble volume flux with height, bubble expansion due to decreasing pressure acts to increase it. In common reservoir applications the ideal gas law

together with adiabatic expansion can be used to obtain

$$Q_b(z) = \frac{H_A}{H_T - z}\rho_{bA} \tag{2.17}$$

where dissolution is neglected. H_A is the atmospheric pressure head and ρ_{bA} is the gas density at the reservoir surface. $H_T = H_A + H$ is the total pressure head, where H is the depth of the release. In the deep ocean H is of the order of 1000 m and compressibility effects can generally be ignored.

If dissolution is negligible, (2.17) represents the typical bubble evolution. A more flexible approach, which allows for dissolution, is to track the mass flux of the bubbles via (2.16), and then to calculate their volume flux after determining their density via an appropriate equation of state. Hence, (2.13) and (2.14) together with either (2.16) or (2.17) represent the governing equations. They may be expressed in terms either of the integral variables Q_p, Q_b, and M, or the local variables U_m, b, and C_m, by use of the following relationships:

$$U_m = \frac{2}{\gamma}\frac{M}{Q_p} \tag{2.18}$$

$$b = \left(\frac{\gamma Q_p^2}{2\pi M}\right)^{1/2} \tag{2.19}$$

$$C_m = \frac{Q_b(1+\lambda_1^2)}{\pi\lambda_1^2 b^2(U_m + U_b)}. \tag{2.20}$$

2.2.2 Observations

The previous section presented a theoretical framework for the analysis of simple bubble plumes. This section presents experimental data and discusses several of the assumptions and coefficients underlying this framework.

Profiles and similarity

The assumption of Gaussian profiles for both the continuous and dispersed phases of dilute bubble plumes is supported by experimental evidence over a wide range of experimental conditions and fluids (Kobus 1968, Milgram 1983, Tacke et al. 1985).

Strict similarity for bubble plumes requires that λ_1 and α be constant. Experiments show, however, that both these parameters vary with height, indicating that simple bubble plumes are not strictly self-similar (Wilkinson 1979, Milgram 1983). Fortunately, model results are not sensitive to reasonable variation in λ_1 (Liro et al. 1991). They are more sensitive to α, but reasonable results are obtained using representative average or height-dependent values of α (Milgram 1983, Turner 1986).

Release conditions

The governing equations, as stated, do not apply near the point of gas release (zone of flow establishment or ZFE), where the gas fraction is high and the flow changes rapidly with height. One may avoid analyzing this zone by assigning a virtual release point, such that the virtual plume is identical to the observed plume in the zone of established flow. The height of the virtual release depends on the geometry of the release, and generally lies below the actual release point for a bubble plume (Kobus 1968).

Liro et al. (1991) describes a fairly simple technique for assigning initial conditions above the ZFE: the height of the ZFE is assumed to be approximately five times the diameter of the release port, and the location of the virtual release is assumed to lie an equal distance below the actual port. Applying analytical solutions for a single-phase plume between the virtual origin and the top of the ZFE yields

$$\begin{aligned} b &= \frac{6}{5}\alpha z_0 \\ U_m &= \left(\frac{25 g Q_b (1+\lambda_1^2)}{24 \alpha^2 \pi z_0}\right)^{1/3} \end{aligned}$$

where z_0 is the distance from the virtual release point to the top of the ZFE. While this method is approximate, it provides reasonable estimates of initial conditions when buoyancy, rather than momentum, dominates the flow conditions. Because buoyant plumes are mainly sensitive to the initial buoyancy flux, efforts to model the ZFE more accurately do not yield significant dividends. For plumes where momentum dominates the ZFE, as may be the case in an oil well blowout, an alternate approach may be required (see e.g. Yapa & Zheng 1997*a*).

Bubble characteristics

Significant physical parameters describing bubbles include the slip velocity, u_s, and the spreading rate of the bubble column, λ_1.

In a stagnant environment u_s depends on factors such as bubble size and shape, buoyancy, viscosity, and surfactant concentration (Clift et al. 1978). Bubble shape changes with increasing diameter, progressing from spherical through elliptical to spherical cap. Other effects, such as temperature, also affect rising bubbles (Leifer et al. 2000).

The stable bubble size for a given release is affected by the dispersed phase flow rate and the salinity of the receiving water. For air bubbles in fresh water, the bubble size increases with airflow rate, and is fairly independent of the diffuser geometry (Kobus 1968, Milgram 1983, Tacke et al. 1985). In sea water, however, small bubbles are more stable, and diffuser geometry can play a role, even at low exit velocity (Beyersdorf 1997). In our experiments a diffuser that produced 2 mm bubbles in fresh water produced 0.5 mm bubbles in sea water for the same gas flow rate (Socolofsky 2000). This change in size reduced the slip velocity from approximately 20 cm/s to 7 cm/s.

Given certain bubble properties, other environmental factors can affect the slip velocity. In a bubble plume the flow field surrounding a bubble is complicated by wakes from neighboring bubbles and by the turbulence generated by the plume's shear flow. Many investigators, such as Ditmars & Cederwall (1974), Milgram (1983), Tacke et al. (1985) and Brevik & Killie (1996) have assumed that these turbulent conditions would alter the quiescent water terminal velocity; hence, they chose to treat the slip velocity as a free parameter. Others, such as Liro et al. (1991) and Wüest et al. (1992), kept the quiescent terminal velocity for u_s, omitting it as a calibration parameter. The limited experimental data of Chesters et al. (1980), Roig et al. (1998) and Leitch & Baines (1989) show that the observed slip velocities are indeed comparable to the stagnant water terminal velocity, implying that turbulence in dilute plumes does not significantly alter the bubble terminal velocity.

The bubble core spreading rate is not well understood. Experimental observations indicate that λ_1 is approximately constant with height, but varies widely by interpretation. Milgram (1983) claimed that the small values (in the range of 0.3) of λ_1 reported by Ditmars

& Cederwall (1974) were artifacts of plume wandering. Plume wandering occurs when a bubble plume meanders about its centerline because of recirculation currents set up in confined basins. Ignoring this experimental artifact leads to an overestimate of the plume width and a corresponding underestimate of λ_1. When plume wandering was accounted for, Milgram reported that λ_1 should be in the range of 0.7-0.8 . However, Chesters et al. (1980) report a value of $\lambda_1 = 1$. Socolofsky & Adams (2000*a*), accounting for bubble wander, showed that λ_1 can range from 0.5 to 1.0 depending on B and u_s. Fortunately, plume predictions are only weakly dependent on λ_1 (Liro et al. 1992).

Turbulent entrainment

The turbulent entrainment of an integral model cannot be determined from first principles. Rather, a closure scheme must be assumed. As discussed previously, most investigators have adopted the entrainment assumption, which states that the effective inward (entrainment) velocity over a defined flow interface is proportional to the mean characteristic velocity of that flow (Turner 1986).

Turner (1986) and Fischer et al. (1979) discuss turbulent entrainment in the context of single phase jets and plumes in detail. The most notable result for simple single phase jets and plumes is that the entrainment coefficient, α, is constant. For round jets (no buoyant effects), $\alpha_j = 0.054$, while for round plumes $\alpha_p = 0.083$. The difference between α_j and α_p must be due to differences in the character of turbulence between the two flows, implying that buoyancy affects entrainment rate. The constant values of α are evidence of the flows' self-similarity.

In contrast, the entrainment rate for simple bubble plumes is not universally constant. This fact was first reported in Ditmars & Cederwall (1974), who found that plume average values of α ranged from 0.04 to 0.08 in Kobus's (1968) experiments, increasing with higher gas flow rates. In other experiments, Tacke et al. (1985) reported entrainment coefficients in the range of 0.075 to 0.13.

The most detailed analysis of α for simple bubble plumes is reported by Milgram (1983), who found that local values of α ranged from 0.037 to 0.165. He suggested an empirical

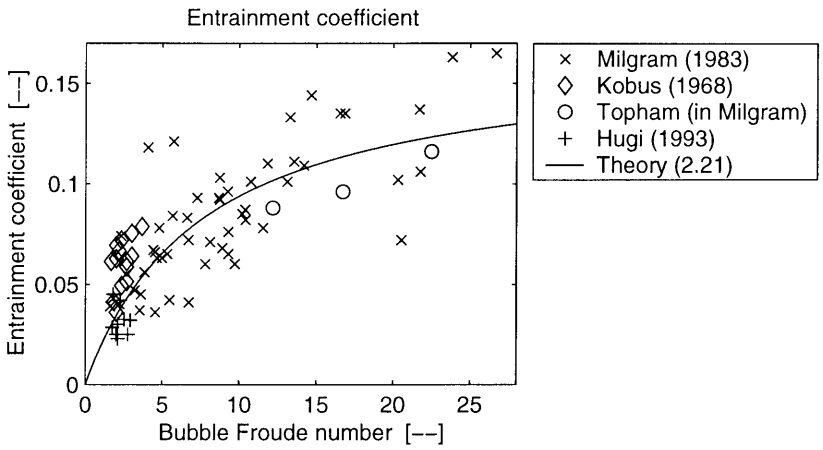

FIGURE 2-4: Correlation of entrainment coefficient with bubble Froude number.

formula for α:

$$\alpha(F_B) = K\frac{F_B}{A + F_B} \tag{2.21}$$

where $K = 0.165$ and $A = 7.598$. F_B is a bubble Froude number, defined as

$$F_B = C_m^{2/5}\frac{L_M}{L_D} \tag{2.22}$$

where $L_M = (Q_b^2/gC_m^2)^{1/5}$ and $L_D = (\sigma_b/g(\rho_w - \rho_b))^{1/2}/C_m^{1/3}$. Milgram suggested that L_M is a characteristic bubble mixing length, and L_D is a characteristic distance separating bubbles. He argued that an increase in the bubble Froude number enhances turbulent entrainment by increasing turbulence near the entrainment interface. Figure 2-4 shows all available data for entrainment coefficient as a function of bubble Froude number (local values of α were not reported by Tacke et al. (1985)). The solid line in Figure 2-4 plots (2.21).

Other closure schemes have been investigated. For instance, Brevik & Killie (1996) and Brevik & Kluge (1999) proposed that the dominant Reynolds stress could be assumed to be self-similar, so that the spreading rate could be defined by an integral constant. Unfortunately, the integral constant, which must be determined experimentally, varies with physical parameters, such as gas flow rate, similarly to α. Hence, alternative schemes do not offer significant advantages over the entrainment assumption.

Momentum amplification

Introduced in (2.4), γ accounts for the fact that the plume is turbulent. The instantaneous vertical plume velocity may be decomposed into mean and turbulent quantities: $u = \overline{u} + u'$. Values of $\gamma > 1$ account for the momentum flux associated with $\overline{u'u'}$.

Milgram (1983) presents an analysis of the momentum amplification effect. There, Milgram correlated γ with a phase distribution number, N_P, that describes the coherency of the bubble column, such that

$$\gamma(N_P) = 1.07 + \frac{D_1}{N_P^{D_2}} \tag{2.23}$$

where $N_P = L_V/L_D$ and $L_V = U_m^2/gC_m$. Correlation with the available data gave $D_1 = 977$ and $D_2 = 1.5$.

A slow stream of isolated bubbles has a low N_P, which gives a high value for γ. Leitch & Baines (1989) also report that turbulent momentum flux increases with decreasing airflow rate, though they found discrepancies between their data and (2.23). In the opposite limit, as $N_P \to \infty$, $\gamma \to 1.07$, the value for a single-phase plume.

2.3 Bubble plumes in stratification

This section incorporates the complications of stratification into our description of axisymmetric bubble plumes. We assume a linear stratification and a stagnant ambient for our analytical results; however, the numerical model described at the end of this section can incorporate arbitrary stratification and any density feedback due to dissolution of the dispersed phase. The final section addresses crossflows.

2.3.1 Theory

Dimensional analysis

There are two independent techniques to derive a set of governing non-dimensional numbers. First, if the important physical parameters can be fully listed, the Buckingham Π theorem can be used to find a set of non-dimensional numbers (Fischer et al. 1979). Second,

if the governing differential equations can be written, the non-dimensional numbers can be derived by normalizing the governing equations. Here, we start with the first method in order to introduce the physics of stratification independent of an analytical model. Later, we will use the non-dimensional groups obtained here to help normalize the governing equations.

We begin with a single-phase plume in stratification where the important independent parameters are the buoyancy flux, B, and the stratification frequency, N, and the desired dependent variable is the trap height, h_T (refer to Figure 2-1). Normalizing h_T by B and N, we define the first non-dimensional group, π_1, as

$$\pi_1 = \frac{h_T}{(B/N^3)^{1/4}}, \tag{2.24}$$

which gives the ratio of the trap height to the characteristic length scale of a stratified single-phase plume, $l_C = (B/N^3)^{1/4}$. From (2.1) we have $\pi_1 = 2.8$.

Turning to multi-phase flow, we consider a sediment plume where expansion and dissolution are negligible and where particle size and slip velocity can be accurately controlled. This introduces two-phase plume physics without the complications of bubble expansion. Several sediment characteristics are important, including size, density, shape, and possibly cohesion. Since u_s is itself a function of these parameters, we assume that the slip velocity incorporates the important characteristics for describing the simple two-phase plume. Thus, a second, non-dimensional group, π_2, may be written as

$$\pi_2 = \frac{u_s}{(BN)^{1/4}} \tag{2.25}$$

where π_2 is the ratio of the slip velocity to a characteristic plume fluid velocity, $u_C = (BN)^{1/4}$.

The Buckingham Π theorem states that π_1 should depend on π_2. Reingold (1994) first attempted to relate h_T to u_s; however, she did not make use of π_2. Additional data, together with the data from Reingold (1994), are presented in Figure 2-5. The relationship plotted in the figure is given by

$$\pi_1 = 2.8 - 0.27\pi_2. \tag{2.26}$$

The trend of reduced h_T for increasing π_2 yields physical insight. Because water that peels

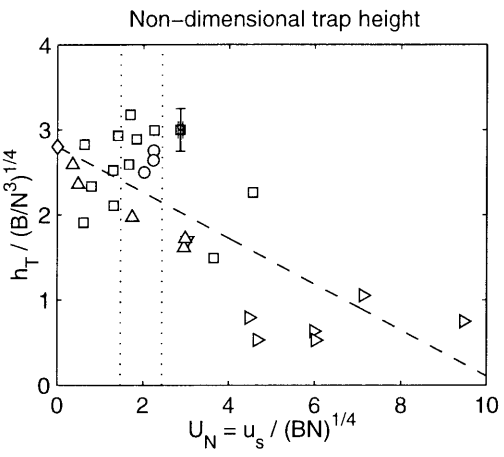

FIGURE 2-5: Dependence of trap height on slip velocity. Sediment and bubble experiments by Reingold (1994) are $\triangle$ and $\triangledown$, respectively. $\triangleright$ are both field and laboratory data from Lemckert & Imberger (1993). $\circ$ are laboratory experiments by Asaeda & Imberger (1993). $\square$ are our laboratory experiments, and $\diamond$ is the single-phase value from (2.1).

from a two-phase plume loses its buoyancy when the bubbles continue to rise, it will trap lower than for a single phase plume, where the fluid and buoyancy are advected together into the intrusion layer.

Completing the dimensional analysis, we consider the pressure effects resulting in bubble expansion. For ideal gas behavior, the important parameter would be the total pressure head, H_T. The only other independent non-dimensional group, π_3, is

$$\pi_3 = \frac{H_T}{(B/N^3)^{1/4}}, \tag{2.27}$$

which is the ratio of H_T to the natural length scale of the plume, l_C.

There are thus three non-dimensional groups describing multi-phase plumes in stratification. The group π_1 comes from single-phase plumes. Introducing the dispersed phase gives π_2, and we have $\pi_1 = f(\pi_2)$ when compressibility effects are negligible. Finally, when compressibility is important, we have all three dimensionless groups, and we expect $\pi_1 = f(\pi_2, \pi_3)$. Since π_2 is the dominant parameter representing the non-dimensional slip velocity, we give it the name $U_N \equiv \pi_2$.

Similarity

Bubble plumes have already been shown to lack strict similarity due to variations in α and λ_1 (see Section 2.2). Stratification adds other effects that degrade the self-similarity of both single-phase and bubble plumes.

Stratification affects self-similarity in two ways: it affects entrainment, and it causes peeling and trapping. For a single-phase plume, the entrainment coefficient may be correlated with the plume Richardson number, R_P, given by

$$R_P = \frac{QB^{1/2}}{M^{5/4}}. \tag{2.28}$$

Alternatively, we could use the plume Froude number, $F_P \sim 1/R_P$. For a single-phase plume in an unstratified environment, the plume Richardson number is a constant, $R_P = 0.557$ (Fischer et al. 1979). In stratification, R_P is not constant, but changes due to entrainment of ambient fluid. The entrainment for a bubble plume in a stratified environment should be similarly affected. This further complicates the correlations for α for bubble plumes stated in Section 2.2.2. Hussain & Narang (1984) proposed a complex expression for entrainment into a bubble plume in a stratified environment, but did not offer experimental verification. Currently, there is no experimental correlation for entrainment of a bubble plume in stratification.

The velocity profile of a self-similar flow has a consistent shape at all heights. This condition is violated in stratification because of peeling events. The velocity profiles at a peeling event, and at the depth where an outer plume intrudes, are fundamentally different from those found elsewhere in the plume. Thus, the plume as a whole is clearly not self-similar.

Nonetheless, the tools granted by the similarity assumption, namely the integral model and the entrainment assumption, may still be used to provide insight into the dynamics of stratified bubble plumes. This is possible because plume properties are weakly dependent on variations in α due to stratification (Turner 1986) and because the plume can be decomposed into rising and descending flows (Asaeda & Imberger 1993). However, the equations from Section 2.2 must be expanded to account for the density effects of stratification.

Flux model

The ambient fluid density, presumed constant in Section 2.2, is described in stratification by the variable $\rho_a(z)$. As the plume entrains water from this stratification profile, the density of the plume water, ρ_w, varies with height. In order to properly account for the buoyancy of the plume water, we define the density defect $\Delta\rho_w = \rho_w - \rho_a$. The variation of $\Delta\rho_w$ requires that new buoyancy flux and force terms be added to those in Section 2.2.1.

In general, determination of the density of the plume fluid in a stratified environment requires knowledge of the concentrations, and thus fluxes, of the stratifying agents, e.g. temperature and/or dissolved solutes (salinity):

$$J(z) = \int_0^\infty 2\pi r(1 - C(z,r))\rho_w c_p(z) T(z,r) u(z,r) dr, \tag{2.29}$$

$$S(z) = \int_0^\infty 2\pi r(1 - C(z,r)) s(z,r) u(z,r) dr. \tag{2.30}$$

J is the heat energy flux, S is the salt flux, c_p, approximated as a constant in most cases, is the specific heat of the plume fluid, T is the temperature of the plume fluid, and s is the salinity of the plume water.

If the fluxes in (2.29) and (2.30) are tracked, water density can be calculated from an equation of state (Gill 1982). However, if the difference between the minimum and maximum ambient densities is small, water density may be approximated as a linear function of salinity and temperature. In this case, it is adequate to track the conservation of density defect, $\rho_r - \rho_w$, where ρ_r is the reference density. The buoyancy flux of the plume water is then defined as

$$B_w(z) = \int_0^\infty 2\pi r(1 - C(z,r)) g \frac{\rho_r - \rho_w(z,r)}{\rho_r} u(z,r) dr. \tag{2.31}$$

To evaluate this integral, we introduce a new profile (assumed Gaussian) which gives the difference in density between the ambient, ρ_a, and the plume fluid:

$$\Delta\rho_w(z,r) = \Delta\rho_{w,m}(z) e^{-r^2/(\lambda_2 b)^2}$$

where $\Delta\rho_{w,m}$ is the centerline value of $\Delta\rho_w$ and λ_2 is the spreading ratio of density defect

to velocity (Fischer et al. 1979). Evaluating (2.31) in terms of $\Delta\rho_w$ gives the new plume buoyancy flux

$$B_w(z) = \frac{gU_m b^2}{\rho_r}\left[(\rho_r - \rho_a) - \frac{\lambda_2^2 \Delta\rho_{w,m}}{1+\lambda_2^2}\right] \tag{2.32}$$

which will be used to form a buoyancy conservation equation.

For the plume force balance, the buoyant force of the bubbles, $\hat{B}_b$, from Section 2.2 is now offset by a negative buoyant force of the entrained water, $\hat{B}_w$, written per unit height as

$$\hat{B}_w = \int_0^\infty 2\pi r g(1 - C(z,r))\rho_w(r,z)dr \approx \pi\lambda_2^2 b^2 g \Delta\rho_{w,m}. \tag{2.33}$$

Governing differential equations

With the additions of the previous section, the governing equations can be derived for the stratified case. The volume (or mass) conservation equation, (2.13), is unchanged from Section 2.2.1. The governing equation for momentum gains a term from (2.33), due to the forcing of the negatively buoyant plume fluid. Thus, (2.14) becomes

$$\frac{dM}{dz} = \frac{\hat{B}_b - \hat{B}_w}{\rho_w} = \frac{\pi g b^2}{\rho_w}\left(\lambda_1^2 C_m \Delta\rho_b - \lambda_2^2 \Delta\rho_{w,m}\right). \tag{2.34}$$

A new equation represents the conservation of buoyancy flux, given by

$$\frac{dB_w}{dz} = 2\pi b U_m \alpha g \frac{\rho_r - \rho_a(z)}{\rho_r}. \tag{2.35}$$

(2.35) indicates that the buoyancy flux of the plume water changes due to entrainment of ambient water that itself has a density defect relative to the reference density. Together with (2.13) and a bubble dynamics sub-model, (2.34) and (2.35) govern a bubble plume in stratification.

More generally, the buoyancy conservation equation can be replaced by the conservation of heat and salinity flux, which follow directly from (2.13):

$$\frac{dJ}{dz} = 2\pi b \alpha U_m \rho_w c_p T_a(z) + \frac{dW_b}{dz}\Delta H_{sol}, \tag{2.36}$$

$$\frac{dS}{dz} = 2\pi b\alpha U_m s_a(z), \tag{2.37}$$

where T_a and s_a are the temperature and salinity of the ambient fluid at a given height and H_{sol} is the heat of solution for the dissolving dispersed phase. Tracking the fluxes of both heat and salinity (plus any other solutes of interest) is sensible when there are multiple stratifying agents or when dissolution of the dispersed phase affects density.

To non-dimensionalize the governing equations, it is useful to recast them as functions of the governing variables U_m, b, C_m, $\Delta\rho_{w,m}$, and $\Delta\rho_b$. The set of dimensionless variables are formed from l_C and u_C. For deep water plumes, where $H \gg H_A$, the length scale for calculating derivatives is chosen based on the trap height, so the combination $(B/N^3)^{1/4}$ becomes the dominant length scale. This contrasts with McDougall (1978), who used H as his normalizing length scale. The other normalization variables in McDougall (1978) will be retained, however, yielding

$$\begin{aligned} z &= \left(\frac{B}{N^3}\right)^{1/4} Z; \qquad b = 2\alpha \left(\frac{B}{N^3}\right)^{1/4} B_N \\ U_m &= U_b V; \qquad C_m = X \\ \frac{\Delta\rho_{w,m} g}{\rho_r} &= \frac{U_b^2}{\lambda_2^2}\left(\frac{N^3}{B}\right)^{1/4} G_w; \qquad \frac{\Delta\rho_b g}{\rho_r} = \frac{U_b^2}{\lambda_1^2}\left(\frac{N^3}{B}\right)^{1/4} G_b \end{aligned}$$

where Z, B_N, V, X, G_w, and G_b are the non-dimensional variables for elevation, width, plume fluid velocity, bubble concentration, plume fluid buoyancy, and bubble buoyancy, respectively.

Inserting the non-dimensional variables, (2.13) and (2.34) become

$$\frac{d}{dZ}\left[VB_N^2\right] = VB_N \tag{2.38}$$

and

$$\frac{d}{dZ}\left[VB_N\right] = \frac{B_N}{\gamma V}(XG_g - G_w), \tag{2.39}$$

respectively. If the buoyancy flux (2.32) is substituted into (2.35) and expanded, the latter

equation becomes

$$\frac{d}{dZ}\left[\frac{VB_N^2 G_w(1+\lambda_1^2)^2}{(1+\lambda_2^2)}\right] = -\frac{VB_N^2}{U_N^2}, \tag{2.40}$$

which gives the conservation of the plume fluid buoyancy, independent of the bubbles. The final equation represents buoyancy changes due to bubble expansion, neglecting dissolution. The gas volume flux can be expressed as a bubble buoyancy flux term by multiplying Q_b by $g(\rho_r - \rho_b)/\rho_r$. Applying conservation of buoyancy to the bubble volume flux and assuming the ideal gas law yields

$$\frac{d}{dZ}\left[(V+1)B_N^2 X G_b(1+\lambda_1^2)^2\right] = \frac{M_{HT}}{(1+Z/(P_{HT})^{1/4})^2}. \tag{2.41}$$

where M_{HT} and P_{HT} were defined in Asaeda & Imberger (1993). P_{HT} is just π_3^4. Asaeda & Imberger (1993) primarily use a different form of P_{HT}, called P_N, in their analyses:

$$P_N = \frac{N^3 H^4}{B}. \tag{2.42}$$

In deep water $H_A \ll H$ and $P_N \approx P_{HT}$. M_{HT} combines the bubble slip velocity and expansion effects and can be written as a function of U_N and P_{HT}, namely

$$M_{HT} = \frac{P_{HT}^{-1/4}}{4\pi\alpha^2 U_N^3}. \tag{2.43}$$

Asaeda & Imberger (1993) also primarily use a different form of M_{HT}, called M_H, in their analyses:

$$M_H = \frac{B}{4\pi\alpha^2 H u_s^3}. \tag{2.44}$$

In the literature, variations of P_N and M_H have been used extensively (e.g. Asaeda & Imberger 1993, McDougall 1978, Schladow 1993, Lemckert & Imberger 1993); whereas, U_N is a new parameter. This came about because researchers have been primarily interested in reservoir destratification, where bubble expansion is a significant physical process.

The non-dimensional governing equations (2.38)–(2.41) together with the dimensional analysis help identify the proper use of these three parameters. U_N enters the conservation of fluid buoyancy equation and the dimensional analysis when the dispersed phase in intro-

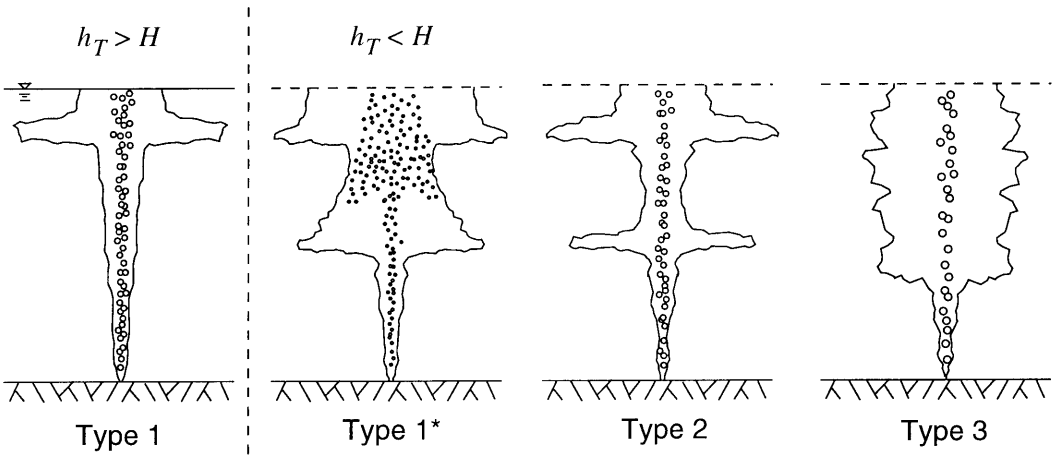

FIGURE 2-6: Schematic of the plume type classification.

duced. It is the fundamental parameter describing the effects of a dispersed phase on plume dynamics. Both P_{HT} and M_{HT} enter with bubble expansion since they are both dependent on the water depth. Because $M_{HT} = f(P_{HT}, U_N)$ we propose that P_{HT} and U_N should be used as the two governing non-dimensional variables for two-phase plumes.

2.3.2 Observations

Plume classification

Asaeda & Imberger (1993) and Lemckert & Imberger (1993) present a wide range of laboratory and field experimental observations. They were primarily interested in the efficiency of reservoir destratification and showed that plumes having one intermediate peel and one surface peel were the most efficient at reservoir mixing. Based on their experimental observations, Asaeda & Imberger (1993) defined three distinct modes of two-phase plume behavior in linear stratification. Shown schematically in Figure 2-6, together with Type 1* to be described shortly, these modes were called Types 1, 2, and 3. The Type 1 plumes have no intermediate intrusions, detraining all of the entrained fluid in the surface radial jet. The Type 2 plumes have one or more intermediate intrusions, but each intrusion is a distinct layer. The Type 3 plumes appear to lose entrained fluid randomly, forming a continuous structure of sub-surface intrusions.

The Type 1* plumes occur when the dispersed phase has a low enough slip velocity

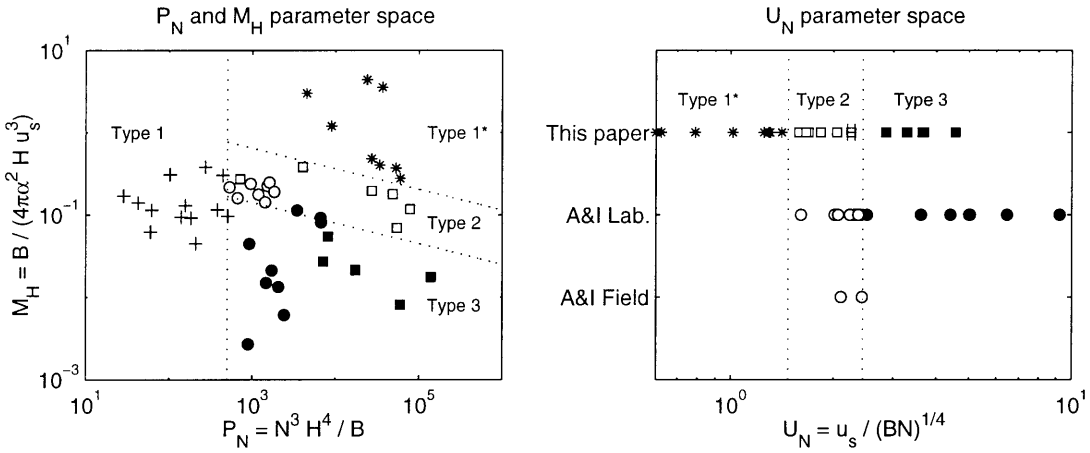

FIGURE 2-7: Correlation of plume type with the governing non-dimensional parameters. Circles and pluses are from Asaeda & Imberger (1993); squares and stars are the current authors. Pluses are Type 1 plumes, stars are Type 1* plumes, open symbols are Type 2 plumes and filled symbols are Type 3 plumes. The Asaeda & Imberger (1993) data include field and laboratory experiments.

compared to the turbulence at the plume peel that the bubbles peel with the fluid. In most of the experiments reported in the literature, the bubble slip velocity is about 20 cm/s, too high to be affected by the peeling fluid. However, our experiments with oil, fine air bubbles and sediment ($u_s = 3 - 8$ cm/s) show that Type 1* plumes exist and differ from Type 2 plumes: the bubble core is more spread out above the first peel, and fluid is re-entrained out of the intrusion and carried upward by the peeled bubbles as they reform the secondary plumes.

The Type 3 plumes actually result from inefficient peeling events, where only a portion of the entrained fluid is detrained. In this case, detraining fluid may have been lifted a significant elevation, and may be denser than intrusions below it. This instability allows Type 3 peels to overlap, yielding the random, continuous-peeling nature of the Type 3 plume. In contrast, Type 1* and 2 plumes detrain most of their water at each peel. As a result, the peels do not overlap but remain localized at separate intrusion levels. Because the plume source originates as if it were above a peel with complete detrainment, the first peel in any plume must be Type 1* or 2.

Using P_N and M_H, Asaeda & Imberger (1993) were able to predict plume Types 1, 2, and 3. The plot to the left in Figure 2-7 shows the plume type parameter space defined

by Asaeda & Imberger (1993). Figure 2-7 contains all of the data in Asaeda & Imberger's (1993) paper, along with data from our own experiments.

As discussed in the previous section, we prefer to use P_N and U_N and to avoid M_H. If we neglect bubble expansion, then we can limit ourselves further to U_N alone. The plot to the right in Figure 2-7 shows an alternate plume-type prediction scheme using U_N. Type 1* plumes are generated for U_N from zero up to about 1.5. Type 2 plumes exist for U_N between about 1.5 and 2.4. For U_N greater than about 2.4 plumes are Type 3. The Type 1 plumes defined by Asaeda & Imberger (1993) do not plot in this parameter space since the reservoir depth is neglected. Also, in the case of air bubbles where the reservoir depth is of the order of H_A, bubble expansion would be significant, and P_N should be added to the analysis. As illustrated in the figure, however, the existing data are well represented using U_N alone.

Experiments

Our experiments with two-phase plumes in stratification have addressed two issues. First, plumes were observed over a wide range of the non-dimensional parameter space in order to broaden our understanding of plume typology; these data were presented in the previous section. Second, as discussed in this section, measurements were made to quantify the induced flow field to provide validation data for numerical models.

These experiments were conducted in the Parsons Laboratory at MIT using a 1.2 m square by 2.4 m deep tank. The tank is stratified using the two-tank method (Asaeda & Imberger 1993), creating a linear profile with a stratification frequency of N, typically 0.3 s^{-1}. Multiple dispersed phases were investigated, including air, oil and sediment (which forms an inverted plume). The flow field was visualized by injecting Rhodamine 6G dye at the diffuser source and illuminating a slice of the plume through the centerline with a LASER light sheet (called the LASER induced fluorescence (LIF) method). Quantitative measurements included plume length scales from the visualization and pre- and post-experiment profiles of salinity and dye tracer. Additional details of the experiments are presented in Socolofsky (2000) and Socolofsky & Adams (2000*a*, 2000*b*).

To interpret the raw density and dye concentration profiles, a conceptual model of a plume

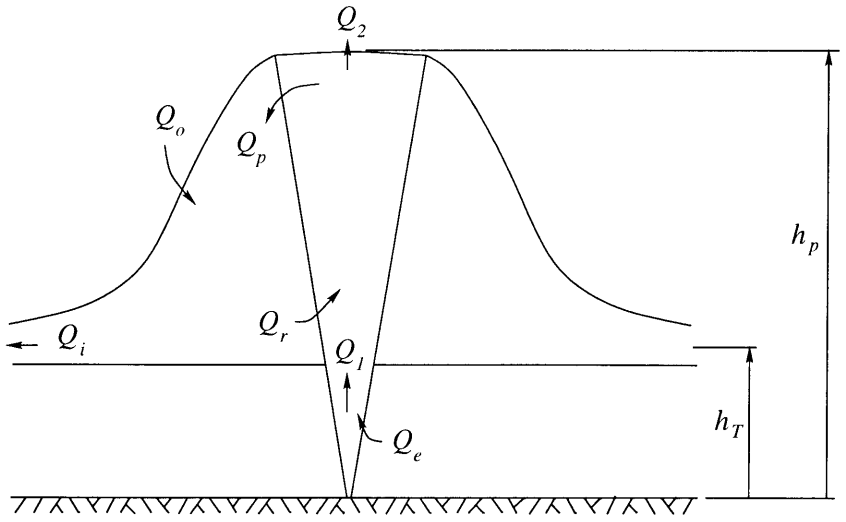

FIGURE 2-8: Schematic model of a plume peel showing definitions of the plume volume fluxes and characteristic heights.

peel was created (see Figure 2-8). Two characteristic heights and seven volume fluxes are defined. The two heights are measured from the dye concentration profiles (h_T is the center of mass of the intrusion, and h_P is the point of the minimum dye concentration between peels). The power of this conceptual model is in dealing with the exchange of fluid between the downdraught and upward moving plumes. In this model, this exchange is simplified into the recirculating flow, Q_r, which is calculated from volume conservation as described in detail below.

Because velocity measurements in stratified ambients are difficult to obtain, we instead determine plume volume fluxes. Following Leitch & Baines (1989) and Baines & Leitch (1992), the net volume flux integrated across the plume is

$$Q(z) = A\frac{\partial \rho_a/\partial t}{\partial \rho_a/\partial z} \tag{2.45}$$

where A is the cross-sectional area of the tank and t and z are the time and spatial coordinates. Using this equation, the flux at the bottom of the peel, Q_1, and the flux at the top of the peel, Q_2, are directly computed. One more flux, $Q_1 - Q_i$, is obtained by taking the maximum negative (downward) flux in the peeling region.

Three more equations follow from conservation of volume; from Figure 2-8

$$Q_e = Q_1 \tag{2.46}$$

$$Q_1 + Q_r = Q_2 + Q_p \tag{2.47}$$

$$Q_p + Q_o = Q_r + Q_i. \tag{2.48}$$

A final equation uses the dye concentration profile, taken at the end of the experiment. By integrating the dye profile, the mass of dye at each level can be calculated. The fraction of dye injected that remains trapped in the intrusion, f^* (measured from the dye profiles), is assumed to equal the fraction of plume fluid that peels, f; from Figure 2-8

$$f = \frac{Q_p}{Q_p + Q_2} \approx f^*, \tag{2.49}$$

which gives us a closed set of equations.

This simple model was applied to the first peel of a sample Type 1* plume with an airflow rate of 3 mL/s and bubble slip velocity of 7 cm/s. The entrainment below the shrouded region was 300 ± 30 mL/s, and the net upward flux through the peel was 100 ± 30 mL/s. 93% of the plume fluid peeled, which resulted in 1000 ± 300 mL/s peeling, 870 ± 300 mL/s recirculating, and 580 ± 80 mL/s intruding. Socolofsky & Adams (2000*b*) presents a more general approach where the volume fraction of fluid peeled is not assumed equal to f^*, but rather an optimization scheme is used to calculate the seven flow rates and their associated tracer and salinity fluxes. For this example with a large f^*, the results are largely unchanged and the errors are reduced. Section 2.3.3 presents a comparison of these fluxes with results from an integral model.

2.3.3 Models

The governing equations presented in the previous sections are useful for analytical purposes. To form a complete model formulation, one must add a mechanism for determining behavior at a peeling event. Though peeling can be added, models of this type, called single plume models, predict behavior of the rising plume while neglecting the dynamics of the

intrusion flow. An alternative type of formulation, called a double-plume model, explicitly models the dynamics of the intrusion flow as well as the rising inner plume. This section reviews the relative merits of different models.

Model formulations

Single-plume models are attractive because they represent initial value problems. All that is required in addition to the flux definitions and governing equations of Section 2.2.1 and 2.3.1 is a scheme for describing peeling events. Without such a scheme, numerical integration of the governing equations cannot continue past the first peeling event. The actual dynamics of peeling events, however, are not at present well understood, so the approaches used to date are approximate.

In the models described by Liro et al. (1992) and Thorkildsen et al. (1994), peeling occurs at the height where the net buoyancy of the plume, i.e. the right-hand side of (2.34), becomes negative. At this point, a certain fraction of volume and momentum flux is removed from the plume, so that the plume again becomes positively buoyant. Integration then proceeds to the next peeling event. The fate of the water lost from a given peeling event is not explicitly modeled.

Schladow (1993), in a study of the evolution of stratification of a reservoir mixed by an air bubbler, described a model in which the governing equations are integrated until the momentum flux approaches zero. Schladow assumed that all of the fluid leaves the plume at this point and ultimately intrudes into the environment at its depth of neutral buoyancy. His combined plume-reservoir model successfully predicted the time for reservoir turnover due to bubbling.

Double-plume models have been formulated by McDougall (1978), Asaeda & Imberger (1993), and Crounse (2000). To account for the dynamics forced by stratification, each of these models decomposes the bubble plume into inner and outer plumes. The inner and outer plumes are described by separate volume (Q_i and Q_o, not related to the fluxes in the previous section), momentum (M_i and M_o), and buoyancy (B_i and B_o) fluxes. Because the property profiles are no longer expected to be Gaussian, these models cast these fluxes in

terms of simpler top-hat profiles. For example, the inner plume profiles are

$$\begin{aligned} u_i(z,r) &= u_i(z),\ r \le b_i, \\ C(z,r) &= C(z),\ r \le \lambda_1 b_i, \\ \rho_i(z,r) &= \rho_i(z),\ r \le \lambda_2 b_i, \end{aligned}$$

where b_i is the top-hat inner plume width. Defining $\Delta\rho_i = \rho_i - \rho_a$, the fluxes for the inner plume become

$$Q_i = \pi u_i b_i^2, \tag{2.50}$$

$$M_i = \gamma \pi u_i^2 b_i^2, \tag{2.51}$$

$$B_i = \pi u_i b_i^2 g \frac{\Delta\rho_i}{\rho_r}. \tag{2.52}$$

For simplicity, this definition of B_i expresses buoyancy flux in reference to ρ_a, unlike (2.32). Top-hat and Gaussian flux quantities are interchangeable using

$$b_i = \sqrt{2}b,\ u_i = \frac{U_m}{2},\ \alpha_i = \sqrt{2}\alpha.$$

The flux expressions for the outer, intruding plume are identical to the inner plume, except that the outer velocity is u_o (positive for upward-flowing and negative for downward-flowing outer plumes), the density defect is $\Delta\rho_o$, and the area of the outer plume is $\pi(b_o - b_i)^2$, rather than πb_i^2.

McDougall (1978) proposed a model which splits the plume into two coflowing annular plumes. The inner plume consists of a rising flow of bubbles and water, while the outer plume consists only of water. These plumes interact through mixing across the plume boundaries. McDougall reasoned that the mixing between the plumes, and between the outer plume and the ambient, could be parameterized with the entrainment assumption, so that the entrainment fluxes are defined as

$$E_i = 2\pi b_i \alpha_i (u_i - u_o) \tag{2.53}$$

$$E_o = 2\pi b_i \alpha_o u_o \tag{2.54}$$

$$E_a = 2\pi b_o \alpha_a u_o \tag{2.55}$$

where E_i is the entrainment flux from the outer plume to the inner plume, E_o is the entrainment flux from the inner to the outer plume, and E_a is the entrainment flux from the ambient environment to the outer plume, all per unit height. α_i, α_o and α_a are entrainment coefficients governing the three entrainment fluxes. Just as entrainment transported volume and associated buoyancy from the ambient to the plume flow in single-plume models, these entrainment fluxes transport volume and associated buoyancy and momentum between the inner plume, the outer plume, and the ambient environment. The mixing assumptions are based in part on Morton (1962), who applied the entrainment assumption to coaxial, coflowing single-phase jets. This particular application of the entrainment hypothesis has not been clearly verified by experiment. Although this model can produce peeling events, which occur when the outer plume momentum approaches zero, it does not model the intrusion flow which originates at a peeling event.

Whereas McDougall's (1978) plumes were coflowing, Asaeda & Imberger (1993) formulated a double-plume model which incorporates counterflowing plumes. In this model, the inner plume encompasses all of the upward-moving fluid and bubbles (i.e. both McDougall's inner and outer upward-flowing plumes are treated together), while the outer plume represents the descending intrusion flow. Mixing between the inner and outer plumes and the ambient environment are modeled with relationships identical to those of McDougall (1978), except that in this case $u_o < 0$, so the entrainment fluxes (2.53)–(2.55) become

$$E_i = 2\pi b_i \alpha_i (u_i - u_o) \tag{2.56}$$

$$E_o = 2\pi b_i \alpha_o u_o \tag{2.57}$$

$$E_a = 2\pi b_o \alpha_a u_o. \tag{2.58}$$

Asaeda & Imberger (1993) found that $2\alpha_i \approx \alpha_o \approx \alpha_a$, which also agrees with McDougall (1978), produced the best fit of the model to their experimental data for trap height and number of sub-surface intrusions.

To solve the model, the governing equations of the inner plume are integrated from the virtual origin to the point where the momentum flux of the inner plume approaches zero. At this point, Asaeda & Imberger approximate the peeling process by assuming that 100 percent of the inner plume fluid exits the plume and begins to descend. The governing equations of the outer plume are integrated downward from this point until the plume reaches neutral buoyancy, at which point the outer plume is assumed to intrude into the ambient environment. As the properties of the inner plume had been initially calculated without the presence of the outer plume, the process of integration of the inner plume, and then the outer plume, must be repeated until the predicted flows converge. Once this is achieved, a new inner plume is initialized above the previous peel location, and the process is repeated until the surface is reached.

The Asaeda & Imberger model formulation accounts for the fact that the location of the intrusion is often significantly below the depth of the peeling event. The assumption that all of the plume fluid detrains at a peeling event is reasonable, as the actual percentage for a typical Type 2 plume has been observed to be approximately 90 percent (Socolofsky & Adams 2000*b*). However, 100 percent peeling dictates that the outer plume intrudes at some depth between peeling events, and cannot overlap a lower outer plume segment. Hence, this approach does not apply to Type 3 plumes.

A more general method for modeling the peeling process is to treat detrainment as a process analogous to turbulent entrainment, so that the flux of fluid out of the inner plume is expressed in terms of local plume conditions. Crounse (2000) proposed the detrainment equation

$$E_p = \epsilon \left(\frac{u_b}{u_i}\right)^2 \left(\frac{B_i}{u_i^2}\right) \tag{2.59}$$

where ϵ is an empirical parameter. This exact relationship has not been experimentally confirmed, but it reflects the observed physical process. The percentage of volume flux which is lost over a Type 2 peeling event can be matched by varying ϵ. Furthermore, use of this equation allows simulation of Type 3-like behavior.

Taking into account all of the discussed interactions between the inner and outer plumes, the governing equations for a double-plume model can be derived from the equations pre-

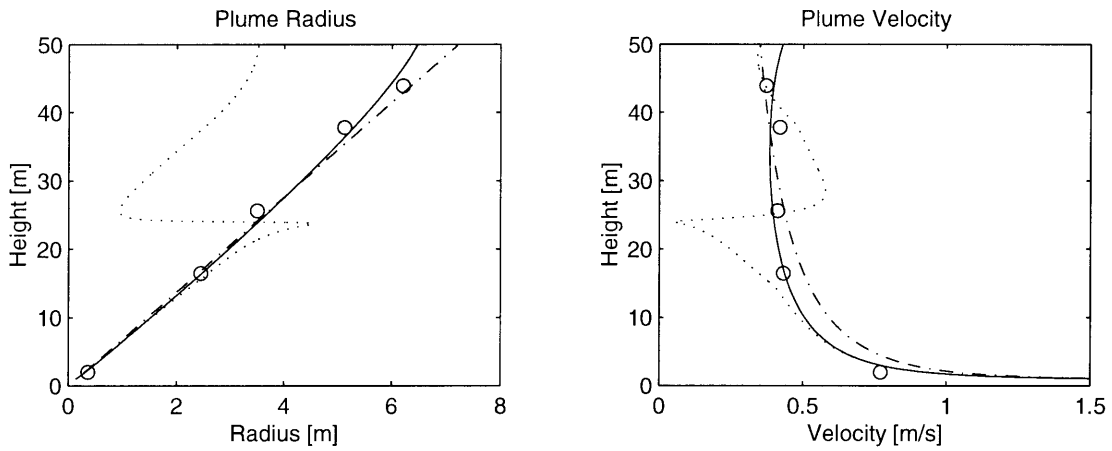

FIGURE 2-9: Radius and velocity profiles for three different modeled plumes. The single-phase plume is represented by a dash-dot line, the simple bubble plume by a solid line, and the stratified bubble plume by a dotted line. Data for a simple bubble plume from Milgram (1983) are indicated by ○. All cases have a source buoyancy flux of $B = 0.19$ m^4/s^3.

sented in Section 2.2.1 and 2.3.1. For example, the volume flux equations become

$$\frac{dQ_i}{dz} = E_i + E_o + E_p, \tag{2.60}$$

$$\frac{dQ_o}{dz} = -E_i - E_o - E_a - E_p, \tag{2.61}$$

for the inner and outer plumes, respectively.

Treatment of peeling as a continuous process requires a different iteration scheme than that of Asaeda & Imberger (1993). Given initial conditions, the inner plume is integrated upward until either the bubbles have fully dissolved, or a surface is reached. Then, starting from the top of the plume, outer plume segments are initiated wherever the peeling flux E_p is significant. The outer plume is then integrated downward until the plume intrudes. Then, the next lower outer plume is initiated, and so on down the plume. As a consequence, overlapping outer plumes completely mix. This process is then iterated until the fluxes between the inner and outer plumes are consistent. Convergence is readily achieved for Type 2 plumes with a limited number of peels, but becomes more difficult as the plume approaches Type 3 behavior.

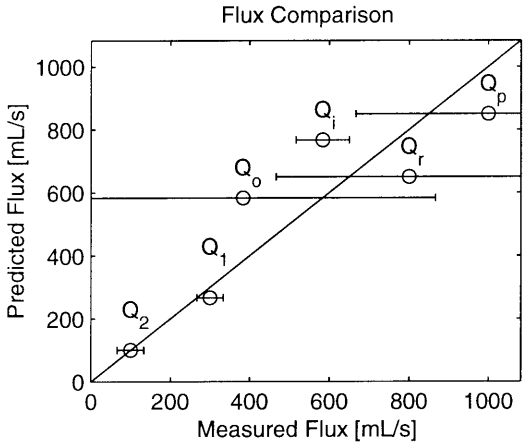

FIGURE 2-10: Comparison of model results with experimental fluxes.

Model results

Figure 2-9 illustrates model results for three different plumes having identical initial buoyancy fluxes. The three cases modeled are a single-phase plume, a bubble plume in a homogeneous environment, and a bubble plume in a linearly stratified environment ($N = 0.04\ s^{-1}$, $U_N = 1.2$). Experimental data from Milgram (1983) for a simple bubble plume are plotted for comparison.

The modeled single-phase and two-phase simple plumes are rather similar. The plume radii are both nearly linear with height. The velocity of the simple bubble plume is slightly lower than that of the single phase plume at lower elevations because the effective buoyant force per unit height is smaller in the bubble plume than in the simple plume. As the bubbles expand with height, the buoyancy flux increases and the fluid accelerates. The simple two-phase plume model results match the data from Milgram.

The only difference between the two modeled bubble plumes is the presence of stratification. The properties of the stratified plume are initially similar to the other plumes, but diverge as the plume fluid is arrested by buoyant forces and subsequently detrains. Above the peel the plume reforms, but is significantly smaller than the simple bubble plume at all points above the plume.

Figure 2-10 compares model results with experimental flux calculations as described in Section 2.3.2. All of the predicted fluxes lie within the range of experimental error except

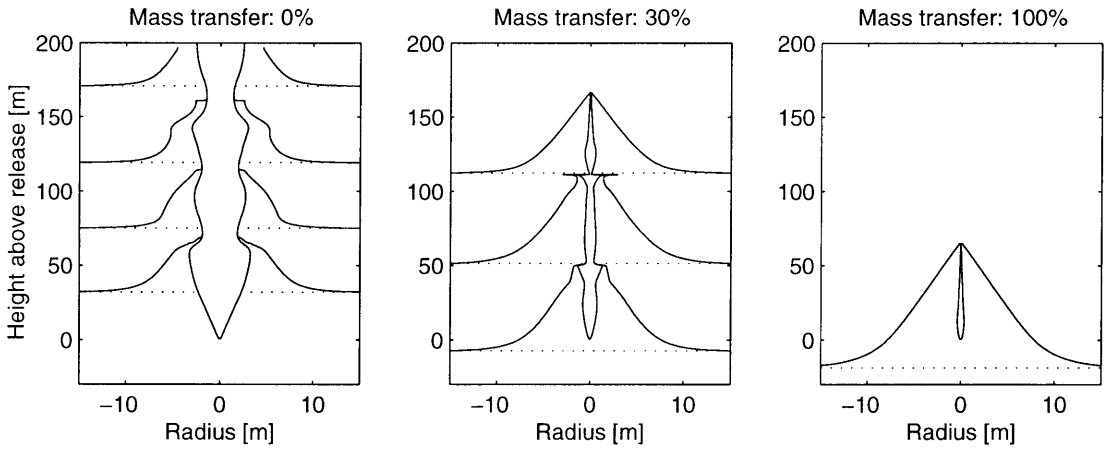

FIGURE 2-11: Profiles of CO_2 droplet plumes. Shown are the inner and outer plume radii of three plumes resulting from the release of buoyant CO_2 droplets ($B = 10^{-3}$ m^4/s^3; initial diameter = 0.4 cm) at 800 meters depth with a typical ocean stratification ($N = 0.003$ s^{-1}). The mass transfer rate is varied between zero and 100 percent of that predicted by (2.15). The case without mass transfer, which continues to the water surface, has been truncated for clarity.

for Q_i, the flux of fluid intruding into the ambient. Because the experiment was conducted in a finite tank, it is possible that the experimental value of Q_i is suppressed by blockage due to the boundary.

Figure 2-11 shows model results for continuous releases of liquid CO_2 in a stagnant, stratified environment, such as might occur in an oceanic CO_2 sequestration scheme. The only difference among the three cases presented is the dissolution rate of the CO_2 droplets, which profoundly affects the plume structure. The dissolution can be strongly affected by the formation of a hydrate film on the surface of the CO_2 droplets, a process that is not completely understood (Wong & Hirai 1997). Not only does the dissolution lead to reduced positive buoyancy with height, but the dissolved CO_2 also increases the density of the plume water. Thus, the effects of increased dissolution are amplified.

Alternative models

The advantages of integral models are that the governing equations allow insight into the dynamics of the flow, they are computationally efficient, and they produce reasonably accurate results in many cases. However, it is clear that integral models gradually lose their

validity as the plume structure becomes less self-similar, due to factors such as stratification.

Integral models are not the only tool for modeling multi-phase flows: more rigorous computational fluid dynamic codes, which solve the 3-D Navier-Stokes equations, may also be used. They generally follow one of two approaches. In the Lagrangian/Eulerian approach, individual particles of the dispersed phase are tracked as they advect through a fluid modeled by the Navier-Stokes equations. In the Eulerian/Eulerian approach, both phases are described by the Navier-Stokes equations (Jakobsen et al. 1997). These types of models have been mostly applied to confined multi-phase flows such as bubble columns (e.g. Lapin & Lübbert 1994, Jakobsen et al. 1997), although some investigators have examined bubble plumes as well (Alendal & Drange 2000, Chen et al. 2000, Sato & Hama 2000).

2.4 Bubble plumes in crossflow

Returning to bubble plumes in unstratified environments, this section addresses the complications of a uniform, flowing ambient, or crossflow. We use dimensional analysis to classify the possible range of behavior of bubble plumes in a crossflow and present the results of some of our experiments.

2.4.1 Theory

Crossflows affect a wide range of plume properties, changing the basic plume dynamics. Even in the case of single-phase plumes, crossflows enhance entrainment, deflect the plume centerline, can deform the plume shape into a vortex pair, and can cause fluid to leak in the downstream wake of the plume (Fischer et al. 1979, Davidson & Pun 1999, Yappa & Zheng 1997*a*). Bubble plumes are affected similarly, and have additional complications due to the slip velocity of the dispersed phase.

Analysis of single-phase jets and plumes

As a basis for understanding bubble plumes in a crossflow, we first look at single-phase jets and plumes. Davidson & Pun (1999) studied the effects of crossflow on a single-phase

momentum jet. Because the mean jet, entrainment, and turbulent velocities all decrease with height above the source, the effect of a uniform crossflow on the jet increases with height. Following Davidson & Pun (1999), three modes of behavior can be anticipated based on the height, z, relative to a characteristic jet length scale in a crossflow,

$$l_{jc} = \frac{M_0^{1/2}}{u_\infty}, \tag{2.62}$$

where M_0 is the jet momentum flux and u_∞ is the crossflow velocity. For $z/l_{jc} < 0.14$ the jet is Gaussian, adequately described by the stagnant water equations, but deflected by the vector sum of the crossflow and the mean vertical jet velocity. At greater elevations, the jet begins to leak fluid in the downstream wake, but concentration and velocity profiles remain reasonably Gaussian. However, for $z/l_{jc} > 1$, the Gaussian model begins to fail, and the jet becomes strongly affected by the current.

The length scale, l_{jc}, is proportional to the height where the jet entrainment velocity, u_e, balances with the crossflow velocity. Fischer et al. (1979) report that u_e varies with height as

$$u_e = 7\alpha_j \frac{M_0^{1/2}}{z}. \tag{2.63}$$

Combining (2.62) and (2.63), we find that the entrainment velocity equals the crossflow velocity at $z/l_{jc} = 7\alpha_j = 0.4$, a value between the point where leakage begins and where the Gaussian structure breaks down (Davidson & Pun 1999).

Pun & Davidson (1999) investigated buoyant plumes and showed that they behave similarly. A crossflow is considered weak when the Gaussian model still applies. When the Gaussian model is no longer adequate, the crossflow is considered strong, and Hugi (1993) reported that a plume in a strong crossflow resembles a line thermal. Applying similar scaling principles to buoyant single-phase plumes, Pun & Davidson (1999) find a characteristic length scale for plumes in crossflow,

$$l_{pc} = \frac{B}{u_\infty^3}. \tag{2.64}$$

Using the results of Davidson & Pun (1999), $z/l_{pc} = 0.003$ gives the point where fluid begins to leak, $z/l_{pc} = 0.06$ gives the point where the entrainment velocity equals the crossflow

velocity, and Pun & Davidson (1999) report $z/l_{pc} = 0.5$ is the transition height at which the plume resembles a line thermal.

Complications due to slip velocity

Because the fluid and the bubbles move at different velocities, the crossflow can create a separation between the rising plume fluid and the bubbles, as depicted in Figure 2-2. In the simplest model, the bubble trajectory is given by the vector sum of the crossflow velocity and the bubble rise velocity. This introduces two important effects. First, this leads to a fractionation of the bubbles: fast rising bubbles stay in front, and slow rising bubbles move to the back of the bubble plume (Hugi 1993). Second, since the vertical velocity of the bubbles is the plume fluid velocity plus the bubble slip velocity, the trajectory of the bubble column is steeper than the trajectory of the entrained fluid. Unless the bubble core turbulence is sufficient to keep the entrained plume fluid with the bubbles, the fluid and the bubbles will separate, in which case the traditional view of an integral model will no longer hold.

Hugi (1993) conducted a series of experiments in a 3 m deep tank with air flow rates of 1 to 9 mL/s, slip velocities of 17 to 30 cm/s, and crossflow velocities of 1.2 to 7.9 cm/s. The crossflow was simulated by towing the bubble source. From visual observation, bubble fractionation was verified. Lagrangian integration of LDV measurements taken at a point as the plumes passed by indicted that fluid entrained in the front of the plume was indeed ejected in the lee of the plume after being elevated a short distance, indicating separation. Dye injected with the bubble plume also confirmed separation. Hugi (1993) concluded that coherent, self-similar plumes would not form in a crossflow because of the separation between the rising bubbles and the entrained fluid.

We have conducted similar experiments in a 0.8 m square cross-section flume. Our experiments confirmed Hugi's (1993) observation that the fluid and bubbles can separate, but suggest that there is a critical height, h_S, associated with the onset of separation. To analyze our experiments, we define two non-dimensional velocities: $u_s/(B/z)^{1/3}$ and $u_\infty/(B/z)^{1/3}$, which are the slip and crossflow velocities normalized by the characteristic plume fluid rise velocity. Substituting h_S for z and invoking the Buckingham Π theorem, the separation

height should be derived from

$$\frac{u_\infty}{(B/h_S)^{1/3}} = f\left(\frac{u_s}{(B/h_S)^{1/3}}\right). \tag{2.65}$$

This relationship is calibrated to our experiments in Section 2.4.2.

Complications due to stratification

In the presence of both a crossflow and stratification, there are competing forces tending to break down plume similarity. The dimensional analysis presented previously can help identify the dominant processes. If the height h_T for plume trapping due to stratification is significantly below the height h_S where currents cause separation, then stratification is dominant, and the plume can be modeled as in Section 2.3. In the case where the heights are reversed, the crossflow would dominate, and stratification can be ignored.

Models

Despite the potential loss of similarity, integral models have been applied to study multi-phase plumes in crossflows. Yapa & Zheng (1997*a*) presents a model of an ocean blowout and Yapa & Zheng (1997*b*) validates the model to some shallow field data in the North Sea. Their model implicitly assumes that bubbles or droplets do not separate from the rising plume fluid prior to trapping. Socolofsky & Adams (2000*c*) presents a modeling algorithm using h_S. The multi-phase plume is integrated as a mixture up to the separation height, taken as the lower of h_S or h_T. Above this transition, the entrained fluid is modeled as a buoyant, single-phase jet in the lee of the bubble column, where the initial momentum is the momentum of the mixed model at the separation height. The bubbles are modeled above the separation height as the vector sum of the bubble slip velocity and the crossflow. An alternate model, presented by Johansen (1999), accounts for the separation directly: when the slip velocity of the bubbles is great enough that they would be lost on the leading edge of the plume, the droplets are ejected from the integral model and tracked separately.

Experiment I.D.	Flow Rate			u_∞	h_S
	Air [mL/s]	Oil [mL/s]	Alcohol [mL/s]	[cm/s]	[cm]
Exp-B8	33	0	0	2	–
Exp-C8	17	17	0	5	–
Exp-C19	0	0	2.5	5	–
Exp-C14	0	10	0	5	–
Exp-B3	3	0	0	5	16
Exp-B10	3	0	0	10	7
Exp-C16	10	10	0	10	28
Exp-C15	4	0	2.5	5	15

TABLE 2.1: Experimental parameters for selected crossflow experiments.

2.4.2 Observations

The experiments confirmed the presence of fractionation and separation. For plumes with high buoyancy and low crossflow velocity, separation did not occur by the time the bubbles reached the water surface, and the situation is classified as a weak crossflow. In other experiments, separation did occur and the conditions are classified as strong crossflow. Table 2.1 presents the parameters of the experiments shown in the following figures.

Weak crossflows

In weak crossflows, some entrained fluid stays with the bubble plume from the injection point to the flume surface. Figure 2-12 shows four representative experiments in weak crossflows.

While major separation between the lightest dispersed phase and the other components of the plume does not occur before the plume reaches the surface, two forms of detachment, or leakage, are observed. First, as reported by Davidson & Pun (1999) for single-phase jets, some entrained fluid leaks into the downstream wake. Comparing frames (a.) and (b.) in Figure 2-12 to frames (c.) and (d.), the detachment is much greater for air bubble plumes than for the oil or alcohol plumes, even though the crossflow velocity was greater for the oil and alcohol plumes. This is explained by the fact that bubbles with higher

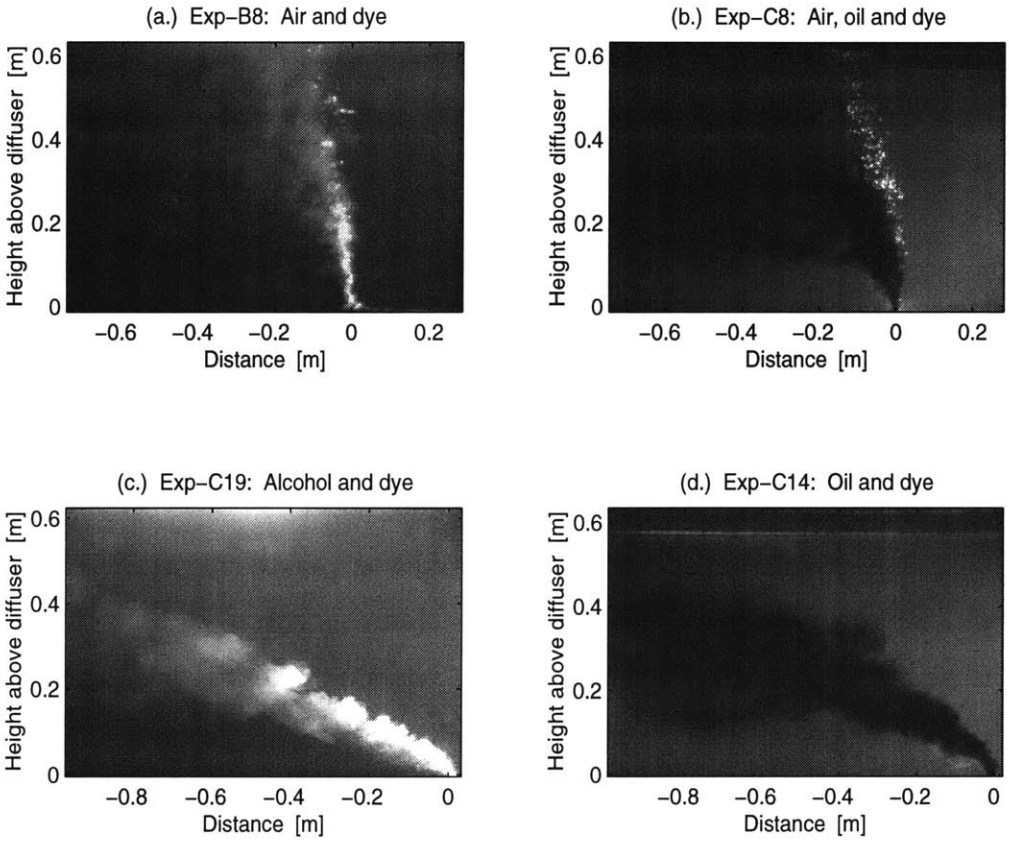

FIGURE 2-12: Experiments showing multi-phase plumes in weak crossflows. Experimental conditions are summarized in Tab. 2.1.

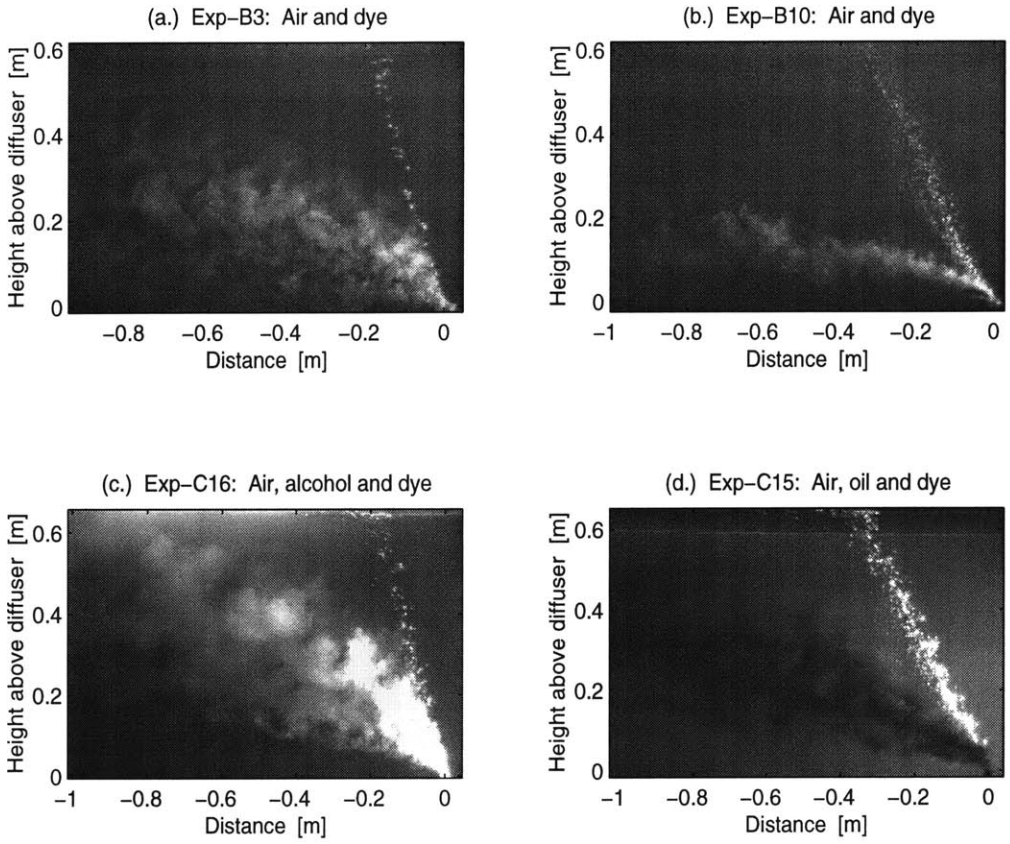

FIGURE 2-13: Experiments showing multi-phase plumes in strong crossflows. Experimental conditions are summarized in Tab. 2.1.

slip velocities advect much faster than their accompanying entrained fluid (Leitch & Baines 1989). The second form of leakage is seen by the fractionation of the bubbles and droplets in the crossflow, leaking smaller bubbles into the downstream wake. Frame (b.) in Figure 2-12 is the most striking example of fractionation, where the air bubbles lead in the front and the oil bubbles fall to the back of the plume, but dye marking the entrained fluid is present throughout the plume.

Strong crossflows

In strong crossflows there is significant separation between the dominant dispersed phase and the entrained fluid and the separated fluid rises independently in the far field. Figure 2-13 shows four representative experiments in strong crossflows. Frames (a.) and (b.) in Figure 2-13 are for two-phase air-bubble plumes and frames (c.) and (d.) are multi-phase alcohol and air and oil and air plumes, respectively.

For the air-bubble plumes, complete separation occurs between the entrained fluid and the rising bubble column. Dye injected near the release point separates from the bubble column, but continues to rise in the far field even though the dye and entrained fluid are neutrally buoyant due to acceleration within the bubble column. This indicates that, beyond the point of separation, the injected dye tracer behaves like a momentum jet. Detachment is also observed throughout the mixed and separated plume regions. Above the separation height, the trajectory of the bubble column appears linear, represented by the vector sum of the group rise velocity of the bubbles and the crossflow velocity. This further indicates that the bubble column in a strong crossflow is not plume-like above the separation height since the downstream coordinate of a pure plume should vary as the $\frac{4}{3}$-power of height above the diffuser (Fischer et al. 1979).

For the multi-phase plumes in frames (c.) and (d.), complete separation occurs between the air bubbles and the other dispersed phase, but further separation is not observed between the separated oil and alcohol plumes and their entrained fluid. Following the description above, the separated oil and alcohol plumes are accelerated in the plume region before they separate; thus, they should be represented as buoyant momentum jets in the far field. Fractionation and leakage remain as characteristic features of these plumes.

Separation height

From a suite of 25 experiments (which includes those presented in this section) Socolofsky & Adams (2000*c*) calibrated (2.65) as shown in Figure 2-14, yielding,

$$\frac{u_\infty}{(B/h_S)^{1/3}} = 6.32 \left(\frac{u_s}{(B/h_S)^{1/3}} \right)^{-2.36} . \tag{2.66}$$

2.5 Summary

The defining character of a multi-phase plume is the relative independence of the dispersed phase from the surrounding fluid. In this chapter we have summarized this characteristic in the parameter u_s, the slip velocity. The main effects of u_s are to erode the self-similarity and to reduce the effective buoyant force of the multi-phase plume.

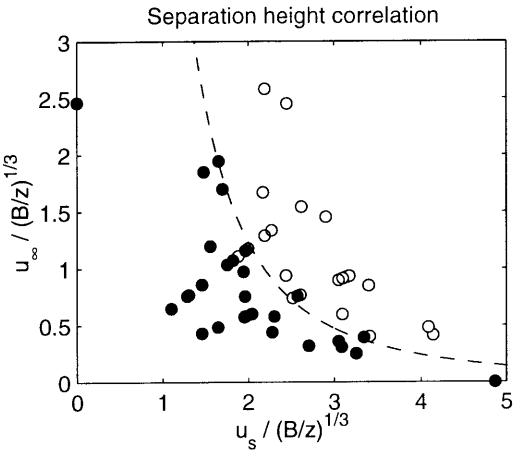

FIGURE 2-14: Transition height correlation for multi-phase plumes in a crossflow. Filled circles indicate heights below which the phases remain mixed; open circles indicate heights above which one or more phases have separated. The dashed line plots the relationship in (2.66).

In homogeneous environments, the bubble motion leads to a variable entrainment coefficient, α, and variable spreading ratio for the bubbly core, λ_1. Although non-constant α and λ_1 imply the loss of strict similarity, an integral model, such as described in Section 2.2, continues to perform well due to relative insensitivity of the model to variation in these parameters over their expected range of environmental values (Turner 1986, Liro et al. 1992).

Stratification breaks down similarity in two different ways. First, the variation of α is enhanced by stratification. Second, the stratification causes a separation between the bubbles and plume fluid at a peel, completely eliminating self-similarity.

In addition to its effects on self-similarity, u_s in stratification affects other plume properties. First, because the peeled water loses its buoyancy when the bubbles continue to rise, the intrusion layers form much lower than predicted by trap height equations for single-phase plumes. Second, the magnitude of u_s for a given release changes the efficiency of plume peeling. Higher u_s causes greater leakage and lower efficiency. As the efficiency decreases or when density changes caused by dissolution increase the tendency for intrusions to overlap, plumes tend toward Type 3 behavior. The effects of u_s in stratification can be analyzed using U_N and P_N. Together these non-dimensional numbers correlate with the variable trap height of multi-phase plume intrusions and with the overall plume efficiency or typology.

Two types of integral models were discussed to deal with the effects of stratification. Single-plume models were applied as didactic tools to illustrate the interplay of forces in the bubble plume. For numerical modeling, double-plume models capture more of the flow characteristics. These models address the break down in similarity at a peel directly by separating the plume peeling and intrusion flows from the upward-moving, nearly self-similar plume core.

In a crossflow, similarity is degraded due to advection of the entrained plume fluid away from the bubbles by the crossflow itself. In weak crossflows, the bubbles fractionate, leaving small bubbles in the wake of the plume. Under these conditions, integral models incorporating the crossflow were shown to apply. As the crossflow increases, however, the bubbles separate completely from the entrained fluid, and self-similarity is lost. When separation occurs, the bubbles should be modeled individually, and the ejected fluid can be treated as a buoyant momentum jet.

Chapter 3

Behavior of multi-phase plumes in stagnant stratification[1]

Abstract: This paper introduces the non-dimensional slip velocity, U_N, as the appropriate parameter for describing stratified multi-phase plumes, where U_N is definded as the ratio of the bubble slip velocity, u_s, to a characteristic plume fluid rise velocity, $(BN)^{1/4}$; B is the total kinematic buoyancy flux, and N is the Brunt-Vaisälä buoyancy frequency. U_N is first derived by dimensional analysis, then its role in controlling plume behavior is demonstrated by non-dimensionalizing the governing integral plume equations. To investigate correlations of plume properties with U_N, laboratory experiments in linear stratification were conducted using air, oil and glass beads (creating an inverted plume). A new type of plume behavior is identified, called Type 1*, in which weak bubbles are dispersed by horizontal motion at the first peel, creating a diffuse secondary plume as they rise out of the intruding flow. Plume properties, including plume type behavior, trap and peel heights, mass fraction of passive tracer peeled, and bubble spreading ratio, are shown to correlate with U_N.

3.1 Introduction

Multi-phase plumes occur in a wide range of natural and engineered systems (Schladow 1993, Lemckert & Imberger 1993, Wüest et al. 1992, McDougall 1978, Park & Yang 1997), but

[1]This chapter submitted to the *Journal of Fluid Mechanics* as Socolofsky & Adams (2000), "Multi-phase plumes in stratification: Dimensional analysis."

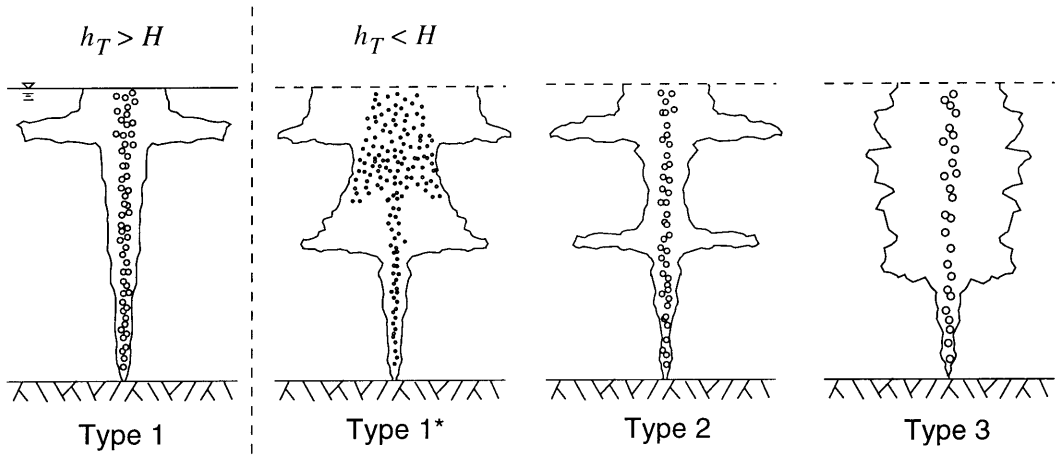

FIGURE 3-1: Schematic of the plume type classification. h_T is the trap height of the first peel.

interest in two specific applications, ocean sequestration of CO_2 to mitigate potential global climate change and the clean up of oil spills and well blowouts from deep-water oil fields, has created the need to better understand multi-phase plumes in the context of the deep ocean (below 800 m). Because dissolving CO_2 lowers the pH, the dilution in a CO_2 plume is the primary interest (Caulfield et al. 1997, Adams et al. 1997, Crounse 2000, Alendal & Drange 2000, Sato & Hama 2000, Chen et al. 2000). In the oil spill case, the primary objective is to predict the fate of the oil in the water column (Topham 1975, McDougall 1978, Yappa & Zheng 1997*a*, 1997*b*, 1999). In both cases field experimentation is difficult, environmentally taxing, and expensive; hence, it is desirable to extend laboratory-scale results to the deep ocean through non-dimensional correlations and through numerical models.

Several properties of stratified multi-phase plumes have been investigated in the laboratory and in shallow field studies by previous authors. These including trap height (Topham 1975, McDougall 1978, Matsunashi & Miyanaga 1990, Asaeda & Imberger 1993, Lemckert & Imberger 1993), intrusion layer flux (Topham 1975, Matsunashi & Miyanaga 1990, Lemckert & Imberger 1993), and various aspects of the plume surface expression (Asaeda & Imberger 1993, Lemckert & Imberger 1993). Asaeda & Imberger (1993) also introduced a plume classification that identified three distinct modes of behaviour, depicted schematically in Figure 3-1. Type 1 plumes have no sub-surface intrusions. Type 2 plumes have distinct, steady sub-surface intrusions. Type 3 plumes have irregular, unsteady sub-surface

intrusions. Transition from Type 1 through Type 2 to Type 3 behaviour is achieved by decreasing the buoyancy flux or increasing the stratification strength (Asaeda & Imberger 1993). The other plume type shown, Type 1*, is a new type identified by our experiments where the bubbles are dispersed by the initial intrusion formation. Plume type is described further in Section 3.5.

Because previous studies were conducted in shallow systems, often for application in reservoir destratification, bubble expansion has been assumed to affect the plume dynamics, and as a result, existing correlations for plume properties are depth-dependent (Asaeda & Imberger 1993, McDougall 1978, Milgram 1983, Wüest et al. 1992, Lemckert & Imberger 1993, Leitch & Baines 1989, Patterson & Imberger 1989, Schladow 1993). By contrast, in the deep ocean and for relatively incompressible dispersed phases (such as liquid CO_2 and oil), pressure changes and, therefore, droplet expansion, are negligible over the natural length scale of the plume, and plume properties are expected to be independent of depth for a given set of initial conditions. Thus, depth-dependence should be removed from existing correlations before they can be applied with confidence to deep-ocean plumes.

In addition to using experimental correlations, a range of numerical models have been developed both for reservoir destratification and for the deep-ocean CO_2 and oil-spill plumes. These include two and three dimensional computational fluid dynamic (CFD) models (Alendal et al. 1998, Sato & Hama 2000, Chen et al. 2000) and a range of integral plume models (Crounse 2000, Caulfield et al. 1997, Yapa & Zheng 1997*a*, Asaeda & Imberger 1993, Wüest et al. 1992, Thorkildsen et al. 1994, McDougall 1978).

Because of their scale, integral plume models are the better suited to study near-field plume dynamics. In the simplest integral model, the plume is treated as a single, upward flowing plume that rises to a terminal level, ejects a prescribed fraction of fluid and buoyancy flux, and then restarts to form a secondary plume (Liro et al. 1992, Thorkildsen et al. 1994). Double plume models are somewhat more sophisticated, allowing an inner radial plume to interact with one or more outer annular plumes, as well as modelling the descent of the ejected fluid to the intrusion layer (McDougall 1978, Asaeda & Imberger 1993, Crounse 2000). In the McDougall (1978) and Asaeda & Imberger (1993) double plume models, all of the inner plume fluid peels into the downdraught plume when the inner plume net momentum

flux drops to zero. The Crounse (2000) double plume model incorporates a detrainment algorithm that provides for variable volume detrainment at each discretization step based on a balance between the bubble lifting capacity and the negative buoyancy of the entrained water.

Although these models are physically based, they rely on assumptions about the amount of fluid that peels, the entrainment formulation and coefficient values, and on a parameterization of the dispersed phase (usually, the slip velocity and turbulent bubble Schmidt number). Data to validate these assumptions are sparse and only include indirect measures, such as the trap height and intrusion layer dilution. These model uncertainties impact predictions for CO_2 and oil-spill plumes because they affect the intrusion layer formation, which controls the dilution of CO_2 and the distribution of oil in the water column.

To address these issues, and the limitations of existing correlations for the deep ocean cited above, this paper derives a new governing plume parameter and presents laboratory experiments that provide new data for models. Section 3.2 introduces the processes affecting multi-phase plumes in stratification. Section 3.3 presents a detailed dimensional analysis that suggests the non-dimensional slip velocity, U_N, which is depth-independent, as the appropriate governing parameter for multi-phase plumes. Literature data are combined with our own experiments, described in Sections 3.4 and 3.5, to test the applicability of the new parameterization. Section 3.6 presents the correlations of plume properties, including peeling fraction for a passive tracer and bubble spreading ratio, with U_N. Section 3.7 discusses the correlations to gain a better physical understanding of the processes controlling multi-phase plumes and demonstrates their relevance to field-scale applications.

3.2 Effects of buoyancy

Figure 3-2 shows a schematic of an idealized Type 2 multi-phase plume in linear stratification similar to that described by Asaeda & Imberger (1993). As the dispersed phase rises, it entrains ambient fluid and forms a buoyant inner core plume whose outer edge is depicted by the dashed lines. Eventually, the negative buoyancy of the entrained fluid is too great for the bubble drag to support and the fluid detrains, or peels. The peeling region of the plume can

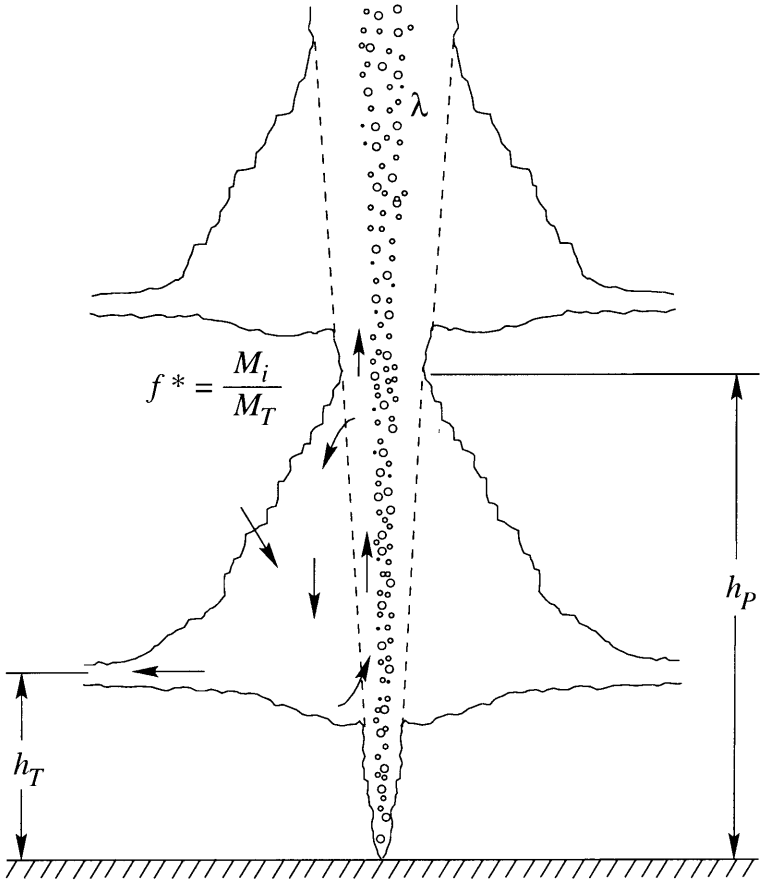

FIGURE 3-2: Schematic of a Type 2 multi-phase plume in linear stratification.

be compared to a turbulent fountain: large-scale eddies rising in the inner core are ejected to the side and fall back on the plume. This process, averaged over many eddies, creates the annular structure of the downdraught plume (shown by the downward-pointing arrows), which shrouds much of the upward plume. The outer plume overshoots neutral buoyancy at the bottom of its descent, due to its excess negative momentum, and then rebounds and intrudes laterally into the ambient. The bubbles of the inner core plume maintain their buoyancy, however, and continue to rise through the detrainment zone, forming additional plume structures.

Several important variables for the first plume peel are identified in the figure. These include the intrusion level or trap height, h_T, the peeling height of the detrainment zone, h_P, the ratio between the bubble core width and the inner plume core width, λ (a type of turbulent Schmidt number $1/\lambda^2$), and the fraction of passive tracer that peels, $f^* = M_i/M_T$, where M_i is the mass of tracer found in the intrusion and M_T is the total mass of tracer injected.

As we will show, the plume behaviour is quite sensitive to the peeling efficiency, given by the fraction of inner-core fluid that peels in the detrainment zone (which is closely related to f^*), since fluid continuing beyond the peeling zone adds a flux of negative buoyancy to the secondary plume. For the Type 2 plume depicted in the figure, this negative buoyancy flux is small. When this flux is larger, as in Type 3 plumes, intrusions may begin to overlap and the entire plume may be shrouded by a downdraught region. Because the initial plume discharge has no entrained fluid (i.e. only the positive buoyancy flux of the bubbles), the first intrusion always exhibits Type 2 characteristics and cannot descend below the injection point.

3.3 Dimensional analysis

To predict plume quantities two independent methods can be used to derive a set of governing non-dimensional parameters: formal dimensional analysis through the Buckingham Π Theorem or non-dimensionalization of the governing equations. To illustrate the physics of multi-phase plumes in stratification, independent of an analytical model, we begin with the

Buckingham Π Theorem. Because we arrive at a novel set of parameters, the governing equations are also non-dimensionalized to illustrate differences with previous authors.

To derive the set of governing parameters, consider first a single-phase plume in linear stratification. The important independent variables are the total kinematic buoyancy flux, $B = gQ_b(\rho - \rho_b)/\rho$ and the Brunt-Vaisälä stratification frequency, $N = [-(g/\rho)(\partial\rho/\partial z)]^{1/2}$, where Q_b and ρ_b are the volume flow rate and density of the effluent at the source, respectively, ρ is the ambient density and z is the positive vertical-upward coordinate. These two variables can be combined to form characteristic scales for length, $l_C = (B/N^3)^{1/4}$, velocity, $u_C = (BN)^{1/4}$, and volume flux, $Q_C = (B^3/N^5)^{1/4}$.

For illustration purposes, we will use the trap height, h_T, as the dependent variable in the dimensional analysis. Then, normalizing h_T by l_C, we introduce the first non-dimensional group, π_1, given by

$$\pi_1 = \frac{h_T}{(B/N^3)^{1/4}}, \tag{3.1}$$

which is the ratio of the trap height to the natural length scale of the plume. Crawford & Leonard (1962) reported the relationship $\pi_1 = 2.8$ for single-phase plumes, and Turner (1986) demonstrated its applicability from laboratory scales up to the scales of forest fires and volcanic eruptions.

Turning to the simplest multi-phase flow, consider an incompressible dispersed phase, such as an inverted sediment plume where particle expansion and dissolution are negligible. This introduces two-phase plume physics without the complications of bubble expansion. Several characteristics describe the effect of the dispersed phase, including size, density, shape, and possibly cohesion (Ruggaber 2000). Since the slip velocity (or terminal fall velocity), u_s, is itself a function of these parameters, we assume that u_s incorporates the important two-phase characteristics affecting the plume. This is similar to the assumption initiated by Kobus (1968) and used by many others for the analysis of air bubble plumes (e.g. Ditmars & Cederwall 1974, McDougall 1978, Asaeda & Imberger 1993, Crounse 2000). Normalizing u_s by u_C gives a second non-dimensional group, π_2, defined by

$$\pi_2 = \frac{u_s}{(BN)^{1/4}}, \tag{3.2}$$

which is the ratio of the slip velocity to the characteristic plume fluid rise velocity. From the Buckingham Π Theorem, we expect that $\pi_1 = f(\pi_2)$; this hypothesis is verified in Section 3.6.

To complete the formal dimensional analysis, we introduce bubble expansion. Assuming adiabatic expansion of an ideal gas, bubble expansion depends only on the total pressure head, $H_T = H + H_A$, where H is the reservoir depth and H_A is the atmospheric pressure head. Normalizing H_T by l_C we have

$$\pi_3 = \frac{H_T}{(B/N^3)^{1/4}}, \tag{3.3}$$

which is the ratio of the total head to the plume natural length scale. (3.3) suggests that bubble expansion becomes important (π_3 of order one) when the natural plume length scale is of the order of the total pressure head, which is true for many reservoir applications. Although the dependence of plume characteristics on H or H_T has been investigated by others, few of the existing experimental data for trap height have significant bubble expansion over l_C; hence, the final relationship $\pi_1 = f(\pi_2, \pi_3)$ cannot be verified with existing data. This is discussed further in Section 3.6.

Previously, plume properties have been correlated with various versions of the plume number, P_N, and the parameter M_H, defined by Asaeda & Imberger (1993) as

$$P_N = \frac{N^3 H^4}{B} \tag{3.4}$$

$$M_H = \frac{B}{4\pi\alpha^2 H u_s^3}, \tag{3.5}$$

where α is an entrainment coefficient (taken as 0.083). P_N represents the ratio of the total depth to the plume natural length scale (raised to the fourth power), and M is a measure of the effective buoyancy flux of the bubbles as reduced by the bubble slip (Asaeda & Imberger 1993). Comparing these parameters to the non-dimensional groups in (3.1) to (3.3) and assuming $H \gg H_A$, we find $P_N \approx \pi_3^4 = P_{HT}$ and $M_H \approx 1/(4\pi\alpha^2\pi_3\pi_2^3) = M_{HT}$, where P_{HT} and M_{HT} replace H with H_T in their definitions of P_N and M_H. Therefore, correlating plume properties to π_2 and π_3 allows the same flexibility as using P_N and M_H.

The parameters P_N and M_H were derived originally by normalization of the governing

plume integral model equations. The equations of mass and momentum conservation for Gaussian velocity, bubble and buoyancy profiles are well known (see e.g. McDougall 1978, Asaeda & Imberger 1993) and are given by

$$\frac{d(U_m b^2)}{dz} = 2\alpha b U_m \tag{3.6}$$

$$\frac{d(U_m^2 b^2)}{dz} = \frac{2gb^2}{\gamma}\left[\lambda_1^2 C_m \frac{(\rho_r - \rho_b)}{\rho_r} - \frac{\lambda_2^2 \Delta\rho_{w,m}}{\rho_r}\right], \tag{3.7}$$

where U_m is the centerline plume fluid velocity, b is the nominal half-width of the Gaussian plume fluid velocity profile, γ is a momentum amplification factor, C_m is the centerline dispersed phase void fraction, ρ_r is a constant reference density, λ_2 is the density defect profile spreading ratio, and $\Delta\rho_{w,m}$ is the centerline density difference between the ambient and the plume fluid densities.

Previous authors incorporate the bubble expansion and the entrainment of ambient fluid into a single equation for buoyancy conservation (McDougall 1978, Asaeda & Imberger 1993). This introduces an inconsistency since the bubbles are transported faster than the plume fluid due to their slip velocity. To avoid this problem, we introduce separate equations for the conservation of plume fluid and bubble buoyancy flux (assuming air bubbles and the Ideal Gas Law), namely:

$$\frac{d}{dz}\left[\frac{gU_m(\lambda_2 b)^2 \Delta\rho_{w,m}}{\rho_r(1+\lambda_2^2)}\right] = -U_m b^2 N^2 \tag{3.8}$$

$$\frac{d}{dz}\left[\frac{\pi g(U_m + U_B)(\lambda_1 b)^2 C_m(\rho_r - \rho_b)}{\rho_r(1+\lambda_1^2)}\right] = \frac{gQ_0 H_A(\rho_r - \rho_b)}{\rho_r(H_T - z)^2}, \tag{3.9}$$

where U_B, introduced by McDougall (1978), is the modified bubble slip velocity given by $u_s(1+\lambda_1^2)$ and Q_0 is the air bubble volume flow rate at standard temperature and pressure (STP).

Using the characteristic scales introduced earlier, the above integral equations are non-dimensionalized using the variables

$$z = \left(\frac{B}{N^3}\right)^{1/4} Z; \qquad b = 2\alpha\left(\frac{B}{N^3}\right)^{1/4} B_N$$

$$U_m = U_B V; \qquad C_m = X$$

$$\frac{\Delta\rho_{w,m} g}{\rho_r} = \frac{U_B^2}{\lambda_2^2}\left(\frac{N^3}{B}\right)^{1/4} G_w; \qquad \frac{\Delta\rho_b g}{\rho_r} = \frac{U_B^2}{\lambda_1^2}\left(\frac{N^3}{B}\right)^{1/4} G_b$$

where Z, B_N, V, X, G_w, and G_b are the non-dimensional variables for elevation, width, plume fluid velocity, bubble concentration, plume fluid buoyancy, and bubble buoyancy, respectively. This set of non-dimensional variables differs from previous authors by using l_C as the normalizing length scale instead of H. Inserting these definitions into (3.6) to (3.9), we obtain the system of equations:

$$\frac{d}{dZ}\left[VB_N^2\right] = VB_N \tag{3.10}$$

$$\frac{d}{dZ}\left[VB_N\right] = \frac{B_N}{\gamma V}(XG_b - G_w) \tag{3.11}$$

$$\frac{d}{dZ}\left[\frac{VB_N^2 G_w(1+\lambda_1^2)^2}{(1+\lambda_2^2)}\right] = -\frac{VB_N^2}{\pi_2^2} \tag{3.12}$$

$$\frac{d}{dZ}\left[(V+1)B_N^2 XG_b(1+\lambda_1^2)^2\right] = \frac{M_{HT}}{(1+Z/\pi_3)^2}, \tag{3.13}$$

which depend on the parameters π_2 and π_3 (recall $M_{HT} = 1/(4\pi\alpha^2\pi_3\pi_2^3)$). From these equations it becomes clear what each parameter represents. The governing parameter for (3.12), the conservation of fluid buoyancy, is π_2. Thus, when bubble expansion is negligible, (3.13) is zero and π_3 is no longer a relevant parameter. When bubble expansion is important, both π_2 and π_3 govern the system of equations. For making correlations we suggest using π_2 and π_3 separately (i.e. we omit the combined parameter M_{HT}), but we neglect π_3 in this paper since we are not concerned with bubble expansion.

From both (3.2) and (3.12) π_2 is the parameter that incorporates the effect of the dispersed phase on the plume dynamics. Hence, we will investigate its ability to predict plume attributes, and because it is a non-dimensional slip velocity, we will rename it as $U_N \equiv \pi_2$.

3.4 Methods

Laboratory experiments were conducted in a stagnant, stratified tank 1.2 m square by 2.4 m tall. The tank was stratified with salt (NaCl) using the two-tank method (Asaeda &

Imberger 1993). Density profiles were recorded using a Head micro-scale conductivity and temperature (CT) probe or an Ocean Sensors OS300 CT probe. Rhodamine 6G fluorescent dye tracer (excitation and emission frequencies 480 nm and 560 nm, respectively) was injected at the base of the plume using a collar diffuser at a rate of 0.1 mg/s. Dye profiles were recorded using a Chelsea Aqua-Tracka *in-situ* field fluorometer connected to an Ocean Sensors OS200 conductivity, temperature and depth (CTD) profiler. LASER induced fluorescence (LIF) images were created using a Coherent 6 W argon-ion LASER (two LASER lines at 494 nm and 515 nm) connected by a fiber optic cable to a cylindrical lens, generating a 1.5 cm-thick light sheet through the centerline of the plume. Shadowgraph images were created using a point light source placed 3 m away from the tank. Images were captured at variable framing rates using a Matrox Pulsar computer framegrabber and a Pulnix TM9701 digital progressive scanning CCD camera. Using a cut-on filter at 530 nm with the LIF method, LASER light scattered by the bubbles could be removed, yielding images of the fluorescing dye only; removing the filter provided images of the bubbles.

Plumes were created from air bubbles ($\rho_b = 0.0014$ g/cm^3), oil droplets (vegetable oil with $\rho_b = 0.930$ g/cm^3 and crude oil from the Gulf of Mexico with $\rho_b = 0.871$ g/cm^3), and glass beads (creating an inverted plume with $\rho_b = 2.50$ g/cm^3). For the air experiments two diffusers were used, a Coral Life limewood saltwater aquarium airstone and a standard composite aquarium airstone. The limewood diffuser created very fine bubbles that were measured with a phase Doppler particle analyzer (mean diameter of 550 μm and $u_s = 7.2$ cm/s). The standard aquarium airstone bubbles were larger, and their slip velocity was measured by timing the rise of bubbles behind a rapidly towed source as in Hugi (1993) (mean diameter of 2 mm and $u_s = 23$ cm/s). Both oils were injected through a 0.7 mm diameter spray nozzle. The vegetable oil created larger droplets (because of higher viscosity) and a narrower distribution of sizes (because the crude oil was a mixture of many compounds). Slip velocities were measured by timing the rise of individual droplets ($u_s = 10$ cm/s for the vegetable oil and u_s ranged from $\mathcal{O}(1)$ mm/s to 10 cm/s with the bulk of the oil rising at 8 cm/s for the crude oil). To provide greater control over the dispersed phase characteristics, Ballotini glass impact beads from Potters Industries, Inc. were used. Slip velocities for three size classes were measured in settling column tests and agreed well with fall velocity data

from Dietrich (1982) for spheres (Class D: diameter of 260 μm and $u_s = 3.2$ cm/s; Class B: diameter of 560 μm and $u_s = 7.1$ cm/s; and, Class A: diameter of 770 μm and $u_s = 11$ cm/s).

Air flow was measured by ColeParmer electronic air mass flow meters (two meters with ranges 0.0–1.0 Std L/min and 1.0–10 Std L/min) and controlled by a pressure regulator. Oil was injected using a calibrated Cole Parmer MasterFlex pump. The beads were released from a hopper through an inverted funnel. The buoyancy flux throughout the experiments for each of the dispersed phases remained constant to within a tolerance of $\pm 3.5\%$.

Plume structure, including the trap height, peel height, and bubble spreading ratio (defined as the ratio of the width of the bubble column to the width of dye tracer marking the edge of the plume), was taken from the LIF images. Trap height and peel height were also measured by interrogation of the pre- and post-experiment salinity profiles and the dye concentration profiles. The integrated dye profile provided a measure of the fraction of passive tracer that peels with the peeling fluid, f^*.

Dye concentrations could not be estimated from the LIF images due to variations in the index of refraction caused by the stratification. McDougall (1979) used alcohol solutions to match the refractive index in a linearly stratified ambient; however, this technique is not practical at this scale. Nash et al. (1995) used *in-situ* measurements of temperature to account for variations in the index of refraction for a two-dimensional flow, but this was not possible due to the internal wave field present during our experiments.

Table 3.1 presents the conditions for these experiments.

3.5 Observations

Our experiments confirmed the observations of previous authors (Asaeda & Imberger 1993, Lemckert & Imberger 1993, McDougall 1978, Baines & Leitch 1992) and identified a new type of behaviour for small, weak bubbles we call Type 1*. In general, multi-phase plume behaviour changes in response to the initial conditions (B), ambient stratification (N), and the characteristics of the dispersed phase (u_s). In the following figures, both B and N are kept constant ($B = 2 \cdot 10^{-5}$ m^4/s^3, $N = 0.3$ s^{-1}), and only u_s changes, having values of 7.2, 11.1, and 23.3 cm/s for the plume Types 1*, 2, and 3, respectively. Thus, as U_N

Exp. ID	ρ_b [g/cm^3]	u_s [cm/s]	B [m^4/s^3 $\cdot$ 10^{-5}]	N [s^{-1}]	Type	h_T [cm]	h_P [cm]	f^*	λ
so50	0.871	8	1.16	0.31	T1*	41	72		
Air1	0.0014	7.2	1.99	0.31	T1*	44	75	0.93	0.81
Air2	0.0014	7.2	1.99	0.31	T1*	44	70	0.90	0.74
Air4	0.0014	7.2	1.99	0.31	T1*	44	75	0.88	0.82
exp1	0.0014	7.2	1.99	0.31	T1*				
L015	0.0014	7.0	19.9	0.31	T1*	70	100		0.82
l250	0.0014	7.2	2.63	0.31	T1*				
lime1	0.0014	7.2	6.63	0.27	T1*				
T033	0.0014	7.2	2.63	0.31	T1*	37	90		
T04	0.0014	7.2	6.63	0.36	T1*	39	78	0.91	
Sed4	2.5	3.2	2.79	0.28	T1*	36	86	0.89	
Sed5	2.5	3.2	2.25	0.30	T1*	48	77	0.92	0.98
g07a	0.0014	23.3	92.9	0.50	T2				
Sed1	2.5	7.1	1.36	0.23	T2	58	110	0.91	0.61
Sed2	2.5	7.1	1.24	0.27	T2	41	71	0.83	
Sed6	2.5	11.1	1.84	0.32	T2	46	83	0.86	0.70
shad1	0.0014	23.3	66.3	0.25	T2				
Air3	0.0014	23.3	1.99	0.31	T3	34	48	0.58	0.61
Air5	0.0014	23.3	13.3	0.31	T3	74	120	0.81	0.59
g50a	0.0014	23.3	6.63	0.25	T3	38	57		0.51
s25o	0.930	10	0.34	0.25	T3				
T013	0.0014	23.3	5.23	0.31	T3				

TABLE 3.1: Experimental conditions for stratified experiments.

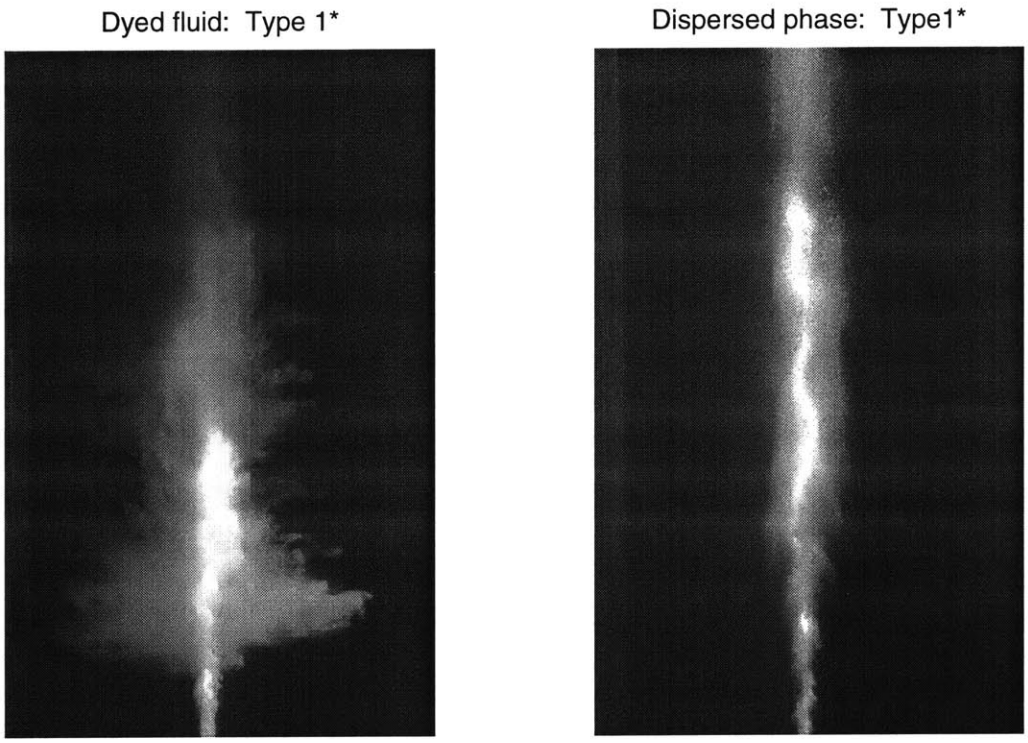

FIGURE 3-3: LIF images of a Type 1* plume. The dyed-fluid image has the filter on, the dispersed phase image has the filter off.

increases, a progression of plume types is observed. Each of the following figures also shows two views of each plume, one showing the dyed fluid only (using the cut-on filter) and the other showing the dispersed phase and some residual dye (with the cut-on filter removed).

3.5.1 Type 1* plumes

Figure 3-3 shows a Type 1* plume. For these plumes, the slip velocity is low compared to the velocity of the entrained fluid (small U_N) and the bubble motion is weak relative to the motion of the plume fluid. As expected for the first peel and intrusion, a distinct detrainment zone and intrusion layer with Type 2 characteristics is observed. However, because the bubble motion is weak compared to the detraining eddy motion, this first peel disperses the bubble core horizontally, with some of the smaller bubbles leaving the inner core and intruding partially with the detraining water. As the detrained fluid decelerates, the slip velocity begins to dominate and the bubbles rise out of the intruding flow to join the subsequent plume above the detrainment zone, taking some ambient fluid upward into

the secondary plume.

The secondary plume that forms above the first peel has a much more diffuse inner bubble core and is surrounded by fine bubbles that were carried down in the previous downdraught plume. As a result, the second downdraught plume contains bubbles that peeled from the second detrainment zone and bubbles that are intercepted as they rise out of the first intrusion. Over the next one or two peels, the detrainment zones become less distinct, and the plume peel behaviour exhibits Type 3 characteristics (continuous and overlapping peels).

Because the inertia of the bubble core is weak compared to the plume fluid velocity, the diffuse bubble column in the subsequent peels swings back and forth as eddies detrain from side to side. Thus, the fountain-like nature of the peeling events gives a sinuous trajectory to the bubble column.

As indicated by the dye in the figure, Type 1* plumes transport some entrained fluid through the first peel, but most of the dye injected at the source is trapped in the first intrusion layer.

3.5.2 Type 2 plumes

Images of a Type 2 plume are shown in Figure 3-4. For Type 2 plumes, the upper-level intrusions do not overlap the downdraught plumes and the main body of each intrusion remains distinct. The plume shown in the figure is near the boundary between Type 2 and Type 3 behaviour; thus, some of the detraining water intrudes in several smaller intrusions along the downdraught plume, but two dominant intrusions are identifiable.

Type 2 plumes have distinct non-overlapping intrusions because of their high peeling efficiency and because the bubbles rise fast enough (larger U_N) that the inner bubble core is not dispersed by the peeling fluid. The efficiency of the detraining zone is evident in the shadowgraph images (not shown) where a distinct edge is observed to the upward rising core fluid and the detrainment zone, and very little entrained water is seen to continue upward with the bubbles into the secondary plume. The peeling efficiency is also evident in the dye distribution as most of the dye ends up in the initial intrusion; however, the faster-rising bubbles strip more fluid from the peeling zone than in the Type 1* case so that more dye

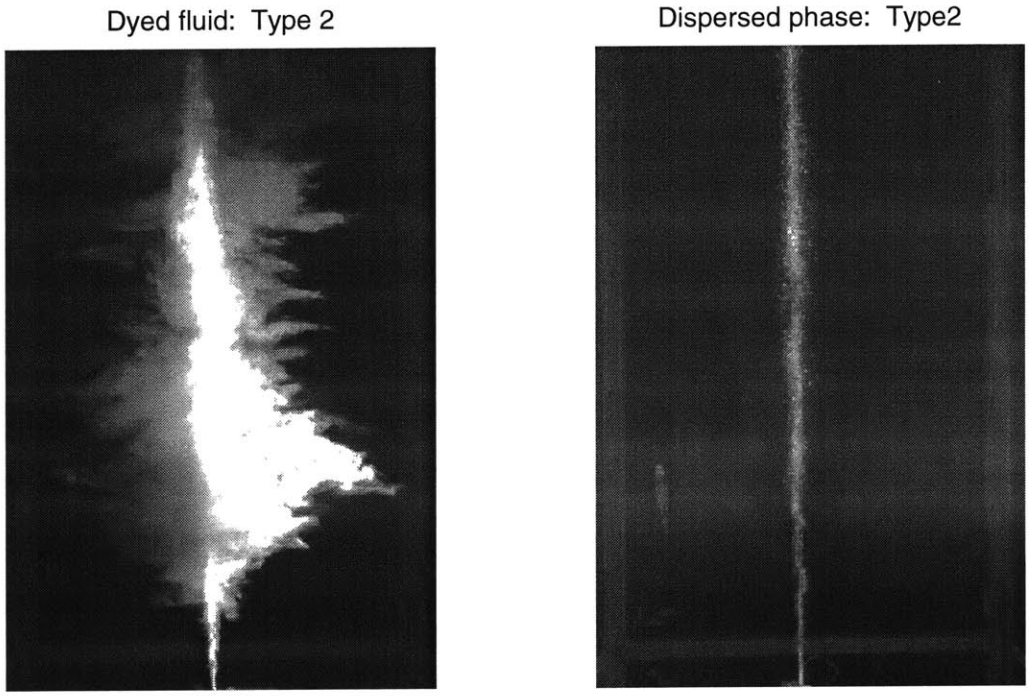

FIGURE 3-4: LIF images of a Type 2 plume. The dyed-fluid image has the filter on, the dispersed phase image has the filter off.

reaches the upper intrusions. Although it could not be observed directly in our limited-depth tank, because each peel is not 100% efficient, it is possible for some negatively buoyant water to be carried a great distance before peeling. Thus, plume peels may begin to overlap in the upper regions, causing deep-water plumes to transition to Type 3-like behaviour with height.

Although the bubbles do not disperse horizontally at the detrainment zone, because the plume fluid stops rising, the bubbles are observed to become congested as they loose the excess velocity of the plume fluid at the terminal level. The small amount of fluid transported through the detrainment zone appears to be directly connected with the bubble wakes, which was also observed by Leitch & Baines (1989).

3.5.3 Type 3 plumes

Figure 3-5 shows images of a Type 3 plume. Comparing this plume to that in Figure 3-4, the intrusions overlap the downdraught plumes in the Type 3 case and appear to have more

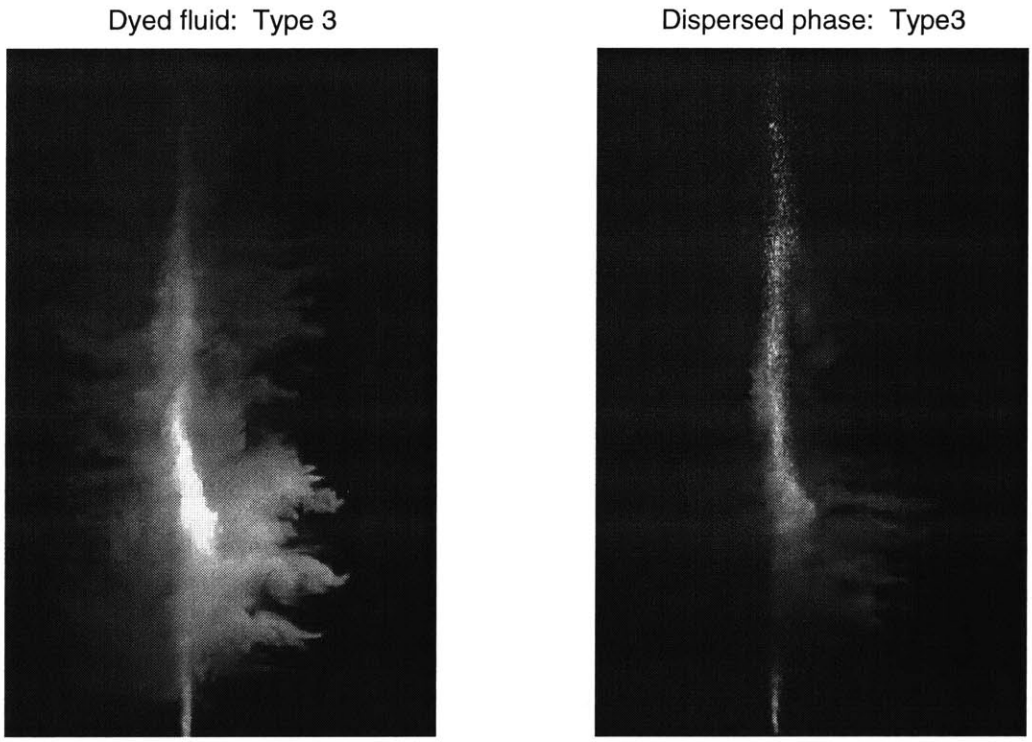

FIGURE 3-5: LIF images of a Type 3 plume. The dyed-fluid image has the filter on, the dispersed phase image has the filter off.

uniform volume flux over the height of the plume.

The uniform plume width with height seen in the figure is evidence that the upward plume volume flux and, therefore, upward velocity and detrainment flux, are nearly constant. This type of intrusion structure is indicative of uniform mixing at a boundary. The bubbles create mixing by lifting packets of fluid short distances along the inner plume core. Eddies soon detrain and form the finger-like intrusions depicted in the figures.

The overlapping nature of the Type 3 plume is due to the fast rising bubbles that strip fluid from the detraining eddies. Type 3 plumes do not exhibit a distinct detrainment zone, and downward flowing fluid appears to originate continuously along the upward rising core as eddies are randomly ejected and loose the buoyant lift of the narrow bubble column. The bubbles remain in a tight core, unaffected by the detrainment events, and because the rising fluid maintains a nearly constant velocity, no bubble congestion zones are observed.

As indicated by the dye, the detrained fluid completely shrouds the upward rising plume core. Dye is transported well above the injection point and above the initiation of de-

trainment. As recorded in the dye profiles, the dye concentration drops off logarithmically, indicating a fairly constant detrainment flux.

3.6 Results

This section presents correlations of plumes properties with the new governing parameter, U_N. Physical insight into the dynamics of plumes can be drawn from these correlations because of the definition of U_N itself as the ratio of two velocity scales, u_s/u_C. When u_s is small compared to u_C, the bubbles and packets of rising fluid interact over longer time scales and follow similar trajectories—in the limit of a single-phase plume, the buoyancy and the fluid are indistinguishable. As u_s increases relative to u_C, individual bubbles interact with entrained fluid packets over shorter time periods and become more independent of the entrained fluid. The relative independence of the bubbles from the entrained fluid is what accounts for the variation of plume properties with U_N.

3.6.1 Plume type

In Figure 3-6 we plot plume type in the M_H-P_N plane (as was done by Asaeda & Imberger (1993) for plume Types 1, 2, and 3) and in the single-parameter U_N-space. The data plotted in the figure include field and laboratory data from Asaeda & Imberger (1993) together with data from our own experiments (refer to Table 3.1).

The plume type boundaries plotted in Figure 3-6 support the dimensional analysis presented above. First, the vertical line in the M_H-P_N plane has not changed from Asaeda & Imberger (1993) and plots the constant value $P_N = 500$, which separates Type 1 plumes from the other types. Since U_N does not include the depth, it cannot be used to predict the occurrence of Type 1 plumes. This is acceptable for a deep-ocean correlation parameter since Type 1 plumes are not likely to occur. Second, in the U_N-space, the vertical lines indicate the constant values of 1.5 and 2.4 as the transitions between Types 1* and 2 and Types 2 and 3, respectively, based on correlation with the available data. Rewriting $M_H = f(U_N, P_N)$ and substituting the transion values of 1.5 and 2.4 for U_N gives the downward sloping tran-

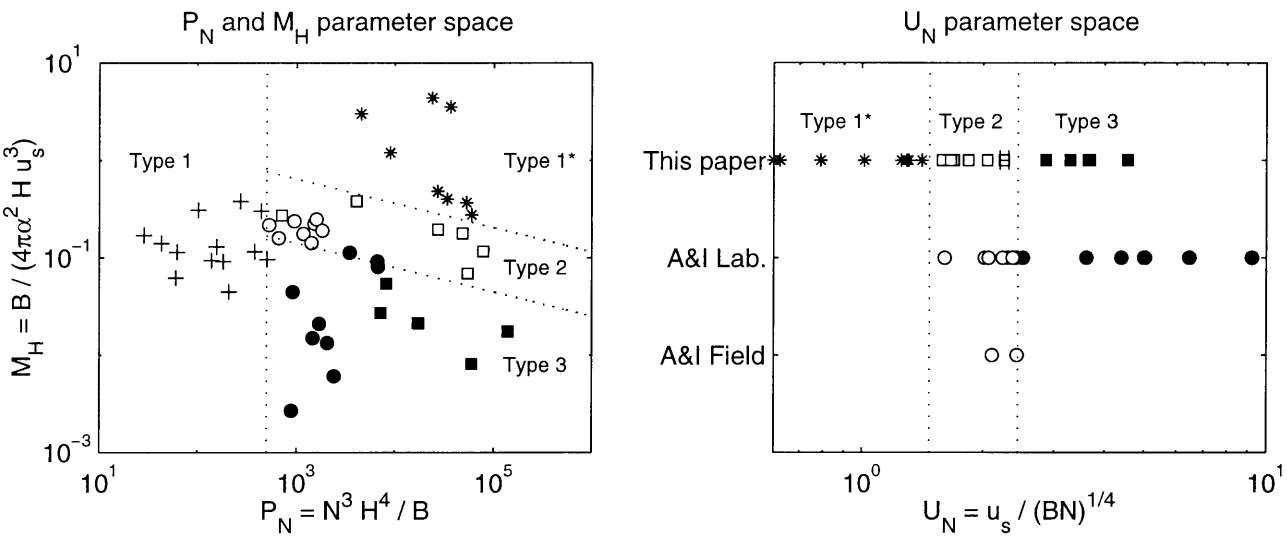

FIGURE 3-6: Correlation of plume type with the governing non-dimensional parameters. Circles and pluses are from Asaeda & Imberger (1993); squares and stars are the current authors. Pluses are Type 1 plumes, stars are Type 1* plumes, open symbols are Type 2 plumes and filled symbols are Type 3 plumes. The Asaeda & Imberger (1993) data include field and laboratory experiments. Typical error bars are shown for one data point.

sition lines plotted in the M_H-P_N plane. Because the transitions have a slope of $-\frac{1}{4}$, the H-dependence of the Type-transitions is removed from the M_H-P_N plane. The fact that all of the data are well-predicted by these new transition lines confirms our assertion that the existing data do not have significant bubble expansion over the natural length scale l_C and demonstrates that plume type is not strongly dependent on depth. Hence, plume type (excluding Type 1) can be predicted using U_N alone.

3.6.2 Intrusion trap and peel heights

Figure 3-7 compares the two dominant plume length scales, h_T and h_P, to U_N. In the remaining figures, the vertical dotted lines plot the plume Type transitions, and the data points in the figures are for the first peel only. For a single-phase plume, u_s is effectively zero, the non-dimensional trap height (h_T/l_C) is equal to 2.8 and the non-dimensional peel height (h_P/l_C) is equal to 3.8 (Crawford & Leonard 1962, Morton et al. 1956, Turner 1986). Multi-phase plumes are expected to approach single-phase behaviour as the slip velocity approaches zero since separation among the phases would no longer occur, and, therefore, the buoyancy

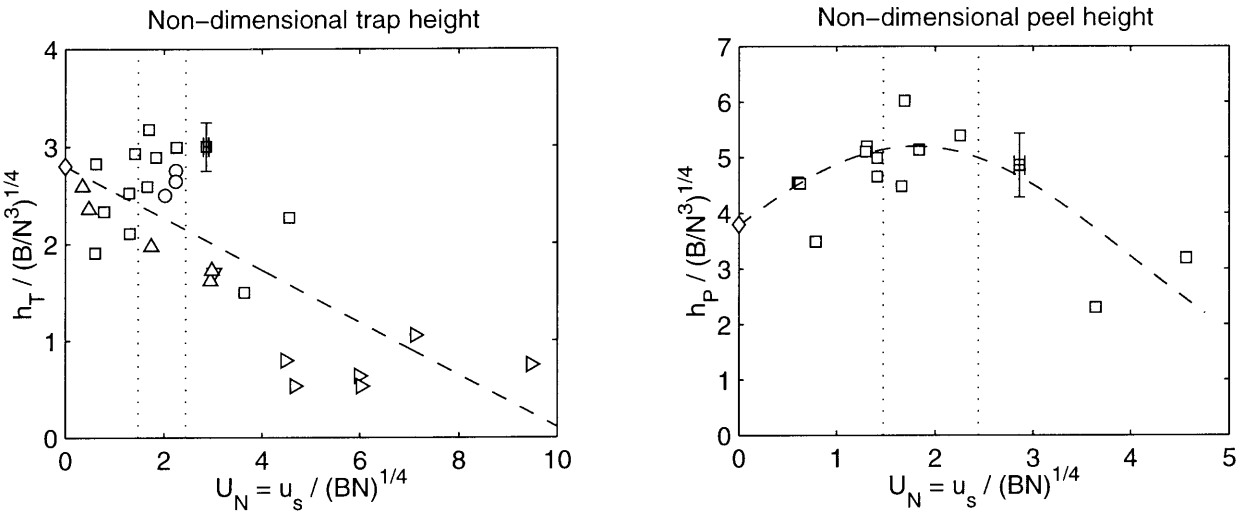

FIGURE 3-7: Correlation of plume trap and peel heights to U_N. Right-pointing triangles are data from Lemckert & Imberger (1993); up- and down-pointing triangles are data from Reingold (1994). As in Figure 3-6, circles are from Asaeda & Imberger (1993) and squares are the current authors. Typical error bars are shown for one data point.

of the dispersed phase would never leave the plume. From the figure, we see that trap height decreases from this single-phase value as U_N increases. The peel height, h_P seems to increase with increasing U_N until reaching a maximum value at about U_N=1.8 and thereafter decreases monotonically with increasing U_N. The curves plotted are $h_T/l_C = 2.8 - 0.27U_N$ and $h_P/l_C = 5.2\exp(-(U_N - 1.8)^2/10.1)$.

Considering h_T first, the trend for multi-phase intrusions to lie below the single-phase trap height is due to the separation of the negatively buoyant fluid from the positively buoyant dispersed phase. For low U_N the bubbles stay with the intruding fluid longer, increasing h_P and allowing more mixing to occur in the upper levels of the stratification, resulting in a higher h_T. As U_N increases, the bubbles leave the detraining fluid without being affected by the peel (as in Types 2 and 3) and the intrusions must descend farther before reaching a level of neutral buoyancy.

The trend in h_P with increasing U_N demonstrates the effect of the downdraught plume. For low U_N the plumes approach single-phase values of h_P as expected. As U_N increases, the bubbles become less affected by the dispersing motion in the peeling region and the detrained fluid loses its buoyancy earlier. This loss of buoyancy forces the detraining fluid to

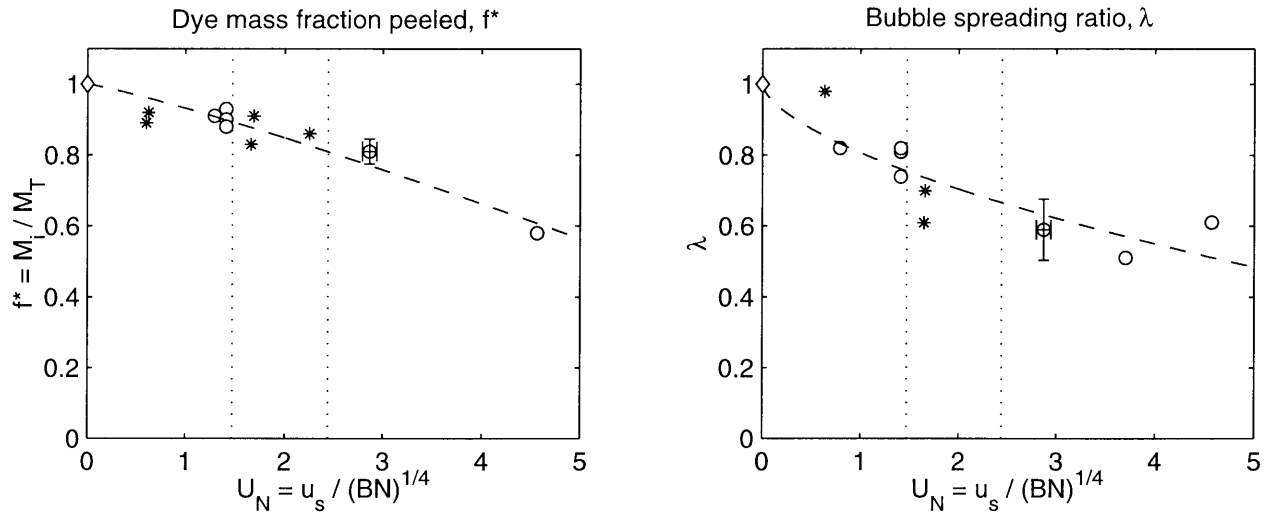

FIGURE 3-8: Correlation plots for dye mass fraction peeled and for the bubble spreading ratio. Circles represent air-bubble experiments, and stars represent glass-bead experiments with typical error bars shown for one data point.

descend farther before reaching a level of neutral buoyancy, thus increasing the length of the downdraught plume. The downdraught plume then shrouds the inner plume from entraining denser ambient fluid, which allows the plume to rise higher before peeling. This effect of the downdraught plume appears to be maximized in the middle of the region defining Type 2 plumes. As U_N increases further, the bubble column narrows (refer to Figure 3-8) so that it no longer supports the rising plume as effectively; therefore, h_P decreases monotonically in the Type 3 region.

3.6.3 Detrainment zone properties

Figure 3-8 presents data for f^* and λ for our experiments involving air and sediment plumes—no literature data were available for comparison. The single-phase limit for f^* is zero since all the fluid and buoyancy would trap at the terminal level; the single-phase limit for λ is 1.0 since the buoyancy would be spread out to the edge of the plume. Again, there is a trend of decreasing values with increasing U_N. The mass of tracer peeled, f^*, ranges from 0.58 to 0.93, with plume type transition values of about 0.89 and 0.81 for Types 1* to 2 and Types 2 to 3, respectively. Values for the bubble spreading ratio, λ, lie within the range reported for unstratified two-phase plumes of 0.3 to 0.8 (Milgram 1983). Bubble-

column wandering has been cited previously to explain the wide range of reported values. The strong stratification in our tank, however, severely damped basin-scale circulation such that bubble column wandering was negligible, evident only in the upper regions of Type 1* plumes when the bubble column would collide with a detraining eddy. The least-squares correlation regressions plotted are $f^* = 1.0 - 0.07U_N^{1.2}$ and $\lambda = 1.0 - 0.19U_N^{0.61}$.

The two parameters presented in the figure work together in affecting the plumes dynamics. The simplest of these parameters to understand is λ: as the slip velocity increases, the bubble column is less affected by turbulent eddies within the plume, allowing the bubbles to maintain a tighter core. Because a tight bubble core is less efficient at pumping the entrained fluid than a dispersed bubble core, the variation of λ is reflected in f^*. For small U_N the bubbles are well dispersed and entrained fluid eddies are lifted together with the bubbles until the stratification causes detrainment. The bubbles and fluid then detrain together and the plume must start over after the bubbles regroup. For high U_N the entrained eddies interact with the narrow bubble column for a short time and are less evenly suppored. It is, therefore, easier for eddies to spin off to the side of the plume where they either intrude or get entrained back into the rising bubble column. Peeling occurs in this case more frequently and less efficiently, yielding a reduced f^*. Hence, variations in λ and f^* reflect the level of independence between the entrained fluid and the rising bubbles.

The decreasing trend in f^* with increasing U_N also explains the different appearance of the plume types. As f^* decreases, the negative buoyancy flux of entrained fluid moving upward through a detrainment zone increases. Subsequent plume peels, then, contain greater negative buoyancy, and eventually the detraining fluid falls below the previous detrainment point, and the intrusions begin to overlap. In the limit of the Type 3 plume, the entire plume structure is shrouded by the overlapping downdraught plumes. Thus, plume type derives from the peeling efficiency which is controlled by the bubble column structure.

3.7 Implications for field-scale plumes

The correlations presented in the previous section can be applied directly when the idealized laboratory conditions are met in the field. Requirements for the ambient environment

are the assumptions of a linear density profile and stagnant conditions. Non-linear density profiles will affect the intrusion formation; the horizontal motion of flowing ambients provide a second means of separating the entrained fluid from the rising dispersed phase (Hugi 1993, Socolofsky & Adams 2000*c*). Requirements for the dispersed phase are that a unique slip velocity can be defined (i.e. a narrow distribution of bubble sizes) and that chemistry and expansion effects do not alter the bubble characteristics significantly over the characteristic scale l_C. As shown in Figures 3-6 and 3-7, these conditions are commonly met in reservoir destratification applications.

Deep ocean plumes, particularly oil spill and CO_2 sequestration plumes, often do not meet all the requirements outlined in the previous paragraph. Numerical models are one means of including the field-scale complications. The new data and correlations for h_T, h_P, f^*, and λ given above should aid model calibration so that they can be applied with more confidence in the deep ocean (e.g. Crounse 2000, Alendal & Drange 2000, Chen et al. 2000, Sato & Hama 2000). However, the ambient conditions, particularly during slack tide, often do mimic the laboratory conditions, and the insight gained from the correlations presented in the previous section can be used to predict the effects of various dispersed-phase complications at the field scale.

A typical complication is the presence of multiple dispered phases. These arise, for example, in oil-well blowout plumes when a significant portion of natural gas is released with the oil (*in situ* gas/oil ratios range from 1 to 100). The primary interest, then, is the fate of the oil relative to the natural gas. Typically, modellers have assumed that the oil would follow the entrained fluid and be trapped in the initial intrusion layer (McDougall 1978, Yappa & Zheng 1997*a*, 1997*b*). The experiments described above indicate that the oil follows the fluid only for Type 1* plumes where $U_N \leq 1.5$. The bubbles peel in the Type 1* plume because they are weak compared to the plume eddy velocities, which scale with the total buoyancy flux of the plume. This suggests that U_N should be calculated using the slip velocity of the phase that may peel, comparing it to the plume fluid rise velocity defined by the buoyancy flux of all the dispersed phases. This notion was confirmed for a laboratory crude oil plume where large oil droplets remained in the the plume core and fine oil droplets peeled into the intrusion layer.

Chemistry effects that alter the bubble characteristics are also common in field-scale plumes. These include bubble dissolution, which alters the bubble size, and other chemical reactions, such as hydrate formation, that alter the dispersed phase composition and may affect the droplet buoyancy. These effects impact the correlations in two ways. First, the slip velocity will change in response to the bubble size and buoyancy. Second, changes in droplet buoyancy will further affect the plume driving force and, therefore, alter the characteristic plume fluid rise velocity, u_C. As long as these changes are small over the length scale l_C, a mean slip velocity and buoyancy flux can be assumed.

Finally, the unique chemistry of a CO_2 sequestration plume provides a complication where the dissolving droplets enrich the seawater with CO_2 which, in turn, raises the entrained fluid density (Ohsumi et al. 1992). This effect is qualitatively similar to the negative buoyancy flux through a peeling zone associated with having a low f^*. Low f^* corresponds to a higher U_N and Type 3 behaviour. Consequently, we would expect that the effect of CO_2 enrichment would be to increase the frequency of peeling events and to cause detraining fluid to overlap intrusions lower in the water column. This type of continuous peeling would distribute the dissolved CO_2 more evenly in the water column than would discrete Type 2-like intrusions; thus, the density feedback likely enhances dilution which, in turn, would reduce environmental impacts.

3.8 Summary

This paper introduces U_N as a new governing parameter for correlating multi-phase plume properties. We apply U_N to predict plume type and show that several processes, also correlated with U_N, combine to create the resulting plume type. Through laboratory experiments, we also introduce a new plume behaviour called Type 1* in which the dispersed phase is deflected horizontally at the initial peel and follows the detraining fluid down toward the intrusion layer.

From the dimensional analysis, a physical interpretation of U_N was possible, and the governing length, velocity, and volume flux scales were defined. These scales aid in determining the significance of different processes, such as bubble expansion, in affecting the plume dy-

namics or structure. The advantanges of U_N over previous correlations are that it neglects the reservoir depth (thus, it may be applied in the deep ocean) and that it has a physical interpretation as the ratio of the slip velocity to the characteristic velocity of the entrained fluid.

As an aid to numerical models, measurements of plume type and trap height were added to those in the literature, and new measurements of peel height, fraction of tracer peeled, and bubble spreading ratio were made. Combining these calibration data with the physical insight gained from U_N will help to predict the structure of CO_2 and oil-spill plumes in the deep ocean.

Chapter 4

Liquid volume fluxes of two-phase plumes in stagnant stratification[1]

Abstract: This paper presents laboratory measurements of the dominant liquid volume fluxes in two-phase plumes in linear stratification. Experiments were conducted using air bubbles and glass beads (creating an inverted plume). Plume flow measurements were made by comparing pre- and post-experiment salinity and dye tracer profiles. To distinguish between the overlapping upward and downward flows a constrained Bayesian estimation technique was applied to a conceptual model of the plume peeling region. The intrusion layer flux, the ambient and counterflowing entrainment fluxes, the peeling efficiency, and the buoyancy flux escaping the first peel are correlated with the non-dimensional slip velocity, U_N, the ratio of the dispersed phase slip velocity, u_s, to a characteristic plume fluid rise velocity, $(BN)^{1/4}$, where B is the total kinematic buoyancy flux and N is the Brunt-Vaisälä buoyancy frequency. The correlations show that the peeling efficiency is the dominant process controlling the plume structure.

4.1 Introduction

Multi-phase plumes occur in a wide range of natural and engineered systems, including air-bubble plumes for reservoir destratification (Schladow 1993, Lemckert & Imberger 1993, Asaeda & Imberger 1993, Hugi 1993), aeration (Wüest et al. 1992, Hugi 1993), ice pre-

[1]This chapter submitted to the *Journal of Fluid Mechanics* as Socolofsky & Adams (2000), "Multi-phase plumes in stratification: Liquid volume fluxes."

vention (Baddour 1994, McDougall 1978), and contaminant containment (Milgram 1983); continuous sediment plumes resulting from the release of dredged sediments (Koh & Chang 1973); liquid CO_2 plumes for deep-ocean carbon sequestration (Caulfield et al. 1997, Adams et al. 1997, Alendal et al. 1998, Socolofsky & Adams 2000*a*); deep-sea blowouts of oil and gas (Yapa & Zheng 1997*a*, 1997*b*, 1999, Johansen 1999, Socolofsky 2000); and a host of mixing applications in manufacturing (Park & Yang 1997, Johnson & White 1993, Taitel et al. 1995). Because multi-phase plumes transport entrained fluid across density gradients, creating mixing, analysis of multi-phase plumes requires understanding of the entrained fluid fluxes. For instance, reservoir mixing plumes should be designed for maximum efficiency in eroding the stratification (Asaeda & Imberger 1993, Schladow 1993); whereas, reservoir aeration plumes should provide a uniform supply of oxygen to bottom waters without disturbing the stratification (Wüest et al. 1992). Although experiments have been conducted in the field and laboratory for stratified and unstratified two-phase plumes (Leitch & Baines 1989, Baines & Leitch 1992, Lemckert & Imberger 1993, Asaeda & Imberger 1993, Hugi 1993, McDougall 1978, Milgram 1983, Kobus 1968), detailed measurements of the internal flows for a stratified two phase plume have not been made and are needed to calibrate numerical models (e.g. Alendal et al. 1998, Crounse 2000, Asaeda & Imberger 1993, McDougall 1978, Yapa & Zheng 1997*a*, Wüest et al. 1992, Johansen 1999). This paper presents a technique for measuring the internal flows of a two-phase plume in linear stratification and applies the technique to the first peel for such a plume.

A distinguishing feature of multi-phase plumes, as compared to single-phase plumes, is the opportunity for separation between the dispersed phases and the entrained ambient fluid as shown in Figure 4-1. Separation occurs in stratification when the dense entrained fluid can no longer be supported by the dispersed phase and is lost horizontally through a detrainment zone. For clarity in the rest of this paper we will use bubbles to refer to a generic dispersed phase and will use bubbles, droplets or particles, as appropriate, when discussing specific plumes; the term liquid flux will refer to the entrained ambient fluid. Because the bubbles maintain their buoyancy throughout the plume, they continue to rise above the detrainment zone, forming a series of secondary plumes. The detrained fluid, now much denser than the ambient, descends in an outer annular plume, or downdraught plume, eventually intruding

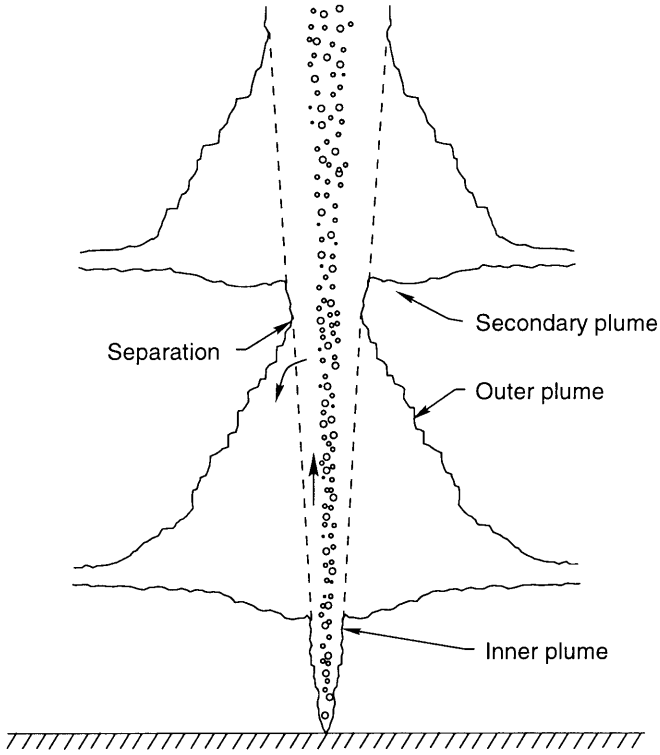

FIGURE 4-1: Schematic of separation for a multi-phase plume in linear stratification.

at a level of neutral buoyancy. Because the detraining fluid looses the buoyancy of the bubbles, the downdraught plume can shroud a significant portion of the upward-rising inner core plume (Crounse 2000, Socolofsky & Adams 2000*a*).

Leitch & Baines (1989) took advantage of the downdraught plume to make volume flux measurements for an air-bubble plume in a step-stratified closed container. When the bubble plume impinged on the steep density interface, the entrained fluid was immediately ejected. As the fluid detrained, it mixed slightly with the lighter, upper-layer fluid, but remained dense enough to intrude into the lower layer. The slight mixing, however, formed a weak density interface between the bottom of the downdraught plume, which occupied the full tank cross-section, and the undisturbed fluid of the lower layer. By tracking the descent velocity of the weak interface, Leitch & Baines (1989) were able to calculate the balancing volume flux of the inner plume at the weak density interface, yielding properties for the plume in a homogeneous ambient. Unlike for a single-phase plume, they found that the entrained liquid flux scaled with the square-root of bubble flow rate and linearly with height, and

that the maximum liquid velocity in the plume was constant with height. Baines & Leitch (1992) extended the technique to a linearly stratified environment using the salt conservation equation to calculate buoyancy fluxes. In this paper, we make use of the latter technique to make net volume flux measurements in a linearly-stratified two-phase plume, and we extend the technique through a simple conceptual model combined with dye tracer profiles to distinguish upward- and downward-flowing components of the measured net plume flux.

The initiation of a downdraught plume in a numerical integral model requires a prediction for the fraction of inner-core fluid that peels in the detrainment zone (Crounse 2000, Asaeda & Imberger 1993, McDougall 1978). Based on laboratory experiments, McDougall (1978) and Asaeda & Imberger (1993) assumed for modelling purposes that all of the entrained fluid peeled at each detrainment. This is despite the fact that McDougall (1978) reported, by watching the motion of neutrally buoyant particles, that the upward and downward volume fluxes actually balanced at a point below the detrainment zone. Leitch & Baines (1989) also observed for step stratification that the peeling efficiency was less than 100% and suggested that the volume flux fraction continuing through the detrainment zone is primarily associated with the bubble wakes and was in the range of 0.2 for their experiments. Thorkildsen et al. (1994) and Caulfield (1996) assumed that a fixed fraction (less than 1.0) of fluid peels at each detrainment, but had no data available on which to base their value. Crounse (2000) developed a variable detrainment algorithm based on a balance between the bubble lifting capacity and the negative buoyancy of the entrained water, and he calibrated the algorithm to data for plume intrusion layer trap height. He observed that the model behaviour was very sensitive to the assumed peeling efficiency. Despite the dependence of models on the peeling fraction, no experimental measurements of this physical quantity have been made.

Models also lack verification data on which to choose an appropriate entrainment model for the counterflowing downdraught and inner core plumes (McDougall 1978, Asaeda & Imberger 1993, Crounse 2000). Because the boundary between the two plumes is a turbulent shear layer, the entrainment assumption should apply, which states that entrainment across a turbulent shear interface is proportional to a characteristic velocity of the turbulent flow (Turner 1986). The difficulty with counterflowing plumes is in determining the direction of the entrainment flux and in defining the appropriate characteristic velocity. McDougall

(1978), who modeled only coflowing inner and outer plumes, assumed that entrainment from the inner to the outer plume was proportional to the outer plume velocity and that entrainment from the outer to the inner plume was proportional to the vector difference in velocity between the inner and outer plumes. This was based in part on Morton (1962) who studied coflowing single-phase jets. Asaeda & Imberger (1993), whose inner and outer plumes were counterflowing, used the same entrainment assumption as McDougall (1978). Crounse (2000) suggested an alternate formulation where the entrainment into the inner plume is proportional to the velocity of the inner plume and not a velocity difference between the counterflowing plumes. Without volume flux data, these entrainment algorithms can only be compared to measured intrusion layer trap heights and model stability considerations (Crounse 2000).

This paper presents laboratory experiments and an estimation technique to quantify the dominant volume fluxes for two-phase plumes in linear stratification. Experiments were conducted using air bubbles and glass beads (creating an inverted plume) to span a range of dispersed phase slip velocities. Section 4.2 describes the laboratory methods and introduces the net volume flux measurement technique described by Baines & Leitch (1992). A conceptual model is introduced in Section 4.3 and combined with dye tracer profiles to dissect the net volume flux into upward and downward flows. A Bayesian parameter estimation technique is developed in Section 4.4 to take advantage of all the experimental measurements and to apply the constraints of the conceptual model. Section 4.5 presents the results of the flux measurements and discusses their implications for modelling and the insight into the behaviour of multi-phase plumes that can be gained from the measurements. The major conclusions are presented in Section 4.6.

4.2 Methods

4.2.1 Facilities and apparatus

Described in added detail by Socolofsky & Adams (2000*a*), laboratory experiments were conducted in a stagnant, stratified tank 1.2 m square by 2.4 m tall. The tank was stratified

with salt (NaCl) using the two-tank method (Asaeda & Imberger 1993). Salinity profiles were recorded using an Ocean Sensors OS300 CT probe mounted on a Parker linear actuator with 2.8 m of travel allowing a vertical resolution of less than 1 cm. Initial profiles were taken a few minutes before each experiment. Profiles for flow calculations could not be taken during experiments because of internal waves; hence, post-experiment salinity profiles were made one hour after an experiment when the waves had dispersed.

As a passive tracer, Rhodamine 6G fluorescent dye (excitation and emission frequencies 480 nm and 560 nm, respectively) was injected at the base of the plume at a rate of 0.1 mg/s using a collar diffuser. To insure uniform mixing in the horizontal plane dye profiles were recorded six hours after an experiment using a Chelsea Aqua-Tracka *in-situ* field fluorometer connected to an Ocean Sensors OS200 conductivity, temperature and depth (CTD) profiler and having a measurement volume of 1 cm^3. Horizontal uniformity was confirmed for several tank locations for three different experiments. Quantitative LIF was not possible due to variations in the index of refraction caused by the stratification (McDougall 1979, Nash et al. 1995, Socolofsky & Adams 2000*a*).

Plumes were created from air bubbles (dispersed phase density $\rho_b = 0.0014$ g/cm^3) and glass beads (creating an inverted plume with $\rho_b = 2.50$ g/cm^3). For the air experiments two diffusers were used, a Coral Life limewood saltwater aquarium airstone (mean bubble diameter of 550 μm and slip velocity $u_s = 7.2$ cm/s) and a standard composite aquarium airstone (mean bubble diameter of 2 mm and $u_s = 23$ cm/s). To provide greater control over the dispersed phase characteristics, Ballotini glass impact beads from Potters Industries, Inc. were used. Slip velocities for the three size classes used were Class D: diameter of 260 μm and $u_s = 3.2$ cm/s; Class B: diameter of 560 μm and $u_s = 7.1$ cm/s; and, Class A: diameter of 770 μm and $u_s = 11$ cm/s.

Table 4.1 presents the conditions for these experiments, described by the dispersed phase slip velocity, u_s, the total kinematic buoyancy flux, $B = gQ_b(\rho - \rho_b)$ and the Brunt-Vaisälä buoyancy frequency $N = [-(g/\rho)(\partial\rho/\partial z)]^{1/2}$ where Q_b and ρ_b are the volume flow rate and density of the dispersed phase at the release, and ρ is the ambient density. The non-dimensional parameter $U_N = u_s/(BN)^{1/4}$ is the ratio of the slip velocity to a characteristic plume fluid rise velocity. Socolofsky & Adams (2000*a*) show that U_N is the governing pa-

Exp. ID	ρ_b [g/cm^3]	u_s [cm/s]	B [m^4/s$^3 \cdot 10^{-5}$]	N [s^{-1}]	U_N	Type
Air1	0.0014	7.2	1.99	0.31	1.44	T1*
Air2	0.0014	7.2	1.99	0.31	1.44	T1*
Air4	0.0014	7.2	1.99	0.31	1.44	T1*
T04	0.0014	7.2	6.63	0.36	1.03	T1*
Sed4	2.5	3.2	2.79	0.28	0.61	T1*
Sed5	2.5	3.2	2.25	0.30	0.63	T1*
Sed1	2.5	7.1	1.36	0.23	1.69	T2
Sed2	2.5	7.1	1.24	0.27	1.66	T2
Sed6	2.5	11.1	1.84	0.32	2.25	T2
Air3	0.0014	23.3	1.99	0.31	4.68	T3
Air5	0.0014	23.3	13.3	0.31	2.91	T3

TABLE 4.1: Experimental conditions for flow measurement experiments.

rameter describing multi-phase plumes in stratification.

4.2.2 Flow measurement technique

Net plume volume fluxes were measured using the technique of Baines & Leitch (1992). From the transport equation for salt in a closed container, Baines & Leitch (1992) show that the net liquid flux integrated across the plume, Q_{net}, is given by the change in the ambient density profile

$$Q_{net} = A\frac{\partial\rho/\partial t}{\partial\rho/\partial z}, \tag{4.1}$$

where A is the cross-sectional area of the tank, $\rho(z,t)$ is the ambient density profile, t is the time coordinate, and z is the vertical spatial coordinate. Figure 4-2 shows a schematic representation of this technique. The net flux given by (4.1) assumes that the cross-section of the plume is small compared to the tank cross-section and that molecular and turbulent diffusion transport is negligible (Baines & Leitch 1992). For our experiments, the upward- and downward-flowing plume sections never occupied more than 6% of the tank cross-section; intrusion layers, which do not have to obey this constraint, occupied the full tank cross-section near the end of each experiment.

Because (4.1) is solved by finite difference, we have the further constraint that $\Delta\rho/\Delta z$

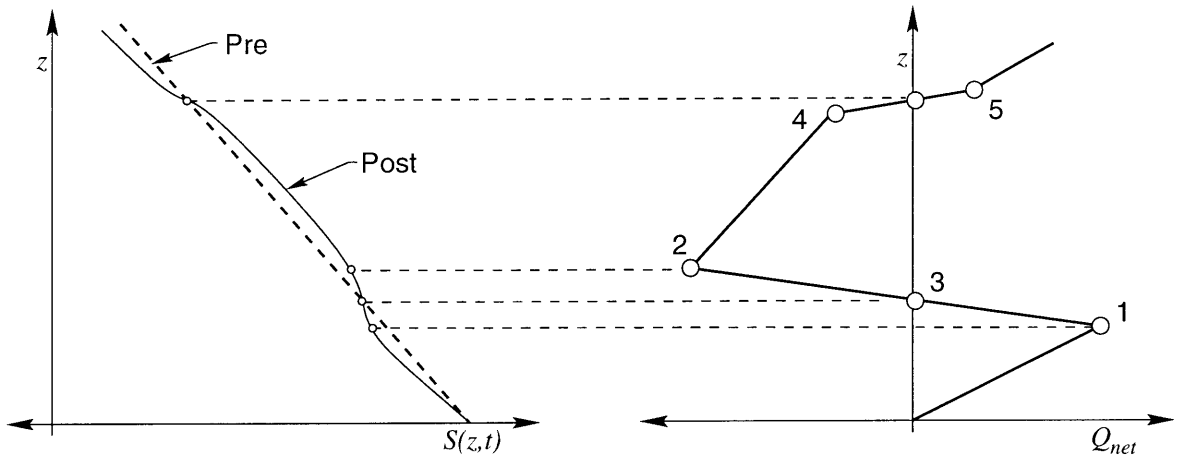

a.) Pre- and post-salinity profiles. b.) Net-flux profile.

FIGURE 4-2: Schematic of plume net volume flux calculation.

be constant over the experiment duration Δt. This is satisfied at the extrema of the net flux profile, labeled as points 1 and 2 in Figure 4-2. Elsewhere, second order terms may become significant; however, this generally occurs as $\Delta\rho/\Delta t$ approaches zero, as at point 3 in Figure 4-2. The model described below relies on measurements from points 1, 2, 4, and 5. Any small errors in points 4 and 5 due to a variable $\Delta\rho/\Delta z$ are compensated for in the optimization by related measurements from the dye and salinity profiles as described in the model that follows.

4.3 Plume flow model

Stratified, multi-phase plumes have both upward flowing water associated with the inner bubble flow and downward-flowing water that descends to form the intrusion layer. Since the plume flux calculated from (4.1) is a net flux, additional methods are needed to distinguish these overlapping flows.

Figure 4-3 shows a schematic of the first peel for a stratified multi-phase plume and introduces an associated simplified flow model (depicted for only half the plume) that identifies seven liquid volume fluxes (Q_1, Q_2, Q_i, Q_{ol}, Q_{oe}, Q_p, and Q_r) and four characteristic heights (h_1, h_i, h_p, and h_2) defined in more detail below. In the model, the complex interaction of

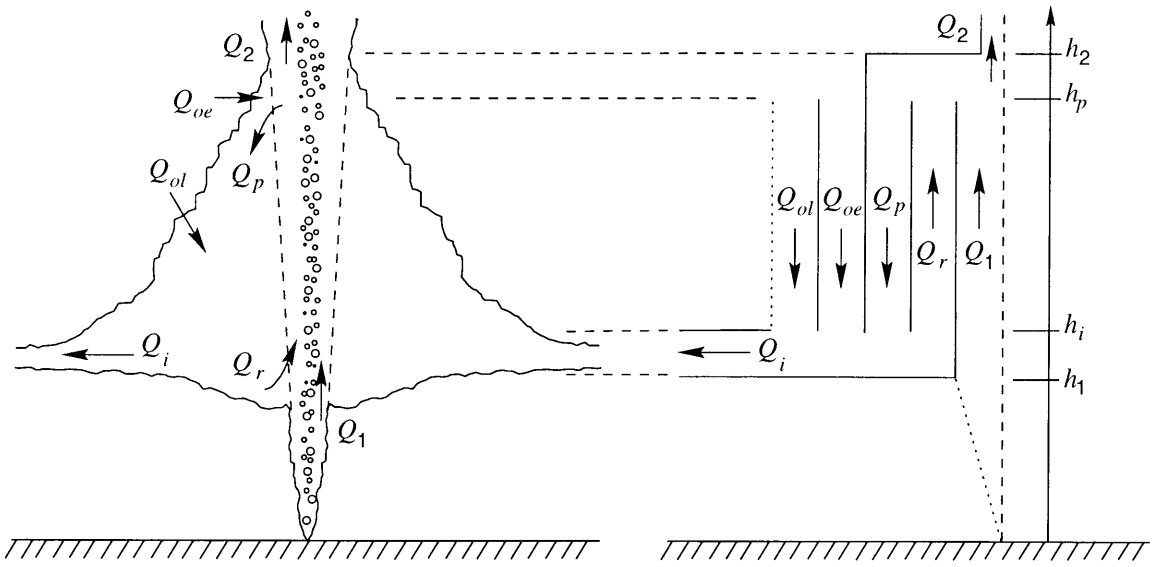

FIGURE 4-3: Schematic of plume flow model showing each of the flow definitions. Each flow also has an associated dye tracer concentration and salinity.

the counterflowing inner and downdraught plumes is simplified into peeling and recirculating flows, Q_p and Q_r. Each of the flows identified in the figure is also associated with a dye tracer concentration (C_1, C_2, C_i, C_{ol}, C_{oe}, C_p, and C_r) and salinity (S_1, S_2, S_i, S_{ol}, S_{oe}, S_p, and S_r). The variables introduced by this model must be estimated from the experimental measurements and constrained to obey the assumptions implied by the conceptual model.

The experimental measurements provide direct and indirect estimates of some of the model parameters. Q_1, the flux at h_1 entering the base of the shrouded region, and Q_2, the flux at h_2 escaping the detrainment zone, can both be measured directly from the net flux profiles since they are not shrouded by the downdraught plume. The two fluxes from the ambient into the downdraught plume, Q_{oe} and Q_{ol}, represent two forms of entrainment: an enhanced entrainment, Q_{oe}, that occurs between h_p and h_2 and a linear entrainment, Q_{ol}, that occurs between h_i and h_p. These two fluxes are treated separately because of a distinct change of slope in the net flux profile at h_p (point 4 in Figure 4-2). The net flux measured just above the intrusion layer at h_i gives the sum $Q_1 + Q_r - Q_p - Q_{oe} - Q_{ol}$. Note that h_i lies above the intrusion layer trap height, h_T. A final flux measured just below the peel zone at h_p gives $Q_1 + Q_{ol} - Q_i$. From the integrated dye profile the total amount of dye injected,

Measurement equations			Constraint equations		
Q_1	=	$Q_{net}(h_1)$	$Q_1 + Q_o - Q_2 - Q_i$	=	0
$Q_1 + Q_r - Q_p - Q_o$	=	$Q_{net}(h_i)$	$Q_p + Q_o - Q_r - Q_i$	=	0
$Q_1 + Q_{ol} - Q_i$	=	$Q_{net}(h_p)$	$C_1Q_1 + C_oQ_o - C_2Q_2 - C_iQ_i$	=	0
Q_2	=	$Q_{net}(h_2)$	$C_pQ_p + C_oQ_o - C_rQ_r - C_iQ_i$	=	0
C_2Q_2	=	$\dot{m}_2$	$C_r - C_i$	=	0
C_iQ_i	=	$\dot{m}_i$	$C_p - C_2$	=	0
S_1	=	$S(\frac{5}{8}h_1)$	C_{ol}	=	0
S_i	=	$S(h_i)$	C_{oe}	=	0
S_{ol}	=	$S(h_i + \frac{3}{8}(h_p - h_i))$	$S_1Q_1 + S_oQ_o - S_2Q_2 - S_iQ_i$	=	0
S_{oe}	=	$S(h_p)$	$S_pQ_p + S_oQ_o - S_rQ_r - S_iQ_i$	=	0
			$S_p - S_2$	=	0
			$S_r - S_i$	=	0

TABLE 4.2: Measurement and constraint equations for Bayesian estimation scheme.

M_T, can be divided into the amount of dye in the intrusion layer, M_i (taken as the mass of dye found below h_2) and the amount of dye escaping the detrainment zone, M_2 (taken as the mass of dye found above h_2). The associated dye mass fluxes give measurements of C_iQ_i and C_2Q_2. Several salinities are measured from the pre-experiment salinity profile: S_i is the salinity at the intrusion depth and S_1 and S_{ol} are taken as the weighted average of the portion of the salinity profile over which those flows entrain water. S_{oe} is the salinity at the peel height, h_p. All of these measurement equations are summarized in the left column of Table 4.2.

The conceptual model implies several relationships among the model variables. A first set of constraints comes from mass conservation. Two independent equations for flow mass conservation are

$$Q_1 + Q_o = Q_2 + Q_i \tag{4.2}$$

$$Q_p + Q_o = Q_r + Q_i. \tag{4.3}$$

(4.2) is derived by considering an outer control volume that completely contains the internal flows Q_p and Q_r. (4.3) is derived by considering an inner control volume for the intrusion layer. Other mass conservation expressions can be written but are linear combinations of

(4.2) and (4.3). Mass conservation equations for dye tracer and salt flux are formed by multiplying each of the flows in (4.2) and (4.3) by their associated concentrations to obtain mass fluxes. Hence, mass conservation provides a total of six constraints.

A second set of constraints comes directly from the definitions implied by the conceptual model. The upper region, where Q_1 and Q_r divide to form Q_p and Q_2, is assumed to be well mixed. This gives $C_p = C_2$ and $S_p = S_2$. Likewise, the intruding region is well-mixed, yielding $C_r = C_i$ and $S_r = S_i$. Finally, the entrained ambient fluid contains no dye: $C_{ol} = 0$ and $C_{oe} = 0$.

The right column of Table 4.2 summarizes all of the flow model constraint equations. This total system of measurement and constraint equations provides 22 equations for the 21 unknown flows, dye concentrations, and salinities, making this an over-determined system.

4.4 Constrained Bayesian estimation

4.4.1 Formulation

To take full advantage of the model presented in the previous section and to allow new measurements to be added in the future we use a Bayesian parameter estimation technique with the Lagrange multiplier method for incorporating all of the constraints (Gottfried & Weisman 1973, Schweppe 1973). In this section we will work in matrix notation and use bold face to represent vectors and matrices.

For ease of notation we first cast the system of equations given above into the canonical form for an estimation problem. Since we are estimating the liquid fluxes, dye concentrations, and salinities, we form the parameter vector, $\boldsymbol{\theta}$, given by

$$\boldsymbol{\theta} = [Q_1, ..., Q_n, C_1, ..., C_n, S_1, ..., S_n]^T, \tag{4.4}$$

where $n = 7$. The measurement vector, $\mathbf{z}$, contains the right-hand side of the measurement equations in Table 4.2 giving

$$\mathbf{z} = [z_1, z_2, ..., z_m]^T, \tag{4.5}$$

where there are $m = 10$ measurements. Our conceptual model can now be written in terms of a measurement equation:

$$\mathbf{z} = f(\boldsymbol{\theta}) + \mathbf{v}, \tag{4.6}$$

where $\mathbf{v}$ is a vector of measurement errors, assumed unbiased, uncorrelated, and Gaussian. Finally, the constraint equations are given by $g(\boldsymbol{\theta})$ and defined such that

$$g(\boldsymbol{\theta}) = 0. \tag{4.7}$$

(4.4) to (4.7) form the complete system of model equations.

The Lagrangian function for the Bayesian estimator is written as

$$J(\boldsymbol{\theta}) = [\mathbf{z} - f(\boldsymbol{\theta})]^T \boldsymbol{C}_v^{-1} [\mathbf{z} - f(\boldsymbol{\theta})] + [\boldsymbol{\theta} - \overline{\boldsymbol{\theta}}]^T \boldsymbol{C}_\theta^{-1} [\boldsymbol{\theta} - \overline{\boldsymbol{\theta}}] + g^T(\boldsymbol{\theta})\boldsymbol{\lambda}, \tag{4.8}$$

where $\boldsymbol{C}_v$ is a matrix of measurement covariances (diagonal for uncorrelated measurements), $\overline{\boldsymbol{\theta}}$ is an initial estimate of the parameters, $\boldsymbol{C}_\theta$ is a matrix of variance estimates for $\overline{\boldsymbol{\theta}}$, and $\boldsymbol{\lambda}$ is a vector of Lagrange multipliers. The first term in (4.8) is the familiar weighted least squares. The second term, called the Bayesian regularization term, takes into account our *a priori* information about $\boldsymbol{\theta}$; thus, $\overline{\boldsymbol{\theta}}$ is called the *prior* vector. The final term in (4.8) incorporates the constraints by the Lagrange multiplier method.

Both the measurement and constraint equations related in Section 4.3 are non-linear since they contain terms of the form QC and QS. We linearize $f(\boldsymbol{\theta})$ and $g(\boldsymbol{\theta})$ in a first-order Taylor series expansion about the nominal parameter values $\boldsymbol{\theta}_0$ and adopt the notation $f(\boldsymbol{\theta}_0) = \boldsymbol{f}_0$ and $g(\boldsymbol{\theta}_0) = \boldsymbol{g}_0$. Substituting and taking the derivative of (4.8) with respect to $\boldsymbol{\theta}$ gives the optimization equation

$$\frac{\partial \boldsymbol{J}}{\partial \boldsymbol{\theta}} = -\frac{\partial \boldsymbol{f}_0}{\partial \boldsymbol{\theta}} \boldsymbol{C}_v^{-1} \left[\mathbf{z} - \boldsymbol{f}_0 - \frac{\partial \boldsymbol{f}_0}{\partial \boldsymbol{\theta}} (\boldsymbol{\theta} - \boldsymbol{\theta}_0) \right] + \boldsymbol{C}_\theta^{-1} \left[\boldsymbol{\theta} - \overline{\boldsymbol{\theta}} \right] + \frac{1}{2} \frac{\partial \boldsymbol{g}_0}{\partial \boldsymbol{\theta}}^T \boldsymbol{\lambda}; \tag{4.9}$$

stationary values are computed at $\partial \boldsymbol{J} / \partial \boldsymbol{\theta} = 0$. Re-arranging and combining with (4.7) gives

the system of equations

$$\left[\frac{\partial \boldsymbol{f}_0}{\partial \boldsymbol{\theta}}^T \boldsymbol{C}_v^{-1} \frac{\partial \boldsymbol{f}_0}{\partial \boldsymbol{\theta}} + \boldsymbol{C}_\theta^{-1}\right] \boldsymbol{\theta} + \frac{1}{2}\frac{\partial \boldsymbol{g}_0}{\partial \boldsymbol{\theta}}^T \boldsymbol{\lambda} = \frac{\partial \boldsymbol{f}_0}{\partial \boldsymbol{\theta}} \boldsymbol{C}_v^{-1} \left(\mathbf{z} - \boldsymbol{f}_0 + \frac{\partial \boldsymbol{f}_0}{\partial \boldsymbol{\theta}} \boldsymbol{\theta}_0\right) + \boldsymbol{C}_\theta^{-1} \overline{\boldsymbol{\theta}} \quad (4.10)$$

$$\frac{\partial \boldsymbol{g}_0}{\partial \boldsymbol{\theta}} \boldsymbol{\theta} = \frac{\partial \boldsymbol{g}_0}{\partial \boldsymbol{\theta}} \boldsymbol{\theta}_0 - \boldsymbol{g}_0. \quad (4.11)$$

Initially, $\boldsymbol{\theta}_0 = \overline{\boldsymbol{\theta}}$.

In the linear case for uncorrelated parameters and measurements the estimate error is given by

$$E\left[(\boldsymbol{\theta} - \hat{\boldsymbol{\theta}})(\boldsymbol{\theta} - \hat{\boldsymbol{\theta}})^T\right] \geq \frac{\partial f(\hat{\boldsymbol{\theta}})}{\partial \boldsymbol{\theta}} \boldsymbol{C}_v^{-1} \frac{\partial f(\hat{\boldsymbol{\theta}})}{\partial \boldsymbol{\theta}}^T + \boldsymbol{C}_\theta^{-1} \quad (4.12)$$

where $E[\,]$ is the expectation, $\boldsymbol{\theta}$ are the true parameter values and $\hat{\boldsymbol{\theta}}$ are the parameter estimates (Schweppe 1973). In our case, where the system is non-linear and the parameters are correlated, this error estimate does not apply. However, (4.12) does suggest how to make the model more well-posed when it is difficult to find a feasible solution.

4.4.2 *Prior* estimate

The *prior* vector $\overline{\boldsymbol{\theta}}$ contains our best estimate of the values of $\boldsymbol{\theta}$ before performing the optimization. It should reflect our knowledge from the measurements, model equations, and our intuition. The covariance matrix $\boldsymbol{C}_\theta$ then contains an estimate of our confidence in the *prior* vector (Schweppe 1973).

For our model the external flows Q_1, Q_2, Q_o, and Q_i can be calculated directly from the measurements and mass conservation equations. The internal, recirculating flows, Q_r and Q_p, are more difficult to estimate and require the full set of measurements and constraints. As a prior estimate, however, we chose the internal flows to both be of order Q_1. The *prior* estimates of the external dye concentrations and salinities are also estimated directly from the measurement and constraint equations. The internal values of C_r, C_p, S_r, and S_p are calculated using the *prior* estimates of Q_r and Q_p and the pertinent model equations. Because there are 22 model equation for the 21 parameters, not every equation can be satisfied by the *prior* vector $\overline{\boldsymbol{\theta}}$, and the optimization uses the uncertainty in the measurements and *prior*

estimate to converge on a global optimum that exactly satisfies all of the constraints.

The covariance matrix of the *prior*, $\boldsymbol{C}_\theta$, is formed by propagating the measurement errors through the equations used to obtain $\overline{\boldsymbol{\theta}}$. The exception is that *prior* estimates for Q_r and Q_p are assumed to be known within $\pm 2Q_1$.

4.4.3 Typical results

Figure 4-4 shows typical results for experiment T04 that illustrate how the Bayesian estimation technique is implemented. First, (4.1) is applied to the pre- and post-experiment density profiles to generate the net liquid flux profile. Second, measurements are obtained from the net flux, salinity and dye profiles. Because the net flux profile is not very smooth, best-fit lines are calculated to match the piece-wise linear segments of the profile. Two inputs are obtained from these linear regressions: the intersections of the lines provide Q_{net} at the heights h_1, h_i, h_p, and h_2; the deviation of the net flux profile from the linear regressions provides the estimation error for the net flux measurement needed by $\boldsymbol{C}_v$. The other necessary measurements and their corresponding measurement errors are taken from the salinity and dye profiles. Third, the Bayesian estimation technique is run to obtain the optimized parameter values. The plot in the lower right of Figure 4-4 shows the linear regression and the actual measured net flux profile together with the optimized estimates (depicted as circles) from the Bayesian estimator. Error bars shown in the figure represent the measurement error assumed in the optimization.

For the two experiments for Type 3 plumes with $U_N > 2.4$ the intrusion layer for the secondary plume overlapped the peel height slightly and the net flux measured at h_2 was not exactly equal to Q_2 and was actually negative for experiment Air 3. Since dye is always recorded above the first peel, Q_2 cannot be negative and it was necessary to give a *prior* estimate and measurement of Q_2 that was positive. Given any positive value, the model was then stable and gave results consistent with the other experiments, unconstrained due to the high error assumed for the *prior* and measurement for that experiment. Thus, the measured dye distribution and the regularization term in the Bayesian estimation model allowed this technique to be applied where upper-level intrusions slightly overlapped the first detrainment

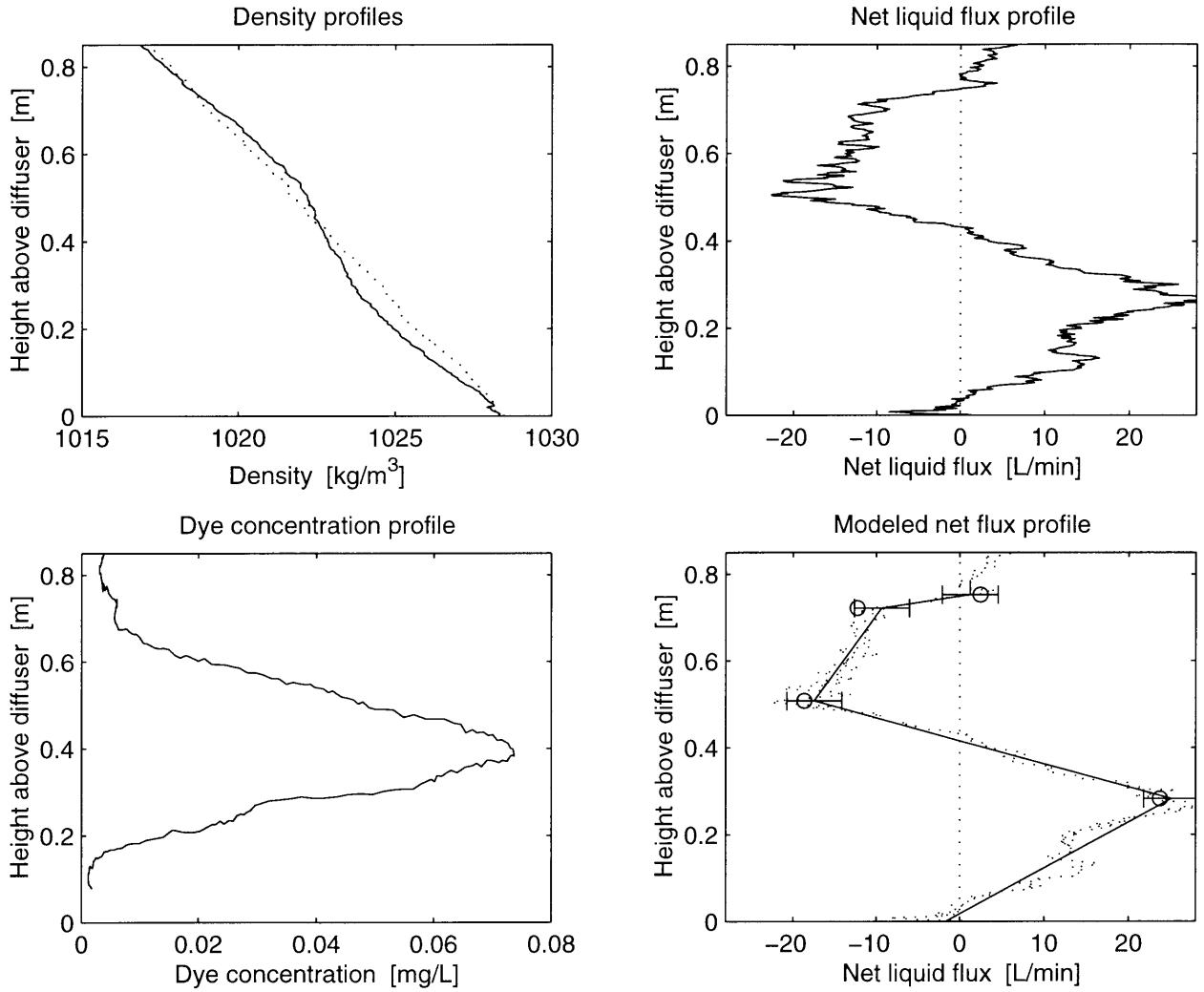

FIGURE 4-4: Example calculation for the next flux profile for experiment T04. For the modeled results, the solid lines are the best-fit lines to the measured net flux profile and the circles are the modeled flows, taking into account the dye and salinity fluxes. Horizontal error bars depict the measurement errors assumed in the optimization.

Exp. ID	Non-dimensional liquid fluxes							f	B_2
	Q_1	Q_2	Q_{ol}	Q_{oe}	Q_i	Q_p	Q_r		
Air1	0.22	0.03	0.19	0.20	0.58	0.43	0.24	0.93	0.09
Air2	0.21	0.03	0.03	0.31	0.52	0.48	0.31	0.94	0.08
Air4	0.25	0.04	0.07	0.21	0.48	0.50	0.30	0.92	0.11
T04	0.30	0.02	0.09	0.18	0.54	0.53	0.25	0.95	0.10
Sed4	0.22	0.01	0.06	0.20	0.47	0.38	0.17	0.97	0.04
Sed5	0.31	0.03	0.06	0.26	0.60	0.66	0.39	0.96	0.02
Sed1	0.23	0.03	0.10	0.18	0.49	0.63	0.43	0.95	0.15
Sed2	0.27	0.05	0.02	0.18	0.42	0.47	0.25	0.90	0.14
Sed6	0.20	0.04	0.04	0.20	0.40	0.57	0.41	0.93	0.12
Air3	0.17	0.09	0.08	0.21	0.37	0.29	0.21	0.76	0.12
Air5	0.17	0.05	0.04	0.22	0.37	0.44	0.33	0.89	0.14
MEAN:	0.23	0.04	0.07	0.21	0.48	0.49	0.30	0.92	0.10

TABLE 4.3: Results of the liquid volume flux calculations presented in non-dimensional space.

zone and where direct calculation for a determined system would not be feasible.

4.5 Results

To compare results among all of the experiments, the model estimated parameters are non-dimensionalized using the independent system variables B and N as discussed in detail by Socolofsky & Adams (2000*a*). Liquid fluxes are non-dimensionalized using the characteristic plume liquid flux, $Q_C = (B^3/N^5)^{1/4}$. The dye concentration data, though used by the model, are not analyzed in this paper. From the calculated salinities, the salt flux through the detrainment zone into the secondary plume is of interest and is expressed in terms of a buoyancy flux, B_2, normalized by the dispersed phase buoyancy flux, B. Throughout the remainder of this paper, as we discuss the trends for each variable, we are generally refering to the non-dimensional space. These trends can be applied to the dimensional variables, such as Q_1, if we interpret the variation to be due to changes in u_s while holding B and N constant. Table 4.3 summarizes the results obtained for each of the experiments.

The values presented in Table 4.3 are correlated in Figures 4-5 through 4-9 to the non-dimensional slip velocity, U_N, introduced by Socolofsky & Adams (2000*a*) as the ratio of

the dispersed phase slip velocity, u_s, to a characteristic plume fluid velocity, $(BN)^{1/4}$. Error bars for U_N shown in the figures were calculated by propagating the measurement errors for u_s, B, and N through the definition of U_N. Vertical error bars were calculated from the experiment repeatability by taking the standard deviation of the results for experiments Air1, Air2, Air4, Sed4, and Sed5. These experiments were treated as replicates because they have very similar values of U_N. The sediment experiments are combined with the bubble experiments since the plume structure depends most on the slip velocity as opposed to other dispersed phase characteristics (Reingold 1994, Socolofsky & Adams 2000*a*). The vertical dotted lines in the figures show the critical values of U_N for transition among the plume Types 1*, 2 and 3 as defined by Socolofsky & Adams (2000*a*).

Correlations with U_N are derived from two types of regressions. For variables that do not have a known single-phase value (i.e. a value for $U_N = 0$), simple linear regressions are computed of the form

$$\hat{y} = mU_N + b \tag{4.13}$$

where $\hat{y}$ is the computed dependent variable and m and b are regression coefficients. For data that do have a known single-phase value, non-linear regressions are computed of the form

$$\hat{y} = a + cU_N^d \tag{4.14}$$

where a is the single-phase value and c and d are regression coefficients, obtained by minimizing the squared error between $\hat{y}$ and the model estimates. Multi-phase plumes are expected to approach single-phase behaviour as the slip velocity approaches zero since separation among the phases would no longer occur, and, therefore, the buoyancy of the dispersed phase would never leave plume. In principle, single phase values could be obtained for all the variables presented; unfortunately, data are only available for Q_i. Single phase values for Q_2, f, and B_2 are also known since there would be no secondary plume, and all upward-flowing fluid would descend to the intrusion layer.

As a means of evaluating the correlations, the regressions are also analyzed for their goodness of fit and to test the statistical significance of their implied dependence on U_N. Because the regression equations were obtained using a least-squares technique, we use the

	Non-dimensional liquid fluxes								
	Q_1	Q_2	Q_{ol}	Q_{oe}	Q_i	Q_p	Q_r	f	B_2
r^2	0.49	0.73	0.0049	0.024	0.54	0.30	0.0093	0.81	0.52
$\|t\|$	2.93	4.99	0.21	0.47	3.2	1.97	0.29	6.20	0.68
m	-0.029		-0.0028	-0.0057		-0.053	-0.0072		
b	0.28		0.077	0.22		0.58	0.31		
a		0.0			0.9			1.0	0.0
c		0.026			-0.38			-0.048	0.082
d		0.77			0.24			0.86	0.44

TABLE 4.4: Fit statistics and regression equations. The two regression equations are of the form $\hat{y} = mU_N + b$ and $\hat{y} = a + cU_N^d$.

coefficient of determination, r^2, to test the goodness of fit (see e.g. Mays & Tung 1992). To test whether the obtained dependence on U_N is significant, we use a t-test as described by Walpole & Myers (1972). For $n - 2 = 9$ degrees of freedom $|t| > 1.83$ corresponds to a 0.05 significance level for the correlation. Table 4.4 presents fit statistics and regression coefficients for each of the figures that follow. The correlations reported in the table match the constraint equations in Table 4.2 to within ± 0.04 of non-dimensional flow even though the regressions were not constrained to match the model.

4.5.1 Plume liquid fluxes

Figure 4-5 shows the four plume fluxes that interact with the ambient fluid. For this, and all following figures, the vertical dotted lines plot the transition values between Types 1*, 2 and 3 plume behaviour as described by Socolofsky & Adams (2000*a*). No literature data are available to compare with these four fluxes.

Figure 4-6 shows the intrusion layer flux along with four laboratory and field values from Lemckert & Imberger (1993) obtained in step stratification. The values selected from Lemckert & Imberger (1993) for comparison in the figure were limited to plumes that were predicted to peel before reaching the reservoir surface. Wright et al. (1991) showed for single-phase jets that the surface peel can dilute the inner core flow by up to 5 times due to the excess momentum in the jet when it impinges on the reservoir surface. Values from

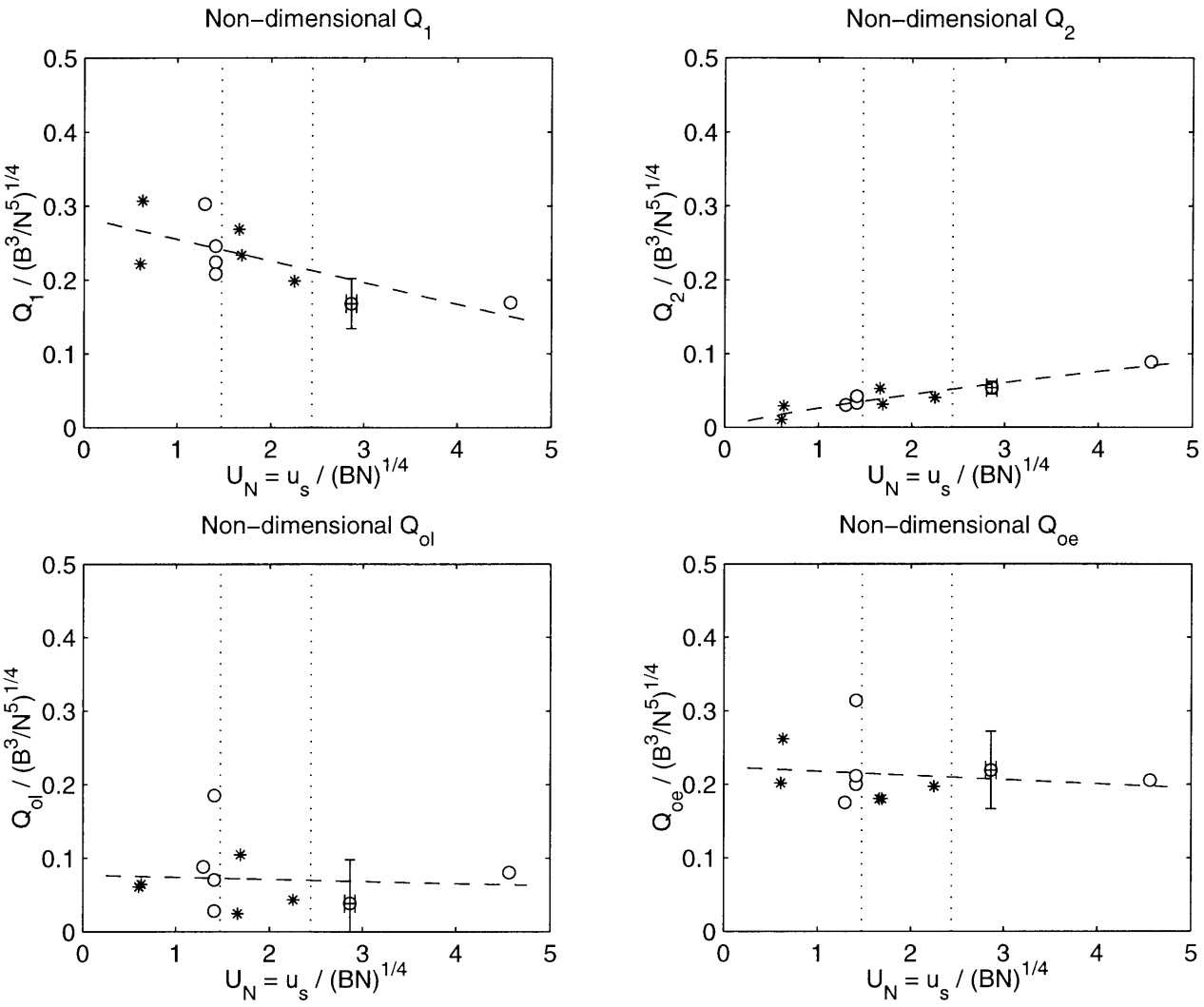

FIGURE 4-5: Correlation of selected non-dimensional plume volume fluxes to U_N. Circles represent air-bubble experiments; stars represent glass-bead experiments. Typical error bars are shown for one data point.

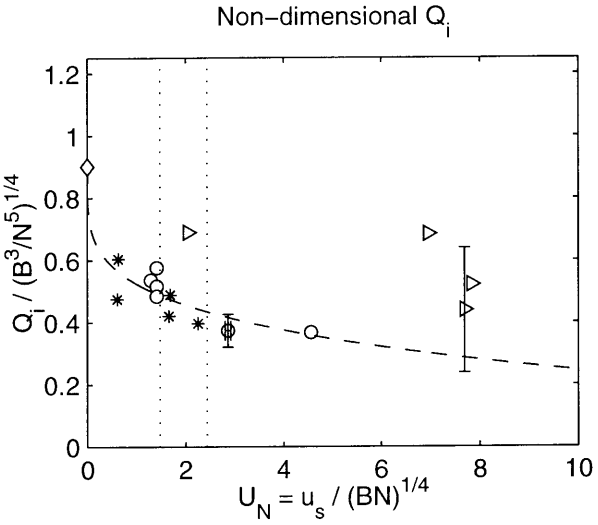

FIGURE 4-6: Correlation of non-dimensional intrusion layer flux to U_N. Right-pointing triangles were reported in Lemckert & Imberger (1993) with typical error bars as shown. For the current authors, circles represent air-bubble experiments, and stars represent glass-bead experiments with typical error bars shown for one data point. The dashed line plots the correlation presented in Section 4.5.

Lemckert & Imberger (1993) that did not meet our critera for comparison ranged from 0.3 to 1.2 with a mean of 0.7 in the non-dimensional Q_i space. The single-phase value is taken as 0.9, the dilution at the trap height for a buoyant plume in linear stratification as reported in Fischer et al. (1979).

The peeling and recirculating flows are presented in Figure 4-7. Although the *prior* estimates of the non-dimensional Q_p and Q_r were approximately 0.2 ± 0.4, a reasonably clear variation among experiments is obtained. Other stationary points for Q_p and Q_r were obtained when the error in the *prior* estimate was set very large (greater than ± 10); however, these alternate solutions had values too high to be physically reasonable. Thus, using the moderately uncertain *prior* estimate of ± 0.4 allowed the regularization term to keep the optimization from converging on these unreasonable stationary points, but because the *prior* error estimate was still large (± 0.4) the estimates obtained were not significantly biased by the *prior*.

Regression statistics for Q_{ol}, Q_{oe} and Q_r reported in Table 4.4 show a weak correlation (small $|t|$) with U_N. In fact, at the 0.05 significance level, these variables may be predicted by their mean values, independent of U_N. The composite variable $Q_o = Q_{ol} + Q_{oe}$ is also

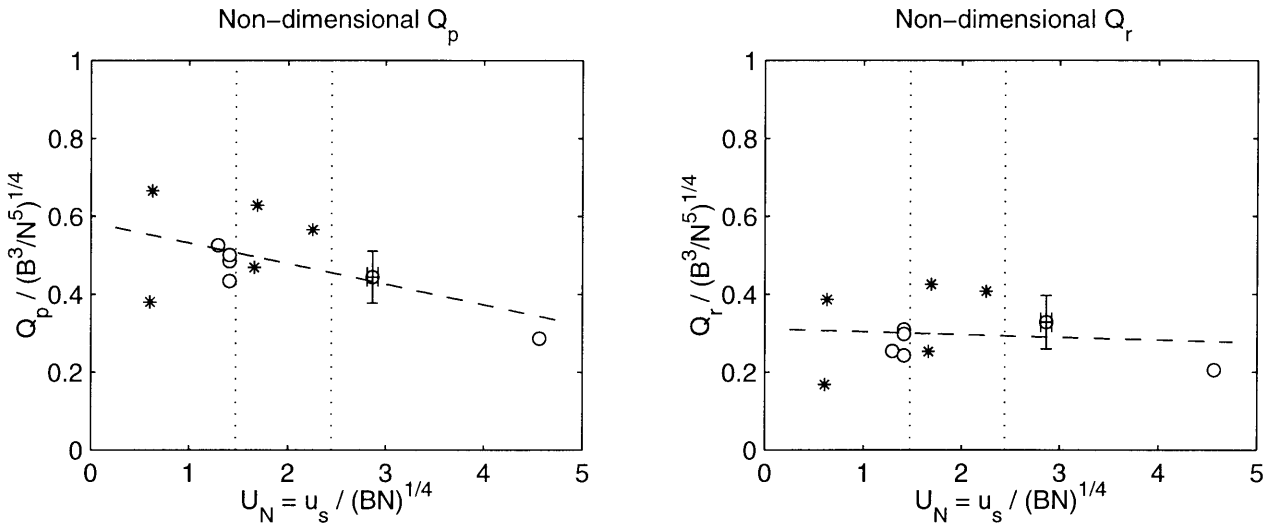

FIGURE 4-7: Correlation of non-dimensional peeling and recirculating fluxes to U_N. Circles represent air-bubble experiments; stars represent glass-bead experiments. Typical error bars are shown for one data point.

independent of U_N ($|t| = 0.58$). The presumed reason for this independence is that each of these flows represents an entrainment flux into or out of the downdraught plume, which is itself a single-phase plume where U_N would be zero. The only dependence these flows can have on U_N is through the initial buoyancy flux, B_p, provided to the downdraught plume through Q_p, or through interaction with the inner plume, as might have been the case for Q_r. Although the decreasing trend of Q_p with increasing U_N is significant at the 0.05 level, the entrainment flux Q_o at a given height scales with the associated initial buoyancy flux to the $\frac{1}{3}$ power, yielding a weak correlation. Hence, these results suggest that entrainment into and out of the downdraught plume is independent of the dispersed phase characteristics.

An additional single-phase flux is the intrusion layer flux Q_i. This flux does depend on U_N at the 0.05 significance level, and actually has a stronger correlation than does Q_p. This results from two effects. First, Q_i depends on Q_p directly, since the majority of the detraining flux ends up in the intrusion layer. Second, as Q_p decreases with U_N the entrainment fluxes Q_o and Q_r are similarly, though weakly, affected, providing a positive feedback for the dependence of Q_i on U_N.

As observed in experiments by Socolofsky & Adams (2000*a*), the downdraught plume falls farther to reach a level of neutral buoyancy in the two-phase case than for a single-

phase plume; thus, we might have expected Q_i to lie above the single-phase value due to the opportunity for greater entrainment. This does not appear to be the case because of the shrouding effect of the downdraught plume, which inhibits entrainment into the inner plume and, thereby, decreases the inner plume flux available to Q_p. As U_N increases, the shrouding downdraught plume gets longer, Q_p decreases, and since the dilution of Q_p from Q_o and Q_r remains constant, Q_i goes down correspondingly. In summary, the dependence of Q_i on U_N is a result of the overall plume structure, influenced in part by the presence of the downdraught plume.

The decreasing trend of Q_1 with increasing U_N is another direct result of the decreasing intrusion layer height. Because Q_1 is taken at the base of the intrusion layer, as the intrusion layer height decreases there is less opportunity for entrainment and Q_1 must reduce accordingly.

This dependence of Q_1 on U_N is also evidence that the entrainment coefficient, α, for the inner plume is not a strong function of U_N. The data provided in Milgram (1983) can be used to show that the entrainment coefficient in a uniform ambient is proportional to $C_m^{1/6}$, where C_m is the centerline void fraction for the dispersed phase. Socolofsky & Adams ($2000a$) showed that the bubble spreading ratio, λ, decreased with increasing U_N, which would cause C_m and, therefore, α, to increase with U_N if the plume width stayed constant. However, a relationship of $\alpha \propto C_M^{1/6}$ is very weak, and these results for Q_1 suggest that the decrease in intrusion layer height is more significant than variations in α. Further, the effects of stratification on α may be much greater than the effects of C_m.

The remaining flux, Q_2, provides the greatest impact on the resulting plume structure. The increasing trend of Q_2 with increasing U_N is significant at a level greater than 0.05. Increasing Q_2 provides a negative buoyancy flux into the secondary plume, shown in Figure 4-9 as the negative buoyancy flux of the plume fluid, B_2, normalized by B and given a positive value. This negative buoyancy flux causes subsequent peels to occur earlier and provides an opportunity for upper level intrusions to overlap intrusions lower in the profile, resulting in the Type 3 plume behaviour described by Socolofsky & Adams ($2000a$) and Asaeda & Imberger (1993). Hence, the variation of Q_2 with U_N provides a physical mechanism for plume type to depend on U_N.

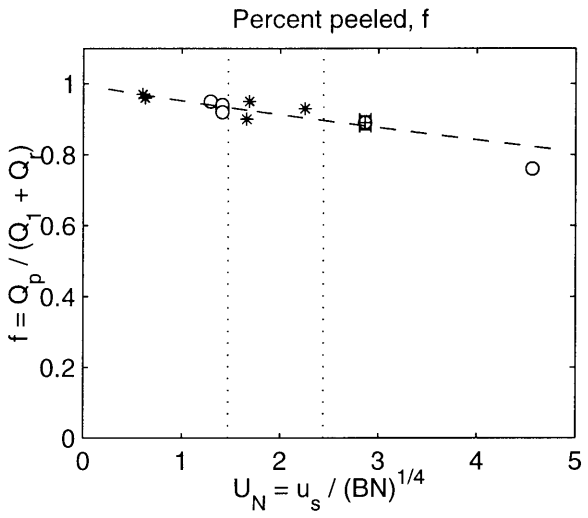

FIGURE 4-8: Correlation of peel fraction to U_N. Circles represent air-bubble experiments; stars represent glass-bead experiments. Typical error bars are shown for one data point.

4.5.2 Peeling efficiency

Figure 4-8 shows the percent of fluid that peels at the initial intrusion formation. The convenience of the conceptual model used here is that it easily defines the percent of fluid that peels,

$$f = \frac{Q_p}{Q_1 + Q_r}. \tag{4.15}$$

Although the estimate errors for Q_p and Q_r are relatively large, errors in f are stabilized by the model non-linearity and the cross-correlation of Q_p and Q_r through the dye tracer profiles.

The decreasing trend of f with U_N is more statistically significant than for any of the other variables. Since f is a complement of Q_2, new physical insight is not gained. However, f remains an important parameter for modelling since it provides a means for models to set Q_2.

4.5.3 Peeling zone buoyancy flux

Figure 4-9 shows the buoyancy flux of fluid that escapes into the secondary plume. Inspection of Table 4.4 suggests that the dependence of B_2 on U_N over the full range ($0 < U_N < 5$)

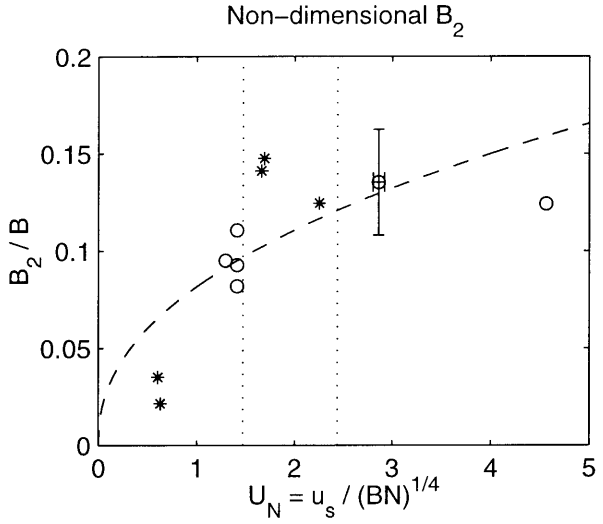

FIGURE 4-9: Correlation of the buoyancy flux escaping the detrainment zone to U_N. Circles represent air-bubble experiments; stars represent glass-bead experiments. Typical error bars are shown for one data point.

is not significant at the 0.05 level. This is misleading because of the preponderance of data at high U_N where the non-dimensional B_2 approaches a constant. For $U_N < 2.4$ the dependence is in fact significant at the 0.05 level. In addition, the single-phase value of $B_2 = 0$ supports the strong variation of B_2 with U_N suggested by the correlation curve. However, the asymptotic behaviour of B_2 above $U_N = 2.4$ is evidence that the detrainment flux in a Type 3 plume is constant.

4.6 Conclusions

The dominant entrained fluid fluxes for a stratified two-phase plume have been measured using the net flux method of Baines & Leitch (1992) combined with dye tracer profiles and a conceptual model of the plume. To incorporate all of the system measurements and to enforce the constraints implied by the conceptual model, a Bayesian estimation technique was applied to evaluate the plume liquid fluxes. The Bayesian method also helped achieve physically realistic estimates for this non-linear system through the stability derived from the regularization term.

The non-dimensional variables for Q_{ol}, Q_{oe}, and Q_r were independent of U_N. This was

explained by the fact that these variables represent entrainment fluxes into a single-phase plume where U_N is zero.

The dependence of the non-dimensional variables Q_1 and Q_i on U_N is a direct result of the structure of the plume, or plume type. Q_1 decreases with U_N because the intrusion layer height decreases, limiting the distance over which ambient fluid is entrained. Q_i decreases with U_N because more of the plume is shrouded and because peeling is less efficient, resulting in decreased entrainment into the inner plume and decreased volume of fluid peeled.

The dependence of the non-dimensional variables for Q_2, f, and B_2 on U_N provide a physical mechanism controlling plume structure. At higher U_N peeling occurs less efficiently; thus, Q_2 increases with U_N. This flux through the detrainment zone into the secondary plume carries an associated negative buoyancy, B_2, that eventually allows subsequent intrusions to overlap. Hence plume structure (flow rates, dimensions, and plume type), which is dependent on U_N, is controlled entirely by the peeling characteristics, incorporated in the relationship for f.

Integral-type models can be adapted to mimic plume behaviour by incorporating the observations made here for entrainment and detrainment: the volume fraction that peels at each detrainment should be calibrated to measurements of f; the counterflowing entrainment algorithm should follow single-phase entrainment laws and also be calibrated to the fluxes measured here. By incorporating these two processes through physically-based algorithms, such models should accurately predict plume entrained fluid fluxes and type behaviour for a full range of laboratory, field, and industrial conditions.

Chapter 5

Multi-phase plumes in uniform and stratified crossflow[1]

Abstract: Laboratory experiments of multi-phase plumes in uniform and stratified crossflows are presented. In uniform crossflow, multi-phase plumes behave as mixed single-phase plumes up to a critical height, h_S, where the entrained fluid separates from the dominant dispersed phase. From the experimental results, an empirical relationship for h_S was calibrated giving $u_\infty/(B/h_S)^{1/3} = 6.3(u_s/(B/h_S)^{1/3})^{-2.4}$, where u_∞ is the crossflow velocity, B is the total kinematic buoyancy flux of the mixed plume, and u_s is the slip velocity. Above h_S the separated continuous-phase plume behaves like a momentum jet and the bubble column follows the trajectory of the vector sum of u_s and u_∞. In stratified crossflow, the trap height in quiescent water, h_T, was compared to h_S. For $h_T \ll h_S$, the plumes are stratification-dominated and separation occurs at $h_T = (2.8 - 0.27u_s/(BN)^{1/4})(B/N^3)^{1/4}$, where N is the Brunt-Vaisälä buoyancy frequency. For $h_T \gg h_S$, the plumes are crossflow-dominated, and separation occurs at h_S. A simple single-phase model was modified to predict the fate of the separated plume above h_S.

5.1 Introduction

Multi-phase plumes have many environmental applications, including air bubble plumes used for reservoir destratification (Asaeda & Imberger 1993, Schladow 1993, Lemckert &

[1]This chapter submitted to the *Journal of Hydraulic Research* as Socolofsky & Adams (2000), "Multi-phase plumes in uniform and stratified crossflow."

Imberger 1993), aeration (Wüest et al. 1992), ice prevention in harbors (McDougall 1978), and contaminant containment (Milgram 1983); continuous particle clouds resulting from the release of dredged sediments (HAVIS Environmental 1994, Koh & Chang 1973); liquid CO_2 plumes for deep-ocean carbon sequestration (Alendal & Drange 2000, Adams et al. 1997, Liro et al. 1992); and deep sea blowouts of oil and gas (Johansen 1999, Yappa & Zheng 1999, 1997*a*, 1997*b*, McDougall 1978). In many of these applications crossflows are present. Our interest here is in predicting the fate of oil released in a well blowout. Typically, gas is emitted along with the oil in a blowout (*in situ* gas/oil ratios range from 1 to 100), and the plume which develops is mainly due to the gas bubbles (Topham 1975). Although the effect of crossflows on single-phase plumes and jets has been investigated (e.g. Davidson & Pun 1999, Pun & Davidson 1999, Huang et al. 1998, Wright 1984), little is known about their effect on plumes generated by multiple dispersed phases. This paper presents laboratory experiments to investigate multi-phase plume behavior in crossflows.

A distinguishing feature of multi-phase plumes is the possibility of separation of the dispersed phases (bubbles, droplets, or particles) and the continuous phase (the entrained ambient fluid). Separation occurs when horizontal motion strips entrained fluid away from the dispersed phase. For clarity, we will use bubbles to refer to the dispersed phase in a generic multi-phase plume, and we will use bubbles, droplets or particles as appropriate when discussing specific plumes.

Figure 5-1 illustrates two effects of separation for a bubble plume in a crossflow. First, at some height above the source, the crossflow separates the entrained fluid from the rising bubbles. This occurs as the rise velocity of the entrained fluid decreases with height allowing the crossflow to have an increasing effect. Second, as observed by Hugi (1993), crossflows transport bubbles having different slip velocities (terminal rise velocities) differentially downstream; this is called fractionation. Fractionation distributes the buoyancy over an increasing horizontal area with height. We show here that the crossflow separates the entrained fluid from the bubbles at a discrete height, h_S, below which the bubbles and entrained fluid behave like a mixed, coherent plume and fractionation is negligible, and above which the separated fluid may be treated as a buoyant momentum jet.

Separation in bubble plumes has been studied in detail for stratified ambients without

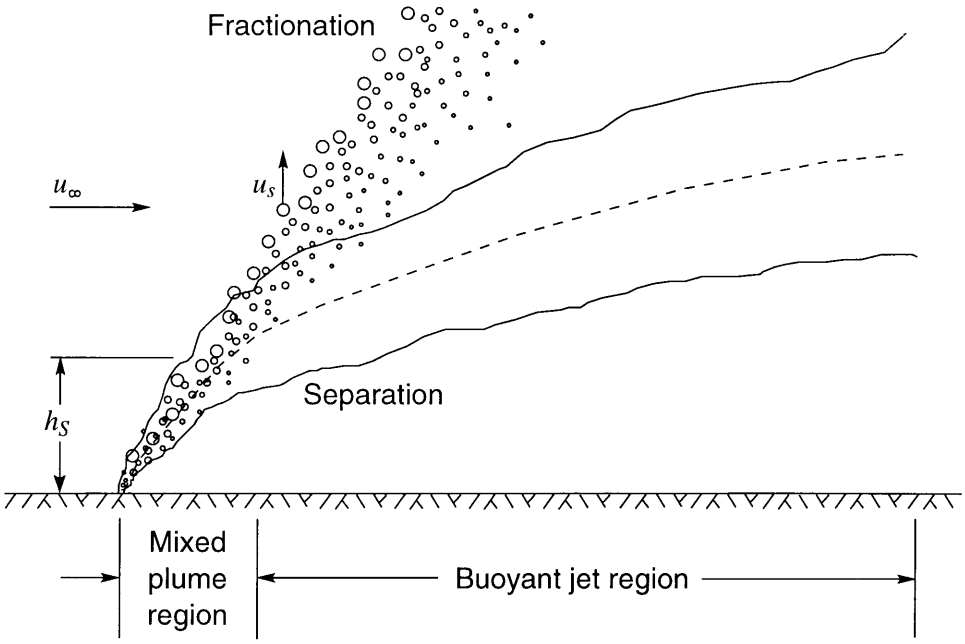

FIGURE 5-1: Definition sketch for a two-phase plume in a crossflow.

crossflow (Crounse 2000, Socolofsky et al. 2000, Asaeda & Imberger 1993, Lemckert & Imberger 1993, Wüest et al. 1992, McDougall 1978). Separation occurs in stratification when the dense entrained fluid can no longer be lifted by the bubbles, but rather separates from the plume and forms a horizontal gravity current at the level of neutral buoyancy. McDougall (1978) observed this behavior for laboratory and field-scale plumes and developed a double-plume model that treats the upward-moving bubble core separately from an outer ring of entrained fluid that evolves into the intrusion layer. The model predicted the intrusion layer heights, but was not stable when the outer plume transitioned to the intrusion flow. Asaeda & Imberger (1993) modified McDougall's model by decoupling the separation process from the equations of motion. In their model, all of the upward flowing bubbles and fluid are lumped together in an inner plume core. When the momentum flux of the inner plume approaches zero, a fraction of the entrained fluid is ejected, forming a downward-flowing annular outer plume that interacts with the inner plume. Asaeda & Imberger assume 100% loss of entrained fluid; Crounse (2000) proposed a more sophisticated, empirical equation derived from dimensional arguments. This type of modified double-plume model has been applied successfully to laboratory and field-scale experiments (Crounse 2000, Asaeda & Im-

berger 1993, Lemckert & Imberger 1993). Thus, separation controls the fate of entrained fluid but does not affect plume dynamics outside the separation zone.

Models applied to well blowouts vary in their treatment of separation. McDougall (1978) treated plumes in a quiescent ambient and assumed that oil would separate with the peeling fluid in stratification and become trapped in the first intrusion due to the slow rise velocity of the oil droplets and due to the expected formation of neutrally buoyant oil-in-water emulsions (McDougall 1978, Topham 1975). The model of Yapa & Zheng (1997*a*, 1997*b*) simulates the physical and chemical processes impacting a well blowout plume in quiescent and flowing ambients, but ignores crossflow separation. Yapa & Zheng (1997*a*) account for the trapping effect of stratification and simulate the lateral deflection due to a crossflow using a single-phase approach. The oil is assumed to remain in the intrusion layer and spread out; the gas bubbles are ignored above the initial intrusion. The model was expanded in Yapa & Zheng (1999) to consider separation of the oil from the intrusion layer by including a surface oil slick and a random-walk algorithm for transporting the oil from the intermediate intrusion layer to the surface. The revised model was calibrated to field experimental data. Because of the shallow depth (100 m) and strong stratification ($N = 0.01$ s^{-1}) in the field experiment, the plumes were stratification dominated (see Section 5.7, below), forming a single intrusion layer; thus, the model performed well. Johansen (1999) models both stratification and crossflow separation, but crossflow separation is based on an *ad hoc* algorithm that ejects bubbles when their simulated trajectory takes them out of the plume on the upstream edge.

Existing laboratory experiments for bubble plumes and single-phase jets and plumes in a uniform crossflow have illustrated features similar to separation. Hugi (1993) performed a detailed laboratory study of bubble plumes in crossflow. He observed that dye injected at the base of the bubble column did not rise to the surface, but rather became trapped in a vortex street in the wake of the plume. He also noted that the bubbles fractionated in the crossflow. As a result, he assumed that a coherent plume stage never developed, i.e., that separation occurred immediately. Davidson & Pun (1999) for single-phase momentum jets and Pun & Davidson (1999) for single-phase buoyant plumes, both of which provide some analogy to a multi-phase plume, observed tracer detachment due to a crossflow. As part of their analyses, they identified three flow regimes that evolved with height. Initially,

the jets and plumes are weakly advected and tracer spread and dilution data are consistent with Gaussian integral model predictions. A little higher above the source, detachment of tracer from the main body of the jet or plume begins: this is called leakage. Detachment occurs when ejected vortices are no longer entrained back into the jet or plume and are, therefore, advected downstream by the crossflow. Higher still, jets and plumes transition to a strongly advected case where model predictions based on a Gaussian model no longer apply and the behavior approaches that of a line thermal or momuntum puff. Davidson & Pun (1999) and Pun & Davidson (1999) correlate the transition heights between flow regimes with the governing dimensional variables: the crossflow velocity, u_∞, the total kinematic momentum flux of the jet, $M_0 = \pi u_0^2 d_p^2/4$, and the total kinematic buoyancy flux of the plume, $B_0 = \pi u_0 d_p^2(\rho - \rho_p)/(4\rho)$, where u_0 is the jet or plume exit velocity, d_p is the pipe diameter, ρ is the ambient density, and ρ_p is the plume fluid density. These variables combine to define the transition heights, $h_{tr,j} = C_1 M_0^{1/2}/u_\infty$ and $h_{tr,p} = C_2 B/u_\infty^3$, where subscripts j and p refer to jets and plumes, respectively. $C_1 = 1.0$ and $C_2 = 0.5$ define the transitions to strongly advected behavior (Davidson & Pun 1999, Pun & Davidson 1999).

This paper presents laboratory experiments to investigate the nature of separation in multi-phase plumes due to uniform and stratified crossflows. The experiments were conducted with multiple dispersed phases (air, oil and alcohol) in a range of crossflow velocities (0 to 10 cm/s). Separation heights were determined from flow visualization using LASER induced fluorescence (LIF). Section 5.2 presents a dimensional analysis similar to Davidson & Pun (1999) as a framework for analyzing the experimental results. Sections 5.3 and 5.4 present the methods and observations. The critical separation height is correlated to the governing dimensional variables in Section 5.5, and Section 5.6 proposes a separation algorithm to adapt a typical single-phase model to predict the fate of entrained fluid and fine oil droplets separated from a bubble plume due to a crossflow. Section 5.7 extends the results to a stratified ambient by analyzing a set of exploratory experiments. The combined results are discussed at the field scale in Section 5.8, followed by the conclusions in Section 5.9.

5.2 Dimensional analysis

To scale the laboratory results to the field, the governing dimensional variables and their functional dependence on non-dimensional groups must be determined. Wright (1984) analyzed the general case of a single-phase buoyant jet in a stratified crossflow and identified the following independent variables: the source discharge, Q, the initial jet kinematic momentum flux, M, the initial jet kinematic buoyancy flux, B, the crossflow velocity, u_∞, the stratification strength given by the Brunt-Vaisälä buoyancy frequency $N = [-(g/\rho)(\partial\rho/\partial z)]^{1/2}$, and the height above the discharge, z. For a two-phase plume, we introduce one more independent variable, the slip velocity, u_s, defined as the terminal rise velocity of an individual bubble in a quiescent fluid (Milgram 1983). Any dependent variable, ϕ, is a function of these independent variables:

$$\phi = f(Q, M, B, u_\infty, u_s, N, z). \tag{5.1}$$

Wright (1984) used these variables (without the slip velocity) to form several characteristic length scales that were then used to classify a given flow and predict the dilution at the terminal level and the trajectory of the centerline.

For a two-phase bubble plume, a few simplifications of (5.1) can often be made. First, above a short elevation the initial momentum, M, can be neglected. This is possible because the bubbles or droplets have very little momentum (i.e. they reach terminal velocity almost immediately) and because the plume starts off with zero volume flux of the continuous phase so that all of the entrained fluid must be accelerated from rest by the drag from the bubbles. Second, as with single phase plumes, the variable Q may also be neglected above a short elevation since a pure plume develops as a result of its buoyancy, $B = gQ\Delta\rho/\rho$, without memory of its initial volume flux (Wright 1984).

By introducing u_s, the dimensional analysis becomes more complicated compared to the single-phase case. For a single-phase buoyant plume in an unstratified ambient ($\phi = f(B, u_\infty, z)$), there are only two characteristic velocity scales: u_∞ and a characteristic plume fluid velocity, given as $u_C \propto (B/z)^{1/3}$. This leads to a single variable representing a non-dimensional velocity scale, $u_\infty/(B/z)^{1/3}$, or its reciprocal. Introducing u_s gives a third velocity scale and several different non-dimensional velocities can be obtained. To analyze

the experiments in the following sections, we choose to use $(B/z)^{1/3}$ as the normalizing velocity scale. Thus, by invoking the Buckingham Π theorem and substituting a separation height, h_S, for z, the transition heights in an unstratified crossflow can be derived from

$$\frac{u_\infty}{(B/h_S)^{1/3}} = f\left(\frac{u_s}{(B/h_S)^{1/3}}\right). \tag{5.2}$$

Introducing a stratified ambient gives the characteristic plume fluid velocity $u_C \propto (BN)^{1/4}$, defined by Asaeda & Imberger (1993) as the single-phase plume rise velocity in unstratified fluid taken at the height of the stratified intrusion layer. To simplify such a complicated problem, two limiting cases are introduced. First, if the crossflow is strong, separation will occur due to the crossflow before it occurs due to stratification effects, and the separation height can be determined using (5.2), neglecting the stratification. Second, if the crossflow is weak, separation will occur due to stratification effects before it occurs due to the crossflow. In this case, (5.2) can be neglected, and separation is predicted to occur at the trap height, h_T, predicted for stagnant, stratified conditions. For a single-phase plume in stratification, Crawford & Leonard (1962) and Turner (1986) give the relationship

$$h_T = 2.8(B/N^3)^{1/4}. \tag{5.3}$$

Socolofsky & Adams (2000*a*) found that for two-phase plumes in stratification, the single-phase value of h_T is reduced because buoyancy is lost from the intrusion layer as the bubbles separate, causing the intrusion to form deeper in the profile. They suggest the two-phase trap height in stagnant, stratified conditions given by

$$\frac{h_T}{(B/N^3)^{1/4}} = 2.8 - 0.27\left[\frac{u_s}{(BN)^{1/4}}\right] \tag{5.4}$$

where the left-hand side is the non-dimensional trap height, $h_T/(B/N^3)^{1/4}$, and the right-hand side contains the non-dimensional slip velocity, $u_s/(BN)^{1/4}$, the ratio of the dimensional slip velocity to a characteristic continuous phase rise velocity. Thus, we expect that separation heights for two-phase plumes in crossflow should be predicted by (5.2) in the unstratified

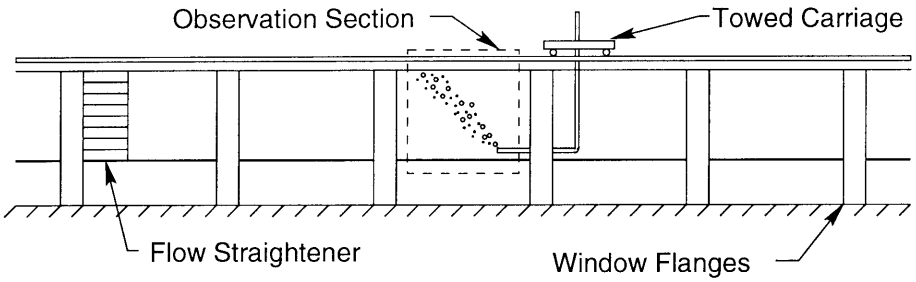

FIGURE 5-2: Layout of the experimental facility. Distance between successive flanges is 1.5 m; total water depth is 0.7 m.

case and for crossflow dominated plumes in stratification, and should be predicted by (5.4) for stratification-dominated plumes in crossflow. Correlations for (5.2) with the experimental data are given in Sections 5.5 and 5.7.

5.3 Methods

Crossflow experiments were conducted using a towed source in a 0.8 m square cross-section by 28 m long flume in the Ralph M. Parsons Laboratory at MIT. Figure 5-2 shows a schematic of the facility. Plumes were visualized using a neutrally buoyant solution of Rhodamine 6G dye. The dye was fluoresced by a vertical light sheet created from a Coherent 6 W Argon-ion LASER connected by a fiber-optic cable to a submerged cylindrical lens placed 2 m upstream of the observation section. The cylindrical lens creates a Gaussian power distribution in the vertical plane of the light sheet. Images were captured using a Pulnix TM9701 1.7 cm progressive scanning CCD camera running a full-frame shutter at a 1/60 s and connected to a Matrox Pulsar PCI framegrabber running in analog mode. A carriage mounted on the flume rails was towed by a variable speed motor yielding speeds of 2 to 22 cm/s. Diffusers were positioned with their orifices 10 cm above the bottom of the tank on an L-shaped PVC mount connected to the carriage. The vertical arm of the PVC mount was near the flume wall, while the diffuser was along the flume centerline. Buoyancy was created by introducing air, alcohol or crude oil with densities of 0.0014, 0.781, and 0.871 g/cm^3, respectively. The oil and alcohol diffusers were 0.7 mm diameter spray nozzle orifices; the air diffuser was a standard aquarium airstone. The air, liquid, and dye supply lines ran

inside the 2.5 cm diameter PVC mount. Slip velocities were measured as in Hugi (1993) by timing the rise of bubbles released from a rapidly towed source (22 cm/s in our case) and are listed in Table 5.1 along with the experimental conditions. Air flow rates were measured using Cole Parmer mass flow meters; liquid flow rates were measured using Cole Parmer MasterFlex pumps calibrated by the bucket-and-stopwatch method.

The behavior of plumes and quantification of transition heights were taken from digitized images captured during the experiments. Although the plumes were visualized using LIF, concentrations could not be estimated because of the vertical Gaussian distribution in the light sheet and because of the attenuation of the LASER by the dye toward the downstream direction. Based on the analysis of Nash et al. (1995), upstream edges of the dyed plumes will appear brighter in the images than their actual concentrations suggest. Real-time *in-situ* measurements of dye concentration would be required to correct the images; hence, the visualization is used only as a marker for the entrained fluid, not as a measure of dilution.

5.4 Observations

The experiments confirmed the presence of fractionation and separation. For plumes with high buoyancy and low crossflow velocity, separation did not occur by the time the bubbles reached the water surface, and the situation is classified as a weak crossflow. In other experiments, separation did occur and the conditions are classified as strong crossflow.

5.4.1 Weak crossflows

In weak crossflows, some entrained fluid stays with the bubble plume from the injection point to the flume surface. Figure 5-3 shows four representative experiments in weak crossflows.

While major separation between the lightest dispersed phase and the other components of the plume does not occur before the plumes reach the surface, two forms of detachment, or leakage, are observed. First, as reported by Davidson & Pun (1999) for single-phase jets, some entrained fluid leaks into the downstream wake. Comparing frames (a.) and (b.) in

Exp-ID	Flow Rate			u_∞	u_s	$h_S\|_{min}$	$h_S\|_{max}$
	Air [mL/min]	Oil [mL/min]	Alcohol [mL/min]	[cm/s]	[cm/s]	[cm]	[cm]
A2	167	0	0	0	17	64	∞
A5	167	0	0	2	17	11	22
A8	167	0	0	10	17	3	10
B1	200	0	0	20	20	2	6
B2	200	0	0	10	20	3	10
B3	200	0	0	5	20	5	16
B4	200	0	0	2	20	12	29
B5	2000	0	0	20	26	7	19
B6	2000	0	0	10	26	14	27
B7	2000	0	0	5	26	22	55
B8	2000	0	0	2	26	64	–
B10	200	0	0	20	17	3	7
B11	200	0	0	10	17	4	7
C1	250	250	0	5	17	8	29
C2	250	250	0	2	17	35	64
C3	250	250	0	10	17	2	11
C4	600	600	0	5	17	10	36
C5	600	600	0	10	17	3	17
C6	2500	250	0	5	17	64	–
C7	2500	250	0	10	17	64	–
C8	1000	1000	0	5	17	64	–
C9	1000	1000	0	10	17	8	30
C10	600	600	0	2	17	64	–
C12	250	250	0	5	17	7	30
C13	600	600	0	5	17	7	40
C14	0	600	0	5	4	64	–
C15	600	600	0	10	17	5	15
C16	250	0	150	5	17	7	28
C17	600	0	360	5	17	19	64
C18	600	0	360	10	17	7	18
C19	0	0	150	5	0	64	∞

TABLE 5.1: Experimental conditions for crossflow experiments; $h_S|_{min}$ and $h_S|_{max}$ are defined in Section 5.5.

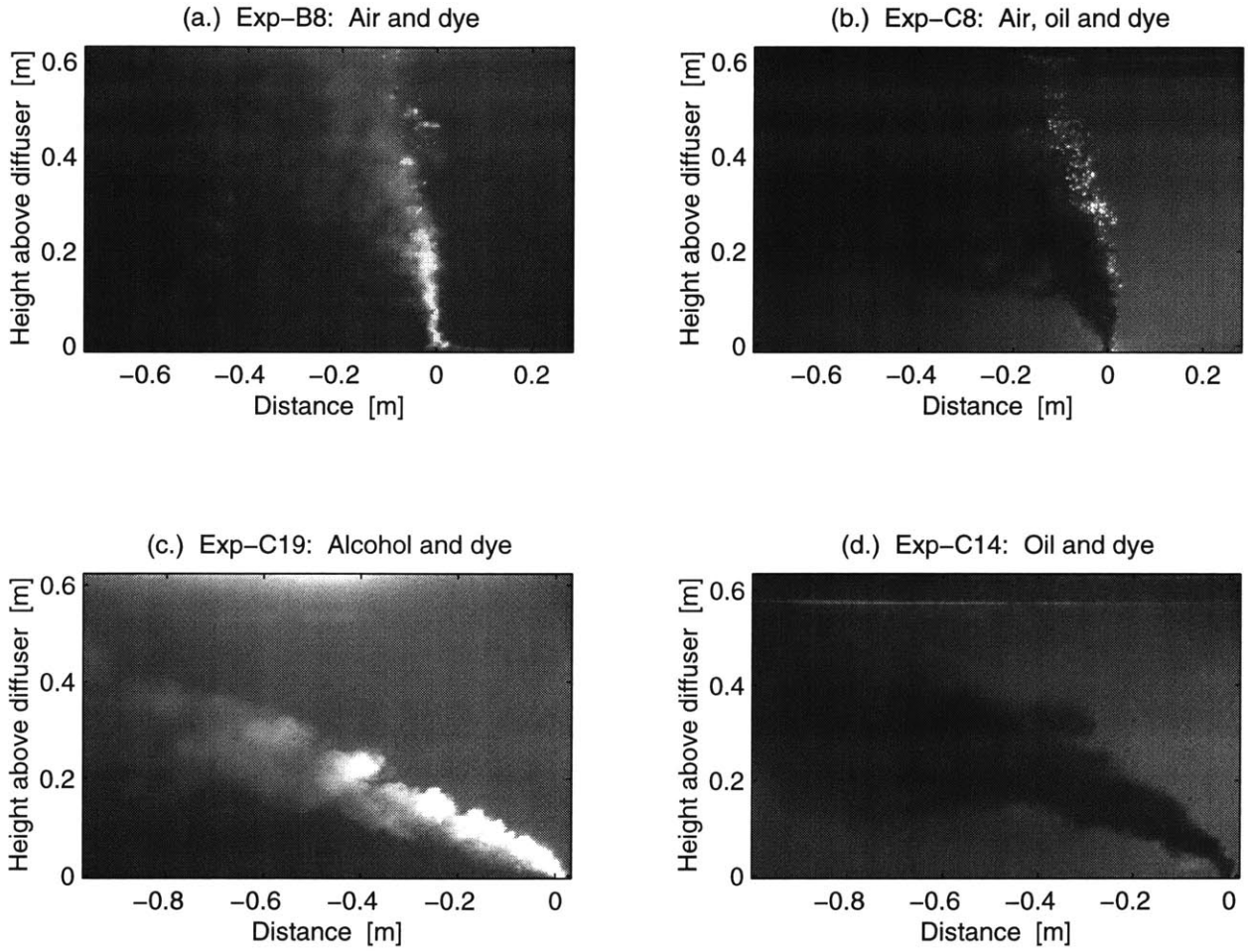

FIGURE 5-3: Experiments showing multi-phase plumes in weak crossflows. Experimental conditions are summarized in Table 5.1.

Figure 5-3 to frames (c.) and (d.), the detachment is much greater for air bubble plumes than for the oil or alcohol plumes, even though the crossflow velocity was greater for the oil and alcohol plumes. This is explained by the fact that bubbles with higher slip velocities advect much faster than their accompanying entrained fluid (Leitch & Baines 1989). The second form of leakage is seen by the fractionation of the bubbles and droplets in the crossflow, leaking smaller bubbles into the downstream wake. Frame (b.) in Figure 5-3 is the most striking example of fractionation, where the air bubbles lead in the front and the oil bubbles fall to the back of the plume. In this frame some of the oil is separating from the plume, but separation is not complete before the surface is reached.

5.4.2 Strong crossflows

In strong crossflows there is significant separation between the dominant dispersed phase and the entrained fluid and the separated fluid rises independently in the far field. Figure 5-4 shows four representative experiments in strong crossflows. Frames (a.) and (b.) in Figure 5-4 are for two-phase air-bubble plumes and frames (c.) and (d.) are multi-phase alcohol and air and oil and air plumes, respectively.

For the air-bubble plumes, complete separation occurs between the entrained fluid and the rising bubble column. Dye injected near the release point separates from the bubble column, but continues to rise in the far field even though the dye and entrained fluid are neutrally buoyant. The continued rise is ascribed to acceleration within the bubble column and indicates that, beyond the point of separation, the injected dye tracer behaves like a momentum jet. Detachment is also observed throughout the mixed and separated plume regions. Above the separation height, the trajectory of the bubble column appears linear, represented by the vector sum of the group rise velocity of the bubbles and the crossflow velocity. This further indicates that the bubble column in a strong crossflow is not plume-like above the separation height since the downstream coordinate of a pure plume should vary as the 4/3-power of height above the diffuser (Fischer et al. 1979).

For the multi-phase plumes in frames (c.) and (d.), complete separation occurs between the air bubbles and the other dispersed phase, but further separation is not observed between

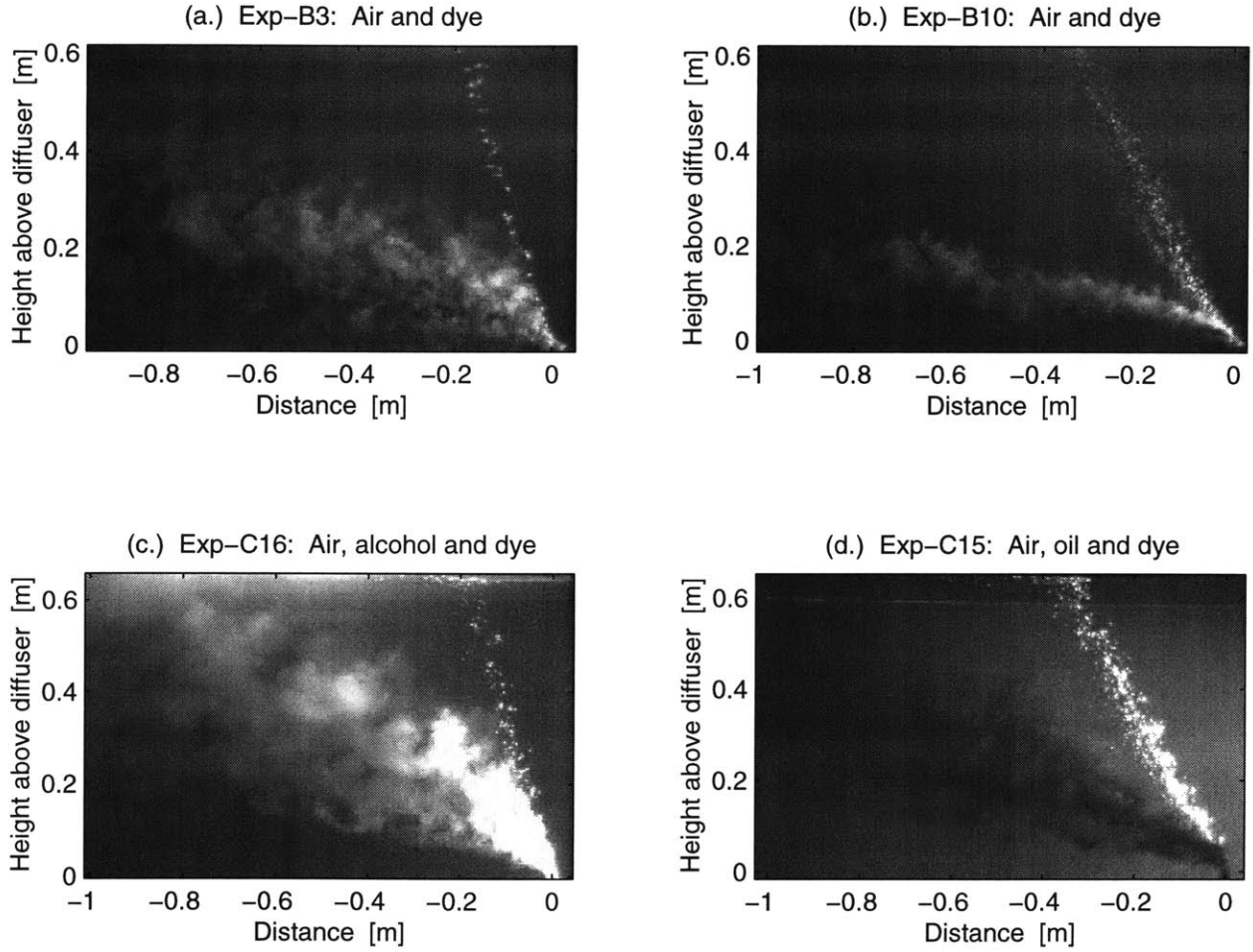

FIGURE 5-4: Experiments showing multi-phase plumes in strong crossflows. Experimental conditions are summarized in Table 5.1.

the separated oil and alcohol plumes and their entrained fluid. Following the description above, the separated oil and alcohol plumes are accelerated in the plume region before they separate; thus, they should be represented as buoyant momentum jets in the far field. Fractionation and leakage remain as characteristic features of these plumes.

5.5 Critical separation height

Images digitized for all the experiments in Table 5.1 were analyzed to determine the height at which separation occurs. As evidenced in Figure 5-3 and 5-4, an exact separation height is difficult to define. To resolve this ambiguity, the following method was used. First, an estimated centerline of the separated plume was followed backwards from the far field until it intersected the centerline of the bubble column. This point was considered not to have separated (i.e. to be still mixed) and is given by $h_S|_{min}$ in Table 5.1. Second, the centerline of the bubble column was followed from $h_S|_{min}$ upward until a point was found in clear water, free from the dye that marked the separating plume. This second point was considered separated and is given by $h_S|_{max}$ in Table 5.1. For plumes that did not separate, the column for $h_S|_{max}$ is left blank.

The relationship in (5.2) is used to find the actual separation height, h_S, from the mixed and separated points in the table. Figure 5-5 plots the mixed and separated data points in the non-dimensional space defined by $u_s/(B/z)^{1/3}$ and $u_\infty/(B/z)^{1/3}$. The dashed line in the figure is a least-squares regression of (5.2) to the boundary between the mixed and separated points in the form $f(x) = ax^b$, yielding

$$\frac{u_\infty}{(B/h_S)^{1/3}} = 6.3\left[\frac{u_s}{(B/h_S)^{1/3}}\right]^{-2.4}. \tag{5.5}$$

Thus, solving (5.5) for h_S gives the best estimate for the actual separation height in each experiment, namely,

$$h_S = \frac{5.1B}{(u_\infty u_s^{2.4})^{0.88}} \tag{5.6}$$

As a means of interpreting the physical significance of (5.5), a heuristic model is also

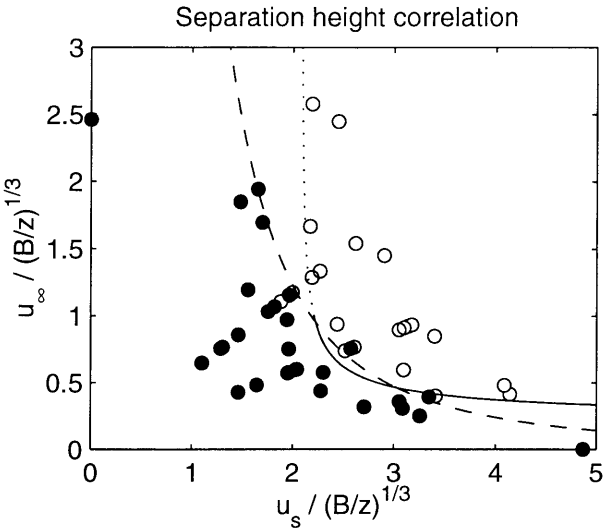

FIGURE 5-5: Transition height correlation for multi-phase plumes in a crossflow. Filled circles indicate heights below which the phases remain mixed; open circles indicate heights above which one or more phases have separated. The dashed line plots the relationship in (5.5) and the dotted line plots the relationship in (5.10).

applied to the data. If we assume the bubble trajectory is given by the vector sum of the slip velocity and the crossflow, then the centerline of the bubble column is described by

$$x_b(z) = \frac{U_a}{U_b} z \tag{5.7}$$

where $U_a = u_\infty/(B/z)^{1/3}$ and $U_b = u_s/(B/z)^{1/3}$. Similarly, taking the upward plume velocity for a single-phase plume as $u_p = C_1(B/z)^{1/3}$ and integrating with the crossflow, the trajectory of a single-phase plume is

$$x_p(z) = \frac{3U_a}{4C_1} z, \tag{5.8}$$

where C_1 in stagnant conditions is given in Morton et al. (1956) as 4.7. Note that the trajectory, x_p, goes as $z^{4/3}$ since U_a is a function of $z^{1/3}$. The first point of interest is where the two trajectories intersect. Equating (5.7) and (5.8) gives

$$U_b = \frac{4C_1}{3}. \tag{5.9}$$

This is the point where the tendency of the bubbles to leave the plume is balanced by the

deflection of the entrained fluid by the crossflow. Separation actually occurs above this point. Since separation is observed in Figure 5-5 for U_b as small as 2.0, (5.9) gives $C_1 \leq 1.5$.

To find the separation height, we seek a point where the bubble centerline intersects with the edge of the entrained fluid. Take the width of the plume as $b = C_2 \alpha z$, where for a stagnant ambient $\alpha = 0.083$ and $C_2 = 1.2$ (Morton et al. 1956). Allowing the plume width to bend over with the plume centerline and accounting for geometric effects leads to the separation criteria given by

$$U_b \left(\frac{3U_a}{4C_1} - \frac{C_1 C_2 \alpha}{\sqrt{C_1^2 + U_a^2}} \right) = U_a \left(1 + \frac{U_a}{\sqrt{C_1^2 + U_a^2}} \right) \tag{5.10}$$

which applies for $U_b > 4C_1/3$. Taking $\alpha = 0.083$ and fitting (5.10) to the data gives $C_1 = 0.78$ and $C_2 = 3.0$. The solid and dotted curve in Figure 5-5 plots (5.10). The solid curve is for the buoyancy-dominated near-field ($u_\infty/(B/z)^{1/3} \leq 1$) where we expect (5.10) to apply, and the dotted curve is an extrapolation of (5.10) into the crossflow-dominated region where the plume behaves more like a thermal.

This heuristic model provides useful physical insight. First, the calibrated values of C_1 and C_2, being respectively smaller and larger than values for stangnant conditions, are consistent with effects caused by forced entrainment. Second, because the heuristic model predicts a separation consistent with the data, a possible separation mechanism is identified: the entrained fluid is accelerated by the buoyancy of the bubble column, but the bubble column does not follow the $\frac{4}{3}$-power-law trajectory of the continuous phase; thus, the phases separate. Comparing results for (5.5) and (5.10) in the buoyancy dominated region, the heuristic model validates the curve given by the empirical model, which increases our confidence in (5.5). Because (5.10) has to be fit empirically and does not strictly apply above $U_a = 1$, we use (5.5) as the separation criteria in the remainder of this paper.

5.6 Modeling algorithm

The relationship in (5.5) provides a link to simulate both the mixed and separated plumes in a crossflow. To illustrate this algorithm, CORMIX Ver. 3.2, described by Doneker & Jirka

(1990), was selected as a representative single-phase model. CORMIX classifies flows based on a scaling analysis and then simulates the plume as a single-phase buoyant momentum jet in a crossflow using appropriate equations and coefficients.

The proposed method for modeling multi-phase plume separation requires simulating the plume in two stages. In the first stage, the plumes is affected by a weak crossflow and no separation occurs. As seen in Figure 5-3, the on-set of fractionation and leakage are observed, but, as suggested by Davidson & Pun (1999) for single-phase jets, these effects are not expected to alter the plume dynamics. In the first stage the plume is driven by the buoyancy supplied by all the dispersed phases. The second stage begins at the separation height given by (5.5) defined for the slip velocity of the separating phase. There, the buoyancy from the separating dispersed phase is removed from the simulation (along with negligible momentum and volume flux) and the remaining fluid continues to rise in the far field due to the momentum it carries from the mixed stage below (and any excess buoyancy contained in phases yet to separate). This second-stage plume is called the separated plume because it has separated from the primary dispersed phase.

Figure 5-6 presents results for this simplified method. The dashed line simulates the plume ignoring separation; the solid and dotted line represent the modified approach. From frame (a.), which is in a weak crossflow, both approaches appear valid. Hence, the plume below the separation point behaves like a mixed single-phase plume. For frames (b.) through (d.) in strong crossflows, the model that ignores separation does not follow either phase beyond the separation height. The linear trajectory given by the slip velocity matches the bubble trajectory above the separation point, and the second-stage CORMIX prediction, which is initialized with the momentum and buoyancy of the separated plume, follows the trajectory of the separated plume. These results verify that a single-phase model can be reasonably applied to these plumes using (5.5) and simulating the plumes in two stages, a mixed stage and a separated stage.

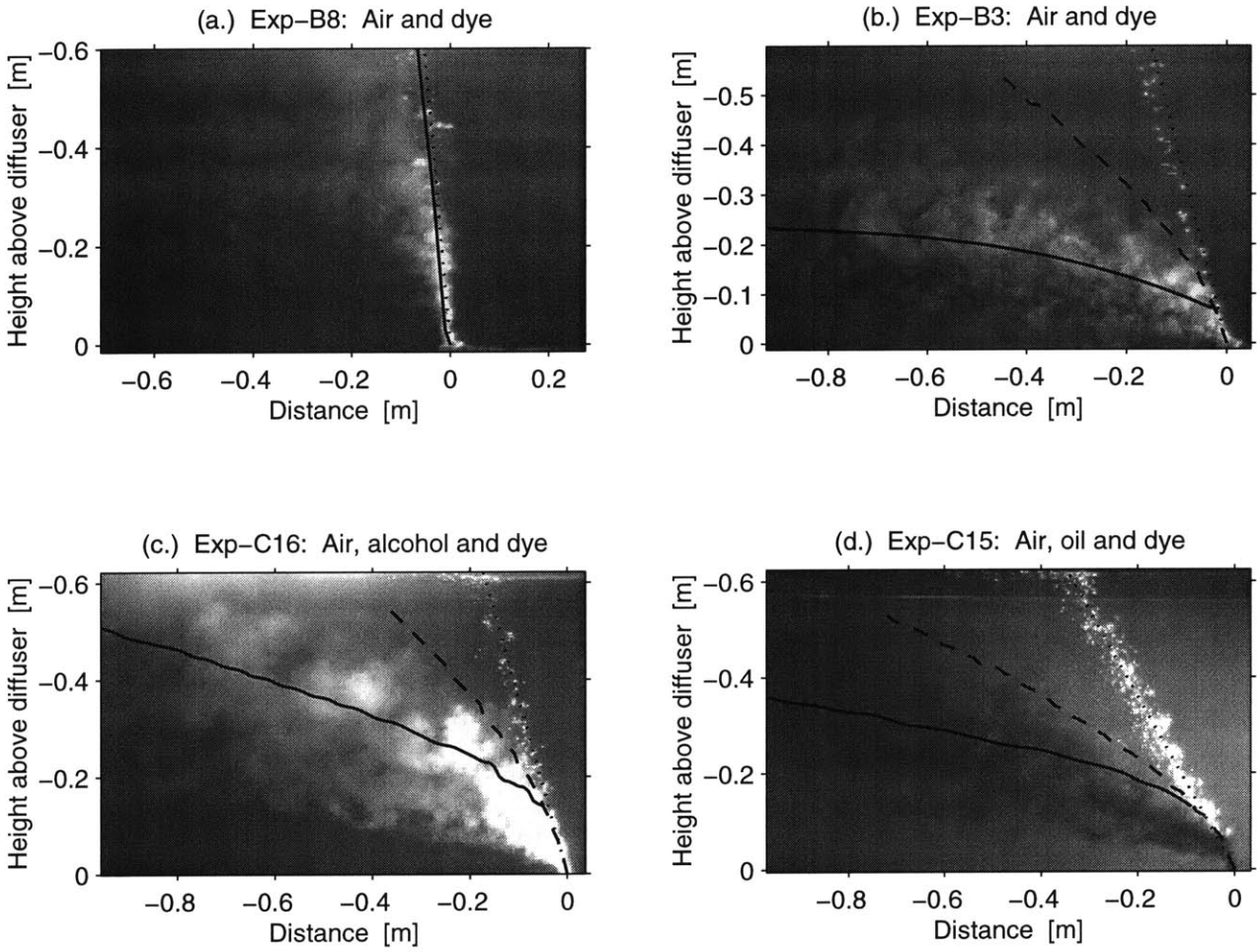

FIGURE 5-6: Model results for multi-phase plumes in a crossflow. The solid and dashed lines plot the centerline predictions for the separating phase using the modified and single-phase approaches, respectively. The dotted line shows the modeled bubble rise trajectory in a crossflow.

Exp-ID	Flow Rate Air [mL/min]	Buoyancy Frequency [s^{-1}]	u_∞ [cm/s]	u_s [cm/s]	h_T [cm]	h_S [cm]	h_{obs} [cm]
S1	100	0.5	0	7.2	$\mathcal{O}(10)$	∞	22
S2	100	0.5	2	7.2	$\mathcal{O}(10)$	$\mathcal{O}(100)$	20
S3	100	0.5	5	7.2	$\mathcal{O}(10)$	$\mathcal{O}(10)$	20
S4	100	0.5	10	7.2	$\mathcal{O}(10)$	$\mathcal{O}(1)$	3

TABLE 5.2: Experimental conditions for crossflow experiments in stratification, where h_{obs} is the observed separation height. The symbol $\mathcal{O}()$ is used for "order of".

5.7 Effects of stratification

Four exploratory experiments were conducted in a stratified crossflow. The laboratory flume described previously was stratified using the two tank method (Asaeda & Imberger 1993) in a 3 m long test section between two bulkheads. The rest of the flume was filled with fresh water to equalize the pressure across the bulkheads. Because of leakage around the bulkheads, the stratification was not exactly linear and the profiles changed slightly between experiments. Table 5.2 lists the conditions for the experiments. Experiment S1, without crossflow, behaved as expected and intruded at the appropriate height based on (5.4). S1 was repeated after experiment S4 to verify that the four experiments were in a comparable stratification.

Figure 5-7 shows the results for experiments S1 and S2. Because the intrusion depth, h_T, due to stratification is less than the separation height for the crossflow, h_S, the plumes are considered stratification dominated. Experiment S2 showed that in this case separation does occur at the height predicted for a stagnant ambient with stratification, but pointed out two important differences with the crossflow. One difference is that the peeling takes place asymmetrically in the crossflow, intruding in the wake of the plume, rather than symmetrically, forming an annular ring surrounding the plume, as in the stagnant case. The other difference is that there is significant leakage in the crossflow below the intrusion layer, whereas, there is no leakage in the stagnant case. The leakage may be due to the following mechanism. Because the entrained fluid is dense relative to the ambient, and because the

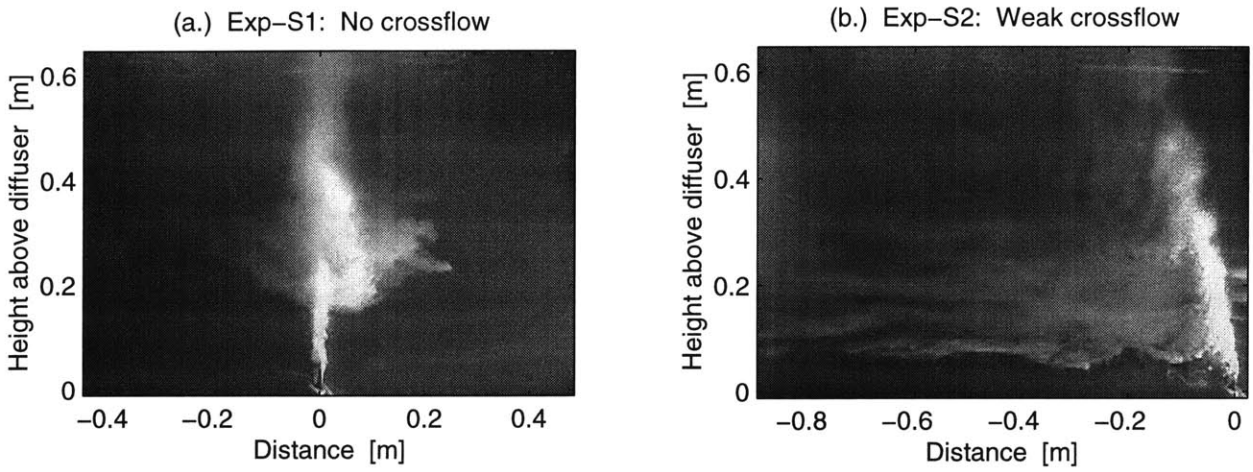

FIGURE 5-7: Air bubble plume in stratification and crossflow. Experimental conditions are summarized in Table 5.2.

bubbles stay in a core area which is narrower than the full width of the plume, the outer edges of a multi-phase plume in stratification are negatively buoyant. Without a crossflow, the drag and entrainment from the inner core slowly lift these outer edges. In the presence of the crossflow, however, those dense outer edges are more easily pulled away and advected downstream.

Experiments S3 and S4 had separation heights due to crossflow that were equal to or less than the separation height due to stratification; thus, these experiments were crossflow dominated. Separation occurred at the heights predicted by (5.5) and formed a separated plume in the far field. The separated plume, however, did not rise as in the unstratified case. This is due to trapping by the ambient stratification. Although the separated plumes still have excess momentum, they also contain dense water (negative buoyancy) entrained from the mixed stage of the plume. As a result, the separated plumes tend to oscillate in the wake around the level of separation.

To include stratification effects, the general model algorithm presented above must be modified to use an appropriate separation height based on a comparison of crossflow and stratification strengths. For the crossflow-dominated plumes, the model applies unchanged, assuming that the single-phase model used to predict the trajectories considers the entrainment and buoyancy conservation of the stratified fluid. For stratification-dominated plumes,

Scenario Number	Spill Size	*In situ* flow rate			Slip velocities		
		Oil [m^3/s]	Gas [m^3/s]	Hydrate [m^3/s]	Oil [cm/s]	Gas [cm/s]	Hydrate [cm/s]
1	Leak	0.001	0	0	10	30	10
2	Small	0.001	0.001	0	18	30	10
2h	Small	0.001	0	0.001	18	30	10
3	Medium	0.01	0.01	0	10-18	40	10
3h	Medium	0.01	0	0.01	10-18	40	10
4	Large	0.1	0.1	0	7-18	40	10
4h	Large	0.1	0	0.1	7-18	40	10

TABLE 5.3: Field-scale parameter ranges for oil well blowouts. Slip velocities were estimated from Rygg & Emilsen (1998), Rye et al. (1998), and Clift et al. (1978).

the separation height should be predicted by (5.4). In this case, the separated plume in an intrusion layer is formed by the build-up of neutrally buoyant fluid, the intrusion flow is horizontal, and a separated plume model is not required to predict the trajectory.

5.8 Application to the field scale

The results are applied in this section to the field scale using the relationships for h_S and h_T presented above. Typical physical characteristics of oil well blowouts are summarized in Table 5.3. Flow rates were taken to match assumed spill sizes; slip velocities were estimated by applying relationships in Rye et al. (1998) and Clift et al. (1978) to exit conditions summarized in Rygg & Emilsen (1998). Although thermodynamic conditions at 1000 m depth are favorable for the formation of clathrate gas hydrates (a reaction of gas and water forming a crystaline lattice), it remains an open question whether other formation criteria would be met (e.g. kinetics and presence of nucleation surfaces); hence, we make predictions assuming both extremes of pure gas and pure hydrate plumes.

To predict the behavior of the plumes described in Table 5.3 ambient conditions and physical variables need to be defined. The stratification will be assumed typical of the Gulf of Mexico with $N = 0.002$ s^{-1}. Typical crossflow velocities are taken as 15 cm/s. The densities of the oil and the gas hydrate are each taken as 0.9 g/cm^3; density of pure gas is

Scenario	Net B [m^4/s^3]	Net u_s [cm/s]	$u_s/(BN)^{1/4}$	h_S [m]	h_T [m]	Critical u_∞ [cm/s]
1	0.001	10	2.5	4	38	2
2	0.01	29	4.3	5	44	2
2h	0.02	14	3.0	4	41	2
3	0.1	37	3.1	28	101	5
3h	0.03	10-14	1.2-1.7	43-81	94-104	9-14
4	1.0	37	1.7	280	235	21
4h	0.2	9-14	0.6-0.9	430-1100	197-216	37-84

TABLE 5.4: Field-scale plume behavior for oil well blowouts.

calculated using the Ideal Gas Law.

Table 5.4 presents several calculations that predict the behavior of these blowout plumes under the assumed conditions. Net values for B and u_s are calculated for the mixture of oil and gas or gas hydrate. h_S is computed for the typical crossflow velocity (15 cm/s). The critical u_∞ gives the crossflow velocity necessary to cause crossflow-dominated separation before stratification dominance would take effect.

Several observations can be made from the calculations in Table 5.4. First, the trap height increases with the size of the spill. Second, comparing values for h_T and h_S, leaks and small to medium blowouts are typically current dominated, and large blowouts are typically crossflow dominated. Third, critical crossflow velocities are such that for medium and large blowouts, plume behavior is expected to range from stratification dominated to crossflow dominated as the tidal flows change from slack to flowing tidal ranges. Hence, understanding the process of crossflow separation is important for predicting the fate of oil in the majority of blowout scenarios.

5.9 Conclusions

This paper presented laboratory experiments of multi-phase plumes in uniform and stratified crossflow that identify two mechanisms for separation between the dispersed phases and the entrained fluid. First, crossflows cause separation when their horizontal motion over-

comes the restoring force of entrainment and advects the entrained fluid away from the rising dispersed phases. Second, stratification causes separation when the entrained fluid becomes too dense to be carried by the dispersed phase and it intrudes horizontally into the ambient.

By analyzing the experiments in uniform crossflows, multi-phase plumes were shown to have a mixed zone that behaves like a single-phase plume followed by a separated region above a critical separation height, h_S, where the phases must be analyzed separately. A dimensional analysis identified two non-dimensional velocities (the non-dimensional crossflow and bubble slip velocities) which combine to form a correlation equation for predicting h_S.

Further experiments in stratified crossflows confirmed the assumption that plumes could be classified as either crossflow or stratification dominated. Crossflow-dominated plumes occur for $h_S \ll h_T$ and can be analyzed in the near field by neglecting the stratification. Stratification-dominated plumes occur for $h_S \gg h_T$ and can be analyzed in the near field by neglecting the crossflow but recognizing that the intrusions will form asymmetrically in the downstream direction.

The modeling algorithm developed to predict the fate of the separated fluid above the separation height allows single-phase models to be applied to multi-phase plumes in crossflow. Since the modeling algorithm correlates well with our experimental observations, the separated plume can be thought of as a buoyant momentum jet, where the initial buoyancy and momentum are provided by the entrainment and acceleration of the mixed phase below the separation height.

Chapter 6

Issues for further research

6.1 Laboratory studies

Several additional laboratory studies could be conducted to continue research on multiphase plumes for application to CO_2 sequestration and to oil well blowouts. Since the apparatus and analysis techniques applied in this thesis have been thoroughly investigated, further insights would require modest to extensive changes to the apparatus or new development of the analysis techniques. Hence, the following paragraphs describe new experiments that could be conducted and some of the issues complicating further measurements.

6.1.1 Stagnant stratification

The experiments in stagnant stratification could first be extended to study the second and higher-order peels. Because Type 3 peels have significant overlapping intrusions and nearly continuous detrainment in their upper regions, the analysis would be limited to Type 1* and 2 peels unless significant changes were made to the flow estimation technique.

Two experimental difficulties for the Type 1* and 2 plumes would also need to be addressed. First, because these plumes have efficient peels, dye would have to be introduced into the inner core somewhere above the first peel and below the second intrusion level. To do this would require several experimental repetitions or a dynamic means of positioning the dye outlet during the experiment and before dye is released. The oscillating elevation of

the peeling region could cause some problems by engulfing some of the dye and carrying it down to the first intrusion. The second difficulty comes in getting a sufficient signal in the salinity profiles to make net flux measurements. From the experiments already conducted we observed that the net pumping flux of the first peel is greater than for the upper-level peels. To get a sufficient signal in the salinity profiles may require running the experiment two to three times longer. Doing so introduces two more problems. First, the initial peel would reach the edges of the tank, begin to back-up on the inner core and start to rise, thereby, compromising a steady-state assumption for the duration of the experiment. Second, motions set up by the peeling and intruding flows initiate internal waves. In the experiments conducted for this thesis, the waves were a limiting factor on the allowable duration of an experiment. As the experiments run longer, the waves grow in amplitude and have even been observed to break, causing a catastrophic change to the appearance of the plume before wave breaking. These problems can likely be solved; however, they were beyond the scope of this thesis.

A simpler study of the upper-level peels could investigate whether Type 2 plumes transition to Type 3 behavior in their upper peels. This study would require a different degree of stratification and a different dispersed phase slip velocity than investigated in this thesis. Here, Type 2 plumes were created having two or three subsurface peels. To get more peels, the plumes tended toward Type 1* or Type 3 for my set of slip velocities, buoyancy fluxes, and stratification. Since the Type prediction using U_N is now verified, it should be possible to find an experimental design that would achieve the desired form of Type 2 plume. Then, by running the experiments and visualizing the plume (dye may need to be injected at multiple levels), the plume behavior could be observed and analyzed.

A third investigation of the upper-level peeling behavior could be made for CO_2 plumes in our laboratory tank at atmospheric pressures. By injecting ultra-pure CO_2 bubbles, our preliminary investigations show that the CO_2 will fully dissolve before reaching the surface for CO_2 flow rates comparable to the air flow rates used in the other experiments presented in this thesis. It could then be observed whether the plume type changed in response to the changes in bubble slip velocity as the bubbles dissolved. Two complications would have to be addressed. The first addresses the bubble dynamics. The bubble slip velocities would

have to be determinable (perhaps through application of a numerical model that tracked the dissolution of the bubbles with height), and the slip velocity would have to be fairly stable over the length scale l_C so that each peel would be representative of the behavior for a particular bubble size. The second complication addresses dissolution chemistry. The CO_2 flow rates would have to be small enough that the density effect of CO_2 enrichment of the entrained fluid was negligible; otherwise, the type characteristics observed may change in response to CO_2 enrichment and not in response to changes in the bubble size. Application of the model by Crounse (2000) to these experiments may help distinguish between these two competing effects.

A final laboratory study for stagnant-stratified multi-phase plumes would be to make particle imaging velocimetry (PIV) measurements of the counterflowing inner and outer plumes. To accurately match the index of refraction through the tank so that images may be analyzed quantitatively would require using a smaller facility. The scale of typical Nd:YAG LASERs used for PIV measurements would also necessitate a smaller investigation region. From the experience of Asaeda & Imberger (1993) and others, this should not prose a substantial problem. Another difficulty would be to find an appropriate tracer particle since the notion of a neutrally buoyant particle would not be appropriate for tracking a patch of fluid in stratification as it undergoes mixing. Colloidal particles with very small settling velocities could probably be used. Once the counterflowing region could be visualized with PIV, however, the mechanisms for entrainment between the plumes could be investigated and an appropriate entrainment model could be developed. Without such measurements, entrainment models can only be calibrated to the measurements presented in Chapters 3 and 4.

6.1.2 Crossflows

First, an extension of the experiments in a uniform ambient could be done, testing the behavior of separation for ambient fluid entrained at elevations above the initial separation height. For predicting the distribution of oil in the water column from a well blowout, the separation criteria given in Chapter 5 apply. But, because the bubbles are spreading

and fractionating in the crossflow, fluid entrained at an arbitrary height in the plume may separate at a different location downstream from that predicted by (5.5). This information would be useful for predicting the dilution for a CO_2 plume in a crossflow.

Another extension could utilize a recirculation current to test the effects of ambient turbulence. Because the instantaneous eddie velocities are much greater in a turbulent crossflow than for the towed plumes investigated in this thesis, separation may be affected; thus, the separation criteria presented in Chapter 5 should be extended to reflect these differences.

Finally, stratified crossflow plumes should be studied to identify the mechanism causing enhanced detachment of entrained fluid in stratification and to investigate the conditions where both stratification and crossflow separation are predicted to occur at the same elevation.

6.2 Field studies

Several of the extensions identified in the previous section could more easily be studied in the field where there would be no edge effects and where the depth is virtually unlimited. Obvious limitations in the field, however, include non-uniform ambient currents and the difficulty and expense of making measurements in deep water.

There may be a field experiment of an air-bubble plume conducted in Japan in late 2000 or early 2001 to test a remotely operated vehicle (ROV) that will be used in the upcoming international CO_2 field experiment. One open question for designing an air-bubble experiment that should serve as a prototype for a CO_2 or oil well blowout plume is whether to design the experiment to match specific parameters of the full-scale plume or whether it is sufficient to match the governing non-dimensional variables. For the base-case CO_2 plume anticipated for the international field experiment the buoyancy flux is $9 \cdot 10^{-4}$ m^4/s^3, u_s is 9.3 cm/s, and U_N would be 2.3 for conditions off the coast of the Big Island of Hawai'i. Ironically, using the limewood diffuser at the same depth and location with a flow rate of 0.35 Std L/min (in the same rage as the experiments conducted in the laboratory for this thesis) produces a plume having a U_N of 2.0. The slip velocity of the bubbles would be 4.0 cm/s if we assume

that the bubble size would be the same as is created in the lab at atmospheric pressure (an untenable assumption, at best, but something that could be investigated in a high-pressure tank prior to a field deployment). The resulting air-bubble plume would not have the same chemistry effects as in the full CO_2 plume, but would provide a benchmark for assessing the expected behavior and needed measurement suite, especially in the initial stages of the plume formation.

6.3 Numerical modeling

Finally, the results presented in this thesis should be rigorously applied to calibration of the integral plume model developed by Crounse (2000). The easiest step would be to first calibrate his detrainment algorithm, incorporating the entrainment coefficients predicted by Milgram (1983) and the turbulent bubble Froude number given in Chapter 3. Next, to apply the model to Type 3 plumes, the model must be extended to allow several overlapping intrusion layers to form at each level (i.e. extend the double-plume model to a multi-adaptive plume model). This is necessary since we have observed in the laboratory that overlapping plumes do not immediately mix even when they form an unstable stratification profile. They are instead stabilized by excess momentum coupled with continued mixing with the stratified ambient fluid. The final step in model calibration would be to match the flow measurements and trends with U_N presented in Chapter 4. Crounse (2000) began this process by calibrating to one experiment for the full suite of flux measurements and showed a promising trend in the model for Q_i that had the same variation with U_N as presented in Chapter 4. By completing the calibration, the model could be applied to the field-scale and for chemistry effects not included in the laboratory with greater confidence.

Appendix A

Methods

This appendix presents the methods used for the stagnant, stratified, and crossflow experiments. Sections A.1 and A.2 describe the apparatus and discuss the limitations in the equipment. Section A.3 presents a detailed error analysis applied for the experimental results.

A.1 Stagnant experiments

The experiments were conducted in the Parsons Laboratory at MIT using the new tank depicted in Figure A-1 and a variety of ancillary components. Housed on the first floor of the main lab, the apparatus consists of the following components:

- A 1.22 m square by 2.44 m tall glass-walled experimental tank.
- Diffusers and pumps for buoyancy sources, including air, a range of oils, and a range of sediments and glass beads.
- Tanks and piping for the two-tank stratification method, capable of producing step- and linearly-stratified ambient conditions.
- A micro-density profiler consisting of a conductivity and temperature (CT) probe mounted on a belt-driven linear positioner.

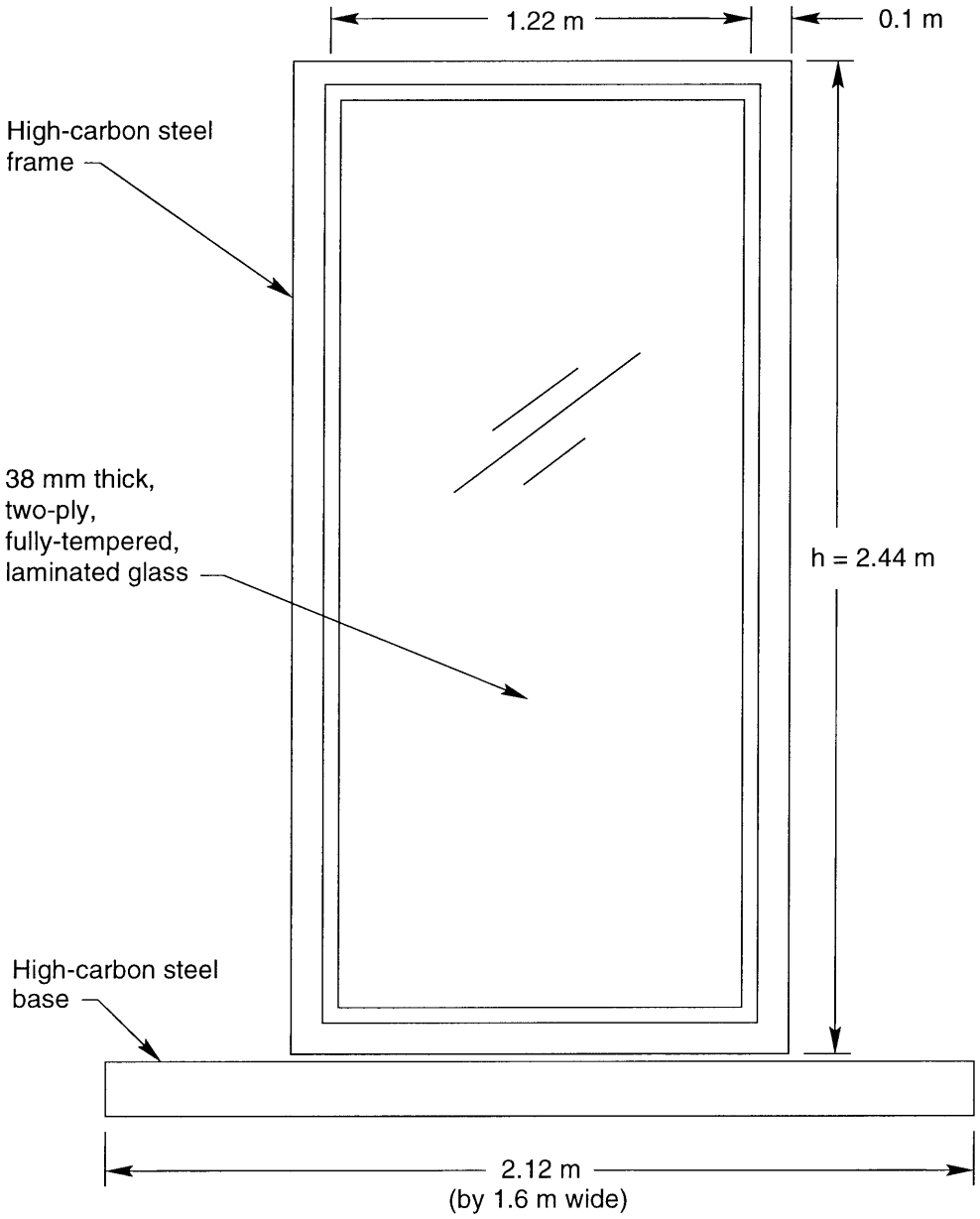

FIGURE A-1: Elevation view of the stagnant experimental tank.

- A full range of visualization hardware, including injected dye tracer, a LASER light sheet, a shadowgraph light, and a CCD camera connected to a computer frame grabber.
- A fluorescence profiler for measuring dye concentrations consisting of an in-situ fluorometer mounted to a conductivity, temperature and depth (CTD) profiler.

The following sections describe each of these components in detail.

A.1.1 Experimental tank

The most fundamental component of the apparatus is the experimental tank, shown in elevation view in Figure A-1. It is constructed of two-ply, fully-tempered laminated glass. Each of the glass plies is 19 mm thick and is joined to the other by a 6 mm thick clear layer of poly vinyl butyral. The glass wall dimensions were selected from the design standard *ATS 132 Glass for Aquariums* by the Libbey–Owens–Ford Co. (1990), and the tank was built on-site by Excalibur Glassworks, Inc. of Woburn, Massachusetts in June, 1997.

The height of the tank was selected to balance an economical design with the need to have at least two discrete, Type 2 peels for a modest bubble flowrate and stratification. At the time the tank was designed, relationships for peeling characteristics from Asaeda & Imberger (1993) and from Reingold (1994) were the only ones available. Asaeda & Imberger correlated the number of sub-surface peels, n, to the non-dimensional parameter P_N in the equation

$$n = \text{int}\left(0.22 P_N^{1/4}\right) \tag{A.1}$$

where the int-function always rounds down to the nearest integer. Because stock glass comes in 1.2 m by 2.4 m sheets, it was desirable to use those dimensions for the tank. Selecting a gas flow rate of 2 Std L/min and a salinity difference of 35 ppt from the top to the bottom of the tank, $P_N = 6580$. Plugging into Equation A.1 gives $n = 2$ sub-surface peels, satisfying the first requirement. Similarly, Reingold (1994) gives a predicted intrusion depth for the first peel of 0.77 m, well below the half depth of 1.2 m. The second criteria was to have Type 2 plume behavior. Asaeda & Imberger (1993) correlated plume Type with P_N and M_H. For the above conditions, $M_H = 0.59$, which plots in the Type 2 regime of Asaeda &

Imberger's (1993) Figure 4. Thus, a tank depth of 2.4 m was accepted. Based on experiments presented in Chapters 3 and 4, the tank proved to be adequately dimensioned, and a full range of plume types can be studied using a variety of stratification strengths and buoyancy sources and flow rates.

A.1.2 Buoyancy sources

In order to investigate a wide range of plume behavior, a variety of buoyancy sources and diffusers were used. Air bubbles are the most common dispersed phase reported in the literature; therefore, air diffusers form the baseline of these experiments. Because bubble size (and, therefore, slip velocity) is very difficult to control using air, commercially available glass beads were also used. Reingold (1994) was the first to suggest modeling bubbles using particles, and her approach is verified and extended by these experiments. Finally, because of its similarity to liquid CO_2 and because of the interest in underwater oil spills, two oils are also tested.

Air bubbles

Air is supplied in the Parsons Laboratory from a basement tap into the building pressurized air supply and is turned on and off by a ball valve. Downstream of the ball valve is an air filter to remove particles and moisture droplets, followed by a pressure control valve. The pressure control valve is the PRG 501-60 air pressure regulation gauge, supplied by Omega Engineering, Inc. of Stamford, Connecticut. The gauge measures from 0 to 415 KPa (0 to 60 psi) and maintains a constant pressure regardless of downstream adjustments. The flow rate is measured by one of two air mass-flow meters (models E-32648-18 (0 to 10 Std L/min) and E-32648-12 (0 to 1 Std L/min) from Cole Parmer Instrument Company of Vernon Hills, Illinois). The meters are accurate to $\pm$ 0.5% of the full scale and operate on a heat transport principle. The two meters are mounted in parallel and the applicable meter is selected using two additional ball valves. Analogue signal output from the flow meters can be routed to the computer and recorded during an experiment. It was found that the airflow reached steady-state within about 10 s of being turned on and did not drift during experiments;

therefore, real-time flow rate monitoring was not done for the experiments.

Size distributions of air bubbles are controlled by the diffuser design and the ambient salinity. Four air diffusers were investigated in order to get a wide variation in bubble slip velocity. These were a 0.7 mm diameter orifice air brush nozzle, a 2.5 mm diameter orifice straight tube, a limewood saltwater aquarium aerator (by Coral Life Company), and a standard green aquarium airstone. Both the 2.5 mm orifice and the air brush nozzle produce mainly large bubbles with a wide bubble size spectrum; hence, they were not used in the quantitative experiments. The other two diffusers produce uniform bubbles in two different size regimes: the limewood diffuser gives very fine bubbles and the green airstone creates larger bubbles. Beyersdorf (1997) documented the effect of salinity on bubble size. Due to the influence of the ionic properties of the solution, small bubbles are more stable in saline water than in fresh water. For the limewood diffuser, the effect of salinity is dramatic. For the green airstone, the dominant bubble size does not change in saltwater over freshwater, but a second, smaller-sized mode appears in the bubble size spectrum, though at a small enough fraction of the buoyancy flux not to influence plume dynamics. Thus, among the diffusers tested, two diffusers giving different bubble sizes were used in the experiments (small limewood bubbles and larger airstone bubbles).

To estimate the slip velocity of the bubbles from the limewood diffuser, a phase-Doppler particle analyzer (PDPA) housed at the University of Hawai'i Look Laboratory was used. The PDPA provides bubble size data based on backscatter of the LASER light and assuming the bubbles are spherical. The small bubbles created by the limewood diffuser pass the assumption of sphericity. From the bubble sizes, the slip velocity of bubbles were estimated from relationships in Clift et al. (1978) which are based on several non-dimensional numbers, including the Morton number, M, the Eötvös number, E_o, and the Reynolds number, R_e, defined as

$$M = \frac{g\mu^4\Delta\rho}{\rho^2\sigma^3} \tag{A.2}$$

$$E_o = \frac{g\Delta\rho d_e^2}{\sigma} \tag{A.3}$$

$$R_e = \frac{\rho d_e u_s}{\mu} \tag{A.4}$$

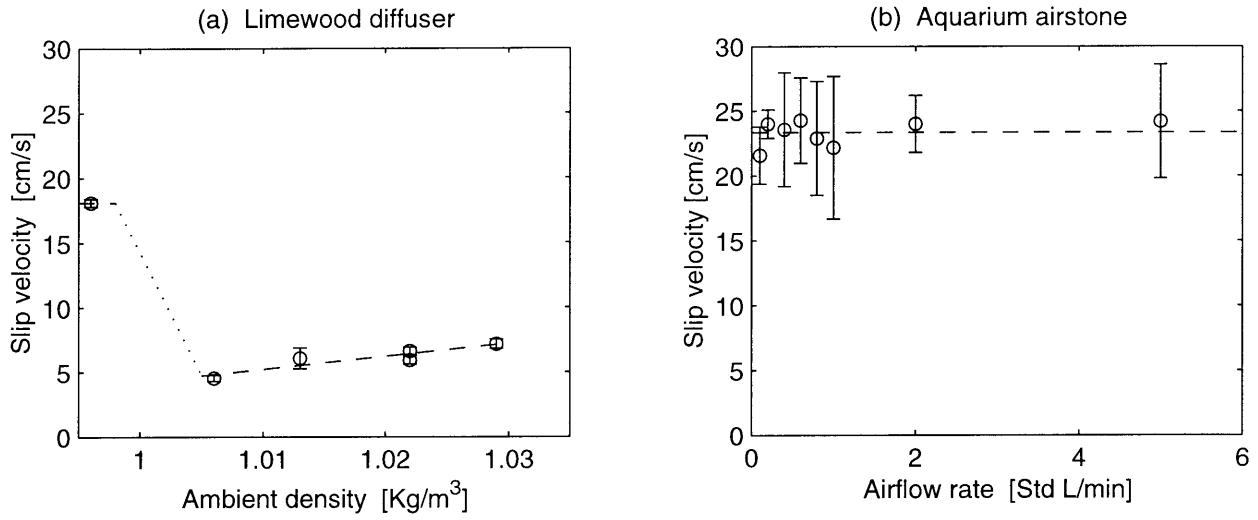

FIGURE A-2: Slip velocities computed for (a) the limewood diffuser and (b) the aquarium airstone.

where μ is the , $\Delta\rho$ is the , ρ is the , σ is the , d_e is the and u_s is the . Using these numbers, the bubble slip velocity is computed from R_e based on the algorithm:

$$H = \frac{4}{3} E_o M^{-0.149} \left(\frac{\mu}{\mu_w}\right)^{-0.14} \tag{A.5}$$

$$J = \begin{cases} 0.94H^{0.757} & \text{if } 2 < H \leq 59.3 \\ 3.42H^{0.441} & \text{if } H > 59.3 \end{cases} \tag{A.6}$$

$$R_e = M^{-0.149}(J - 0.857) \tag{A.7}$$

where μ_w is the . Based on the PDPA data, the bubble size was independent of the airflow rate and the location in the plume for airflow rates below 2 Std L/min(the highest flow measured); however the bubble size did depend on the salinity. Bubble size was measured for solutions of NaCl and of seawater taken from 40 m depth near the Look Laboratory. For simplicity, correlations are presented with density (measured using a Paar density meter) instead of salinity; Figure A-2(a) shows the results. The error bars represent $\pm$ one standard deviation of the computed slip velocity for the mean bubble size.

Bubbles generated by the standard aquarium airstone were too large to measure using the PDPA; hence, slip velocities were computed following Hugi (1993). The aquarium diffuser was mounted on the crossflow apparatus described in Section A.2 and towed at 22 cm/s.

Bead class	Slip Velocity		Bubble Size	
	Mean [cm/s]	Std. Dev. [cm/s]	Mean [μm]	Std. Dev. [μm]
Glass D	3.2	0.3	263	17.8
Glass C	4.7	0.6	386	31.0
Glass B	7.1	1.1	557	31.9
Glass A	11.1	1.2	770	50.4
Glass A-100	14.3	1.4	963	91.5
Glass A-205	20.0	0.9	1550	110

TABLE A.1: Particle characteristics for glass beads.

Assuming the bubble group effect was minimized by the high tow velocity, the slip velocity was estimated from the deflection of the bubble column toward the downstream. This method was verified for the limewood diffuser for $\rho_w = 997$. Figure A-2(b) shows the correlation for the aquarium airstone. Since the airstone did not show dependence on salinity, the slip velocities are plotted versus airflow rate. The mean value (plotted as the dashed line in the figure) is 23.3 cm/s.

Particles

As shown in Figure A-2, air bubble slip velocity is fixed for a given diffuser and ambient salinity; thus, sediment particles were used to systematically control slip velocity and study its effect over a range of flow rates. Reingold (1994) was the first to relate continuous sediment plumes to bubble plumes and found that bubbles of the same slip velocity created similar plumes to sediment particles, given that the buoyancy fluxes and stratification remained constant.

Glass beads were used in these experiments for their uniform size, shape, and fall characteristics. Table A.1 provides the physical characteristics of the glass beads used in these experiments. The size distribution was measured by Ruggaber (2000). Fifty beads in each size class were randomly selected to compute the distribution. I measured slip velocities for 15 beads in each size class by controlled settling column tests. The following empirical

relationship presented in Dietrich (1982) correlates size to slip velocity:

$$\begin{aligned}\log(W^*_{sphere}) &= -3.76715 + 1.92944\log(D^*) - 0.09815\log(D^*)^2 \\ &\quad -0.00575\log(D^*)^3 + 0.00056\log(D^*)^4 \end{aligned} \tag{A.8}$$

where the non-dimensional diameter and terminal velocity are given by

$$\begin{aligned} D^* &= \frac{(s-1)gd^3}{\nu^2} \\ W^* &= \frac{u_s^3}{(s-1)g\nu} \end{aligned}$$

where s is the specific gravity and ν is the kinematic viscosity of the ambient fluid. Figure A-3 presents the data in Table A.1 together with the empirical relationship in (A.8). Although the relationship is less reliable as the diameter decreases, it matches the measured data for the glass beads quite well. Deviations from (A.8) are probably due to non-sphericity of the glass beads (reported by the manufacturer as 80% spherical). For calculations in this thesis, the data in Table A.1 will be used instead of the empirical relationship.

The glass beads are released in one of two ways. In the first method, a sediment reservoir is attached to a standard funnel and allowed to empty by gravity. By testing the apparatus with an analytical balance, the flow rate remains constant and is independent of the reservoir depth as long as the funnel orifice is completely covered by the sediment. In the second method, sediment is released using a screw auger designed for handling powders in industrial applications. The auger was custom built by Auger Manufacturing Specialists of Frazer, Pennsylvania. A Cole Parmer MasterFlex pump (E-07595-50) is used to turn the auger during experiments. Because of the gap between the auger blades and the side channel, beads tend to jam the auger blade; hence, only sizes C and D can be released from the auger.

Oil droplets

Oil droplets provide buoyancy sources with specific gravities much closer to 1.0 (from 0.1 to 0.5). As already introduced, oil droplets are interesting because they are of similar

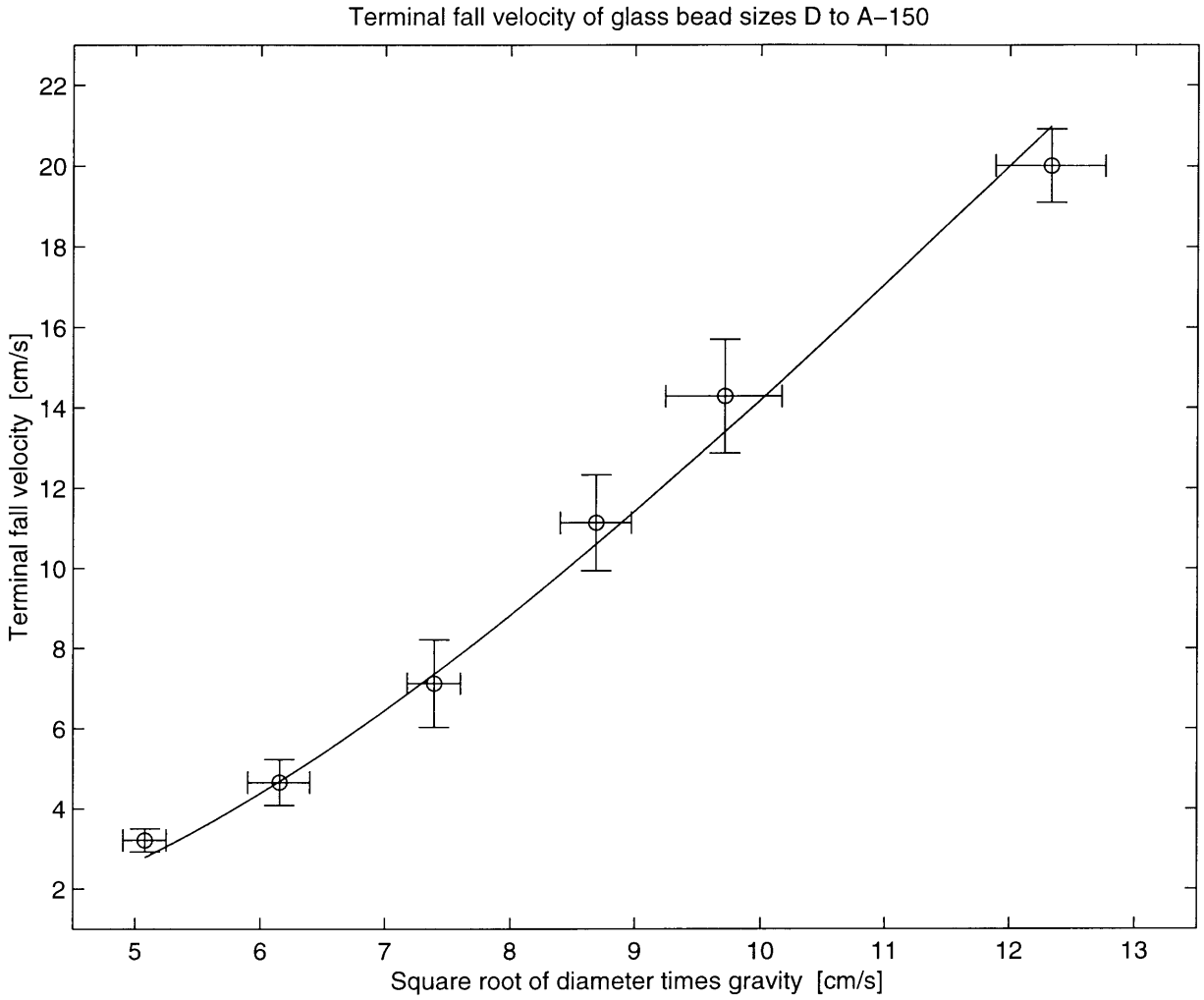

FIGURE A-3: Terminal fall velocity of glass beads for sizes D (smallest) to A-150 (largest). Vertical error bars represent plus and minus one standard deviation of measured slip velocities for a sample size of 15. Horizontal error bars represent plus and minus one standard deviation of measured bead diameter for a sample size of 50.

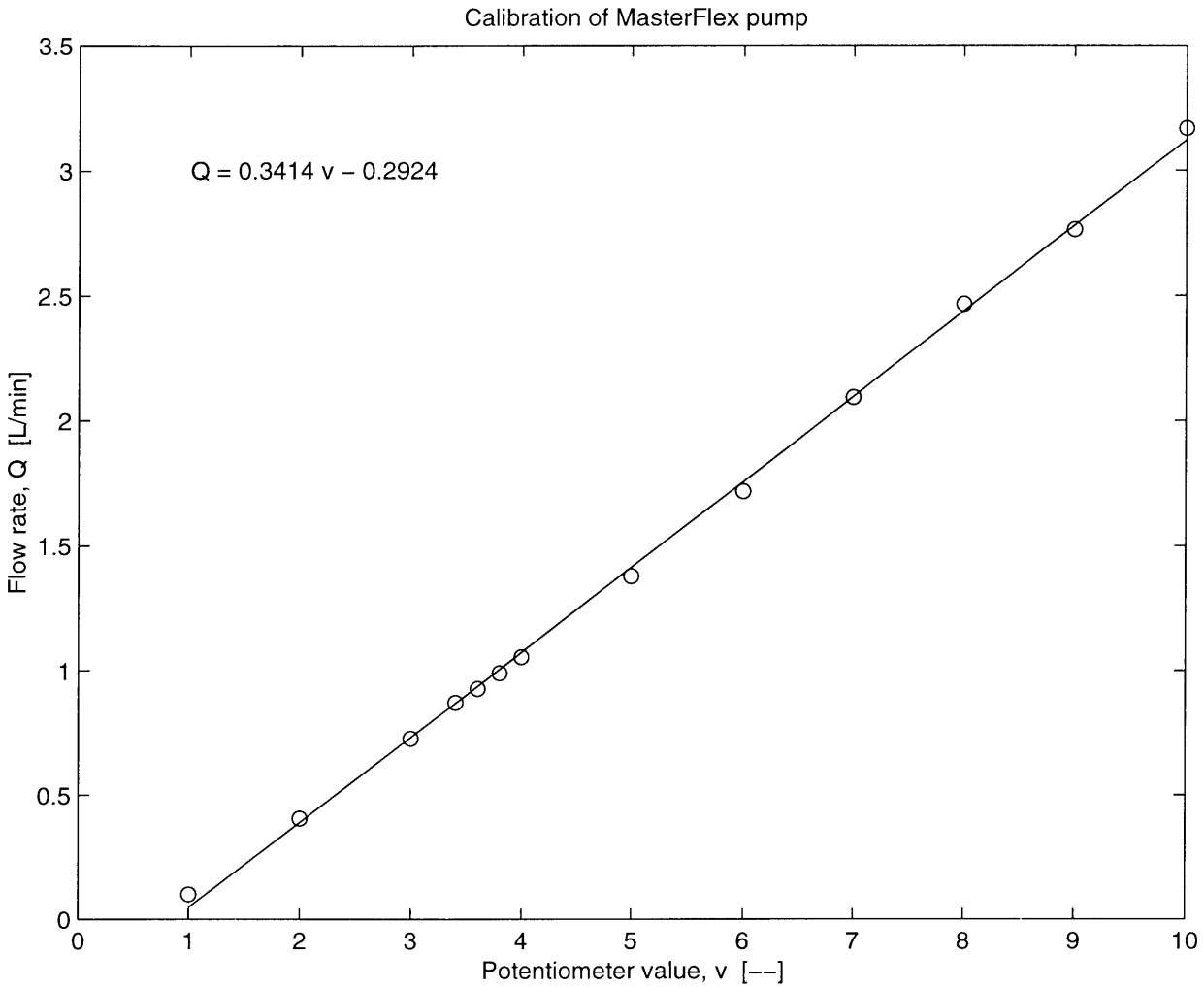

FIGURE A-4: Pump flow rates for MasterFlex oil pump.

density and immiscibility to CO_2 and because of our interest in deep water oil well blowouts.

Two different oils were used: a generic vegetable oil and a crude oil from the Gulf of Mexico (GOM-oil). The oils were injected using a Cole Parmer MasterFlex pump (E-07595-50) with L/S 36 tubing (E-06429-36) and a low-flow sprayer nozzle (E-83251-00). Pump flow rates were measured using the bucket and stopwatch method; the correlation to the pump potentiometer value is presented in Figure A-4. The vegetable oil had a high surface tension and produced large droplets with a mean slip velocity of 10 cm/s (measured by timing the rise of individual droplets) and a narrow bubble size distribution. The aromatic solvents in the GOM-oil reduced the surface tension significantly for that oil, allowing very fine droplets to form. Because the GOM-oil is also a mixture of oils, a wide range of droplet sizes was created. The slip velocity of droplets for the GOM-oil was estimated using the towed method

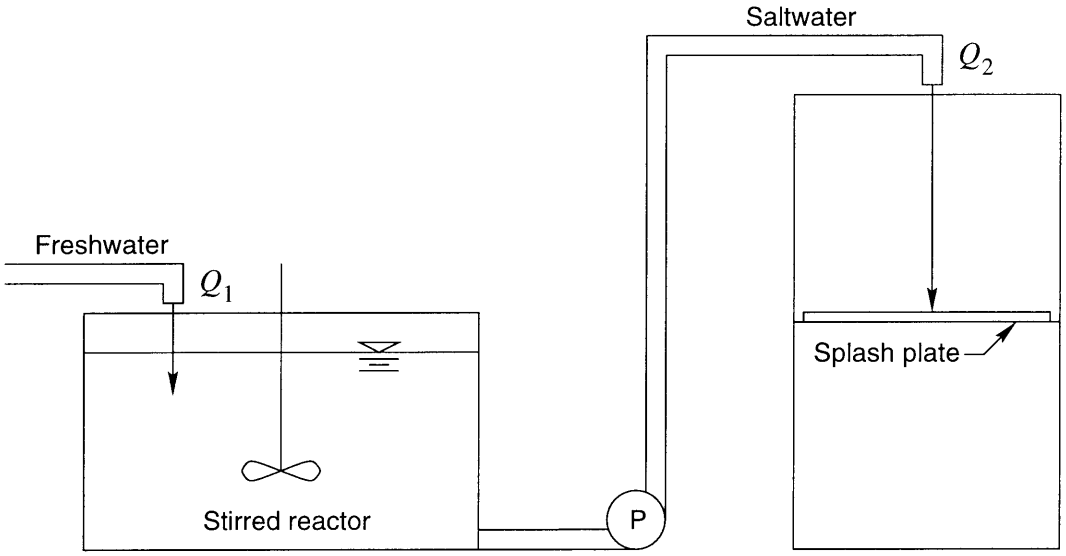

FIGURE A-5: Schematic of the two-tank stratification method.

from Hugi (1993) (see above discussion on air bubbles) and ranged from $\mathcal{O}(1)$ mm/s up to 10 cm/s with a mean of 8 cm/s.

A.1.3 Two-tank stratification system

The experimental tank is stratified using the two-tank method. Figure A-5 presents a schematic of this method, which derives its name from the second tank, used to prepare the salt solution before it is pumped into the experimental tank. Initially, the water in the stirred reactor has a density equal to the desired maximum density of the profile. As the experimental tank is filled, freshwater is added to the stirred reactor, making the density of water pumped into the experimental tank decrease monotonically during filling. A perforated splash plate dissipates the energy of the water as it enters the experimental tank so that a stratification profile develops.

Using the two-tank method, any arbitrary stratification profile can be created. Consider an initial volume, V_0, in the stirred reactor having a salt concentration of C_0. If freshwater is pumped at a rate Q_1, and the saltwater is pumped at a rate Q_2, then analyzing the mixing tank as a continuously stirred reactor gives the concentration of salt in the tank effluent over

time, $C(t)$, as

$$\frac{C(t)}{C_0} = \left(\frac{V_0 - (Q_2 - Q_1)t}{V_0} \right)^{\frac{Q_1}{Q_2 - Q_1}} . \tag{A.9}$$

For a linear profile, the exponent must equal +1, giving $Q_2 = 2Q_1$. To have a zero salt concentration at the top of the experimental tank in the linear case, V_0 must be half the volume of the experimental tank.

The two-tank method as constructed for these experiments can create step- and linearly-stratified profiles. To create an arbitrary profile, real-time flow control valves would need to be added. In the existing system, freshwater flows from the 3.8 cm (1.5 in) Cambridge water tap through a hose into a line diffuser in the bottom of the 3 m by 1.5 m by 1 m deep tank used by Reingold (1994). The mixed saltwater is then pumped by a 0.75 KW (1 hp) pump from the drain in the bottom of the stirred reactor through another hose to the top of the experimental tank, just as depicted in Figure A-5. To prevent a vortex from forming in the outlet of the stirred reactor, a four-sheet thick patch of horse hair is placed over the outlet inside the tank, and a minimum water depth of 10 cm is maintained whenever the pump is on. As a result, a zero salt concentration at the top of the profile in the experimental tank cannot be achieved.

To monitor the flow rates during stratification, both the freshwater and mixed water lines are run through rotometers, each having a scale of 0.4 to 3.6 l/s (6 to 60 gpm). The freshwater flows unfiltered into the diffuser in the stirred reactor. The mixed water, however, can be filtered by a dual pair of filters placed in parallel in the saltwater line, downstream of the pump. A range of filter sizes can be used to remove particulate matter from the mixed water. Without any filtration, the pump can achieve a stable maximum flow rate of about 1.9 l/s.

At the outlet of the piping system, above the experimental tank, air can entrain upstream to an elbow-joint about 1 m above the tank. The most stable flow is achieved, however, when the pipe is flowing full. Hence, as soon as the pump is turned on, the entrained air is expelled from the pipe by covering the outlet with one hand and allowing the pipe to fill with water. Once the pipe is running full, it transitions to laminar flow and does not re-entrain water upstream of the outlet.

The splash plate is constructed of a 115 cm by 105 cm sheet of 6 mm thick Lexan. The sheet is perforated with 16 mm diameter holes and covered with a solid sheet of horse hair. A 45 cm square sheet of aluminum is placed on top of the horse hair where the saltwater jet hits the splash plate, and an odd-shaped scrap of horse hair covers the aluminum plate. Styrofoam packing scraps are glued to the bottom of the splash plate to make it buoyant.

Mixing under the splash plate has been monitored using shadowgraph visualization while the experimental tank is being filled. The aluminum plate adequately deflects the initial jet so that no short-circuiting to one or a cluster of the perforations occurs. A nearly uniform mixing layer is observed below the splash plate that is approximately 8 cm thick and slightly (1 to 2 cm) deeper in the middle than the sides. Below this mixing layer, thin density currents smooth out the horizontal variations in the salinity profile.

Figure A-6 shows a sample density profile together with the analytical linear profile computed from Equation A.9. The no-flux boundary condition and the fact that the mixing tank is not quite emptied cause the actual profile to deflect from the linear profile at the top of the tank. There is no deflection at the bottom because the probe did not measure all the way to the bottom, and because there is less mixing at the bottom, creating a thinner boundary layer. The fluctuations from the linear profile in the middle of the tank arise from unsteady fresh and mixed water flows and from the fact that the line diffuser does not mix as efficiently as a well-mixed reactor.

To consider the effect of variation from the linear profile, the buoyancy frequency, which is the important parameter for controlling the plume behavior, is computed. Figure A-7 shows the buoyancy frequency of the profile in Figure A-6 as a function of depth. Neglecting 10 cm from the top of the profile where the no-flux boundary condition is met, the buoyancy frequency changes by $\pm 25\%$ about a mean of 0.33 s^{-1}. Since the variations in N do not persist over large lengths and because plume type scales as $1/N^{1/4}$ and trap height scales as $1/N^{3/4}$, this deviation from a constant buoyancy frequency is not expected to impact the experimental results.

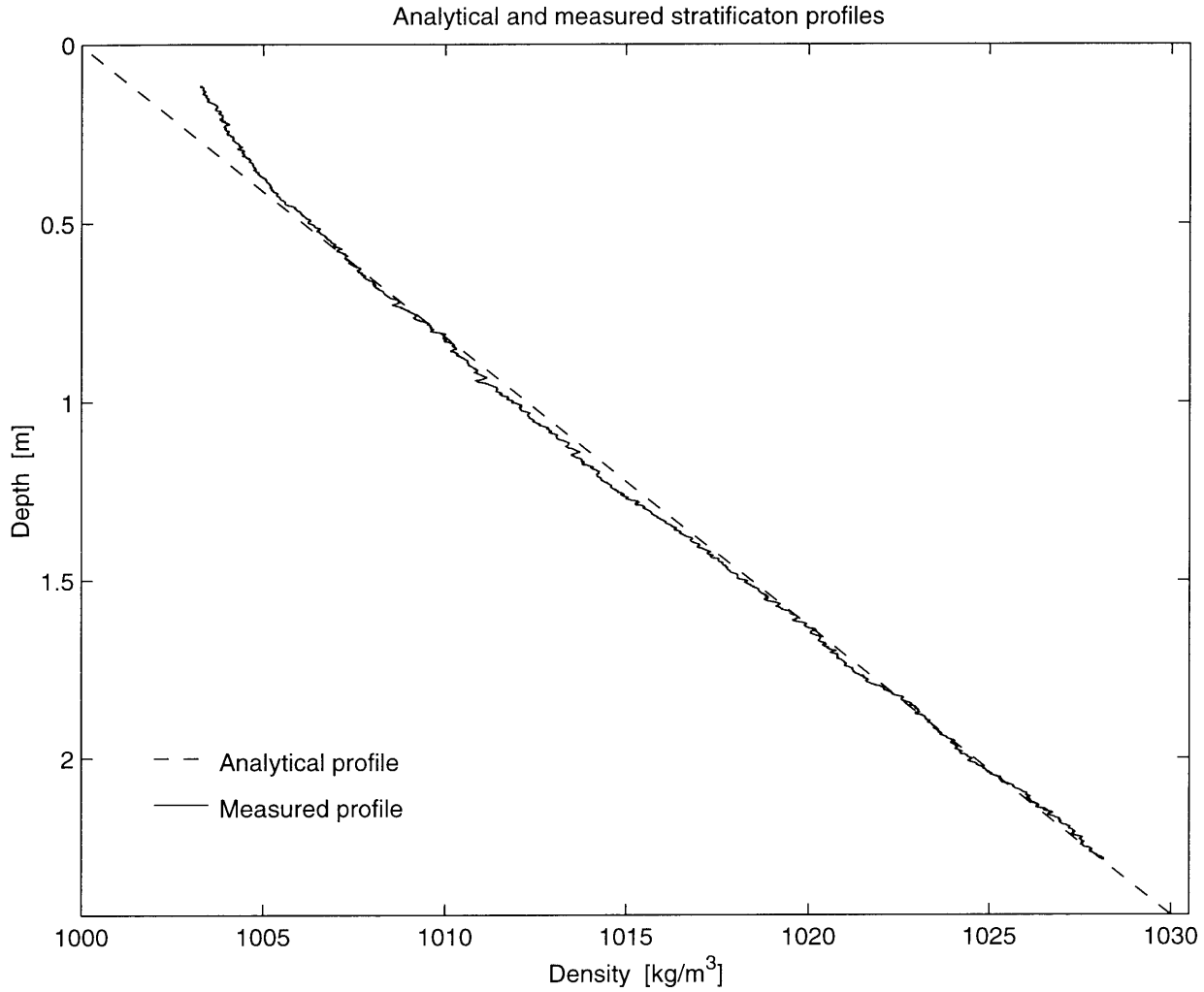

FIGURE A-6: Salinity profile set up in large experimental tank for freshwater and saltwater flow rates of $Q_1 = 0.9$ and $Q_2 = 1.7$ l/s, respectively.

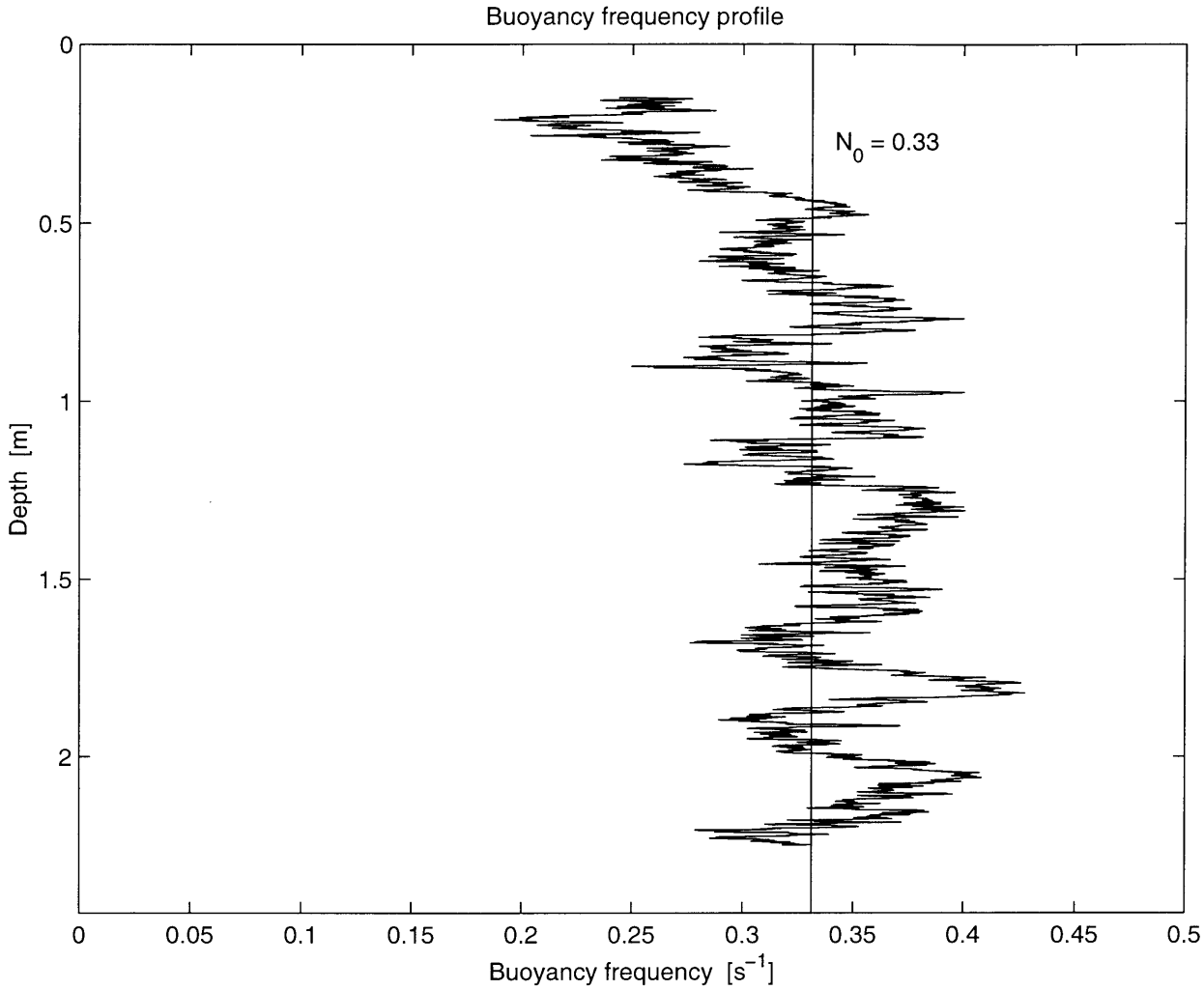

FIGURE A-7: Buoyancy profile set up in large experimental tank for freshwater and saltwater flow rates of $Q_1 = 0.9$ and $Q_2 = 1.7$ l/s, respectively.

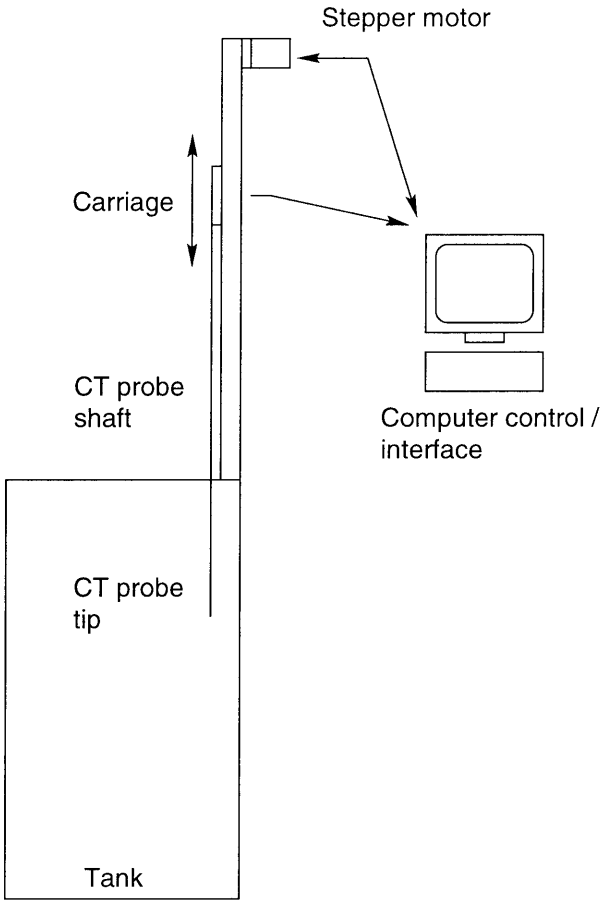

FIGURE A-8: Schematic of the density profiling system showing the CT probe connected to the linear positioner mounted above the tank.

A.1.4 Density profiler

Density profiles are taken using a CT probe connected to a belt-driven linear positioner as depicted in Figure A-8. The belt drive, with a length of travel of 2.71 m, is mounted on the top of the tank in one corner. Attached to the belt drive carriage is a custom CT probe with a corresponding shaft length of 2.71 m. As the carriage moves up and down, the CT probe tip moves an equal distance. Both the linear positioner and the CT probe send electronic messages to a computer I/O card; hence, conductivity, temperature, and carriage position can be recorded simultaneously during a profile and stored on the computer hard drive.

Belt-driven linear positioner

The belt-driven linear positioner is a Parker HLE 60 Series, single axis, linear actuator supplied by Empire Automation of Woburn, Massachusetts (part number HLE060RB. NL. E. 2712. DA0000. MBL. SP7. GAW03. H1. ZA. LH1). It is controlled by a separate stepper motor and communications box (the Parker Zeta6104-83-93). Together, the motor-carriage unit has a load capacity of 710 N and can travel at speeds up to 5 m/s.

The principle of a stepper motor is that its shaft turns a fixed amount for each step command, represented as an electronic impulse issued from a computer. The controller box supplied with the Zeta6104 monitors the steps taken, issues stepping impulses, and communicates with the computer over the COM1 port. The Zeta6104-83-93 takes 25,000 steps per revolution and has a maximum velocity of 2 million steps per second with an accuracy of $\pm 0.02\%$ of the maximum velocity. It also has a positioning range of 2.14 billion steps of absolute accuracy (i.e. ± 0 steps).

Running in ENC1 mode, 25,000 motor steps corresponds to one pulley revolution on the belt drive, which translates into 125 mm of travel for the carriage. For a normal density profile, the carriage moves 2.1 m, or 420,000 steps. Since the position of the motor is known with absolute accuracy, the CT probe tip location is known to within one motor step, or $5\text{x}10^{-6}$ m. However, the slight error introduced for acceleration and deceleration of the carriage results in a repeatability of ± 84 steps, or 0.4 mm. Therefore, our ability to position the CT probe exceeds the resolution of the probe (the separation distance between the C and T probes is > 0.4 mm).

Communication with the Zeta6104 control box from the computer can either be made from within Motion Architect, the Windows NT software provided with the motor controller, or by issuing ASCII text commands from within a communications package, such as LabVIEW. Testing and routine commands are generally done within Motion Architect. Once a set of instructions for a given task has been chosen, a LabVIEW program is written to issue the commands in their correct order and make simple decisions based on information coming into the computer over the I/O lines.

Conductivity and temperature probes

Two CT probes have been used in these experiments, a Head MicroScale CT instrument (Model 125) manufactured by Precision Measurement Engineering of Encinitas, California with a custom shaft and an Ocean Sensors modified OS300 manufactured in San Diego, California.

The Head CT probe consists of a sensor (6 mm cross-section), a rigid, stainless steel shaft (6 mm cross-section) connecting the sensor to the preamp, a sensor cable, and an electronics bridge. The probe shaft is inserted into a 1.3 cm diameter aluminum electrical conduit, and the probe tip is protected by a 1.3 cm diameter shield; thus, the frontal area for the length of the probe is 1.3 cm in diameter.

Because the CT Model 125 has to be calibrated after every 8 hours of use, the CT probe must be calibrated separately for each experiment and for any profiles taken more than 8 hours apart. Once calibrated, the conductivity measurement has a stability of better than 1% of the C reading, and the temperature has a stability of better than 0.01 °C (Head 1997). Two solutions are used in the calibration: a warm freshwater solution, and a cold saltwater solution. The temperature of each solution is measured with a standard thermometer from the VWR supply with a resolution of 0.1 °C. The density of the saltwater solution is measured using a Paar Digital Density Meter (Model DMA 35). The accuracy of the density meter was tested by taking density measurements of known solutions. The density measurement is accurate to within 0.001 g/cm^3. The density and temperature of the saltwater solution is converted to conductivity for calibration using the method in Head (1997).

The OS300 CT probe consists of a CT sensor tethered to an electronics processing module. The CT probe and tether are attached to the 1.3 cm diameter aluminum electrical conduit and give a constant frontal area equal to that with the Head CT probe. The OS300 probe also has a pressure transducer, but the response time of the transducer is too slow to be of use while profiling. The OS300 probe was calibrated by Ocean Sensors in their calibration lab; hence, no on-site calibration is necessary. The conductivity measurement is accurate to ± 0.02 mS/cm and the temperature is accurate to ± 0.01 °C. Density is computed from the conductivity of NaCl solution and temperature using the method in Head (1997).

A.1.5 Flow visualization system

The primary purpose of the various flow visualization techniques is to provide qualitative information about the induced flow field. Accurate quantitative measurements are not possible from the visualized flow field due to the variable index of refraction that is caused by the salinity stratification.

The visualized flow field in all cases is recorded using a charge-coupled device (CCD) camera and a computer framegrabber. Two main classes of visualization techniques are used. The first relies on the Schlieren effect of the variable index of refraction to produce shadowgraph images. The second employs fluorescent dye with LASER light illumination and are called LASER induced fluorescence (LIF) techniques.

CCD camera and framegrabber

The image acquisition system was designed through a lengthy search of available hardware and was ultimately supplied by Graftek Imaging, Inc. of Austin, Texas. The system consists of the following components:

- Pulnix TM9701-AN black and white progressive scan camera. It uses a 1.7 cm (2/3 in) CCD imager to achieve a resolution of 768 x 484 pixels, or 525 TV-lines. It has dual analogue and digital outputs, full-frame shutter from 1/60 to 1/16,000 s, asynchronous reset capability, and automatic gamma correction ($\gamma = 1$ or 0.45).

- Computar TV zoom lens M6Z 1212: 12.5–75 mm, f1.2–16 lens.

- Matrox Pulsar PCI framegrabber with digital module. The Pulsar framegrabber allows full use of the Pulnix camera functions. At maximum performance the Pulsar card can capture 30 frames per second (fps) directly to the computer RAM. Images are then transfered to the hard disk after acquisition ends, or can be transfered during acquisition at a reduced frame rate of $\leq$ 10 fps.

- Graftek IMAQ driver for Pulsar framegrabber. This software driver allows direct control of the Pulsar framegrabber from within the LabVIEW Advanced IMAQ image acquisition programming language.

- Data cables connecting the camera to the computer. These include a 10 m digital cable and a 30 m BNC analogue cable.

As indicated above, the image acquisition hardware is controlled from within LabVIEW. Two main programs have been written. The first captures images at variable framing rates and saves them to the hard disk after acquisition has ended. The second program plays the images back like a video player with full forward, reverse, slow motion, and frame-by-frame capability.

The image acquisition program itself has two main parts. The first part sets the framegrabber settings for analogue image capture (digital capture does not require any hardware settings). The second part sets the acquisition timing. The framing rates are input by specifying a number of images to capture and the number of images to wait between each captured frame. For instance, to capture 10 images at 30 fps followed by 10 images at 15 fps, you would enter 10 images skipping zero and 10 images skipping one (since the camera frame-rate is fixed at 30 fps). Image acquisition can be started by an external switch, the mouse button, or by an analogue input signal. Therefore, the image acquisition system combines accurate acquisition timing with flexible frame capture to span the range of dynamics observed in the experiments.

Shadowgraph visualization

Aggregate plume characteristics are visualized using the shadowgraph technique. A point source of light on one side of the tank shines through the plume, creating a horizontally averaged two-dimensional image on a screen placed on the opposite tank wall. Hence, as the plume wonders in a helical fashion in the three-dimensional tank, the motion is reduced to side-to-side motion on the shadowgraph image. On the other hand, large-scale eddie motion is easy to track in the shadowgraph image, providing qualitative data on the peeling mechanism.

Figure A-9 shows a schematic of the shadowgraph virtual point light source. The light source is a 1000 W FEL quartz-halogen lamp mounted on a rod mount (supplied by Oriel Corporation). A 50 mm diameter parabolic mirror (F# 2.0) is mounted behind the lamp to

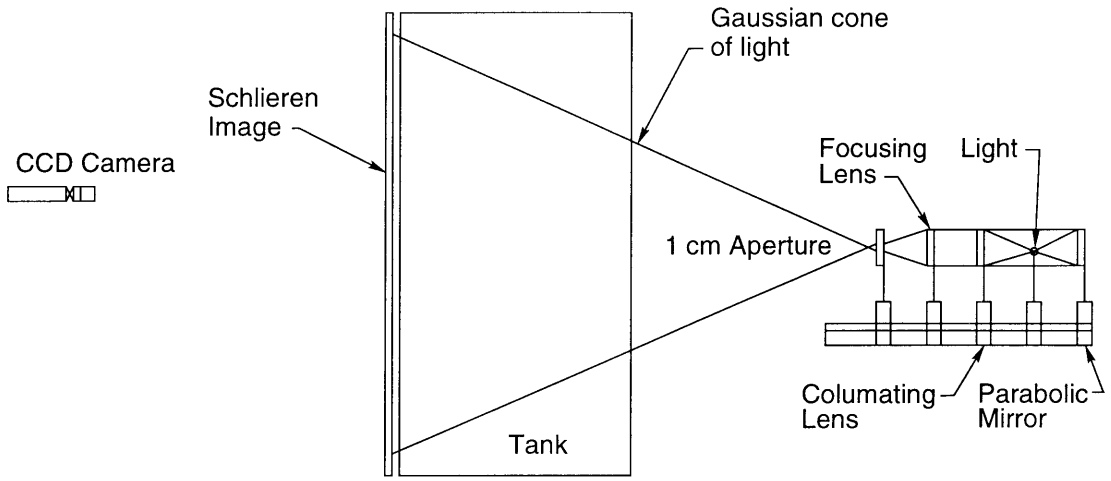

FIGURE A-9: Schematic of the shadowgraph configuration, showing the details of the light source and the hardware placement.

reflect a collimated beam forward. A 50 mm diameter collimating lens (F# 2.0) is placed forward of the lamp to collimate the lamp light. The beam is then focused by a 50 mm diameter doublet lens (F# 1.6), which focuses the lamp light down to an 8 mm diameter disc. A 10 mm diameter fixed aperture is placed at the focal point of the beam to block out stray light. All of the parts are mounted on a triangular bench from Coherent Ealing. Through this system of mirrors, a 1 cm effective diameter light source is created.

The shadowgraph images are focused on a translucent screen (standard mylar) on the opposite side of the tank. Also shown in Figure A-9 is the layout of the shadowgraph imaging system and camera placement. Parallax corrections would be required to make quantitative measurements of any dimensions from the images.

LIF visualization

The LIF visualization technique illuminates a slice through the plume, avoiding the averaging effects of the shadowgraph method. The plume edges must be marked, however, by an inert tracer, in this case, Rhodamine 6G.

The LASER light sheet is created by a cylindrical lens at the end of a fiber optic cable, connected to a 6 W Argon-ion LASER (Innova 70 by Coherent, Inc.). The LASER has two

LASER light lines, one at 494 nm, the other at 515 nm. Due to the dispersion in the fiber optic and other errors due to combining the two wavelengths, the light sheet is about 2 cm thick in the region illuminating the tank.

Rhodamine 6G was the best dye to use for the LIF experiments. It has a broad excitation range, covering both LASER lines, and emits an orange fluorescence with a peak at about 560 nm. Hence, a cut-on filter centered at 530 nm can completely filter out the LASER light with very little attenuation in the fluorescent signal from the Rhodamine 6G. In addition, the existing Chelsea in-situ fluorometer (set up for Rhodamine WT) can measure Rhodamine 6G with high accuracy once a calibration curve is created (see the following section). Hence, Rhodamine 6G gives great flexibility in visualization techniques (filters can eliminate the bubbles from the images if desired) without sacrificing the ability to take quantitative dye concentration profiles.

In order to ensure that the dye tracer is completely mixed throughout the entrained plume fluid, a collar diffuser is used. The diffuser is made of 0.3 cm inner diameter tubing, bent into a 3 cm diameter collar and connected to the source tube by a T-intersection. The collar is perforated with a number of tiny holes which allow the dye to ooze into the flow from all sides of the plume.

A.1.6 Fluorescence profiler

Although the LIF scheme described above does provide nice visualization of the plume, the intensity in the LIF images themselves cannot be related back to concentrations because of variations in the index of refraction caused by the salinity stratification. These variations have been removed in small experiments using alcohol solutions (e.g. McDougall 1979); however, this technique is not practical at this scale. Nash et al. (1995) used *in-situ* measurements of temperature (in our case it would be salinity) to account for variations in the index of refraction for a two-dimensional flow, but this is also not practical for our application.

As an alternative to quantification using LIF, direct in-situ profiles of dye concentration are made using a Chelsea fluorometer strapped to an Ocean Sensors OS200 CTD unit.

Because the measurement volume for the fluorometer is small, the effect of the changing refractive index is minimized and direct concentration profiles can be made. However, the instrument is too heavy and awkward to attach to the linear positioner, so a depth measurement from the CTD must accompany the fluorometer data.

To get accurate profiles of dye concentration, the measurements are taken following an experiment once the internal waves have died down and the dye has mixed horizontally (at least 1 hr following the experiment). Since the Chelsea fluorometer has a frontal diameter of 5 cm and the CTD has a frontal diameter of 3 cm, one pass through the fluid can cause a fair amount of mixing. Therefore, a single profile through the center of the tank is used in the calculations. Multiple profiles have been taken to test for horizontal uniformity and good agreement among profiles was achieved. (I need to say something about dye loss over time).

Calibration

The fluorescence measurements from the fluorometer can be directly related to concentration measurements only after calibrating the fluorometer to a series of solutions of known concentrations. The solution standards were prepared by the method of successive dilution. First, one gram of Rhodamine 6G powder was dissolved in 30 ml of isopropyl alcohol. The alcohol solution was then added to 200 ml of deionized water, yielding an initial solution at a concentration of 4.35 $\pm$ 0.04 g/l. Each successive dilution was obtained by adding a modest amount (about 100 ml) of dye from the previous dilution to 1000 ml of pure water. The concentrations, C, of the various solutions were computed from

$$C = \frac{C_s V_s}{V_s + 1000} \tag{A.10}$$

where C_s is the concentration of known solution and V_s is the volume (in ml) of the known solution that was added to the 1000 ml solution of deionized water. Table A.2 provides the details of the dilutions, the concentrations of the standards, and the errors in the concentration estimates. Background contamination in the lab, however, prohibited making reliable solutions below 5 μg/l.

Solution Number	Solution Added	Volume Added [ml]	Concentration Obtained [mg/l]	Percent Error
0	N/A	0	4350	1.01
1	0	24	102	1.02
2	1	100	9.26	1.02
3	2	150	1.21	1.02
4	2	60	0.524	1.02
5	3	100	0.110	1.02
6	3	70	0.0791	1.02
7	4	100	0.0477	1.02
8	4	60	0.0297	1.02
9	5	100	0.0010	1.02
10	5	80	0.00814	1.02
11	6	70	0.00517	1.02
12	6	40	0.00304	1.02
13	7	30	0.00139	1.02

TABLE A.2: Prepared Rhodamine 6G standards for calibration of the Chelsea in-situ fluorometer. Successive dilutions of the prepared standards yielded accurate concentrations, as show by the reported percent error (based on a numerical error analysis). Contamination in the lab, however, prevented making reliable standards below 5 μg/l.

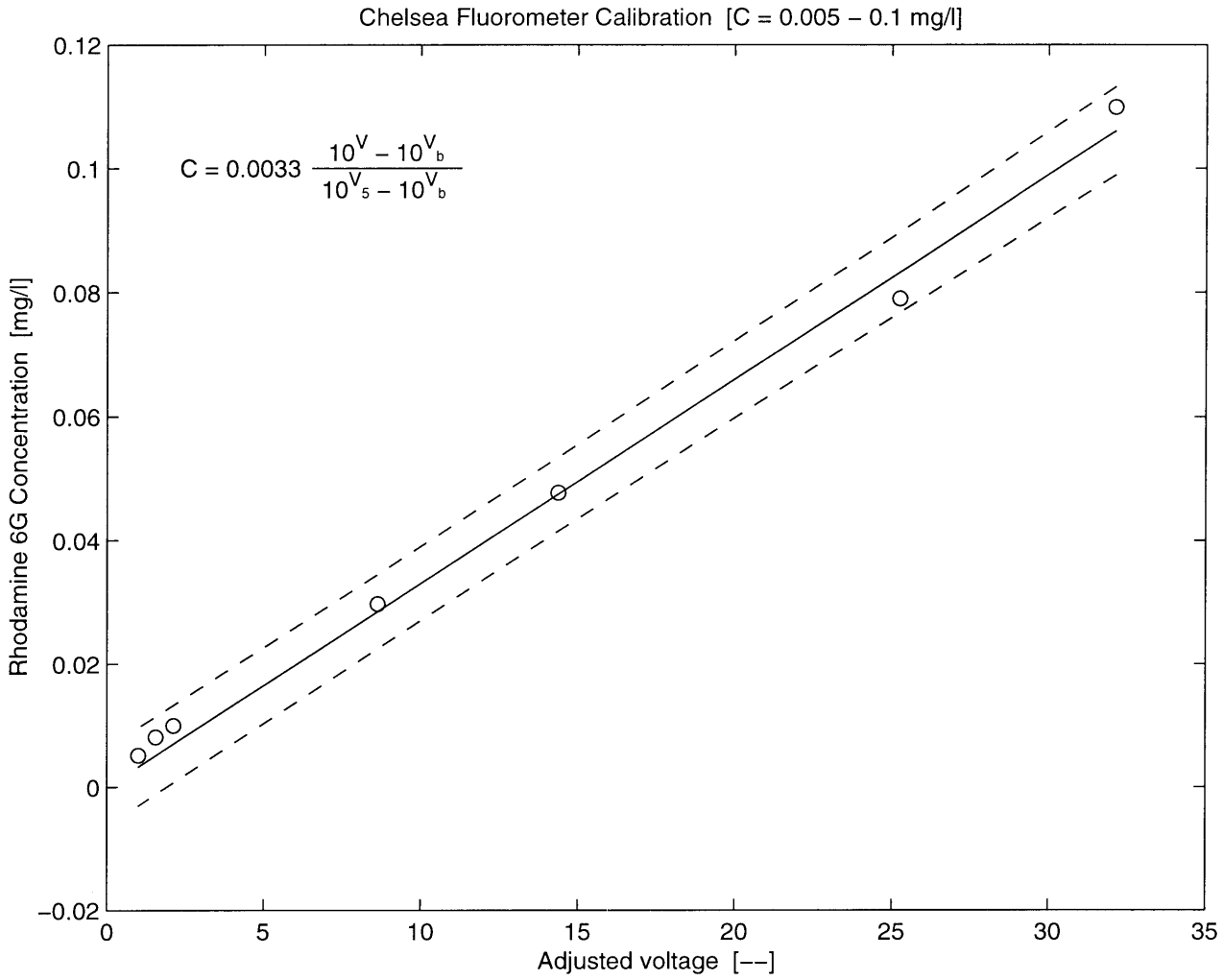

FIGURE A-10: Rhodamine 6G calibration curve for the Chelsea fluorometer. The dashed line is the 95 % confidence limit of the regression (assuming Gaussian error distributions).

The fluorometer was calibrated to the standard solutions by placing a beaker containing 250 ml of standard in the fluorometer's measurement volume and recording 1 minute of fluorometer output (the measurement cycle on the fluorometer is 10 Hz). The first 25 data points were discarded because the fluorometer has about a two second delay between the start of data acquisition and the steady-state operation of the instrument. Once data acquisition has started, however, rapid variations in concentration can be accurately measured. It is only the start-up period which has problems. Occasionally, a measurement of -0.01 is recorded in the dataset; all of these spurious measurements (maximum of 10 data points per standard solution measured) were also discarded.

Figure A-10 presents the calibration obtained. The equation suggested by Chelsea In-

struments for relating the measured voltages, V, to concentration is

$$C = C_0 \frac{10^V - 10^{V_b}}{10^{V_1} - 10^{V_b}} \tag{A.11}$$

where V_b is the background fluorescence and V_1 is the voltage obtained for a concentration of 1 μg/l. Measuring the fluorescence of the deionized water provided a measure of $V_b = 0.87 \pm 0.02$. As seen in the graph, measurements below 5 μg/l do not follow the linear relationship; therefore, V_1 was taken as the voltage for the 5 μ/l measurement. Through standard least squares regression of the transformed data, C_0 was calculated to be 0.0033 $\pm$ 0.0002. The regression has a coefficient of determination of 0.994 and a standard error of estimate of 0.003.

Error estimates for the voltage measurements were taken as the standard deviation of the voltage output from the fluorometer. Error bars are not plotted in Figure A-10 because they are actually smaller than the data symbols plotted in the figure. Hence, the variability in the figure is due to contamination from the background rhodamine and other fluorescent dyes in the lab and is not due to error in the measurement technique. Therefore, the 95% confidence limits of the regression plotted in the figure will be used as an estimate of the measurement error associated with concentration measurements.

A.2 Crossflow experiments

The crossflow experiments were conducted in the Parsons Laboratory at MIT using the wave flume depicted in Fig. A-11. The portion of flume we used measured 0.9 m deep x 0.8 m wide x 15 m long.

A.2.1 Setting up a crossflow

The crossflow can be created in two different, yet comparable ways:

- **Pump:** There is a pump that recirculates the water through the flume. Its flow rate is controllable, using an upstream gate valve, and ranges from 10 to 100 L/s. These flow rates correspond to velocities of 1.4 to 14 cm/s when the tank is full.

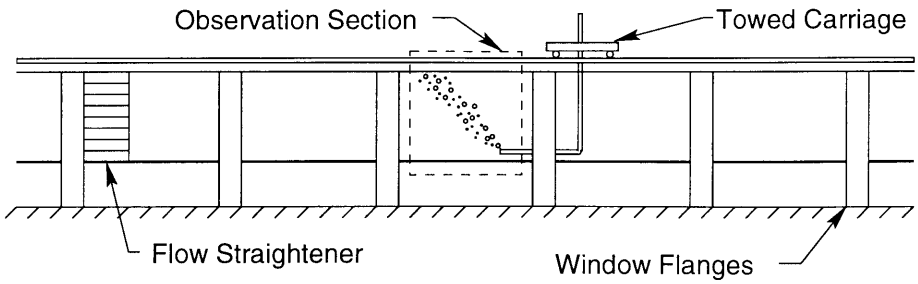

FIGURE A-11: The experimental flume at Parsons Laboratory, MIT. Distance between successive flanges is 1.5 m.

- **Motor:** We also built a towing mechanism that can push or pull a diffuser mounted along the bottom of the tank. In this method the crossflow is simulated using a moving frame of reference. The towing mechanism consists of a 1750 rpm variable speed motor with a 30:1 reducer gear box, attached through synchronous belts and gears to a carriage. The carriage has wheels and runs on rails, mounted on the top of the tank, enabling it to travel the length of the tank.

Crossflow velocities generated by the pump were measured using a Sontek acoustic Doppler velocimeter (ADV). Vertical profiles were measured at a stationary point along the center-line of the tank at a range of flow rates to calibrate the pump. Profiles were also taken 0.2 m from each side to check for flow uniformity across the cross-section. To help create a uniform flow, a plastic honeycomb flow straightener was placed upstream of the test section and sealed with attached pieces of horsehair and rubber. Measured velocities varied by about $\pm 20\%$ over the cross-section (i.e., the flow was not quite uniform).

The motor towing speeds were calibrated using a ruler and stopwatch method. The motor tow velocities are accurate and repeatable in the 2 cm/s - 23 cm/s range (20-90% of its maximum rpm). The motor calibration equation relating motor rpm percentage, x, to towing velocity, y, is:

$$y = 0.3x - 4.4. \tag{A.12}$$

Although the motor and belt-drive system is very accurate, errors in u_∞ are introduced due to errors in setting the motor potentiometer. Based on the resolution of the potentiometer dial, crossflow velocities are accurate to ± 0.5 cm/s.

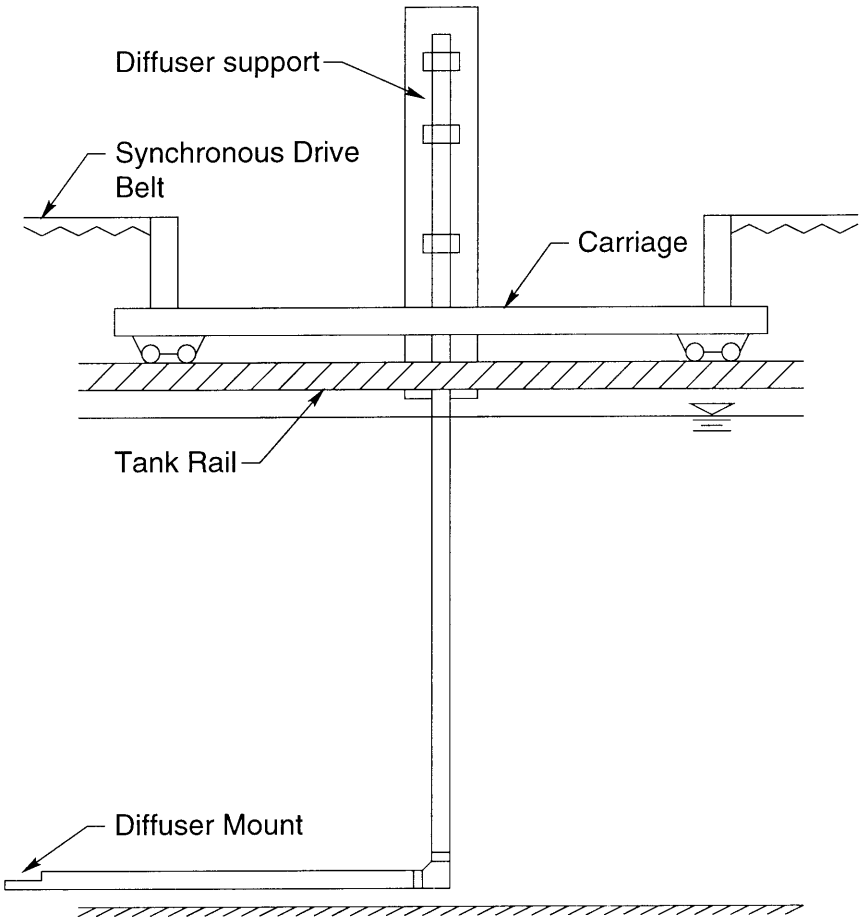

FIGURE A-12: The support and towing mechanism for the diffuser.

A.2.2 Characterizing the diffusers

As shown in Fig. A-12, the diffusers mount to the end of a support arm attached to the carriage. The diffuser mount is attached to the towing carriage using two pieces of PVC pipe joined by a 90 degree elbow. A fluorescent dye is used as a tracer to mark the fluid entrained at the base of the plume. The air diffuser and dye line are both connected to rubber tubing running through the pipe, which is clamped to the carriage. The bubbles are discharged at 7 cm above the bottom of the tank with three different types of diffuser: a 6 cm tall limewood diffuser, a 2.5 cm tall aquarium airstone diffuser, and a 1 cm tall piece of 0.6 cm diameter vinyl tubing. In fresh water, each diffuser produces a slightly different bubble spectrum. The characteristics of the bubbles were measured using two different techniques:

Diffuser	Average droplet diameter [mm]	Average slip velocity [cm/s]
Limewood (fresh)	1.6	18
Limewood (saline)	0.5	7.2
Airstone	2.4	23
Vinyl tube	2.9	26

TABLE A.3: Air bubble characteristics.

- **PDPA:** The Phase Doppler Particle Analyzer (PDPA) housed at the University of Hawaii Look Laboratory was used to characterize the limewood diffuser in fresh and salty water (tapwater, NaCl solutions with tapwater, and seawater taken from 40 m depth). The PDPA assumes the bubbles are spherical, which is a reasonable assumption for these smaller bubbles. Rise velocities were calculated from empirical formulas relating the bubble diameter to terminal velocity in Clift et al. (1978).

- **Towing Technique:** The other diffusers each had bubbles too large to measure using the PDPA; hence, an alternate method was required. Hugi (1993) measured rise velocity by timing the rise of bubbles released from a rapidly towed source. Similarly, we used the towing mechanism described above and timed bubbles as they rose a distance of 63 cm, released from a diffuser towed at 22 cm/s. Bubble diameter was calculated using the same empirical formulas from Clift et al. (1978).

Table A.3 summarizes the bubble characteristics for each diffuser. The data in Tab. A.3 indicate that the three diffusers produce similar bubble slip velocities in fresh water. Concerning their different bubble spectra, the airstone and vinyl tube produce only "large" bubbles ($\approx$ 2.5 mm diameter), while the limewood diffuser produces mainly "large" bubbles, with some "small" bubbles ($\approx$ 0.5 mm diameter).

The small bubbles behave more like oil droplets since they have slip velocities in the range of 7 cm/s. We found that discharging a neutrally buoyant saltwater and alcohol solution near the diffuser head caused many more (estimated as over half the volume flux) small bubbles to form. These small bubbles have an average size of 0.5 mm and slip velocity of 7 cm/s. Based on our size spectrum experiments in Hawaii, the small droplet size is very stable and

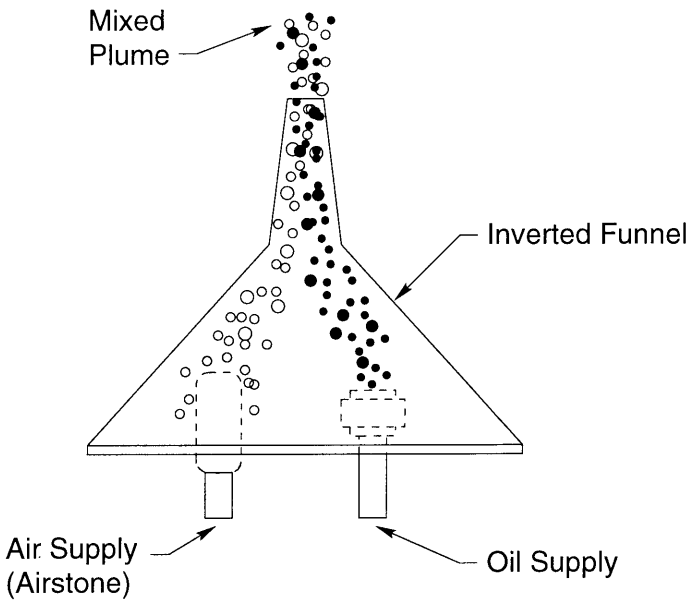

FIGURE A-13: The inverted funnel assembly used to create well-mixed oil and gas plumes.

does not show a dependence on saltwater concentration above the threshold necessary to start producing small bubbles. In addition, once the small bubbles nucleate, they do not coalesce as they rise; hence, the small bubbles continue to rise unchanged to the surface.

A.2.3 Combined oil, gas, and alcohol experiments

In addition to pure air experiments, we also ran experiments with just crude oil, with just alcohol, with air/oil mixtures by volume of 1:1 and 10:1, and with mixtures of alcohol and gas. These experiments varied the oil, alcohol, and gas flow rates and the crossflow velocity. The droplet characteristics of the oil diffusers were not precisely determined; however, the majority of oil droplets by volume had slip velocities in the approximate range of 4 to 8 cm/s. The oil droplet spectrum had a long tail of smaller droplets trailing down to very fine droplets rising in the 1 mm/s and lower velocity range. Alcohol was used to simulate the finest oil droplets since it has an effective slip velocity of 0. These different experiments with various bubble sizes could represent a range of natural gas bubble sizes (with or without hydrates), a range of oil droplet sizes, or a combination. To ensure that the oil and gas and alcohol and gas where equally distributed in the plume, an inverted funnel was used as depicted in Fig. A-13.

A.3 Validity and reliability of measurements

A rigorous error analysis must consider all sources of experimental error. Generally, error can be classified as one of three types: measurement error, random errors, and systematic errors. The easiest of these to quantify is the measurement error, which relates to the resolution and repeatability of a given measurement technique; measurement errors were reported in the previous sections. Random errors are due to fluctuations that cause measurements to have unbiased scatter. These are generally accounted for by statistical means by comparing results for several repeated experiments. Systematic errors are due to identified causes and can, in principle, be eliminated. These include instrument error (poor calibration), observational error (parallax) and theoretical error (due to simplifications in the model system).

A.3.1 Errors in measurement techniques

The analyses reported for these experiments rely on three direct measurements: the captured images, the density profiles, and the dye concentration profiles.

Captured images

Captured images are used to observe plume type and peeling processes and to give supporting measurements of intrusion heights and plume shape. Because the plumes are at a quasi-steady state, camera timing, experimental elapse times, and triggering are not important. Also, because quantitative LIF is precluded by the stratification, variations in pixel intensity caused by random noise and and lens effects can be ignored. Hence, errors relate only to the pixel resolution and the ability to measure vertical dimensions.

- **Measurement error**: As reported above, the camera resolution is 768 x 484 pixels. To exploit the maximum vertical field of view, the camera is positioned during the experiments so that the 768 pixel dimension lies in the vertical. Each experiment has a slightly different resolution, dependent on the lens settings, but generally covers a vertical distance of 1.6 m, yielding a pixel resolution of 2 mm.

- **Random error**: Random errors affect only pixel intensity and can, therefore, be ignored.

- **Systematic error**: There are two kinds of systematic errors: lens spherical aberration and parallax. The lens spherical aberration is eliminated by imaging a grid with cells 5 cm square. Within the area of the lens that contains the plume image, spherical aberration was below the pixel resolution. Parallax is more difficult to remove. The refractive properties of the glass are accounted for by imaging the grid. However, errors due to the variable refractive index in the tank cannot be eliminated. Comparing peaks in the dye profiles with lengths measured from the images indicates that parallax introduces an error of $\pm\mathcal{O}(1)$ cm.

Density profiles

The density profiles are used to calculate the buoyancy frequency and to quantify the plume net volume flux. To compare changes between two profiles taken at two different times, the tank must be completely still, void of internal waves and recirculation flows. Hence, profiles cannot be taken during an experiment or earlier than one hour after an experiment.

- **Measurement error**: The density profiles consist of two dimensions: the vertical coordinate and the fluid density. The vertical positioner is extremely accurate, with a measurement error of ± 0.4 mm. The density measurement depends on measurements of the conductivity (C) and temperature (T). The resolutions of the C and T measurements are limited by the Head probe, with an error in C of 0.4 mS/cm and an error in T of 0.1 °C. Based on the method from Head (1997) for calculating the density of NaCl solutions from C and T, the error in the calculated NaCl concentration based on perfect measurements of C and T would be $\pm\frac{1}{2}\%$. From a Monte Carlo simulation run until the statistics became stationary, the error in density given these measurement and analytical errors is ± 0.4 Kg/m^3. Since the Paar density meter, used to calibrate the Head probe, has a resolution of 1 Kg/m^3, the measurement error for the density coordinate is taken as ± 0.5 Kg/m^3.

- **Random error**: Random fluctuations are introduced through noise in the data acquisition system (primarily the PC I/O card). To reduce the noise, a banded filter with a width of 25 data points is used to smooth the data. Density profiles have 632 data points evenly spaced over 2.3 m; thus, the linear filter width is ± 5 cm. After filtering, the noise is reduced below the resolution of the density measurement ($< 0.5 \mathrm{Kg/m^3}$), but the vertical resolution has been reduced to ± 3 cm (i.e. $\pm 5/\sqrt{2}$ cm for a linear filter).

- **Systematic error**: Systematic error arises for the density profiles through errors in calibration. Within one experiment, the calibration does not change and calculations are based on density differences only. Hence, systematic error does not increase the error in the density profile measurements.

Dye concentration profiles

The dye concentration profiles are used to measure the intrusion height and the mass of dye trapped in each of the intrusion layers.

- **Measurement error**: Like the density profiles, the dye concentration profiles also consist of two dimensions: the vertical coordinate and the dye concentration. For the dye profiles, the vertical coordinate comes from the OS200 CTD device. The accuracy of the OS200 pressure transducer is 5 m, with a resolution of ± 2.5 cm, which is comparable to the resolution of the density profiles after averaging. From Figure A-10, the 95% confidence limit on the dye concentration, which represents two standard deviations in the mean, is essentially constant at ± 0.005 mg/l. For consistency throughout this section, we take the error as one standard deviation, which gives an error in dye concentration measurement of ± 0.003 mg/l.

- **Random error**: Electrical noise is already accounted for in the measurement error for this device, so no further random errors need be added. The dye concentration profiles are not spatially averaged. There are a few data points, however, that are removed from the acquired data: any points with a negative concentration (which occur on

average 5 times per profile and are due to random computer communication errors) are removed.

- **Systematic error**: The effect of the variable index of refraction on the dye concentration measurement is negated by the very small (about 1 cm^3) sampling volume. The only other systematic error is due to the effect of the density profile on the depth measurement. As the device descends, the water density increases and the integrated depth would be off by about 3 cm at the bottom of the tank if a uniform density were used to calculate depth. The actual measured density profile is used; hence, this systematic bias is eliminated.

A.3.2 Errors in measured quantities

The trap height, bubble spreading ratio and crossflow separation height are measured directly by one or more of the systems described above.

Stratification trap height

All three measurement systems provide complementary estimates of the intrusion layer trap height. From the images, the trap height is taken as the elevation at which the dye has intruded furthest into the ambient. From the density profiles, the intrusion depth is estimated as the elevation of the inflection point in the density profile. From the dye profiles, the intrusion depth is taken as the elevation with the highest dye concentration. The reported trap height is the mean of the latter two measurements. The error for additive measurements is the root-mean-square of the individual measurement errors, which gives the error in the measured trap height as ± 2.0 cm.

Bubble spreading ratio

The bubble spreading ratio is taken exclusively from the captured images. First, the cut-on filter is used to capture images of the dye only (the LASER light reflected off the bubbles is absorbed by the filter). Second, the cut-on filter is removed, and images are captured of the bubble column. The ratio of the growth rates of the bubble column to the plume

edge is taken as the bubble spreading ratio. The pixel resolution is very small, but the observational error of selecting the edge of the plume and bubble core is large; hence, errors in bubble spreading ratio are reported as the standard deviation of the estimates made for 3 points for a given experiment.

Crossflow separation height

The crossflow separation height is taken directly from the captured images. Again, the pixel resolution is very small and the measurement error is due entirely to the error involved in selecting a single separation height. The method for selecting the separation height is given in Chapter 5. To account for the variation in separation heights among experiments, all the experiments were plotted togther and the best-fit relationship between non-dimensional crossflow and slip velocity was selected.

A.3.3 Errors in calculated quantities

Errors in each of the measured quantities must be propagated through appropriate means to obtain the errors in calculated quantities. As an example, consider the quantity, F, calculated from n measurements, $\boldsymbol{x} = (x_1, x_2, ..., x_n)$, such that

$$F = f(\boldsymbol{x}). \tag{A.13}$$

Given the individual errors, δx_i, in the measurements, the propagated error in F is calculated as

$$\delta F = \sqrt{\sum_{i=1}^{n} \left(\left(\frac{\partial f}{\partial x_i} \right) \delta x_i \right)^2} \tag{A.14}$$

and (A.14) is known as the measurement error equation.

Experimental parameters

There are five experimental parameters that describe a given experiment, namely, H, u_s, u_∞, B, and N. The error in H comes from the resolution of the measuring tape and the extent of the meniscus and is estimated as ± 0.3 cm. The slip velocity, u_s, is measured by

a number of techniques, and its error was reported in Section A.1.2. The crossflow velocity is due to the towing mechanism; thus, u_∞ is uniform over the depth. The error in the estimation of u_∞ was reported above as ± 0.5 cm/s.

The buoyancy flux is calculated from two measurements: the buoyant fluid flow rate, Q, and the buoyant fluid density, ρ_b. The error in the calculated buoyancy flux is then given by

$$\delta B = \sqrt{\left(\frac{g(\rho - \rho_b)}{\rho}\delta Q\right)^2 + \left(\frac{gQ}{\rho}\delta\rho_b\right)^2} \tag{A.15}$$

where the gravitational constant, g, and the reference density, ρ, are assumed to contribute no error. For air bubbles at a gas flow rate of 0.15 Std L/min, $B = (2.06 \pm 0.07) \cdot 10^{-5}$ m^4/s^3.

For a discretized density profile, the buoyancy frequency is calculated from two points, (z_1, ρ_1) and (z_2, ρ_2), and the estimate error is given by

$$\delta N = \sqrt{\frac{g(\delta\rho)^2}{2\rho(\rho_1 - \rho_2)(z_1 - z_2)} + \frac{g(\rho_1 - \rho_2)(\delta z)^2}{2\rho(z_1 - z_2)^3}}, \tag{A.16}$$

assuming the errors in ρ_1 and ρ_2 are both of order $\delta\rho$ and the errors in z_1 and z_2 are both of order δz. For the density profile in Figure A-6, the buoyancy frequency would be $N = 0.337 \pm 0.005$ s^{-1}.

Plume flux quantities

Calculated plume quantities include the plume volume fluxes and the mass flux of peeled dye. For a discussion of the errors in the flux measurements, refer to Chapter 4, which discusses an optimization scheme to estimate the fluxes from other measurements and presents an error analysis that relies on comparisons of multiple experiments.

Appendix B

Observations

This appendix presents all of the experiments conducted in stagnant, stratified and flowing environments. Chapter 3, 4 and 5 present the analysis of these observations.

B.1 Stagnant experiments

A total of 30 exploratory and quantitative stagnant stratified experiments were conducted. Several of these were replicates in which no images were captured. Table B.1 summarizes the experimental conditions for each of the experiments presented in the following figures. Chapters 3 and 4 present additional refinements and correlate these observations to predictive models. Although the still images are instructive, much insight was gained by observing the experiments first-hand and by watching the videos of the captured images. For instance, in the still photos, it is not possible to tell what fluid is moving up and what is moving down. Both the still images and the moving experiments were drawn upon to describe the three deep-water plume (or peel) types.

B.1.1 Type 1* plumes

At sufficiently low slip velocity compared to the velocity of fluid motions in the plume, the bubbles become weak and are forced around by the motion of the plume fluid. When this occurs at the detrainment zone, the bubbles can leave the inner core and intrude partially

Experiment	Buoyant fluid	Diffuser	Light source	Flow rate [Std L/min]	Slip velocity [cm/s]	Buoyancy frequency [s^{-1}]	Type
so50	GOM-oil	small	LIF	0.50	8	0.31	T1*
air1	air	lime	LIF	0.150	7.2	0.31	T1*
air2	air	lime	LIF	0.150	7.2	0.31	T1*
air4	air	lime	LIF	0.150	7.2	0.31	T1*
exp1	air	lime	LIF	0.150	7.2	0.31	T1*
T033	air	lime	LIF	0.200	7.2	0.31	T1*
T043	air	lime	LIF	0.200	7.2	0.33	T1*
l250	air	lime	LIF	0.250	7.2	0.31	T1*
lime1	air	lime.	shad.	0.500	7.2	0.27	T1*
sed4	glass	funnel	LIF	0.114	3.2	0.28	T1*
sed5	glass	funnel	LIF	0.092	3.2	0.30	T1*
shad1	air	green	shad.	5.0	23.3	0.25	T2
g07a	air	green	LIF	7.0	23.3	0.50	T2
sed1	glass	funnel	LIF	0.056	7.1	0.23	T2
sed2	glass	funnel	LIF	0.051	7.1	0.27	T2
sed6	glass	funnel	LIF	0.075	11.1	0.32	T2
s25o	veg. oil	small	LIF	0.250	10	0.25	T3
air3	air	green	LIF	0.150	23.3	0.31	T3
T013	air	green	LIF	0.394	23.3	0.31	T3
g50a	air	green	LIF	0.500	23.3	0.25	T3
air5	air	green	LIF	1.0	23.3	0.31	T3

TABLE B.1: Parameter values for stagnant experiments. Abbreviations in the table are as follows: veg. oil = vegetable oil, glass = glass beads, green = aquarium airstone, lime = limewood diffuser, funnel = funnel diffuser, and shad. = shadowgraph light.

with the detraining water. As the detrained fluid decelerates, the bubbles regain strength and rise to join the original plume above the detrainment zone, taking some detrained fluid upward into the secondary plume. Such plume behavior is different enough from the Type 2 and 3 plumes that a new type was defined, Type 1* (named to distinguish it from the Type 1 plume defined by Asaeda & Imberger (1993), one in which there are no sub-surface intrusions). Figures B-1 and B-2 present examples of Type 1* plume (or peeling) behavior.

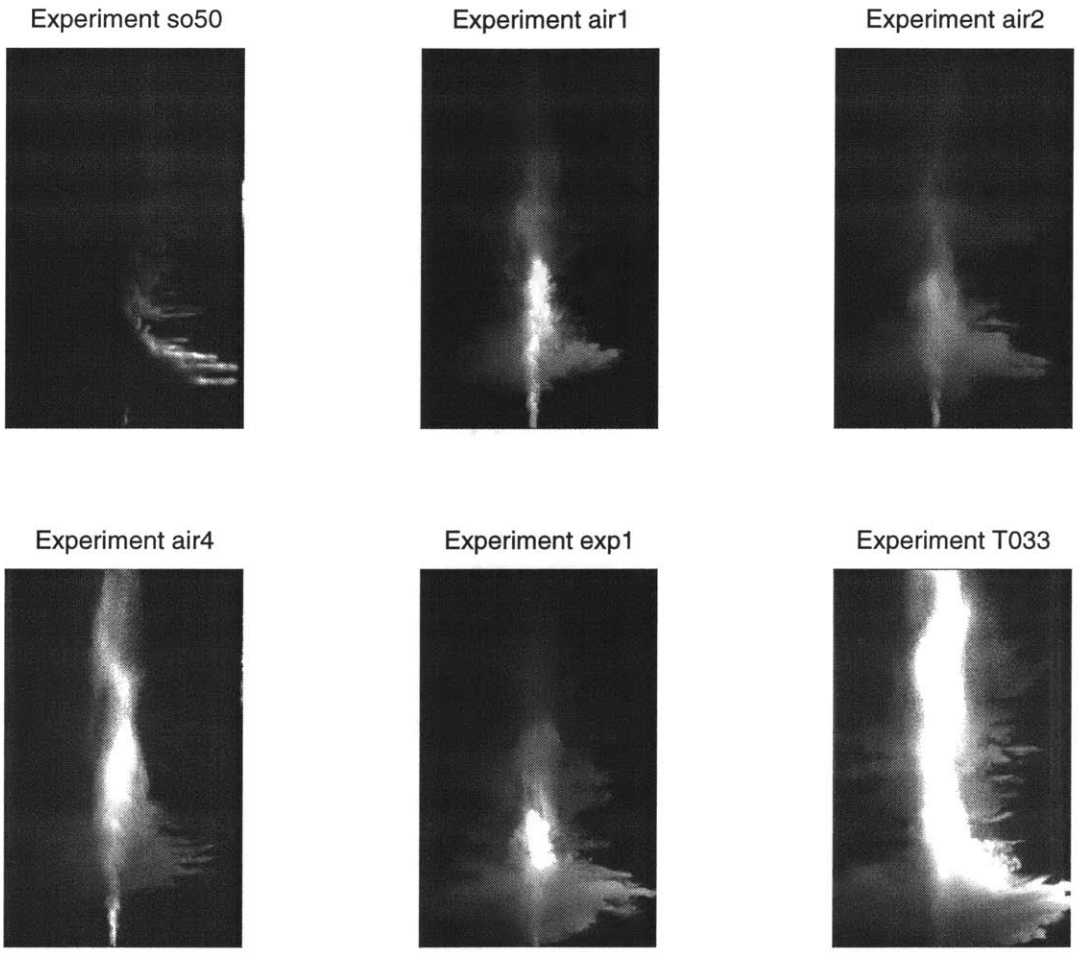

FIGURE B-1: Captured images of Type 1* plumes. Refer for Table B.1 for the experimental parameters.

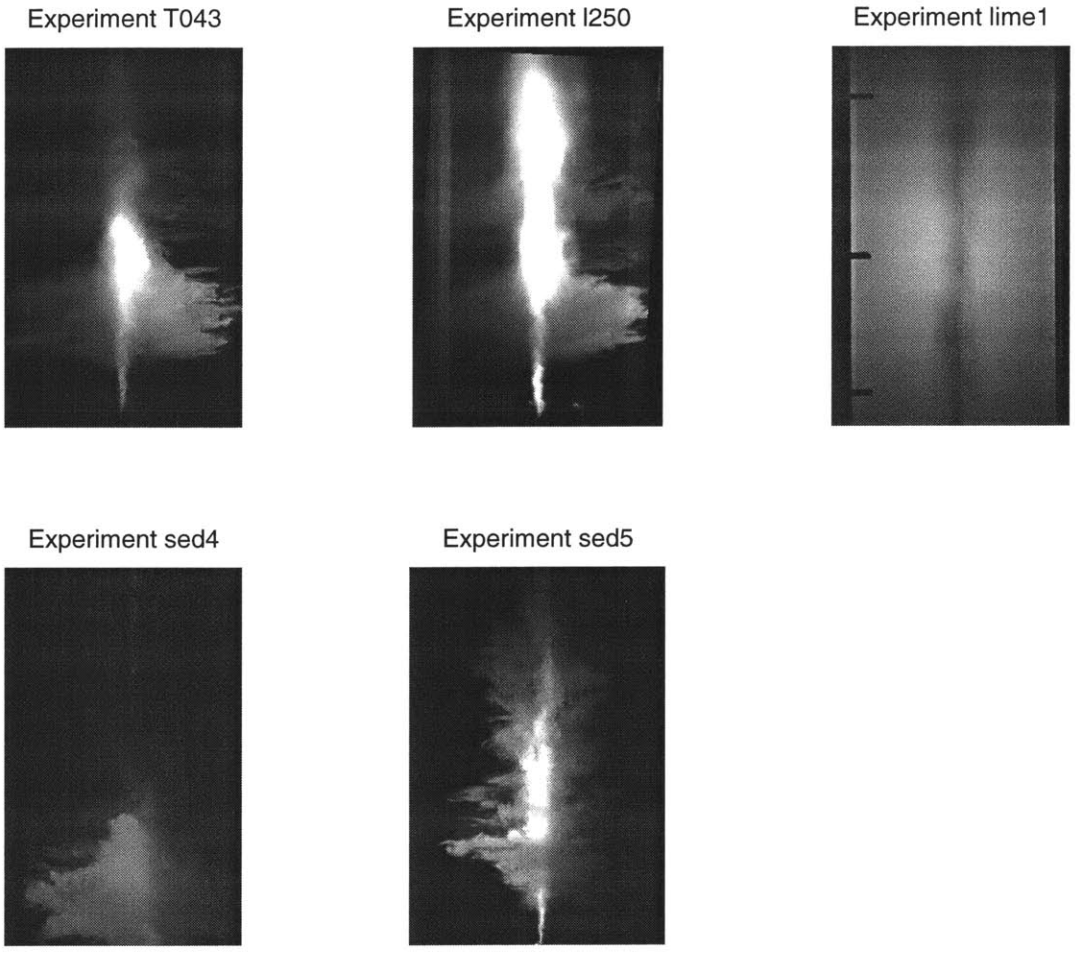

FIGURE B-2: Captured images of Type 1* plumes, continued. Refer for Table B.1 for the experimental parameters.

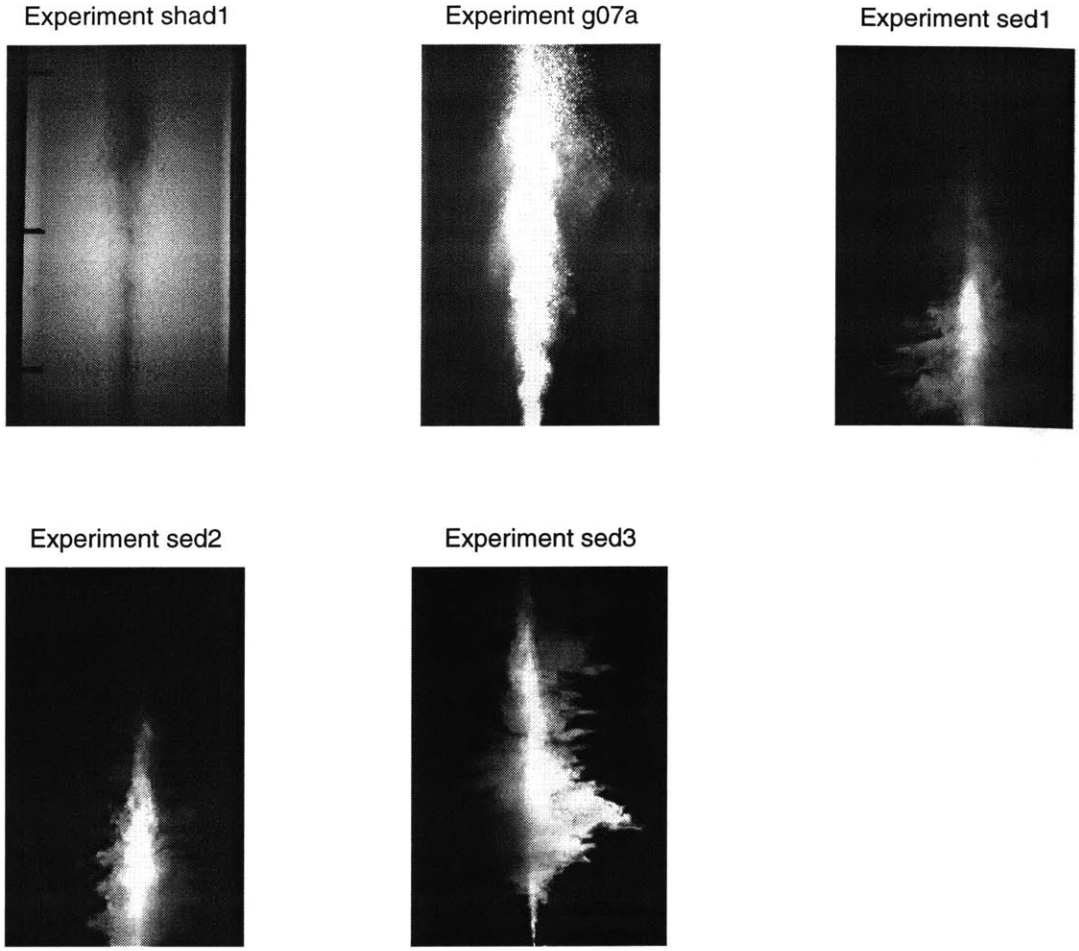

FIGURE B-3: Captured images of Type 2 plumes. Refer for Table B.1 for the experimental parameters.

B.1.2 Type 2 plumes

Type 2 plumes (or peels) have efficient peeling events that produce non-overlapping intrusions; Figure B-3 presents two examples of a Type 2 plume. Although shadowgraph imaging is very instructive in the laboratory, the camera, unfortunately, cannot discern the subtle light changes with only 256 levels of grey and the shadowgraph images are less useful.

B.1.3 Type 3 plumes

In contrast to Type 2 plumes, the Type 3 plume (or peel) has inefficient peeling that leads to overlapping intrusions; Figure B-4 presents several examples of Type 3 plumes.

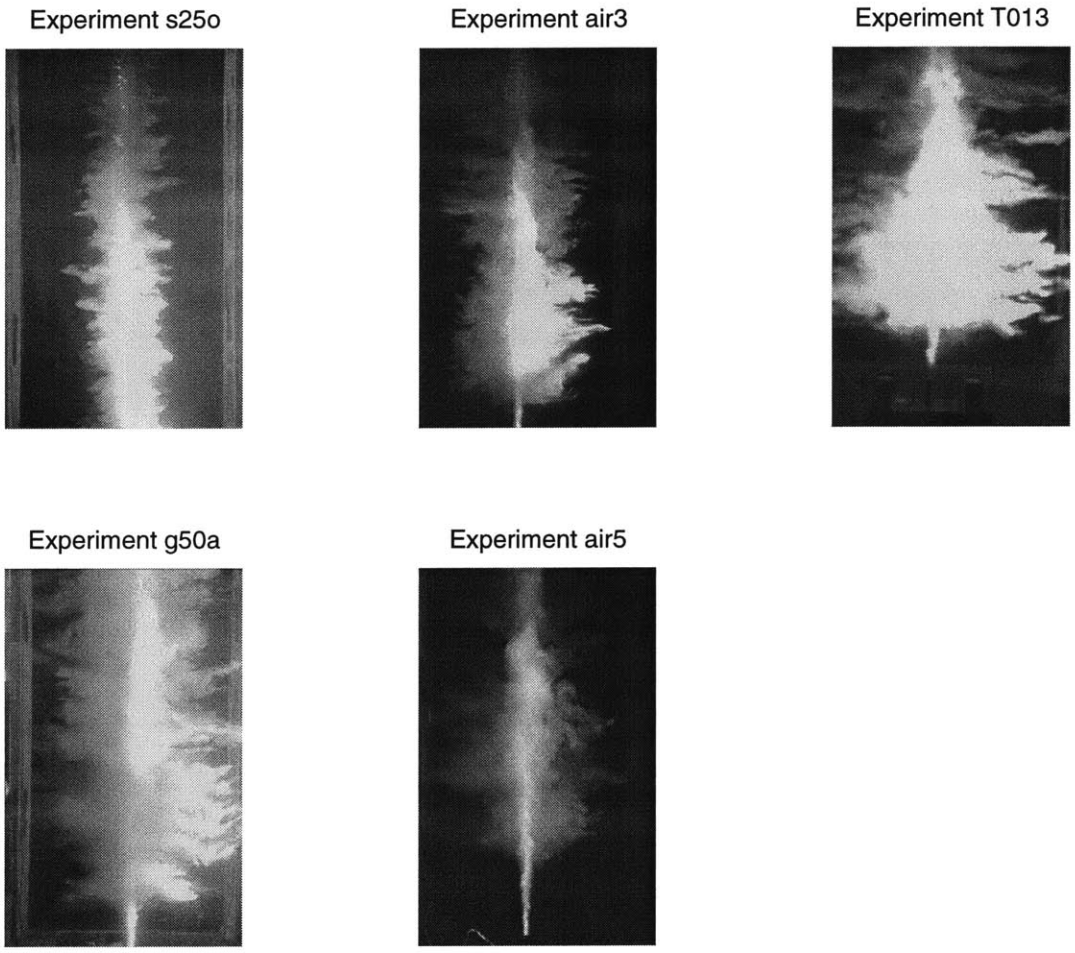

FIGURE B-4: Captured images of Type 3 plumes. Refer for Table B.1 for the experimental parameters.

Each plume in Figure B-4 has essentially the same bubble slip velocity and stratification; the images are organized in increasing buoyancy flux.

B.1.4 Summary

These laboratory experiments indicate a significant difference in behavior among the three deep-ocean plume types, differences that impact the intrusion formation and, thus, the fate of CO_2 and oil in the water column. The important characteristics can be summarized as follows:

- The peeling efficiency controls the character of the intrusions that forms. For efficient peels, the intrusions are distinct and non-overlapping; this is called Type 2 behavior. For inefficient peels, the intruding flow originates continually along the plume core and the intrusions overlap; this is called Type 3 behavior.

- Peeling efficiency depends on the bubble dynamics. If the bubbles adhere to a narrow, fast-rising inner core, eddies that are deflected to the outer edges of the plume are lost and the efficiency is low: Type 3 behavior. As the bubbles spread out and have a lower rise velocity in comparison to the upward velocity of the bulk plume fluid, the eddies are transported more effectively and complete detrainment occurs at a series of terminal levels: Type 2 behavior. When the bubbles occupy the full plume width and have a low rise velocity in comparison to the bulk plume fluid, efficient detrainment occurs in the first peel, but bubbles are transported into the intruding flow. These deflected bubbles entrain fluid from the downdraught plume and catch up to the secondary plume, thus reducing the efficiency of the peel: Type 3 behavior. Hence, efficiency is linked to plume Type, but not necessarily to a single mechanism of plume dynamics.

- A significant portion, often all, of the rising plume core is shrouded by the annular downdraught intrusion flow.

- Type 3 behavior transports entrained fluid vertically more efficiently than Type 2 behavior; thus, dye in Type 3 plumes reaches greater heights than in Type 2 plumes with equivalent buoyancy.

Experiment	Diffuser	Crossflow velocity [cm/s]	Gas flow rate at STP [mL/min]	Saltwater flow rate [mL/min]	Dye Injected ? [yes/no]
A1	Limewood	0	167	0	no
A2	Limewood	0	167	0	yes
A3	Funnel	0	0	860	yes
A4	Limewood	2	167	0	no
A5	Limewood	2	167	0	yes
A6	Funnel	2	0	860	yes
A7	Limewood	10	167	0	no
A8	Limewood	10	167	0	yes
A9	Funnel	10	0	860	yes

TABLE B.2: Parameter values for shake-down experiments.

- Because Type 2 peels are not completely efficient, it is expected that all plumes eventually exhibit Type 3 behavior (though our tank is not deep enough to observe this transition). It is not known whether Type 2 behavior would re-assert itself in such a situation.

B.2 Crossflow experiments

A total of 45 exploratory and quantitative crossflow experiments were conducted in uniform and stratified ambients. The experimental conditions for each of these experiments are summarized in the following sections. Chapter 5 presents additional refinements and correlates these observation to predictive tools.

B.2.1 Gas experiments with the recirculation pump

An initial set of experiments was conducted using air only and the recirculation crossflow generated by the pump. Images captured during these experiments are summarized in Figure B-5. The conditions of each experiment were as shown in Table B.2. The funnel diffuser refers to dense saltwater experiments designed to show the difference between single- and multi-phase plumes. In Figure B-5 the photos for the funnel experiments (column 3)

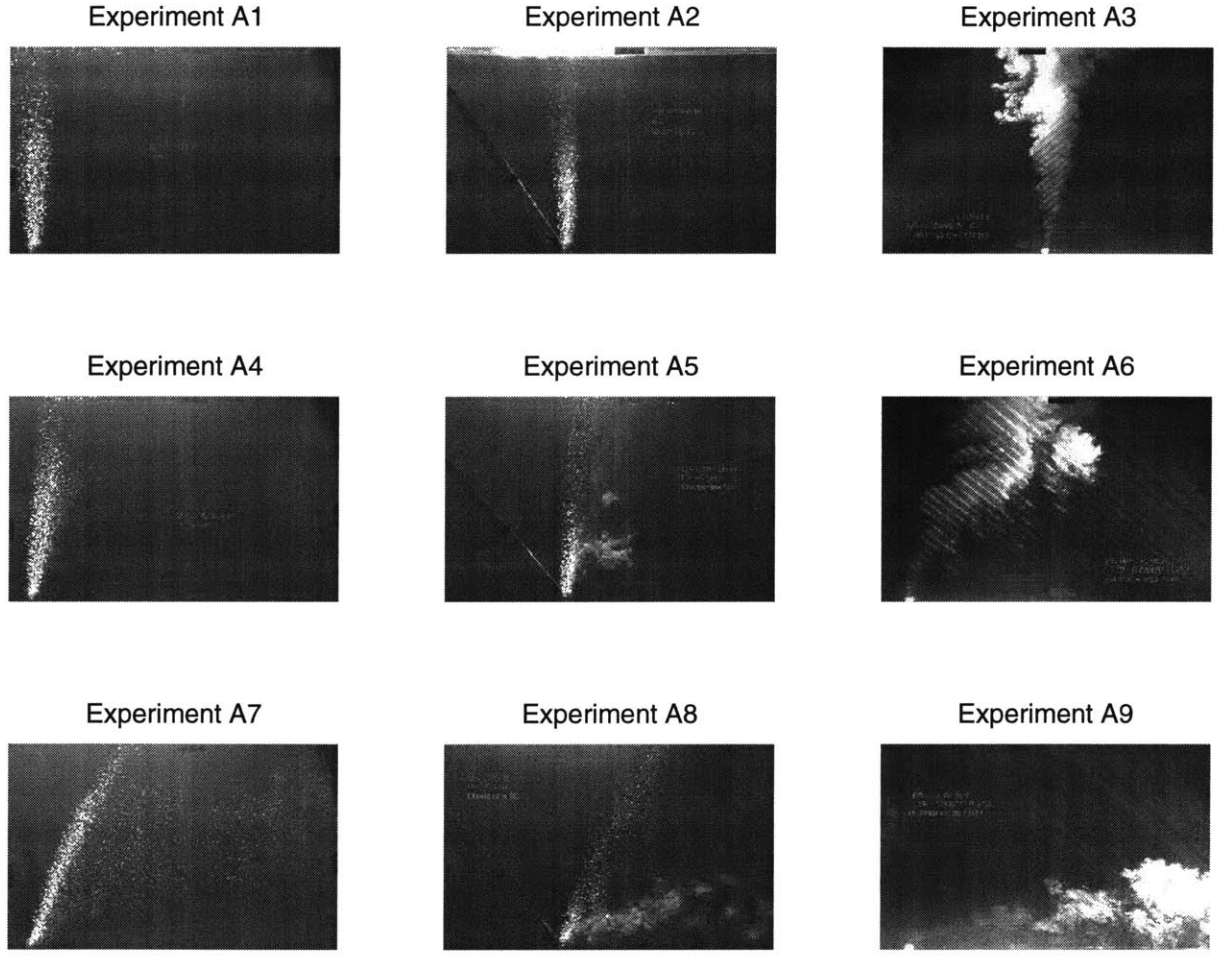

FIGURE B-5: Images of pump experiments with gas, dye, and dense water. Refer to Table B.2 for parameter values.

are shown up-side-down so that they have the same orientation as the bubble experiments with the same absolute buoyancy. The buoyancy flux for the dense water and air bubble experiments was the same, even though the volume flux was quite different. The buoyancy flux should control the behavior of these plumes.

The experiments in column 1 of Figure B-5 were with air only, column 2 had air and injected dye, and column 3 presents the dense water experiments having saltwater and dye.

Based on the various dye injection methods tested during this set of experiments, we decided it was important to inject the dye upstream of the plume to insure that it was entrained and not lost right away on the downstream side. A range of pump flow rates was also tested to help design the towing mechanism. Small bubbles were observed to leave the main bubble plume beginning at a crossflow velocity as low as 2 cm/s. From these experiments the towing mechanism described above was designed and built.

B.2.2 Gas experiments with the towing mechanism

The remaining experiments were conducted using the towing mechanism, the first set of which were designed to observe the fate of dye tracer entrained at the base of pure gas plumes, analogous to the experiments presented in the previous section in column 2 of Figure B-5. The images from this set of tests are cataloged in Figure B-6 and are summarized in Table B.3.

Experiments B1 to B8 were with a 6 mm diameter piece of vinyl tubing, Experiment B9 was with dye only, and Experiments B10 and B11 were with the aquarium airstone.

B.2.3 Oil plume experiments

A wide range of parameter values were tested in the third set of experiments which involved oil, gas, and alcohol in various combinations using the towing mechanism. These experiments are summarized in Figures B-7 and B-8 and are listed in Table B.4.

Three oil flow rates were selected (250, 600, and 1000 mL/min) and four air flow rates were selected (250, 600, 1000, and 2500 mL/min). These flow rates were combined primarily in gas/oil ratios of 1:1 (which corresponds to a gas/oil ratio (GOR) of 100 at 1000 m depth

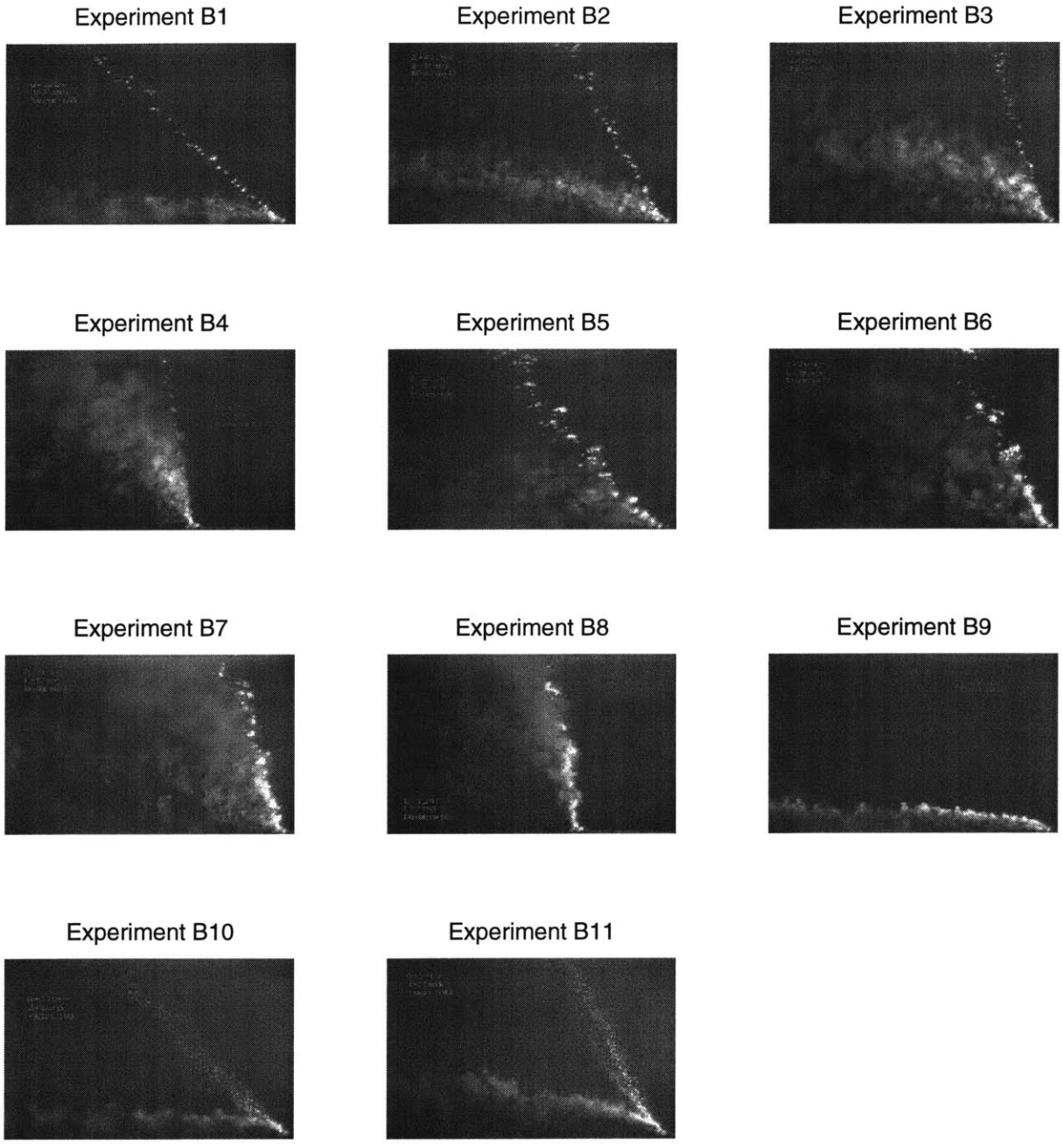

FIGURE B-6: Images of towed experiments with gas and dye. Refer to Table B.3 for parameter values.

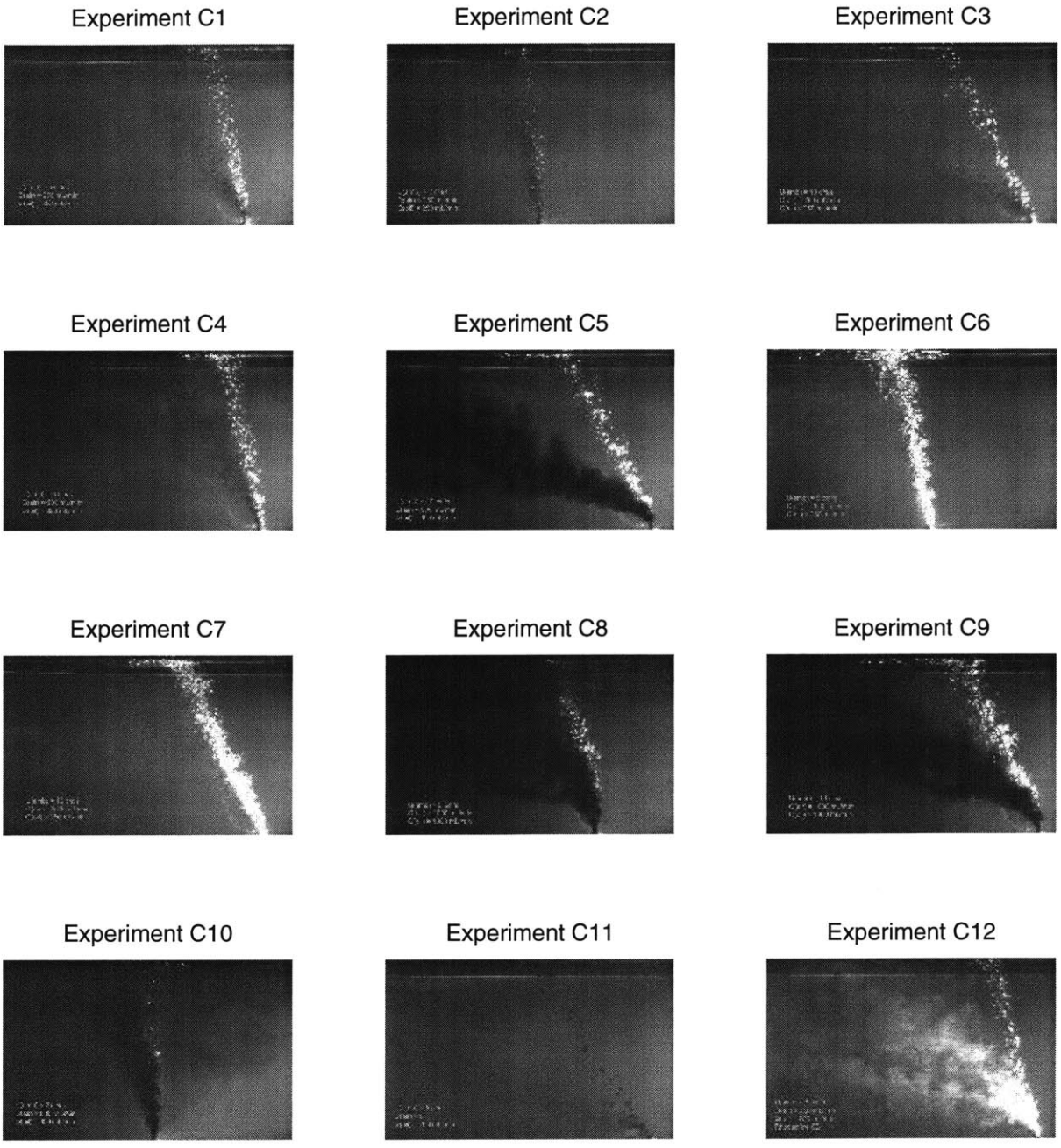

FIGURE B-7: Towed experiments with gas, oil and alcohol. Refer to Table B.4 for parameter values.

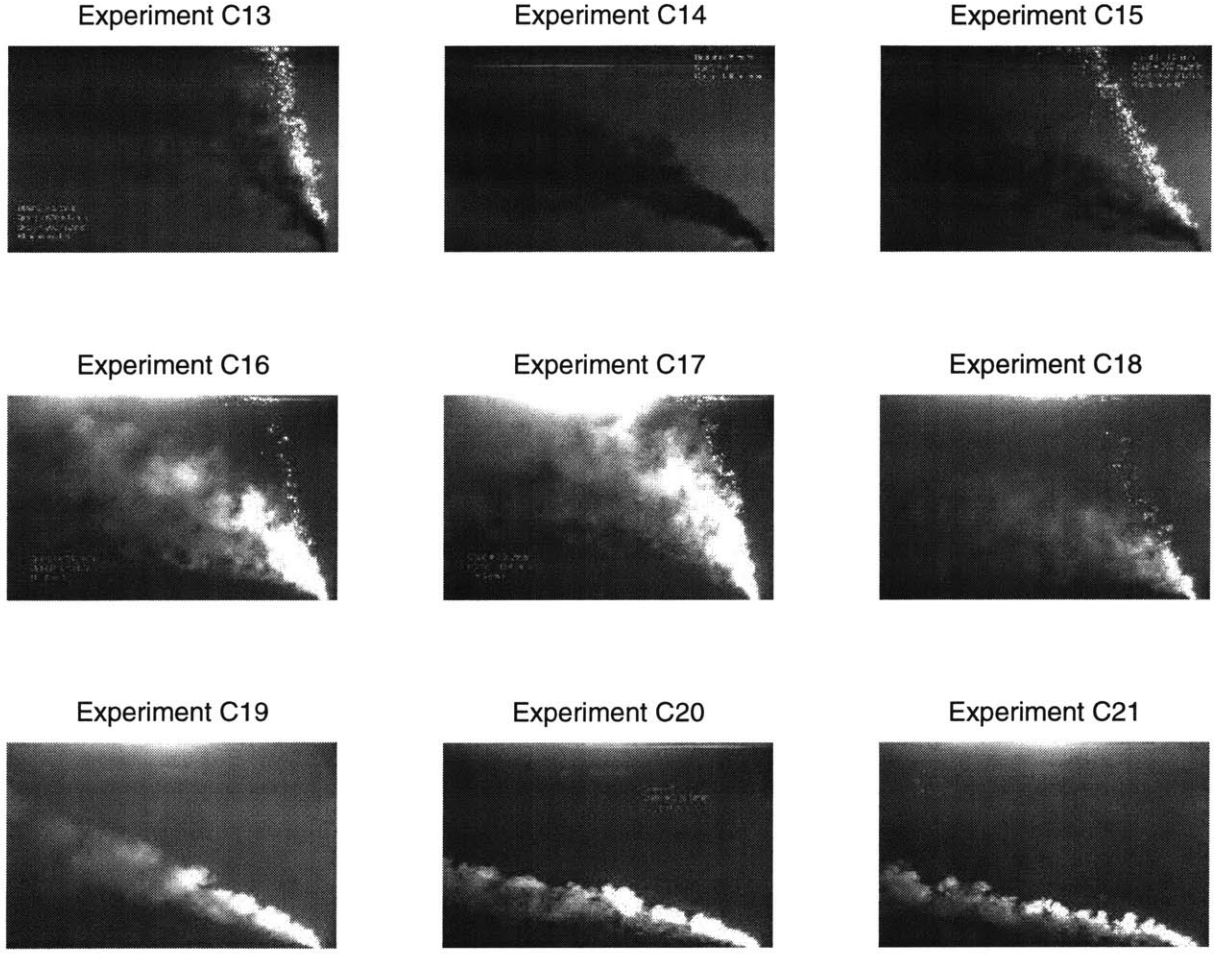

FIGURE B-8: Towed experiments with gas, oil and alcohol, continued. Refer to Table B.4 for parameter values.

Experiment	Diffuser	Crossflow velocity [cm/s]	Gas flow rate at STP [mL/min]
B1	Vinyl Tube	20	200
B2	Vinyl Tube	10	200
B3	Vinyl Tube	5	200
B4	Vinyl Tube	2	200
B5	Vinyl Tube	20	2000
B6	Vinyl Tube	10	2000
B7	Vinyl Tube	5	2000
B8	Vinyl Tube	2	2000
B9	Dye only	10	0
B10	Airstone	20	200
B11	Airstone	10	200

TABLE B.3: Parameter values for air experiments.

in the field), with two experiments (numbers C6 and C7) having a gas/oil ratio of 10:1 (GOR of 1000 in the field, admittedly a high number). Pure isopropyl alcohol was also used in some experiments to simulate the influence of very small oil droplets on the characteristics of the plume (since the equivalent "slip velocity" of alcohol is 0). The density of oil used was 0.87 g/cm^3; the density of alcohol was 0.78 g/cm^3. So that the buoyancy flux of alcohol would be the same as that for oil, two alcohol flow rates were selected (150 and 360 mL/min) which correspond to the two lowest oil flow rates (250 and 600 mL/min, respectively). Dye was added to some of the experiments to aid visualization.

B.2.4 Stratified crossflow experiments

The final set of experiments explored the effect of stratification in a crossflow. The tank was stratified over an 8 m-long section by installing bulkheads at the up- and downstream ends and using the two-tank method. Due to leakage around the bulkheads, the stratification profile changed some during the experiment and was not completely linear. However, the plume trapped in the stagnant case at the predicted trap height (of order 10 cm) so the stratification profile was considered acceptably stable and linear.

Experiment	Crossflow velocity [cm/s]	Gas flow rate at STP [mL/min]	Oil flow rate [mL/min]	Alcohol flow rate [mL/min]	Dye Injected ? [yes/no]
C1	5	250	250	0	no
C2	2	250	250	0	no
C3	10	250	250	0	no
C4	5	600	600	0	no
C5	10	600	600	0	no
C6	5	2500	250	0	no
C7	10	2500	250	0	no
C8	5	1000	1000	0	no
C9	10	1000	1000	0	no
C10	2	600	600	0	yes
C11	5	0	250	0	yes
C12	5	250	250	0	yes
C13	5	600	600	0	yes
C14	5	0	600	0	yes
C15	10	600	600	0	yes
C16	5	250	0	150	yes
C17	5	600	0	360	yes
C18	10	600	0	360	yes
C19	5	0	0	150	yes
C20	10	0	0	360	yes
C21	10	0	0	150	yes

TABLE B.4: Parameter values for oil experiments.

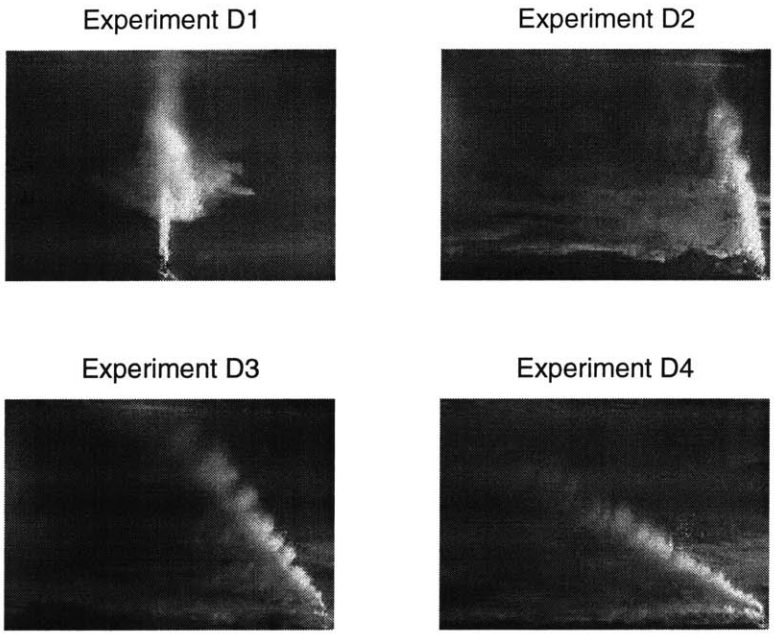

FIGURE B-9: Towed experiments in stratification with gas and dye. Refer to Table B.5 for parameter values.

Experiment	Crossflow velocity [cm/s]	Gas flow rate at STP [mL/min]	Stratification frequency [s^{-1}]	Predicted trap height [m]	Dye Injected ? [yes/no]
D1	0	100	0.5	0.1	yes
D2	2	100	0.5	0.1	yes
D3	5	100	0.5	0.1	yes
D4	10	100	0.5	0.1	yes

TABLE B.5: Parameter values for stratified experiments.

Figure B-9 shows images captured during the experiments and Table B.5 reports the parameter values for each experiment. All four experiments were conducted with air only using the limewood diffuser. The salt used to create the stratification caused the limewood diffuser to produce only small bubbles with a slip velocity of 7.2 cm/s.

B.2.5 Summary

These laboratory experiments indicate a significant difference between the behavior of single-phase and two-phase plumes in a crossflow. These differences are important since

traditional integral plume models ignore some of the physical differences between two-phase and single-phase plumes. The important differences described above can be summarized as follows:

- The trajectories of pure oil, and pure gas plumes are much different from single-phase plumes having the same buoyancy flux because of the effect of the slip velocity of the oil droplets and gas bubbles.

- When there is a distribution of bubble or droplet sizes, rising bubbles and droplets are fractionated by the current, causing large droplets to lead out front with a gradual transition to smaller droplets in the lee of the plume. This was observed even at very low crossflow velocities (2 cm/s and greater).

- Injected dye (which marks entrained ambient water and could also represent fine oil droplets) is observed to leak from the downstream side of a gas or oil and gas plume, even at low current speeds, as observed by Davidson & Pun (1999) for single-phase plumes. Hence, the entrained water and rising bubbles become more independent of each other with increasing current speed and with increasing height above the release point.

- When ambient water, oil droplets and air bubbles become separated, the situation can no longer be modeled with a traditional integral plume model because the different constituents maintain different trajectories. These effects are more extreme for gas/oil/water plumes than for oil/water plumes or for oil/hydrate/water plumes.

- The effects above increase with increasing current speed and droplet/bubble slip velocity and with decreasing flow rate.

- In stratification, the above effects persist until the plume becomes stratification dominated (when the trap height due to stratification is lower than the separation height due to the crossflow). A stratification-dominated plume peels at a height predicted neglecting the crossflow, but the peel is asymmetrical (occurring only on the downstream side of the plume). A crossflow-dominated plume separates at the height expected without

stratification, but the separated plume does not continue to rise in the far-field because it contains dense water entrained below the separation point.

The application of the laboratory tests to the field-scale spills is discussed in Chapter 5.

Appendix C

Plume volume flux calculations

This appendix presents the raw data and calculated results for the 11 experiments described in Chapter 4. The figures present all of the calculated quantites along with plots of the four characteristic flow rates associated with the net-flux profiles. Horizontal error bars in the figures represent the measurement error assumed in the Bayesian estimation algorithm and are centered at the measured value. The open circles show the estimated values obtained through the optimization technique.

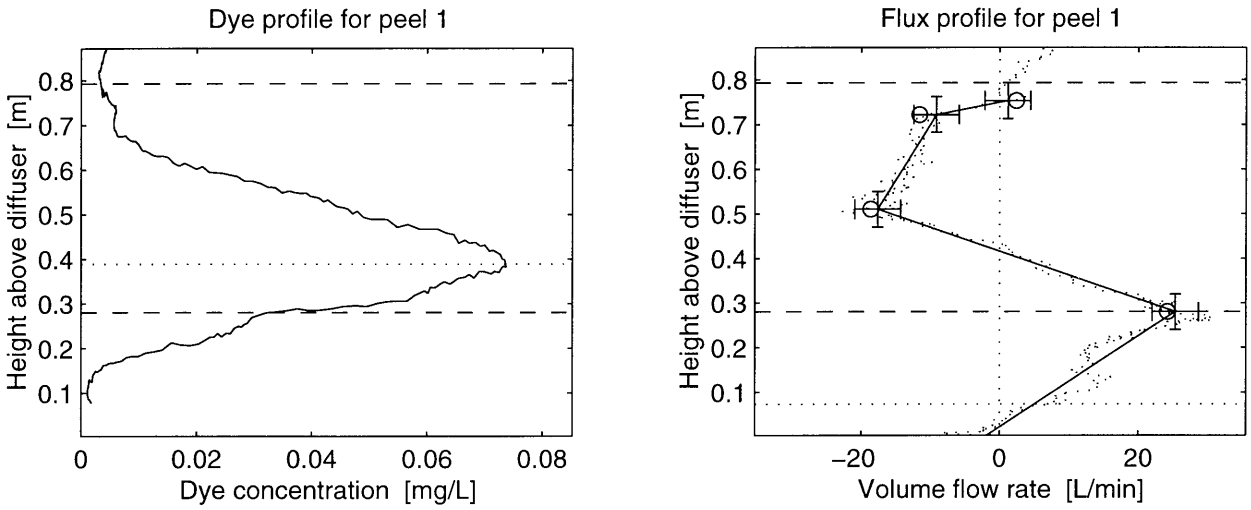

Q1 = 24.2 [L/min]	c1 = 0.39 [mg/L]	p1 = 1026 [Kg/m^3]	B1 = −347.9 [Kg/m^3]
Q2 = 2.43 [L/min]	c2 = 0.31 [mg/L]	p2 = 1024 [Kg/m^3]	B2 = −253.7 [cm^4/s^3]
Ql = 7.04 [L/min]	co = 0 [mg/L]	po = 1023 [Kg/m^3]	Bo = 0 [cm^4/s^3]
Qe = 14 [L/min]	ci = 0.2 [mg/L]	pi = 1023 [Kg/m^3]	Bi = 0 [cm^4/s^3]
Qi = 42.8 [L/min]	cp = 0.31 [mg/L]	pp = 1024 [Kg/m^3]	Bp = −4391 [cm^4/s^3]
Qp = 42 [L/min]	cr = 0.2 [mg/L]	pr = 1023 [Kg/m^3]	Br = −474.8 [cm^4/s^3]
Qr = 20.3 [L/min]	ht = 0.39 [m]	hp = 0.79 [m]	f = 0.95 [−−]

FIGURE C-1: Bayesian estimation results for Experiment T04.

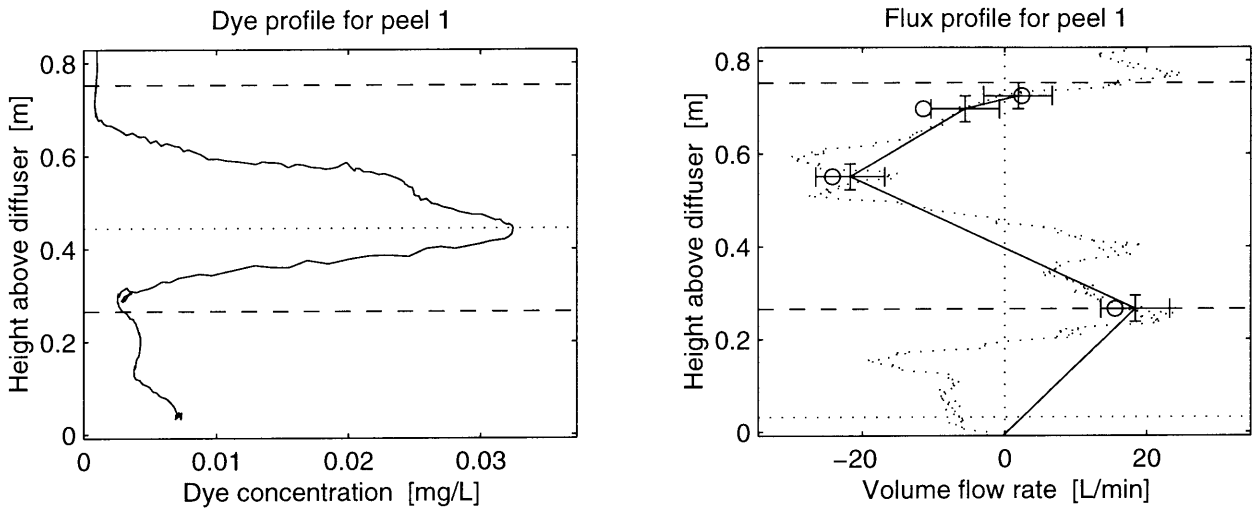

Q1 = 15.5 [L/min]	c1 = 0.27 [mg/L]	p1 = 1025 [Kg/m^3]	B1 = −128.9 [Kg/m^3]
Q2 = 2.4 [L/min]	c2 = 0.18 [mg/L]	p2 = 1024 [Kg/m^3]	B2 = −185.5 [cm^4/s^3]
Ql = 12.8 [L/min]	co = 0 [mg/L]	po = 1022 [Kg/m^3]	Bo = 0 [cm^4/s^3]
Qe = 13.8 [L/min]	ci = 0.096 [mg/L]	pi = 1022 [Kg/m^3]	Bi = 0 [cm^4/s^3]
Qi = 39.8 [L/min]	cp = 0.18 [mg/L]	pp = 1024 [Kg/m^3]	Bp = −2317 [cm^4/s^3]
Qp = 30 [L/min]	cr = 0.096 [mg/L]	pr = 1022 [Kg/m^3]	Br = −307.8 [cm^4/s^3]
Qr = 16.8 [L/min]	ht = 0.44 [m]	hp = 0.75 [m]	f = 0.93 [−−]

FIGURE C-2: Bayesian estimation results for Experiment Air1.

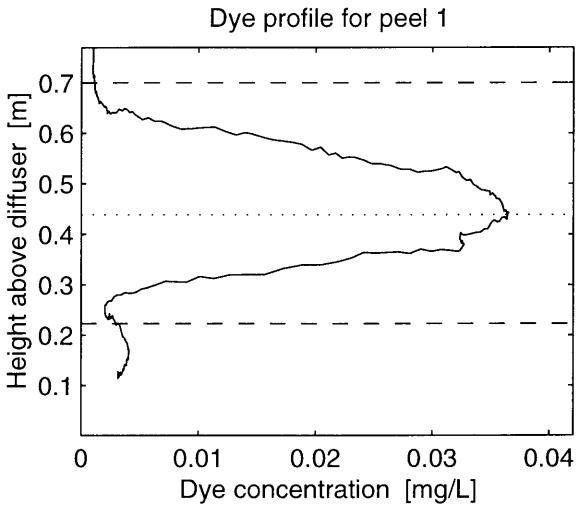

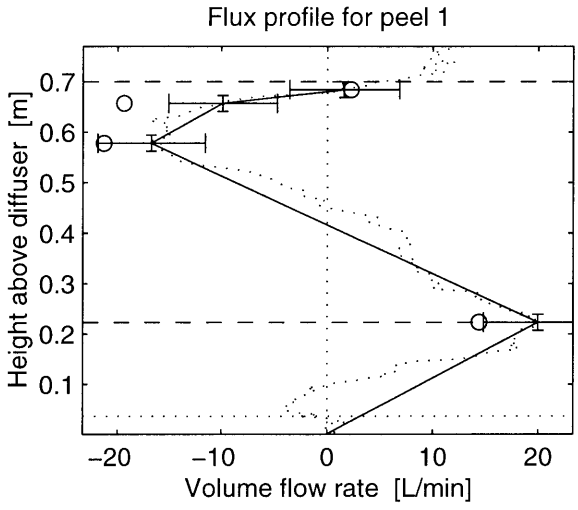

Q1 = 14.4 [L/min]	c1 = 0.29 [mg/L]	p1 = 1027 [Kg/m^3]	B1 = −139.8 [Kg/m^3]
Q2 = 2.29 [L/min]	c2 = 0.18 [mg/L]	p2 = 1025 [Kg/m^3]	B2 = −163.8 [cm^4/s^3]
Ql = 1.94 [L/min]	co = 0 [mg/L]	po = 1023 [Kg/m^3]	Bo = 0 [cm^4/s^3]
Qe = 21.7 [L/min]	ci = 0.11 [mg/L]	pi = 1023 [Kg/m^3]	Bi = 0 [cm^4/s^3]
Qi = 35.7 [L/min]	cp = 0.18 [mg/L]	pp = 1025 [Kg/m^3]	Bp = −2402 [cm^4/s^3]
Qp = 33.5 [L/min]	cr = 0.11 [mg/L]	pr = 1023 [Kg/m^3]	Br = −623.7 [cm^4/s^3]
Qr = 21.4 [L/min]	ht = 0.44 [m]	hp = 0.7 [m]	f = 0.94 [−−]

FIGURE C-3: Bayesian estimation results for Experiment Air2.

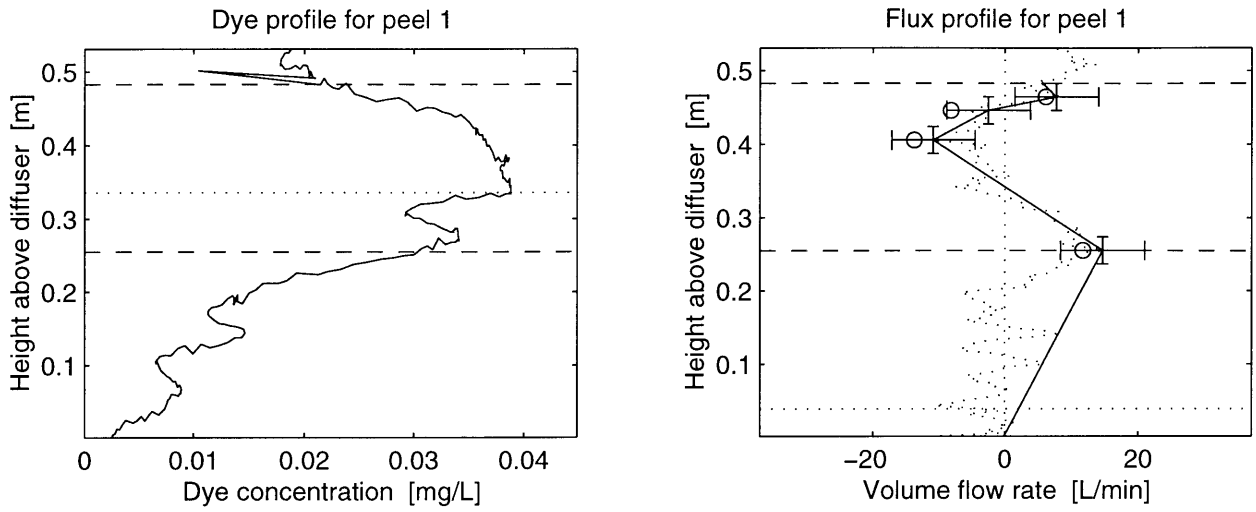

Q1 = 11.7 [L/min]	c1 = 0.51 [mg/L]	p1 = 1027 [Kg/m^3]	B1 = −108.3 [Kg/m^3]
Q2 = 6.15 [L/min]	c2 = 0.32 [mg/L]	p2 = 1025 [Kg/m^3]	B2 = −248.3 [cm^4/s^3]
Ql = 5.54 [L/min]	co = 0 [mg/L]	po = 1024 [Kg/m^3]	Bo = 0 [cm^4/s^3]
Qe = 14.2 [L/min]	ci = 0.16 [mg/L]	pi = 1024 [Kg/m^3]	Bi = 0 [cm^4/s^3]
Qi = 25.4 [L/min]	cp = 0.32 [mg/L]	pp = 1025 [Kg/m^3]	Bp = −797.6 [cm^4/s^3]
Qp = 19.8 [L/min]	cr = 0.16 [mg/L]	pr = 1025 [Kg/m^3]	Br = −179.1 [cm^4/s^3]
Qr = 14.2 [L/min]	ht = 0.34 [m]	hp = 0.48 [m]	f = 0.76 [−−]

FIGURE C-4: Bayesian estimation results for Experiment Air3.

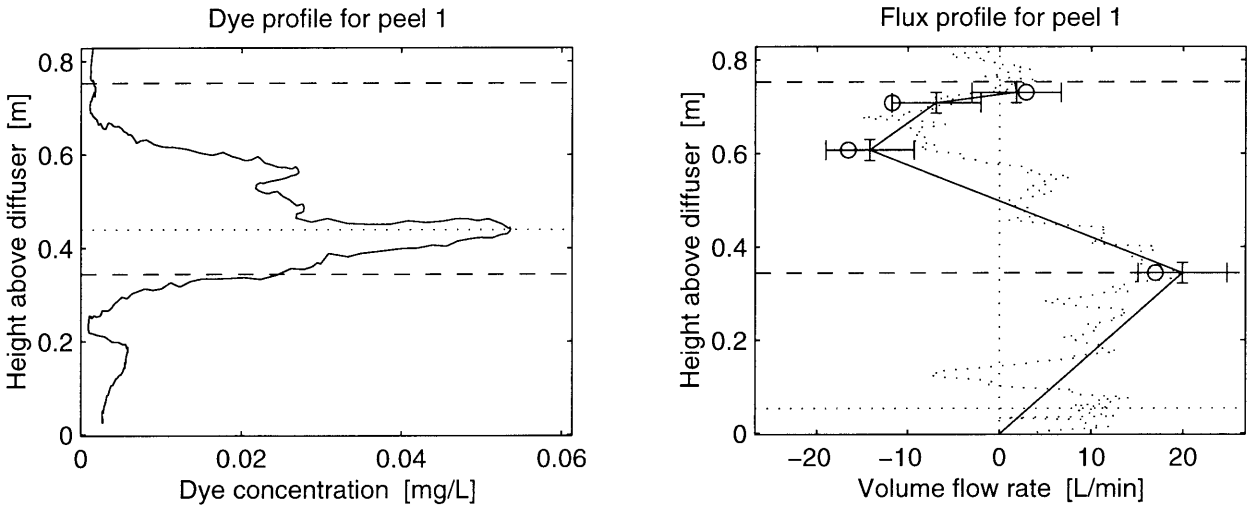

Q1 = 17 [L/min]	c1 = 0.27 [mg/L]	p1 = 1025 [Kg/m^3]	B1 = −376 [Kg/m^3]
Q2 = 2.91 [L/min]	c2 = 0.19 [mg/L]	p2 = 1024 [Kg/m^3]	B2 = −221.2 [cm^4/s^3]
Ql = 4.86 [L/min]	co = 0 [mg/L]	po = 1022 [Kg/m^3]	Bo = 0 [cm^4/s^3]
Qe = 14.6 [L/min]	ci = 0.12 [mg/L]	pi = 1022 [Kg/m^3]	Bi = 0 [cm^4/s^3]
Qi = 33.5 [L/min]	cp = 0.19 [mg/L]	pp = 1024 [Kg/m^3]	Bp = −2637 [cm^4/s^3]
Qp = 34.6 [L/min]	cr = 0.12 [mg/L]	pr = 1023 [Kg/m^3]	Br = −653.2 [cm^4/s^3]
Qr = 20.6 [L/min]	ht = 0.44 [m]	hp = 0.75 [m]	f = 0.92 [---]

FIGURE C-5: Bayesian estimation results for Experiment Air4.

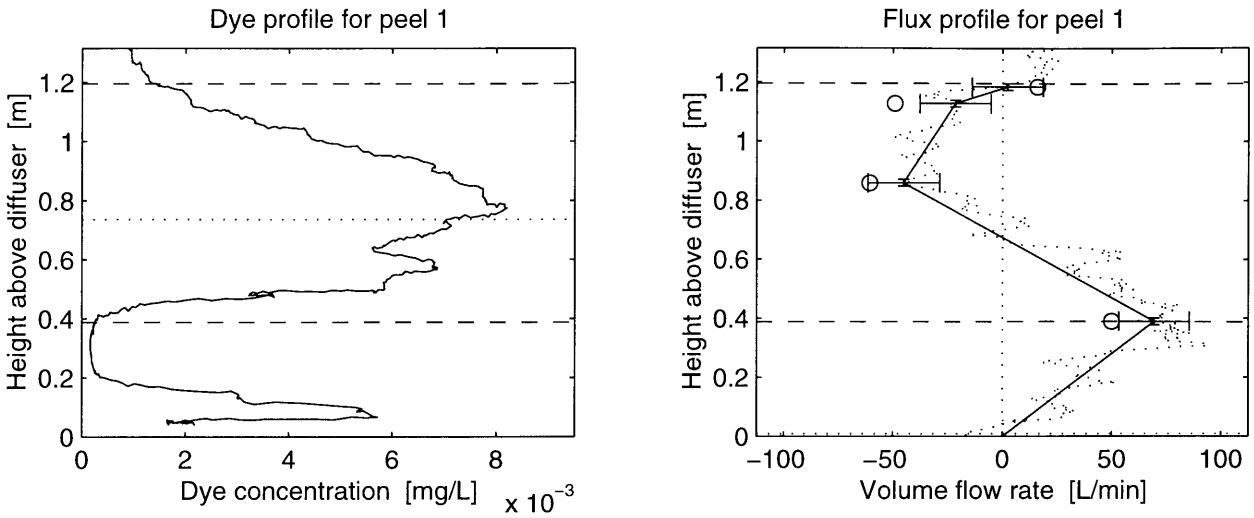

Q1 = 49.9 [L/min]	c1 = 0.067 [mg/L]	p1 = 1025 [Kg/m^3]	B1 = −1117 [Kg/m^3]
Q2 = 16 [L/min]	c2 = 0.039 [mg/L]	p2 = 1022 [Kg/m^3]	B2 = −1799 [cm^4/s^3]
Ql = 11.4 [L/min]	co = 0 [mg/L]	po = 1019 [Kg/m^3]	Bo = 0 [cm^4/s^3]
Qe = 65.1 [L/min]	ci = 0.025 [mg/L]	pi = 1019 [Kg/m^3]	Bi = 0 [cm^4/s^3]
Qi = 111 [L/min]	cp = 0.039 [mg/L]	pp = 1022 [Kg/m^3]	Bp = −1.481e+04 [cm^4/s^3]
Qp = 132 [L/min]	cr = 0.025 [mg/L]	pr = 1020 [Kg/m^3]	Br = −2569 [cm^4/s^3]
Qr = 97.6 [L/min]	ht = 0.74 [m]	hp = 1.2 [m]	f = 0.89 [−−]

FIGURE C-6: Bayesian estimation results for Experiment Air5.

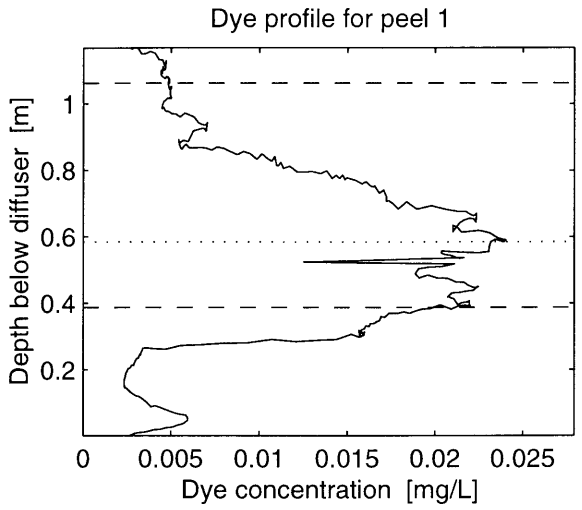

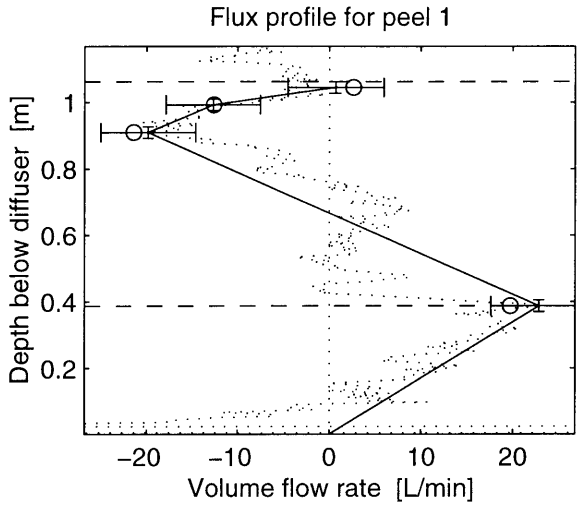

Q1 = 19.7 [L/min]	c1 = 0.29 [mg/L]	p1 = 1002 [Kg/m^3]	B1 = 236 [Kg/m^3]
Q2 = 2.64 [L/min]	c2 = 0.19 [mg/L]	p2 = 1004 [Kg/m^3]	B2 = 200.6 [cm^4/s^3]
Ql = 8.83 [L/min]	co = 0 [mg/L]	po = 1005 [Kg/m^3]	Bo = 0 [cm^4/s^3]
Qe = 15.2 [L/min]	ci = 0.13 [mg/L]	pi = 1005 [Kg/m^3]	Bi = 0 [cm^4/s^3]
Qi = 41.2 [L/min]	cp = 0.19 [mg/L]	pp = 1004 [Kg/m^3]	Bp = 4025 [cm^4/s^3]
Qp = 53 [L/min]	cr = 0.13 [mg/L]	pr = 1005 [Kg/m^3]	Br = 1543 [cm^4/s^3]
Qr = 35.9 [L/min]	ht = 0.58 [m]	hp = 1.1 [m]	f = 0.95 [−−]

FIGURE C-7: Bayesian estimation results for Experiment Sed1.

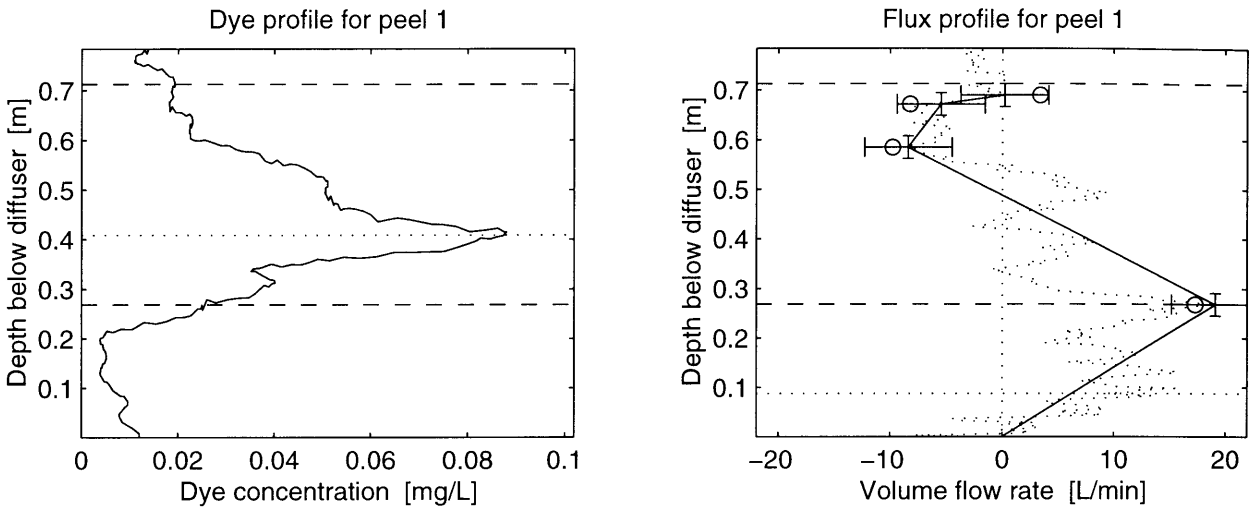

Q1 = 17.3 [L/min]	c1 = 0.55 [mg/L]	p1 = 1005 [Kg/m^3]	B1 = 55.07 [Kg/m^3]
Q2 = 3.4 [L/min]	c2 = 0.43 [mg/L]	p2 = 1006 [Kg/m^3]	B2 = 175 [cm^4/s^3]
Ql = 1.57 [L/min]	co = 0 [mg/L]	po = 1007 [Kg/m^3]	Bo = 0 [cm^4/s^3]
Qe = 11.6 [L/min]	ci = 0.3 [mg/L]	pi = 1007 [Kg/m^3]	Bi = 0 [cm^4/s^3]
Qi = 27.1 [L/min]	cp = 0.43 [mg/L]	pp = 1006 [Kg/m^3]	Bp = 1551 [cm^4/s^3]
Qp = 30.2 [L/min]	cr = 0.3 [mg/L]	pr = 1007 [Kg/m^3]	Br = 370 [cm^4/s^3]
Qr = 16.3 [L/min]	ht = 0.41 [m]	hp = 0.71 [m]	f = 0.90 [--]

FIGURE C-8: Bayesian estimation results for Experiment Sed2.

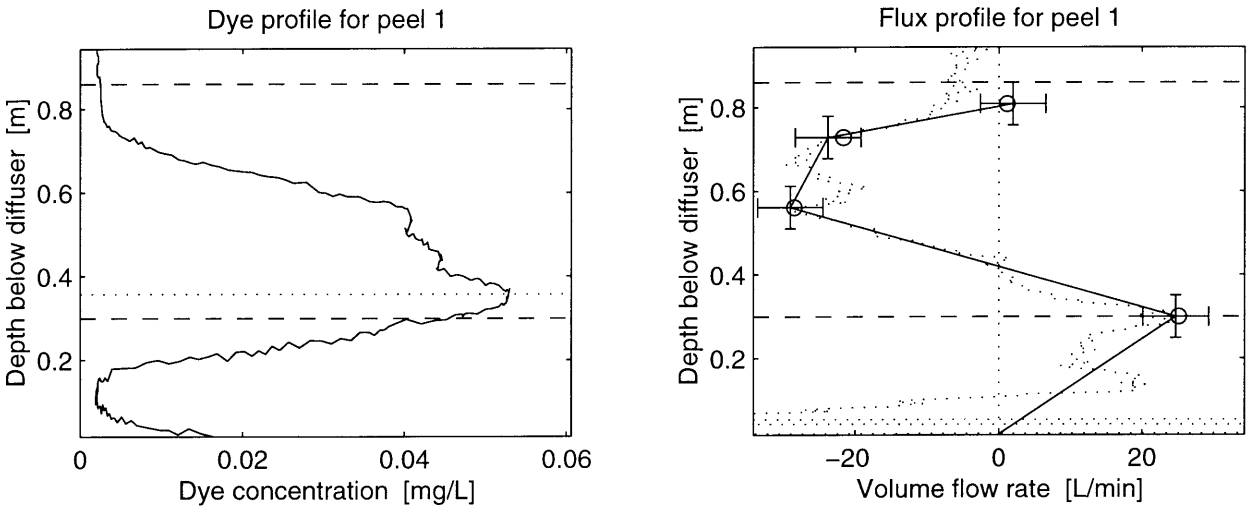

Q1 = 25.1 [L/min]	c1 = 0.31 [mg/L]	p1 = 1005 [Kg/m^3]	B1 = 319.2 [Kg/m^3]
Q2 = 1.19 [L/min]	c2 = 0.23 [mg/L]	p2 = 1006 [Kg/m^3]	B2 = 98.1 [cm^4/s^3]
Ql = 6.9 [L/min]	co = 0 [mg/L]	po = 1007 [Kg/m^3]	Bo = 0 [cm^4/s^3]
Qe = 22.8 [L/min]	ci = 0.14 [mg/L]	pi = 1007 [Kg/m^3]	Bi = 0 [cm^4/s^3]
Qi = 53.7 [L/min]	cp = 0.23 [mg/L]	pp = 1006 [Kg/m^3]	Bp = 3539 [cm^4/s^3]
Qp = 43 [L/min]	cr = 0.14 [mg/L]	pr = 1007 [Kg/m^3]	Br = 438.3 [cm^4/s^3]
Qr = 19 [L/min]	ht = 0.36 [m]	hp = 0.86 [m]	f = 0.97 [--]

FIGURE C-9: Bayesian estimation results for Experiment Sed4.

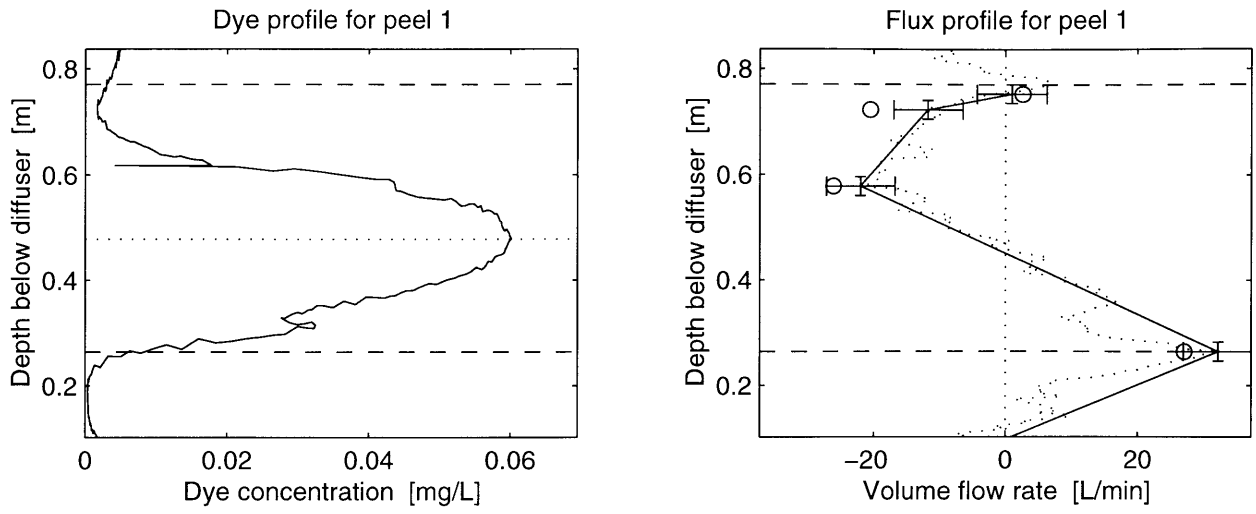

Q1 = 27.1 [L/min]	c1 = 0.24 [mg/L]	p1 = 1006 [Kg/m^3]	B1 = −48.37 [Kg/m^3]
Q2 = 2.58 [L/min]	c2 = 0.17 [mg/L]	p2 = 1007 [Kg/m^3]	B2 = 170.1 [cm^4/s^3]
Ql = 5.67 [L/min]	co = 0 [mg/L]	po = 1009 [Kg/m^3]	Bo = 0 [cm^4/s^3]
Qe = 23.1 [L/min]	ci = 0.12 [mg/L]	pi = 1009 [Kg/m^3]	Bi = 0 [cm^4/s^3]
Qi = 53.3 [L/min]	cp = 0.17 [mg/L]	pp = 1007 [Kg/m^3]	Bp = 3865 [cm^4/s^3]
Qp = 58.7 [L/min]	cr = 0.12 [mg/L]	pr = 1008 [Kg/m^3]	Br = 588.6 [cm^4/s^3]
Qr = 34.1 [L/min]	ht = 0.48 [m]	hp = 0.77 [m]	f = 0.96 [−−]

FIGURE C-10: Bayesian estimation results for Experiment Sed5.

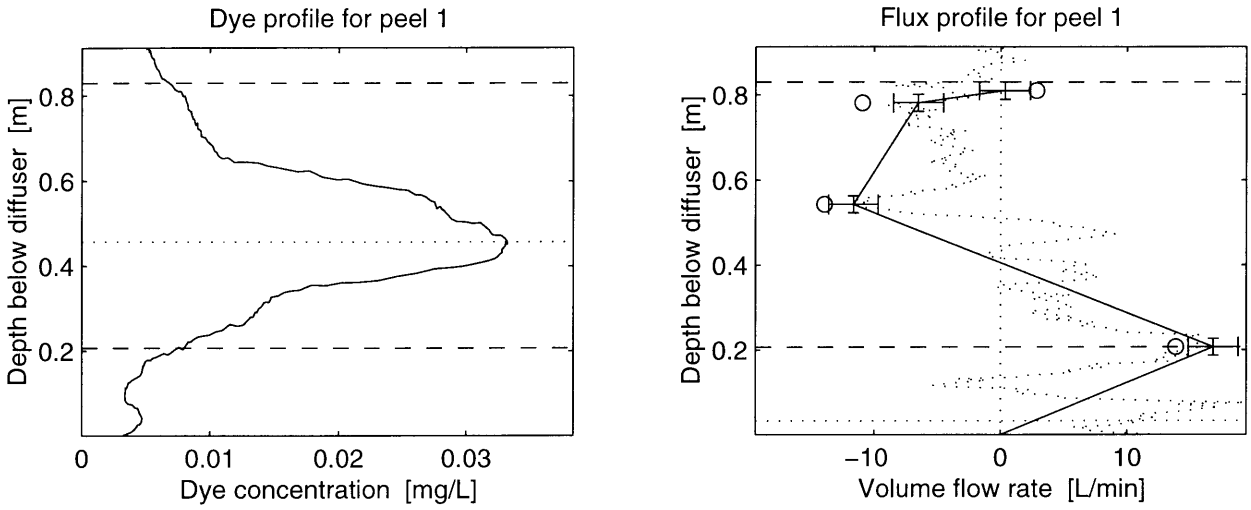

Q1 = 13.9 [L/min]	c1 = 0.38 [mg/L]	p1 = 1006 [Kg/m^3]	B1 = 97.63 [Kg/m^3]
Q2 = 2.83 [L/min]	c2 = 0.23 [mg/L]	p2 = 1008 [Kg/m^3]	B2 = 229.2 [cm^4/s^3]
Ql = 3.02 [L/min]	co = 0 [mg/L]	po = 1009 [Kg/m^3]	Bo = 0 [cm^4/s^3]
Qe = 13.8 [L/min]	ci = 0.16 [mg/L]	pi = 1009 [Kg/m^3]	Bi = 0 [cm^4/s^3]
Qi = 27.8 [L/min]	cp = 0.23 [mg/L]	pp = 1008 [Kg/m^3]	Bp = 3206 [cm^4/s^3]
Qp = 39.6 [L/min]	cr = 0.16 [mg/L]	pr = 1009 [Kg/m^3]	Br = 438.9 [cm^4/s^3]
Qr = 28.6 [L/min]	ht = 0.46 [m]	hp = 0.83 [m]	f = 0.93 [--]

FIGURE C-11: Bayesian estimation results for Experiment Sed6.

Appendix D

Correlation fit statistics

Correlations with U_N presented in Chapter 4 are derived from two types of regressions. For variables that do not have a known single-phase value (i.e. a value for $U_N = 0$), simple linear regressions are computed of the form

$$\hat{y} = mU_N + b \tag{D.1}$$

where $\hat{y}$ is the computed dependent variable and m and b are regression coefficients. For data that do have a known single-phase value, non-linear regressions are computed of the form

$$\hat{y} = a + cU_N^d \tag{D.2}$$

where a is the single-phase value and c and d are regression coefficients, obtained by minimizing the squared error between $\hat{y}$ and the model estimates.

As a means of evaluating the correlations, the regressions are also analyzed for their goodness of fit and to test the statistical significance of their implied dependence on U_N. Because the regression equations were obtained using a least-squares technique, we use the coefficient of determination, r^2, to test the goodness of fit (see e.g. Mays & Tung 1992). To test whether the obtained dependence on U_N is significant, we use a t-test as described by Walpole & Myers (1972). For the linear regressions, we test the null hypothesis that the true slope is the slope obtained by the regression against the alternative that the slope is zero.

To use this same test in the non-linear case, we rearrange (D.2) to obtain

$$\log(\hat{y} - a) = \log(c) + d\log(U_N). \tag{D.3}$$

In this case we use the same t-test to determine if the slope, d, in log-space has a significant non-zero value. The t-value we test is

$$t = \frac{\beta - 0}{s/\sqrt{S_{xx}}}, \tag{D.4}$$

where β is the slope in the linear space (i.e. either m or d, as applicable) S_{xx} is the variance of the independent variable (in this case U_N or $\log(U_N)$) and s is defined as

$$s = \sqrt{\frac{S_{yy} - \beta S_{xy}}{n-2}}. \tag{D.5}$$

S_{yy} is the variance of the dependent variable, S_{xy} is the covariance between the dependent and independent variables, and n are the number of data points (11 for our application). We chose a 0.05 level of significance, which for $n - 2 = 9$ degrees of freedom defines a critical region $|t| > 1.83$ for a given non-dimensional variable to have a significant dependence on U_N. Table 4.4 presents fit statistics and regression coefficients for each of the figures presented in Chapter 4.

Bibliography

Adams, E. E., Caulfield, J. A., Herzog, H. J. & Auerbach, D. I. (1997), 'Impacts of reduced pH from ocean CO_2 disposal: Sensitivity of zooplankton mortality to model parameters', *Waste Management* **17**, 375–380.

Adams, E. E., Golomb, D. S. & Herzog, H. J. (1994), 'Ocean disposal of CO_2 at intermediate depths', *Energy Conserv. Mgmt.* **36**(6–9), 447–452.

Adams, E. E. & Herzog, H. J. (1996), Environmental impacts of ocean disposal of CO_2, Technical Report MIT-EL 96-003, Energy Laboratory, Massachusetts Institute of Technology.

Alendal, G. & Drange, H. (2000), 'Two-phase, near-field modeling of purposefully released CO_2 in the ocean', *J. Geophy. Res.: Oceans (submitted)* .

Alendal, G., Drange, H. & Thorkildsen, F. (1998), Two-phase modeling of CO_2 droplet plumes, Technical Report 153, Nansen Environmental and Remote Sensing Center.

Arrhenius, S. (1896), 'On the influence of carbonic acid in the air upon the temperature of the ground', *Philos. Mag.* **41**, 237ff.

Asaeda, T. & Imberger, J. (1993), 'Structure of bubble plumes in linearly stratified environments', *J. Fluid Mech.* **249**, 35–57.

Auerbach, D. I., Caulfield, J. A., Adams, E. E. & Herzog, H. J. (1997), 'Impacts of ocean CO_2 disposal on marine life: I. A toxicological assessment integrating constant-concentration laboratory assay data with variable concentration field exposure', *Env. Model. and Assess. 2* pp. 333–343.

Aya, I., Yamane, K. & Kojima, R. (2000), Simulation experiment of CO_2 storage at 3600 m deep ocean floor, *in* '5th Int. Conf. Greenhouse Gas Control Tech., Cairns, Australia', IEA Greenhouse Gas R&D Program.

Baddour, R. E. (1994), Thermal-saline bubble plumes, *in* P. A. Davies & M. J. V. Neves, eds, 'Recent Research Advances in the Fluid Mechanics of Turbulent Jets and Plumes', Kluwer Academic Publishers, The Netherlands, pp. 117–129.

Baines, W. D. & Leitch, A. M. (1992), 'Destruction of stratification by bubble plumes', *J. Hydr. Engrg.* **118**(4), 559–577.

Beyersdorf, J. (1997), Verhalten von Luftblasen und Sedimenten in Blasensäulen in abhängigkeit vom Saltzgehalt im Wasser, Mitteilungen, Heft 79, Franzius-Institut f. Wasserbau u. Küsteningenieurwesen, Universität Hannover.

Bolin, B. (1995), Climate Change 1995. IPCC Second Assessment: Synthesis of scientific-technical information relevant to interpreting Article 2 of the UNFCCC, Technical report, Intergov. Panel Climate Change, New York.

Brevik, I. & Killie, R. (1996), 'Phenomenological description of the axisymmetric air-bubble plume', *Int. J. Multiphase Flow* **22**(3), 535–549.

Brevik, I. & Kluge, R. (1999), 'On the role of turbulence in the phenomenological theory of plane and axisymmetric air-bubble plume', *Int. J. Multiphase Flow* **25**, 87–108.

Caulfield, J. A. (1996), Environmental impacts of carbon dioxide ocean disposal: Plume predictions and time dependent organism experience, MS thesis, Dept. of Civ. Env. Engrg., MIT, Cambridge, MA.

Caulfield, J. A., Adams, E. E., Auerbach, D. I. & Herzog, H. J. (1997), 'Impacts of ocean CO_2 disposal on marine life: II. Probabilistic plume exposure model used with a time-varying dose-response analysis', *Env. Model. and Assess. 2* pp. 345–353.

Chen, B., Masuda, S., Nishio, M., Someya, S. & Akai, M. (2000), A numerical prediction of plume structure of CO_2 in the ocean–a near field model, *in* '5th Int. Conf. Greenhouse Gas Control Tech., Cairns, Australia', IEA Greenhouse Gas R&D Program.

Chesters, A., van Doorn, M. & Goossens, L. H. J. (1980), 'A general model for unconfined bubble plumes from extended sources', *Int. J. Multiphase Flow* **6**, 499–521.

Clift, R., Grace, J. R. & Weber, M. E. (1978), *Bubbles, Drops, and Particles*, Academic Press, New York, NY.

Crawford, T. V. & Leonard, A. S. (1962), 'Observations of buoyant plumes in calm stably stratified air', *J. App. Met.* p. 254.

Crounse, B. C. (2000), Modeling buoyant droplet plumes in a stratified environment, MS thesis, Dept. of Civ. Env. Engrg., MIT, Cambridge, MA.

Crowe, C., Sommerfield, M. & Tsuji, Y. (1998), *Multiphase flows with droplets and particles*, CRC Press.

Davidson, M. J. & Pun, K. L. (1999), 'Weakly advected jets in cross-flow', *J. Hydr. Engrg.* **125**(1), 47–58.

Dewey, R. K., Stegen, G. R. & Bacastow, R. (1996), Far-field environmental impacts associated with ocean disposal of CO_2, Technical report, Science Applications International Corporation, San Diego, CA.

Dietrich, W. (1982), *Water Resour. Res.* **18**(6), 1615–1626.

Ditmars, J. D. & Cederwall, K. (1974), Analysis of air-bubble plumes, *in* 'Proc. of 14th Int. Conf. Coastal Engrg., Copenhagen', ASCE, pp. 2209–2226.

Doneker, R. L. & Jirka, G. H. (1990), Expert system for hydrodynamic mixing zone analysis of conventional and toxic submerged single port discharges (CORMIX1), Technical Report EPA/600/3-90/012, USEPA, Wash., D.C.

Fischer, H. B., List, E. G., Koh, R. C. Y., Imberger, J. & Brooks, N. H. (1979), *Mixing in Inland and Coastal Waters*, Academic Press, New York, NY.

Gill, A. (1982), *Ocean-Atmosphere Dynamics*, Academic Press, New York, NY.

Goossens, L. H. J. (1979), *Reservoir Destratification with Bubble Columns*, Delft University Press, Delft, The Netherlands.

Gottfried, B. S. & Weisman, J. (1973), *Introduction to Optimization Theory*, Prentice-Hall, Inc., Englewood Cliffs, New Jersey.

HAVIS Environmental (1994), Mixing zone simulation model for dredge overflow and discharge into inland and coastal waters, Prepared for U.S. Army COE Waterways Experiment Station, Technical Report DACW39-93-C-0109, HAVIS Environmental, Fort Collins, CO.

Head, M. (1997), Microscale conductivity-temperature instrument Model 125 Operator's manual, Technical report, Precision Measurement Engineering, Encinitas, California.

Hirai, S., Takamatsu, R., Tabe, Y., Suzuki, K. & Okazaki, K. (2000), Formation of liquid CO_2 droplets and jets with deformation and growth of hydrate film, *in* '5th Int. Conf. Greenhouse Gas Control Tech., Cairns, Australia', IEA Greenhouse Gas R&D Program.

Huang, H., Fergen, R. E., Proni, J. R. & Tsai, J. J. (1998), 'Initial dilution equations for buoyancy-dominated jets in current', *J. Hydr. Engrg.* **124**, 105–108.

Hugi, C. (1993), Modelluntersuchungen von Blasenstrahlen für die Seebelüftung, Ph.D. Thesis, Inst. f. Hydromechanik u. Wasserwirtschaft, ETH, Zürich.

Hussain, N. A. & Narang, B. S. (1984), 'Simplified analysis of air-bubble plumes in moderately stratified environments', *J. Heat Trans.* **106**, 543–551.

Jakobsen, H. A., Sannaes, B. H., Grevskott, S. & Svendsen, H. F. (1997), 'Modeling of vertical bubble-driven flows', *Ind. Eng. Chem. Res.* **36**, 4052–4074.

Johansen, Ø. (1999), DeepBlow – a Lagrangian plume model for deep water blowouts, *in* 'Proc. 3rd Int. Marine Environ. Modelling Seminar, Lillehammer'.

Johnson, A. B. & White, D. B. (1993), 'Experimental-determination of gas migration velocities with non-Newtonian fluids', *Int. J. Multiphase Flow* **19**(6), 921–941.

Kobus, H. E. (1968), Analysis of the flow induced by air-bubble systems, *in* 'Proc. 11th Int. Conf. Coastal Engrg., London', ASCE, pp. 1016–1031.

Koh, R. C. Y. & Chang, Y. C. (1973), Mathematical model for barged ocean disposal of waste, Technical Report 660/2-73-029, U.S. EPA, Washington, D.C.

Lapin, A. & Lübbert, A. (1994), 'Numerical simulation of the dynamics of two-phase gas-liquid flows in bubble columns', *Chemical Engineering Science* **49**(21), 3661–3674.

Leifer, I., Patro, R. & Bowyer, P. (2000), 'A study on the temperature variation of rise velocity for large clean bubbles', *J. Atm. and Ocean Tech., (accepted)* .

Leitch, A. M. & Baines, W. D. (1989), 'Liquid volume flux in a weak bubble plume', *J. Fluid Mech.* **205**, 77–98.

Lemckert, C. J. & Imberger, J. (1993), 'Energetic bubble plumes in arbitrary stratification', *J. Hydr. Engrg.* **119**(6), 680–703.

Libbey–Owens–Ford Co. (1990), ATS–132 Glass for aquariums, Technical report, Libbey–Owens–Ford Co. Technical Center.

Liro, C. R., Adams, E. E. & Herzog, H. J. (1991), Modeling the release of CO_2 in the deep ocean, Technical Report MIT-EL 91-002, Energy Laboratory, MIT, Cambridge, MA.

Liro, C. R., Adams, E. E. & Herzog, H. J. (1992), 'Modeling the release of CO_2 in the deep ocean', *Energy Conserv. Mgmt.* **33**(5–8), 667–674.

Masutani, S. M., Nishio, M. & Tang, L. (2000), CO_2 jet break-up under simulated deep ocean conditions, *in* '5th Int. Conf. Greenhouse Gas Control Tech., Cairns, Australia', IEA Greenhouse Gas R&D Program.

Matsunashi, S. & Miyanaga, Y. (1990), 'A field study on the characteristics of air bubble plume in a reservoir', *J. Hydrosci. Hydr. Engrg.* **8**(2), 65–77.

Mays, L. W. & Tung, Y.-K. (1992), *Hydrosystems Engineering and Management*, McGraw Hill, New York, New York.

McDougall, T. J. (1978), 'Bubble plumes in stratified environments', *J. Fluid Mech.* **85**(4), 655–672.

McDougall, T. J. (1979), 'On the elimination of refractive-index variations in turbulent density-stratified liquid flows', *J. Fluid Mech.* **93**(1), 83–96.

Milgram, J. H. (1983), 'Mean flow in round bubble plumes', *J. Fluid Mech.* **133**, 345–376.

Morton, B. R. (1962), 'Coaxial turbulent jets', *J. Heat and Mass Transfer* **5**, 955–965.

Morton, B. R., Taylor, S. G. I. & Turner, J. S. (1956), 'Turbulent gravitational convection from maintained and instantaneous sources', *Proc. of the Royal Soc.* **A234**, 1–23.

Nash, J. D., Jirka, G. H. & Chen, D. (1995), 'Large scale planar laser induced fluorescence in turbulent density-stratified flows', *Exp. in Fluids* **19**, 297–304.

Ogasawara, K.-I. & Yamasaki, A. (2000), An experimental study on the mass transfer behavior of liquid CO_2 drops in the simulated ocean condition at the intermediate depth, *in* '5th Int. Conf. Greenhouse Gas Control Tech., Cairns, Australia', IEA Greenhouse Gas R&D Program.

Ohsumi, T., Nakashiki, N., Shitashima, K. & Hirama, K. (1992), 'Density change of water due to dissolution of carbon dioxide and near-field behavior of CO_2 from a source on deep-sea floor', *Energy Conserv. Mgmt.* **33**(5–8), 685–690.

Park, H. J. & Yang, W. J. (1997), 'Turbulent two-phase mixing in gas-stirred ladle systems for continuous casing applications', *Num. Heat Trans. Part A–Applications* **31**(5), 493–515.

Patterson, J. C. & Imberger, J. (1989), 'Simulation of bubble plume destratification systems in reservoirs', *Aquatic Sci.* **51**(1), 1–18.

Pun, K. L. & Davidson, M. J. (1999), 'On the behavior of advected plumes and thermals', *J. Hydr. Res.* **37**(4), 519–540.

Reingold, L. S. (1994), An experimental comparison of bubble and sediment plumes in stratified environments, MS thesis, Dept. of Civ. Envir. Engrg., MIT, Cambridge, MA.

Roig, V., Suzanne, C. & Masernat, L. (1998), 'Experimental investigation of a turbulent bubbly mixing layer', *Int. J. Multiphase Flow* **24**(1), 35–54.

Ruggaber, G. J. (2000), Dynamics of particle clouds related to open-water sediment disposal, Ph.D. Thesis, Dept. of Civ. Env. Engrg., MIT, Cambridge, MA.

Rye, H., Johansen, Ø. & Kolderup, H. (1998), Drop size formation from deep water blowouts, Technical Report STF66 F98090, SINTEF Appl. Chem., Trondheim, Norway.

Rygg, O. B. & Emilsen, M. H. (1998), A parameter study of blowout rates for deep water and their effect on oil droplet and gas bubble generation, Technical report, Well Flow Dynamics, Billingstad, Norway.

Sato, T. & Hama, T. (2000), Numerical simulation of dilution process in CO_2 ocean sequestration, *in* '5th Int. Conf. Greenhouse Gas Control Tech., Cairns, Australia', IEA Greenhouse Gas R&D Program.

Schladow, S. G. (1993), 'Lake destratification by bubble-plume systems: Design methodology', *J. Hydr. Engrg.* **119**(3), 350–368.

Schweppe, F. C. (1973), *Uncertain Dynamic Systems*, Prentice-Hall, Inc., Englewood Cliffs, New Jersey.

Socolofsky, S. A. (2000), Laboratory Experiments of Multi-phase Plumes in Stratification and Crossflow, Ph.D. Thesis, Dept. of Civ. Env. Engrg., MIT, Cambridge, MA (in prep.).

Socolofsky, S. A. & Adams, E. E. (2000*a*), 'Multi-phase plumes in stratification: Dimensional analysis', *Journal of Fluid Mechanics* (submitted).

Socolofsky, S. A. & Adams, E. E. (2000*b*), 'Multi-phase plumes in stratification: Liquid volume fluxes', *Journal of Fluid Mechanics* (submitted).

Socolofsky, S. A. & Adams, E. E. (2000*c*), 'Multi-phase plumes in uniform and stratified crossflow', *Journal of Hydraulic Research* (submitted).

Socolofsky, S. A., Crounse, B. C. & Adams, E. E. (2000), Multi-phase plumes in uniform, stratified and flowing environments, *in* H. Shen, A. Cheng, K.-H. Wang & M. H. Teng, eds, 'Environmental Fluid Mechanics–Theories and Applications', ASCE/Fluids Committee.

Tacke, K. H., Schubert, H. G., Weber, D. J. & Schwerdtfeger, K. (1985), 'Characteristics of round vertical gas bubble jets', *Metal. Trans. B* **16B**(2), 263–275.

Taitel, Y., Barnea, D. & Brill, J. P. (1995), 'Stratified 3-phase flow in pipes', *Int. J. Multiphase Flow* **21**(1), 53–60.

Thorkildsen, F., Alendal, G. & Haugan, P. M. (1994), Modelling of CO_2 droplet plumes, Technical Report 96, Nansen Environmental and Remote Sensing Center, Adv. Griegsvei 3A, N - 5037 Solheimsviken, Norway.

Topham, D. R. (1975), Hydrodynamics of an oilwell blowout, Technical Report 33, Beaufort Sea, Institute of Ocean Sciences, Sidney, B.C., Canada.

Townsend, A. A. (1976), *The structure of turbulent shear flow*, Cambridge University Press.

Turner, J. S. (1986), 'Turbulent entrainment: the development of the entrainment assumption, and its application to geophysical flows', *J. Fluid Mech.* **173**, 431–471.

U.S. EPA (1997), *Brief History of the Clean Water Act*, U.S. EPA Office of Water, http://www.epa.gov/owow/cwa/history.htm.

Walpole, R. E. & Myers, R. H. (1972), *Probability and Statistics for Engineers and Scientists*, Fourth edn, MacMillan Publishing Company, New York, New York.

Wilkinson, D. L. (1979), 'Two-dimensional bubble plumes', *J. Hydr. Div.* **105**(HY2), 139–154.

Wong, C. S. & Hirai, S. (1997), Ocean storage of carbon dioxide—a review of ocean carbonate and CO_2 hydrate chemistry, Technical report, IEA Greenhouse Gas R&D Prog., Cheltenham, UK.

Wright, S. J. (1984), 'Buoyant jets in density-stratified crossflow', *J. Hydr. Engrg.* **110**, 643–656.

Wright, S. J., Roberts, P. J. W., Zhongmin, Y. & Bradley, N. E. (1991), 'Surface dilution of round submerged buoyant jets', *J. Hydr. Res.* **29**(1), 67–89.

Wüest, A., Brooks, N. H. & Imboden, D. M. (1992), 'Bubble plume modeling for lake restoration', *Water Resour. Res.* **28**(12), 3235–3250.

Yapa, P. D. & Zheng, L. (1997*a*), 'Simulation of oil spills from underwater accidents I: Model development', *J. Hydr. Res.* **35**(5), 673–687.

Yapa, P. D. & Zheng, L. (1997*b*), 'Simulation of oil spills from underwater accidents II: Model verification', *J. Hydr. Res.* **35**(5), 688–697.

Yapa, P. D. & Zheng, L. (1999), 'Modeling underwater oil/gas jets and plumes', *J. Hydr. Engrg.* **125**(5), 481–491.

Zic, K., Stefan, H. G. & Ellis, C. (1992), 'Laboratory study of water destratification by a bubble plume', *J. Hydr. Res.* **30**(1), 7–27.